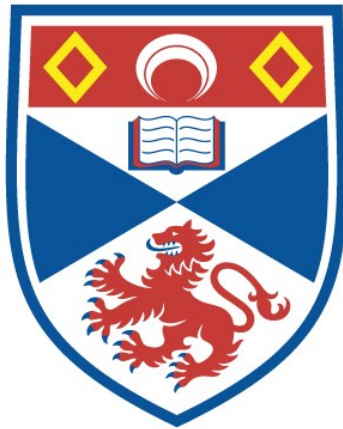


Positive electrode materials for high energy rechargeable batteries

Eun Jeong Kim

A thesis submitted for the degree of PhD
at the
University of St Andrews



2023

Full metadata for this thesis is available in
St Andrews Research Repository
at:

<https://research-repository.st-andrews.ac.uk/>

Identifier to use to cite or link to this thesis:

DOI: <https://doi.org/10.17630/sta/771>

This item is protected by original copyright

Candidate's declaration

I, Eun Jeong Kim, do hereby certify that this thesis, submitted for the degree of PhD, which is approximately 33,600 words in length, has been written by me, and that it is the record of work carried out by me, or principally by myself in collaboration with others as acknowledged, and that it has not been submitted in any previous application for any degree.

I was admitted as a research student at the University of St Andrews in January 2016.

I received funding from an organisation or institution and have acknowledged the funder(s) in the full text of my thesis.

Date

Signature of candidate

Supervisor's declaration

I hereby certify that the candidate has fulfilled the conditions of the Resolution and Regulations appropriate for the degree of PhD in the University of St Andrews and that the candidate is qualified to submit this thesis in application for that degree.

Date

Signature of supervisor

Permission for publication

In submitting this thesis to the University of St Andrews we understand that we are giving permission for it to be made available for use in accordance with the regulations of the University Library for the time being in force, subject to any copyright vested in the work not being affected thereby. We also understand, unless exempt by an award

of an embargo as requested below, that the title and the abstract will be published, and that a copy of the work may be made and supplied to any bona fide library or research worker, that this thesis will be electronically accessible for personal or research use and that the library has the right to migrate this thesis into new electronic forms as required to ensure continued access to the thesis.

I, Eun Jeong Kim, confirm that my thesis does not contain any third-party material that requires copyright clearance.

The following is an agreed request by candidate and supervisor regarding the publication of this thesis:

Printed copy

Embargo on all of print copy for a period of 1 year on the following ground(s):

- Publication would preclude future publication

Supporting statement for printed embargo request

I have publications pending.

Electronic copy

Embargo on all of electronic copy for a period of 1 year on the following ground(s):

- Publication would preclude future publication

Supporting statement for electronic embargo request

I have publications pending.

Title and Abstract

- I agree to the title and abstract being published.

Date

Signature of candidate

Date

Signature of supervisor

Underpinning Research Data or Digital Outputs

Candidate's declaration

I, Eun Jeong Kim, hereby certify that no requirements to deposit original research data or digital outputs apply to this thesis and that, where appropriate, secondary data used have been referenced in the full text of my thesis.

Date

Signature of candidate

Acknowledgements

General acknowledgements

First of all, I would like to express my sincere gratitude to my amazing supervisor, Dr A. Robert Armstrong, for the continuous support during my PhD study, his patience, motivation and immense knowledge. His guidance helped me at all times of my studies. I would also like to thank my second supervisor, Professor John T.S. Irvine for his guidance and support during my PhD.

I am grateful to the past and present members of the JTSI group for their support and helpful discussions. In particular, many thanks to Dr Xiangling Yue for morphology studies of my samples, Dr David Miller for TEM measurements, Dr Paul Connor for the assistance with the set up for electrochemical tests, Dr JinGoo Lee for the arrangement of ICP-OES measurements in Yonsei University, Dr Julia Payne for the help with refinements. Also, I would like to acknowledge Mr Stewart Dickson and Miss Stephanie Linnell for useful discussions on my work and maintenance of glove boxes and Mrs. Julie Nairn for her assistance with various experimental matters.

I am also grateful to various people in the School of Chemistry for their help with the equipment used during my experiments. In particular, many thanks to Dr Yuri Andreev for PXRD measurements, Mrs Maria Nowosielska for ICP-OES analysis, Dr Steve Francis for XPS analysis and Mr. Ross Blackley for SEM training.

I would like to thank Professor Alan V. Chadwick for the acceptance of proposal on B18 at the Diamond Light Source as part of the Energy Material Block Allocation Group SP14239 and Dr Giannantonio Cibin for the measurements of my samples. I would also like to thank Dr Ron I. Smith and Dr Ivan da Silva for PND measurements on Polaris and GEM diffractometers, respectively, at ISIS at the Rutherford Appleton Laboratory. I am also grateful to Dr Kazuki Tsuruta for the provision of beam time and assistance on BL27SU at Spring 8.

I thank Professor Christian Masquelier who provided me an opportunity to join his team and gave access to the laboratory and research facilities during my visit at LRCS. I also thank Professor Laurence Croguennec for useful discussions. Also, I thank Dr David M. Pickup for his help with analysis of XANES data, Professor Reza Younesi, Professor Laurent C. Duda and Miss Le Anh Ma for XPS, XAS and RIXS measurements for my samples and fruitful discussions.

Acknowledgements

I gratefully acknowledge Alistore ERI for the award of a studentship and ScotChem for the Postgraduate and Early Career Researcher Exchanges (PECRE) award.

마지막으로, 박사 과정 동안 늘 뒤에서 묵묵히 응원해주신 사랑하는 두 부모님, 동생 그리고 도련님 가족에게 감사를 표합니다. 언제나 든든한 지원군인 내 사랑 마이 훈에게 글로는 다 표현하지 못할 감사함을 전해요. 사랑해요.

Funding

This work was supported by the Alistore ERI.

Research Data/Digital Outputs access statement

Research data underpinning this thesis are not required to be deposited.

Abstract

With the growth of environmental concerns, rechargeable batteries – lithium ion batteries (LIBs) and sodium ion batteries (SIBs) - have been employed in a large number of different applications. To meet the market needs in terms of their performance, positive electrode materials with high energy density are in high demand.

The aim of this thesis work is to provide strategies which enhance electrochemical performance of LiCoPO_4 as a high voltage positive electrode material for LIBs (chapter 3 and chapter 4) and an insight into the mechanism which triggers oxygen redox activity of P3-type $\text{Na}_{0.67}\text{M}_{0.2}\text{Mn}_{0.8}\text{O}_2$ (M= Mg and Ni in chapter 5 and 6, respectively) as potential candidates for high capacity positive electrode materials in SIBs.

Studies on the improvement of cyclability of LiCoPO_4 were carried out using aqueous binders, of which, sodium carboxymethyl cellulose (CMC) permits more stable cycling performance and better rate capability with respect to the conventional organic solvent-soluble binders. In addition, substitution of magnesium for cobalt was investigated, which demonstrates that doping with magnesium can be one of the solutions to obtain stable capacity on extended cycling.

Both P3-type $\text{Na}_{0.67}\text{Mg}_{0.2}\text{Mn}_{0.8}\text{O}_2$ and $\text{Na}_{0.6}\text{Ni}_{0.2}\text{Mn}_{0.8}\text{O}_2$ were synthesised by a co-precipitation method and studied to understand the origin of abnormal capacity on the first charge. Careful electrochemical and structural characterisation combined with bulk and surface spectroscopic techniques (XAS, XPS) reveal the oxygen redox activity in $\text{Na}_{0.67}\text{Mg}_{0.2}\text{Mn}_{0.8}\text{O}_2$. As a consequence of vacancies in the transition metal layers of $\text{Na}_{0.67}\text{Mg}_{0.2}\text{Mn}_{0.8}\text{O}_2$ prepared under oxygen, reversible oxygen redox is enhanced. Subsequently, substitution of nickel for manganese was carried out to increase capacity using the $\text{Ni}^{2+}/\text{Ni}^{4+}$ redox couple of nickel. The presence of oxygen redox activity in $\text{Na}_{0.6}\text{Ni}_{0.2}\text{Mn}_{0.8}\text{O}_2$ is also demonstrated by using a range of spectroscopic techniques (XAS, SXAS, RIXS), which is stabilised by reduction of nickel through the reductive coupling mechanism.

Table of contents

Acknowledgements.....	1
Abstract.....	3
Table of contents	4
Abbreviations	9
1. Introduction	11
1.1 Importance of rechargeable batteries	11
1.2. Rechargeable batteries overview	12
1.2.1. Energy storage mechanism	12
1.2.2. Lithium-ion battery (LIB)	13
• Positive electrode materials for LIBs.....	13
• Negative electrode materials for LIBs	16
• Electrolytes for LIBs.....	17
• Solid electrolyte interphase (SEI) layer on positive electrode materials for LIBs	17
1.2.3. Sodium-ion battery (SIB)	18
• Positive electrode materials for SIBs.....	18
• Negative electrode materials for SIBs.....	20
• Electrolytes for SIBs.....	20
1.2.4. Design of high energy density batteries.....	21
• Operating voltage of a cell	21
• Anion redox for higher specific capacities	25
1.3. High energy positive electrode materials in LIBs and SIBs.....	29
1.3.1. Lithium cobalt phosphate for LIB	29
1.3.2. Manganese-based sodium layered oxides for SIB	32
1.4. Aims of project	36

Table of contents

1.5. References.....	38
2. Experimental	47
2.1. Synthesis techniques.....	47
2.1.1. Solvothermal method	47
2.1.2. Co-precipitation method.....	47
2.2. Analysis techniques.....	48
2.2.1. Powder X-ray diffraction (PXRD)	48
2.2.2. Powder neutron diffraction (PND)	50
2.2.3. Refinement.....	51
2.2.4. Scanning electron microscopy (SEM)	52
2.2.5. Transmission electron microscopy (TEM)	53
2.2.6. Scanning transmission electron microscopy (STEM)	53
2.2.7. Energy dispersive X-ray spectroscopy (EDS)	53
2.2.8. Inductively coupled plasma optical emission spectroscopy (ICP-OES)	54
2.2.9. Fourier transform infra-red spectroscopy (FT-IR)	54
2.2.10. X-ray photoelectron spectroscopy (XPS).....	55
2.2.11. X-ray absorption spectroscopy (XAS).....	56
2.2.12. Resonant inelastic X-ray scattering (RIXS)	57
2.3. Cell assembly.....	58
2.3.1. Fabrication of electrodes	58
• Cast electrodes.....	58
• Loose powder electrodes	58
2.3.2. Coin cell and Swagelok-type cell assembly	59
2.4. Electrochemical characterisation.....	60
2.4.1. Battery metrics.....	60
• Capacity.....	60
• Specific energy and power density	60

Table of contents

2.4.2. Galvanostatic cycling	61
2.4.3. Cyclic voltammetry.....	62
2.4.4. Electrochemical impedance spectroscopy (EIS).....	62
2.5. References.....	64
3. Lithium cobalt phosphate	66
3.1. Introduction	66
3.2. Experimental methods.....	68
3.2.1. Synthesis of LCP	68
3.2.2. Analyses and characterisation of as-synthesised LCP	69
3.2.3. Exposure of LCP to deionised water (DIW)	69
3.2.4. Preparation of electrodes and characterisation of as-prepared electrodes.....	69
3.2.5. Preparation of cells and electrochemical tests	70
3.2.6. <i>Ex-situ</i> measurements of cycled electrodes.....	71
3.3. Results and discussion.....	72
3.3.1. Characterisation of as-synthesised LCP	72
3.3.2. Electrode formulation using aqueous binders	73
3.3.3. Electrochemical properties of LCP electrodes	74
3.3.4. Role of CMC in enhanced electrochemical performance	79
• Morphology of electrode surface	79
• Molecular structure of binders	81
• Carboxylate groups in binders as a HF scavenger	82
3.3.5. Proof of concept of the role of CMC	83
3.3.6. <i>Ex-situ</i> studies of CMC based electrodes	84
• SEM analysis.....	84
• FT-IR measurements	85
• PXRD analysis	86
3.4. Summary	88

Table of contents

3.5. References.....	89
4. Magnesium doped lithium cobalt phosphate	92
4.1. Introduction	92
4.2. Experimental methods	93
4.2.1. Synthesis of $\text{LiMg}_x\text{Co}_{1-x}\text{PO}_4$ ($x = 0, 0.05, 0.10, 0.15$ and 0.20)	93
4.2.2. Analyses and characterisation of as-synthesised samples.....	94
4.2.3. Preparation of electrodes	94
4.2.4. Preparation of cells and electrochemical tests	94
4.2.5. <i>Operando</i> XRD measurements.....	95
4.2.6. <i>Ex-situ</i> TEM measurement	95
4.3. Results and discussion.....	97
4.3.1. Characterisation of as-synthesised materials	97
4.3.2. Electrochemical behaviour of as-synthesised materials.....	104
4.3.3. Origin of enhanced cycle stability	107
4.4. Summary	113
4.5. References.....	114
5. P3-type magnesium doped sodium manganese oxide	117
5.1. Introduction	117
5.2. Experimental method	118
5.2.1. Synthesis of P3-type $\text{Na}_{0.67}\text{Mg}_{0.2}\text{Mn}_{0.8}\text{O}_2$ materials.....	118
5.2.2. Analyses and characterisation of as-synthesised materials.....	118
5.2.3. Preparation of electrodes	119
5.2.4. Preparation of cells	119
5.2.5. Analyses and characterisation of <i>ex-situ</i> samples	120
5.3. Results and discussion.....	121
5.3.1. Characterisation of as-synthesised compounds	121
5.3.2. Electrochemical properties	124

Table of contents

5.3.3. Structural evolution upon cycling for Air- $\text{Na}_{0.67}\text{Mg}_{0.2}\text{Mn}_{0.8}\text{O}_2$	128
5.3.4. Structural evolution upon cycling for Oxygen- $\text{Na}_{0.67}\text{Mg}_{0.2}\text{Mn}_{0.8}\text{O}_2$	132
5.3.5. Bulk electronic structure study for Air- $\text{Na}_{0.67}\text{Mg}_{0.2}\text{Mn}_{0.8}\text{O}_2$	135
5.3.6. Surface study for Air- $\text{Na}_{0.67}\text{Mg}_{0.2}\text{Mn}_{0.8}\text{O}_2$	135
5.3.7. Exploring abnormal charge capacity on the first cycle	138
5.4. Summary	142
5.5. References.....	143
6. P3-type nickel doped sodium manganese oxide	145
6.1. Introduction	145
6.2. Experimental methods	146
• Synthesis of P3-type $\text{Na}_{0.67}\text{Ni}_{0.2}\text{Mn}_{0.8}\text{O}_2$	146
• Analyses and characterisation of as-synthesised P3-type $\text{Na}_{0.67}\text{Ni}_{0.2}\text{Mn}_{0.8}\text{O}_2$..	146
• Preparation of electrodes	147
• Preparation of cells	147
• Analyses and characterisation of <i>ex-situ</i> P3-type $\text{Na}_{0.67}\text{Ni}_{0.2}\text{Mn}_{0.8}\text{O}_2$	148
6.3. Results and discussion.....	149
6.3.1. Characterisation of as-synthesised P3-type $\text{Na}_{0.67}\text{Ni}_{0.2}\text{Mn}_{0.8}\text{O}_2$	149
6.3.2. Electrochemical properties	150
6.3.3. Bulk electronic structure study for transition metals using XAS.....	152
6.3.4. Electronic structure study for oxygen using SXAS and RIXS.....	154
6.3.5. Oxygen redox activity in $\text{Na}_{0.67}\text{Ni}_{0.2}\text{Mn}_{0.8}\text{O}_2$	157
6.4. Summary	159
6.5. References.....	160
7. General conclusion.....	163
Appendix I	166

Abbreviations

LIB	Lithium ion battery
SIB	Sodium ion battery
SEI	Solid electrolyte interface
EC	Ethylene carbonate
DMC	Dimethyl carbonate
DEC	Diethyl carbonate
PC	Propylene carbonate
LUMO	Lowest unoccupied molecular orbital
HOMO	Highest occupied molecular orbital
SERS	Surface-enhanced Raman spectroscopy
DEMS	Differential electrochemical mass spectroscopy
STEM	Scanning transmission electron microscopy
EELS	Electron energy loss spectroscopy
XAS	X-ray absorption spectroscopy
SXAS	Soft X-ray absorption spectroscopy
TFY	Total fluorescence yield
FY	Total fluorescence yield
TEY	Total electron yield
RIXS	Resonant inelastic X-ray scattering
PXRD	Powder X-ray diffraction
PND	Powder neutron diffraction
SEM	Scanning electron microscopy
TEM	Transmission electron microscopy
EDS	Energy dispersive X-ray spectroscopy
ICP-OES	Inductively coupled plasma optical emission spectroscopy
FT-IR	Fourier transform infra-red spectroscopy
XPS	X-ray photoelectron spectroscopy
XANES	X-ray absorption near edge structure
EXAFS	Extended X-ray absorption fine structure
EIS	Electrochemical impedance spectroscopy
LCP	LiCoPO ₄

Abbreviations

DIW	Deionised water
CMC	Sodium carboxymethyl cellulose
ALG	Sodium alginate
PAA	Polyacrylic acid sodium salt
PVDF	Polyvinylidene fluoride

1. Introduction

1.1 Importance of rechargeable batteries

Today, ever-growing environmental issues and finite fossil fuel resources require new energy storage technologies. Rechargeable batteries are one of the electrochemical energy storage systems which have received considerable attention as a potential solution to deal with the growth of energy demand without increasing carbon footprint.

In electric vehicles, since the introduction of the first rechargeable batteries based on lead-acid, extensive studies have been conducted to improve the ability to store energy per unit volume or per unit mass, energy density, and life span of the batteries. However, the nickel-cadmium or nickel-metal hydride systems are unsatisfactory due to toxicity of cadmium or high cost of nickel, self-discharge problems and a low energy density. Nowadays, the lithium ion battery (LIB) is the dominant choice in this area, with its advantages including enhanced energy density, long cycle life and low toxicity. However, the LIB for electric vehicles needs to be advanced to achieve the specific requirements for mass market penetration, e.g., having gravimetric energy density of about 350 Wh kg^{-1} at cell level, reducing the cost to \$100 per kWh, increasing the driving range to 500 km, decreasing the charge time to 15 min and lasting more than 7 years, according to the US Department of Energy and the Advanced Battery Consortium.¹

In grid energy storage systems, the development of batteries is essential for the successful operation of a system to match energy supply and demand. The LIB has drawn attention because of its advantages such as high round trip efficiency (the ratio of energy put in to energy retrieved from the storage), long cycle life, low maintenance and the flexibility to perform a variety of functions.² Especially, the integration of LIB with intermittent renewable energy sources is an excellent technology for a sustainable planet.³ One of the key requirements for batteries in large-scale energy storage systems is low cost, including raw materials, production and installation of batteries.⁴ In this respect, the sodium ion battery (SIB) has been considered as a promising alternative system to LIBs due to its competitive cost benefit and abundant resource supply. In addition, the knowledge accumulated during LIB research can be translated to the SIB due to the strong similarities in characteristic properties of lithium and sodium ions.

The rechargeable batteries, LIB and SIB, can cover a wide range of applications from electric vehicles to the grid system, leading to minimising the dependence on fossil fuels as well as lowering the emission of greenhouse gases. For the expanded commercialisation of LIB and SIB in those sectors, extensive efforts need to be devoted to the improvement of their active materials, such as positive and negative electrode materials, in order to meet a large number of criteria. For example, the materials should be stable, react in a reversible manner, maintain their crystal structure, have relatively fast ionic and electronic diffusion, be less toxic, be easily synthesised and be low cost.

1.2. Rechargeable batteries overview

1.2.1. Energy storage mechanism

Rechargeable batteries consist of positive and negative electrodes and an electrolyte. In general, the electrodes are cast on an appropriate current collector as a slurry formulated with an active material, a carbonaceous material to enhance the electronic conductivity and a binder to improve adhesion and mechanical strength. The electrolyte, conventionally soaked in a separator, provides ionic transport between the electrodes.

Fig. 1.1 illustrates the schematic configuration of the first generation LIB. In this system, upon charging, an external current is applied, causing removal of lithium ions from the positive electrode. The lithium ions diffuse into the electrolyte and migrate towards the negative electrode. During discharging, lithium ions are extracted from the negative electrode and move to the positive electrode diffusing through the electrolyte. The electrons flow from the negative electrode to the positive electrode on the external circuit, resulting in the current flow which can be used for applications. For the SIB, the mechanism is essentially identical except sodium ions are the ionic carriers. In the research community, new materials for electrodes and electrolyte in both LIB and SIB have been extensively studied to improve battery performance.

Some important electrode materials as well as electrolytes which have been used in LIB and SIB are presented in the following section, mainly focusing on positive electrode materials.

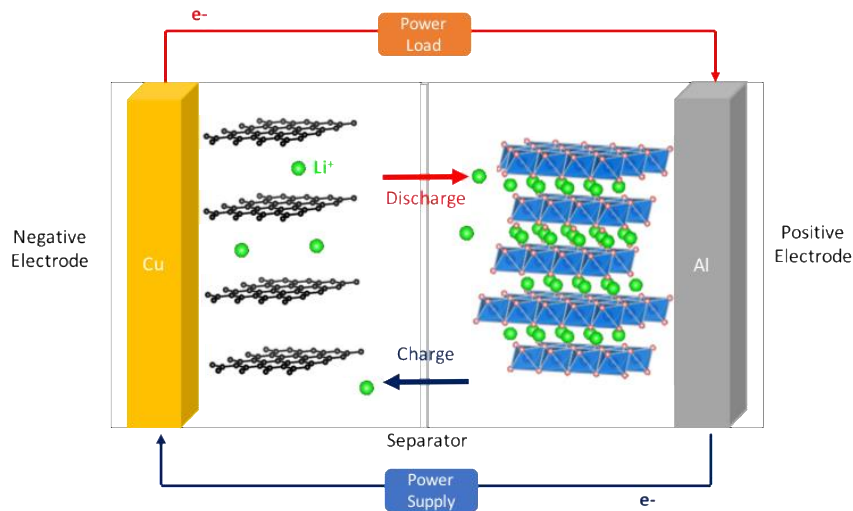


Figure 1.1. Schematic presentation of LIB based on graphite and LiCoO_2 .

1.2.2. Lithium-ion battery (LIB)

- **Positive electrode materials for LIBs**

Lithium cobalt oxide, LiCoO_2 is widely used as a positive electrode material in the LIB for portable electronics due to its high energy density, rate capability and cyclability in limited voltage windows (3.0-4.1 V vs Li/Li^+). LiCoO_2 crystallises in the space group $R\bar{3}m$ and consists of edge-sharing LiO_6 and CoO_6 octahedra (Fig. 1.2) in rhombohedral symmetry.⁵ The main drawback of this material is low reversible capacity, limited to about 130 mAh g^{-1} because of low structural stability. When more than half the lithium ions are removed, a lattice distortion from rhombohedral to monoclinic symmetry is induced, causing a detrimental capacity fade. Reimers et al.⁵ reported that this distortion simultaneously occurs with an in-plane ordering between lithium and vacancy. Later, this ordering in monoclinic $\text{Li}_{0.5}\text{CoO}_2$ was directly observed using electron diffraction.⁶ In addition, the low thermal stability at high temperature gives rise to safety concerns. Thermal stability studies show that LiCoO_2 is stable in air to high temperature but the delithiated phase (Li_xCoO_2 , $x < 1$) is metastable and release oxygen at around 250°C when it is heated in air or inert gas.⁷

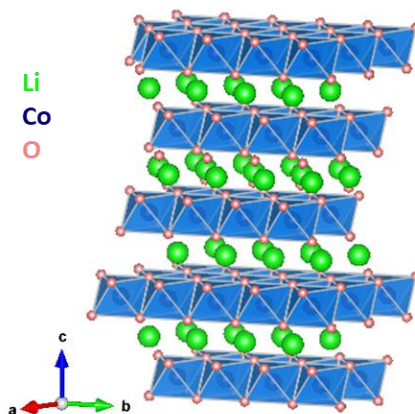


Figure 1.2. Structural representation of LiCoO_2 .

Isostructural lithium nickel oxide, LiNiO_2 , was considered as an alternative material, as nickel provides lower cost and higher capacity. However, preparation of a pure stoichiometric material was challenging. Partial substitution of manganese, cobalt and aluminium for nickel has improved its structural and thermal stability.⁸ In consequence, the optimal composition $\text{LiNi}_{0.80}\text{Co}_{0.15}\text{Al}_{0.05}\text{O}_2$ (NCA) has been used in electric vehicles as well as $\text{LiNi}_{1-x-y}\text{Co}_x\text{Mn}_y\text{O}_2$ ($x = y = 1/3$ for NMC-111).¹

Recently, layered manganese-based lithium-rich oxides, $\text{Li}_{1+x}\text{M}_y\text{Mn}_{1-x-y}\text{O}_2$ ($0 < x + y \leq 1/3$, $M = \text{Co}, \text{Ni}$, and mixture of elements) have gained considerable attention as next generation positive electrode materials due to their cumulative cation and anion redox activity.^{9,10} The structure of these compounds derives from $\text{LiM}_y\text{Mn}_{1-y}\text{O}_2$ ($M = \text{Co}, \text{Ni}$) by substituting lithium for transition metals, and therefore is often written as $\text{Li}[\text{Li}_x\text{M}_y\text{Mn}_{1-x-y}]\text{O}_2$, indicating transition metal layers in square brackets. Despite the large capacity delivered, the compounds suffer from the continuous working voltage decay. The origin of their extra capacity and voltage decay, which has been reported in the literature, involves oxygen loss from the active material^{11,12} and migration of transition metal cations from surface to bulk, tending to form spinel-like structural regions on the surface.^{13,14} Surface coating using carbon, oxides or fluorides has been proposed as an effective way to overcome the issues through suppression of interfacial reaction between the active material and the electrolyte.¹⁵

Lithium iron phosphate, LiFePO_4 , with the olivine structure is one of the positive electrode materials commercialised in electric vehicles and power tools due to its long life span, low toxicity and good thermal stability. LiFePO_4 adopts a triphylite structure, built on distorted hexagonal close-packing oxygen arrangements where lithium and iron ions occupy $4a$ and $4c$ octahedral sites, respectively, and phosphorus occupies tetrahedral sites. Due to the crystal

structure, lithium ions mostly diffuse along the b -axis, leading to limited electrochemical performance. Remarkable improvement has been achieved through the particle size reduction to nanoscale and carbon coating on the surface of particles.¹⁶⁻²⁰ However, the moderate working voltage of about 3.45 V vs Li/Li^+ provides limited energy density. Isostructural lithium cobalt phosphate, LiCoPO_4 , has been considered as an attractive candidate as a high voltage positive electrode as its working voltage is ca. 4.8 V vs Li/Li^+ .

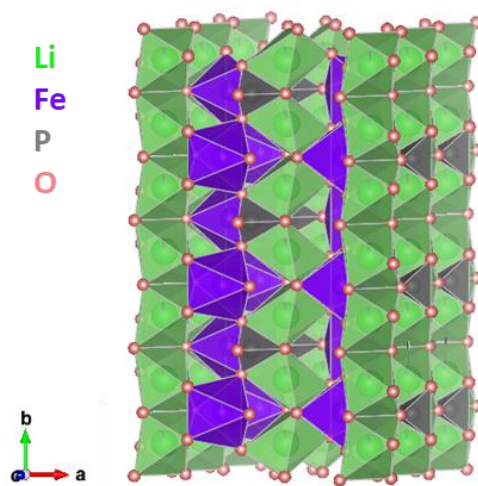


Figure 1.3. Structural representation of LiFePO_4 .

Spinel structure lithium manganese oxide, LiMn_2O_4 , has received extensive interest since the early 1980s owing to low cost and toxicity of manganese.²¹⁻²⁵ In the spinel structure, lithium ions are located on $8a$ tetrahedral sites and manganese are on $16d$ octahedral sites in a cubic close-packed network, providing a 3D lithium ion pathway. However, the dissolution of manganese at elevated temperature causes capacity fade. Partial substitution of manganese with aluminium, iron, cobalt or nickel and surface coating have been considered as promising solutions.

$\text{LiNi}_{0.5}\text{Mn}_{1.5}\text{O}_4$ has gained considerable attention as manganese remains essentially in the tetravalent oxidation state, avoiding the complications associated with Jahn-Teller distortion and Mn dissolution. It shows a high potential plateau at around 4.7 V vs Li/Li^+ where the two redox processes of $\text{Ni}^{2+}/\text{Ni}^{3+}$ and $\text{Ni}^{3+}/\text{Ni}^{4+}$ are involved. $\text{LiNi}_{0.5}\text{Mn}_{1.5}\text{O}_4$ has two different crystal structures in the space groups $Fd\bar{3}m$ (Fig. 1.4a) and $P4_332$ (Fig. 1.4b), depending on the ordering of transition metals in the octahedral sites. In disordered $\text{LiNi}_{0.5}\text{Mn}_{1.5}\text{O}_4$, nickel and manganese are randomly distributed in $16d$ sites. In contrast, nickel and manganese are located in distinct $4b$ and $12d$ sites, respectively, in the ordered material. There has been a

consensus²² that disordered $\text{LiNi}_{0.5}\text{Mn}_{1.5}\text{O}_4$ exhibits more stable long-term performance and high rate capability. However, the influence of transition metal ordering on electrochemical performance has been debated in the literature. In the disordered $\text{LiNi}_{0.5}\text{Mn}_{1.5}\text{O}_4$, nickel and manganese containing rock-salt phase impurities are electrochemically inactive, leading to lower capacity. These impurities may also isolate the spinel particles from direct contact with the electrolyte. Nevertheless, higher conductivity of the disordered structure caused by the presence of Mn^{3+} leads to better electrochemical performance than the ordered structure.²⁶⁻²⁸ Computational modelling also suggests that the formation of Mn^{3+} in the spinel structure promotes cation disorder, facilitating lithium ion transport.²⁹ Structural studies using *ex-situ*, *in-situ* or *operando* techniques revealed that the extended solid-solution region of disordered $\text{LiNi}_{0.5}\text{Mn}_{1.5}\text{O}_4$ contributes to superior electrochemical performance.³⁰⁻³³

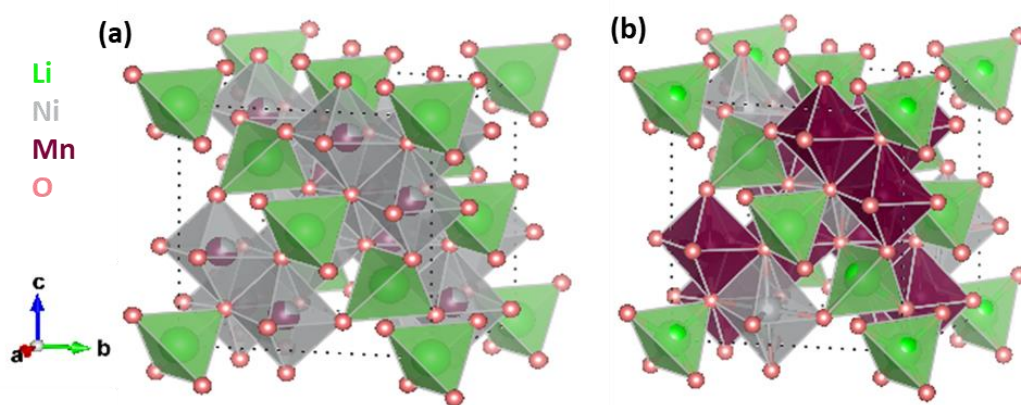


Figure 1.4. Structural representation of (a) disordered and (b) ordered $\text{LiNi}_{0.5}\text{Mn}_{1.5}\text{O}_4$.

- **Negative electrode materials for LIBs**

For negative electrode materials, graphite has remained the dominant choice due to its low working voltage (ca. 0.1 vs Li/Li^+), high specific capacity around 372 mAh g^{-1} and effective formation of solid electrolyte interface (SEI) layer in the presence of ethylene carbonate based electrolyte to prevent exfoliation of graphite.³⁴

Spinel structure lithium titanium oxide, $\text{Li}_4\text{Ti}_5\text{O}_{12}$, has been studied as a negative electrode material and has now been commercialised. $\text{Li}_4\text{Ti}_5\text{O}_{12}$ adopts a defect spinel structure, described also as $\text{Li}[\text{Li}_{1/3}\text{Ti}_{5/3}]\text{O}_4$ where square brackets represent the $16d$ octahedral sites. During charging, three more lithium ions are inserted per formula unit to form $\text{Li}_7\text{Ti}_5\text{O}_{12}$. Despite its high operating voltage (around 1.55 V vs Li/Li^+) leading to lower overall cell voltages, $\text{Li}_4\text{Ti}_5\text{O}_{12}$ exhibits the advantage that it shows almost no changes in the lattice

volume on cycling.³⁵ In addition, this working voltage enables the standard electrolyte to remain intact, bringing enhanced safety and prolonged life span.

Recently, silicon has received considerable attention because it offers ten times higher theoretical capacity (3579 mAh g^{-1}) than graphite and attractive operating voltage (about 0.3 V vs Li/Li^+). However, huge volume changes during electrochemical cycling are a key reason for failure, resulting in large strains in particles that promote micro-crack formation and propagation. Various approaches to solve the issue have included the use of nanoparticles, new binders containing carboxyl groups which exhibit a self-healing effect, i.e., preserving the network between active powder and binders through hydrogen-type interaction.³⁶⁻³⁹

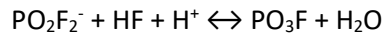
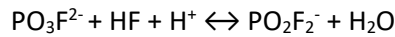
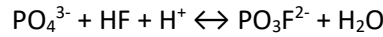
- **Electrolytes for LIBs**

Since alkyl carbonates were found to be the most appropriate solvents for the LIB,⁴⁰ the mixture of ethylene carbonate (EC) and dimethyl carbonate (DMC) and lithium hexafluorophosphate (LiPF_6) as a lithium salt represents the preferred standard electrolyte. The advantages of this electrolyte include high ionic conductivity down to -15°C , high anodic stability of both EC and DMC, high solubility of LiPF_6 in the solvents and the formation of a highly conductive and stable SEI layer on graphite.⁴¹ However, possible decomposition of LiPF_6 can produce hydrogen fluoride (HF). The presence of HF in the electrolyte causes detrimental effects on both the negative and positive electrode materials. In negative electrode materials, especially on graphite, HF reacts with stable SEI species to destroy the passivation layer. In the case of LiCoPO_4 , nucleophilic attack of fluorine anions results in the breakage of phosphorus and oxygen (P-O) bonds of the phosphate anions. Indeed, HF is regenerated catalytically as a side product of the decomposition of LiCoPO_4 , causing a considerable capacity drop in the first few cycles.^{42,43}

- **Solid electrolyte interphase (SEI) layer on positive electrode materials for LIBs**

The formation of a stable SEI layer on not only negative but also positive electrode materials is crucial for successful prolongation of cycle life while preventing further electrolyte decomposition on the surface. In order to form the stable SEI layer on positive electrode materials, studies on the interfacial properties have been carried out and it has been shown that the electrochemical oxidation of LiPF_6 -based conventional electrolyte is a key reason for capacity fade.⁴⁴ In the case of LiMn_2O_4 , electrons produced by the decomposition of the

electrolyte reduce Mn^{4+} to Mn^{3+} in the fully delithiated phase. The resultant Mn^{3+} cations undergo a disproportionation reaction ($2\text{Mn}^{3+} \rightarrow \text{Mn}^{4+} + \text{Mn}^{2+}$) on the surface. The Mn^{2+} cations are dissolved in the electrolyte and move to the graphite, leading to the self-discharge of lithiated graphite.⁴⁵ The electrolyte decomposition is severe above 4.3 V, causing unsatisfactory cycling performance. When LiCoPO_4 is cycled beyond 4.3 V, HF is formed in the presence of traces of water in the electrolyte, which degrades the active material *via* following reactions.⁴³



The reduction of Co^{3+} to Co^{2+} at the end of charge also occurs along with the electrolyte decomposition, forming H^+ , which boosts the above reactions.⁴⁶ Apart from modification of active materials through doping or surface coating, functional additives⁴⁷⁻⁵⁰ and solvents⁵¹⁻⁵³ have shown to be effective to alleviate the degradation of active materials on the surface.

1.2.3. Sodium-ion battery (SIB)

- **Positive electrode materials for SIBs**

Among positive electrode materials for SIBs, layered sodium transition metal oxides (Na_xMO_2 where $0.4 \leq x \leq 1.0$, $M = \text{Ti, Mn, Fe, Co, Ni, Cu, Zn}$ and mixture of elements) have attracted intensive interest due to their high capacities and easy synthesis methods.⁵⁴ The sodium transition metal oxides are built up of sheets of edge-sharing MO_6 octahedra and sodium ions occupying interlayer spaces. Depending on the various oxygen stacking sequences along the *c*-axis, they can be categorised into three groups using the classification proposed by Delmas *et al.*⁵⁵: P3, O3 and P2. The letter indicates the sodium ion coordination environment and the number corresponds to the number of transition metal layers in a hexagonal unit cell. In the P3 structure (Fig. 1.5a), sodium ions occupy trigonal prismatic sites between ABBCCA oxygen stacking, whereas in the O3 structure (Fig. 1.5b) sodium ions are accommodated at octahedral sites between ABCABC oxygen stacking. In the P2 structure (Fig. 1.5c), two MO_2 slabs are in the hexagonal unit cell with sodium ions occupying trigonal prismatic sites between ABBA oxygen stacking. Typically, when the content of sodium ions is between 0.6 and 0.7, P3- and P2-types are structurally stabilised, whereas O3-type is obtained with the

amount of sodium ion being almost 1 in as-synthesised materials. Sodium ion removal from P3, P2 and O3 structures in general induces structural changes.^{56,57} For example, the O3-type materials undergo a phase transition to the P3 structure to reduce the repulsive interaction between transition metal layers through gliding of MO_2 slabs.⁵⁸ The P2 structure can also change into the O2 structure after sodium ion extraction.⁵⁹ These phase transitions significantly affect electrochemical performance especially cycling stability. In addition, the different structures influence kinetics. It has been shown that sodium ions in prismatic sites have a lower energy barrier, leading to higher ionic conductivity.⁵⁹ In O3-type materials, sodium ions move via a hopping mechanism from one octahedral site to an adjacent octahedral site, with a high diffusion barrier. In contrast, sodium ion migration from one prismatic site to a neighbouring prismatic site requires a lower activation energy in the P2 structure.⁵⁹ P2-type $\text{Na}_{2/3}\text{Fe}_{0.5}\text{Mn}_{0.5}\text{O}_2$ is one of the most promising positive electrode materials with an energy density of 520 Wh kg^{-1} vs Na/Na^+ which is comparable to LiFePO_4 (530 Wh kg^{-1} vs Li/Li^+).⁶⁰ However, its large volume change and hygroscopic character are significant drawbacks. In order to improve electrochemical performance of layered sodium transition metal oxides, a large variety of materials have been reported with up to five elements in the transition metal layers.⁶¹⁻⁶³ Most of the reported studies are devoted to O3- or P2-type materials, very few studies have been conducted for P3-type compounds despite the low synthesis temperature, i.e., more eco-friendly than those of P2-type.

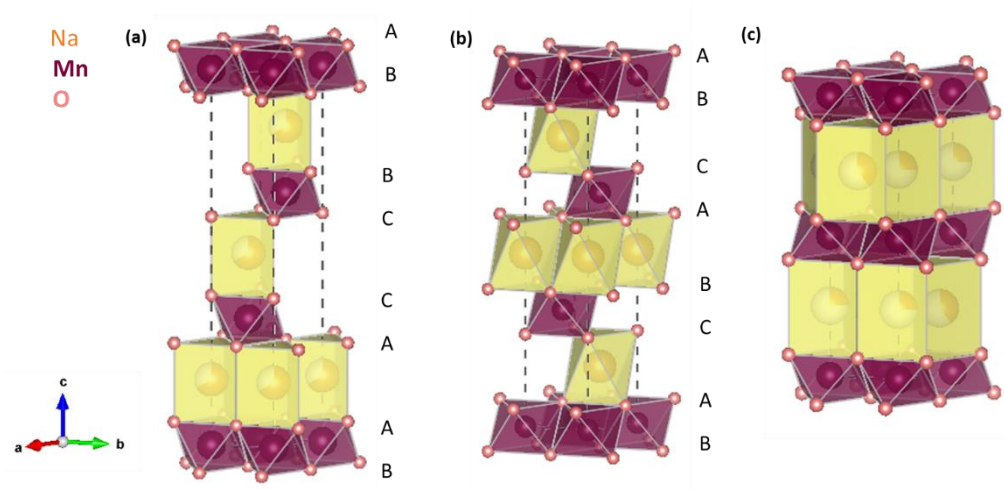


Figure 1.5. Structural representation of (a) P3, (b) O3 and (c) P2 structure of Na_xMnO_2 .

In contrast to the olivine structure of LiFePO_4 , more precisely classified as a triphylite phase, sodium iron phosphate, NaFePO_4 , crystallises as a maricite phase, and shows no electrochemical activity since sodium ions are isolated in 4c octahedral sites while iron

resides in $4a$ octahedral sites. Recently, Kim *et al.*⁶⁴ reported electrochemical activity of NaFePO_4 with the maricite structure, with about 20% carbon. It is shown that maricite structure NaFePO_4 is transformed to amorphous FePO_4 upon the first charge, which allows sodium ions to hop between adjacent sites with lower activation energy along the b -axis. The transformation into the amorphous FePO_4 on the first charge and the reversible sodiation/desodiation via the amorphous phase was also observed by other groups.^{65,66} In the study carried out by Rahman *et al.*,⁶⁵ nanoparticles of NaFePO_4 , entwined within graphene sheets, enhance sodium ion diffusion and tolerance of volume change during cycling. Liu *et al.*⁶⁶ used the electrospinning method to prepare binder-free electrodes of nano-sized (about 1.6 nm) NaFePO_4 , embedded in porous nitrogen-doped carbon nanofibers. The specially designed composite electrodes offer energy density of 168 Wh kg^{-1} in a full cell with carbon nanofiber as the negative electrode material. The importance of electrode architecture on the performance of electrodes is emphasised in both cases. Triphylite phase NaFePO_4 can be prepared by electrochemical lithium/sodium ion exchange from LiFePO_4 . However, its electrochemical performance is poor compared to LiFePO_4 with sluggish kinetics mainly caused by large volume change during cycling.^{67,68}

- **Negative electrode materials for SIBs**

Concerning the negative electrode materials, graphite cannot be used as an intercalation host for sodium ions with conventional electrolytes.^{69,70} Hard carbon, which is difficult to graphitise, highly disordered and contains some parallel stacking of carbon layers, is most commonly used.^{71,72} This structure provides two to three parallel graphene layers and nanoscale porosity. During charge, intercalation of sodium ions occurs through the parallel carbon layers, displaying a slope in the voltage profile. Subsequently the nanoporosity is filled by sodium ions in an analogous manner to adsorption, corresponding to a plateau in the voltage profile.⁷³

- **Electrolytes for SIBs**

As most studies in this field have explored development of new electrode materials, there is no standard electrolyte. The most commonly used electrolyte is based on carbonate solvents such as ethylene carbonate (EC), diethyl carbonate (DEC) or propylene carbonate (PC). For a sodium salt, sodium hexafluorophosphate (NaPF_6) or sodium perchlorate (NaClO_4) are generally used.

1.2.4. Design of high energy density batteries

The energy density of rechargeable batteries is determined by specific capacity and working voltage of the electrode materials in a cell. In order to improve the energy density of the cell, the operating voltage and/or the capacity should be raised without affecting the mass or volume of electrode materials.

- **Operating voltage of a cell**

The difference in chemical potential between negative and positive electrode materials is termed the operating voltage, also known as the open-circuit voltage when no current is applied (Equ. 1.1).^{74,75}

$$eV_{oc} = \mu_{negative} - \mu_{positive} \quad (Equation 1.1)$$

(e : magnitude of the electron charge, V_{oc} : operating voltage with no current applied, $\mu_{negative}$: chemical potential of negative electrode material, $\mu_{positive}$: chemical potential of positive electrode material)

The operating voltage can be limited by electrolyte stability. As shown in Fig. 1.6, thermodynamic stability of the cell requires that the chemical potentials of the electrode materials are located within the electrolyte stability window, which is the difference between reduction and oxidation potential of the electrolyte. Practically, the reduction potential of the electrolyte correlates with the energy of the lowest unoccupied molecular orbital (LUMO) of the reducing species and the oxidation potential is associated with the energy of the highest occupied molecular orbital (HOMO) of the oxidising species in the electrolyte.^{76,77} The intercalation of lithium ions into graphite occurs at about 0.1 V vs Li/Li⁺, which lies just above the LUMO of carbonate based electrolytes in the LIB. In the SIB, the intercalation of sodium ion into hard carbon occurs in the voltage range 0-0.2 V vs Na/Na⁺. In both cases, the formation of the SEI layer permits kinetic stability, ensuring reversible ion transport. Since the chemical potential of negative electrode materials is close to the LUMO and the reduction of carbonaceous based electrolyte produces in general a stable SEI layer, the design of high voltage cells has focused on the modification of the chemical potential of positive electrode materials.

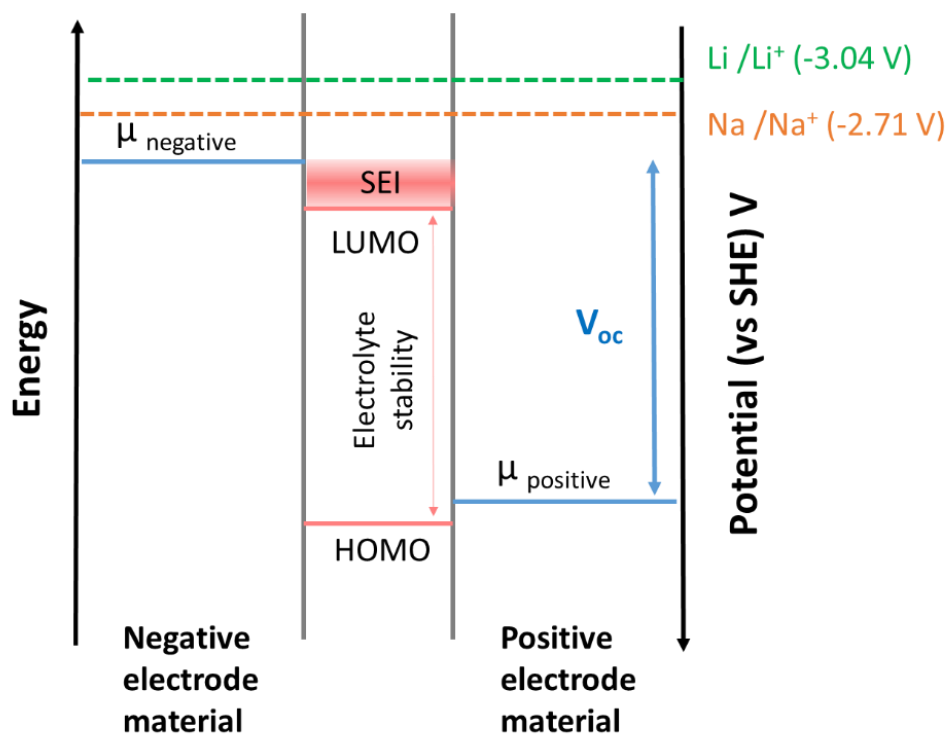


Figure 1.6. Schematic diagram representing energy diagram of negative, positive electrode materials and carbonates based electrolyte.

In general, the chemical potential of the materials corresponds to the energy of the redox couple of the active transition metals,⁷⁵ which relies on various factors such as the crystal structure of the materials, adjacent groups and electronic structure of the transition metals.

The redox couple energy is correlated with the energy required to remove (add) ions from (into) the host crystal, simultaneously oxidising (reducing) the transition metals.⁷⁸ In this aspect, the site energy of the lithium or sodium ion plays a critical role since lower site energy requires more external energy to transfer the ion from occupied sites, resulting in the lower redox couple of the transition metals.²⁵ For example, spinel $\text{Li}_x\text{Mn}_2\text{O}_4$ ($1 < x < 2$) shows two working voltages at about 4.0 V vs Li/Li^+ when $0 < x < 1$ and about 3.0 V vs Li/Li^+ when $1 < x < 2$. The former voltage is associated with the site energy of lithium ion in the $8a$ tetrahedral sites, which requires more activation energy to move the lithium ion. At the latter voltage, the migrating lithium ion is located at $16c$ octahedral sites with higher site energy, therefore less external energy is required.²⁵ Additionally, the coordination of the transition metal affects its redox couple as shown in polyanionic materials.⁷⁹ The change in the redox couple $\text{Fe}^{2+}/\text{Fe}^{3+}$ in the silicate ($\text{Li}_2\text{FeSiO}_4$), borate (LiFeBO_3) and phosphate (LiFePO_4) compounds, where the coordination of iron is tetrahedral, trigonal bipyramidal and octahedral, respectively, reveals

how the structure is associated with the redox couple. As the coordination number increases from $\text{Li}_2\text{FeSiO}_4$ (4 coordination) to LiFePO_4 (6 coordination), iron-oxygen (Fe-O) bonds become less covalent (more ionic) due to more steric hindrance, enabling the redox couple $\text{Fe}^{2+}/\text{Fe}^{3+}$ to shift downwards, delivering higher operating voltage.

Regarding the influence of neighbouring groups on the redox couple, the inductive effect has been widely investigated. The difference in the operating voltage between LiCoPO_4 (ca. 4.8 V vs Li/Li^+) and LiCoO_2 (about 4.0 V vs Li/Li^+) is partially explained by the inductive effect, i.e., the covalent character of cobalt-oxygen (Co-O) bonds is affected by the counter cation from phosphate groups. The presence of phosphorus drives Co-O to be more ionic in character, lowering the redox couple of $\text{Co}^{2+}/\text{Co}^{3+}$ relative to the $\text{Co}^{3+}/\text{Co}^{4+}$ redox couple in LiCoO_2 . In addition, the voltage variation of polyanion electrode materials, crystallising in the same structure, was observed by Manthiram and Goodenough.⁸⁰ In $\text{Li}_2\text{Fe}_2(\text{XO}_4)_3$ ($\text{X} = \text{S}, \text{Mo}, \text{W}$), the covalent character of the bonds between iron and the polyanion ligands, e.g. sulphate (SO_4^{2-}), molybdate (MoO_4^{2-}) and tungstate (WO_4^{2-}), is modified by the counter cation of the ligands. In this study, more covalent oxygen-sulphur (O-S) bonds than oxygen-molybdenum (O-Mo) or oxygen-tungsten (O-W) bonds derived by the higher electronegativity of sulphur decreases the covalent character of iron-oxygen (Fe-O) bonds (more ionic character), which lowers the $\text{Fe}^{2+}/\text{Fe}^{3+}$ redox couple, in consequence $\text{Li}_2\text{Fe}_2(\text{SO}_4)_3$ exhibits the highest working voltage (Fig. 1.7)

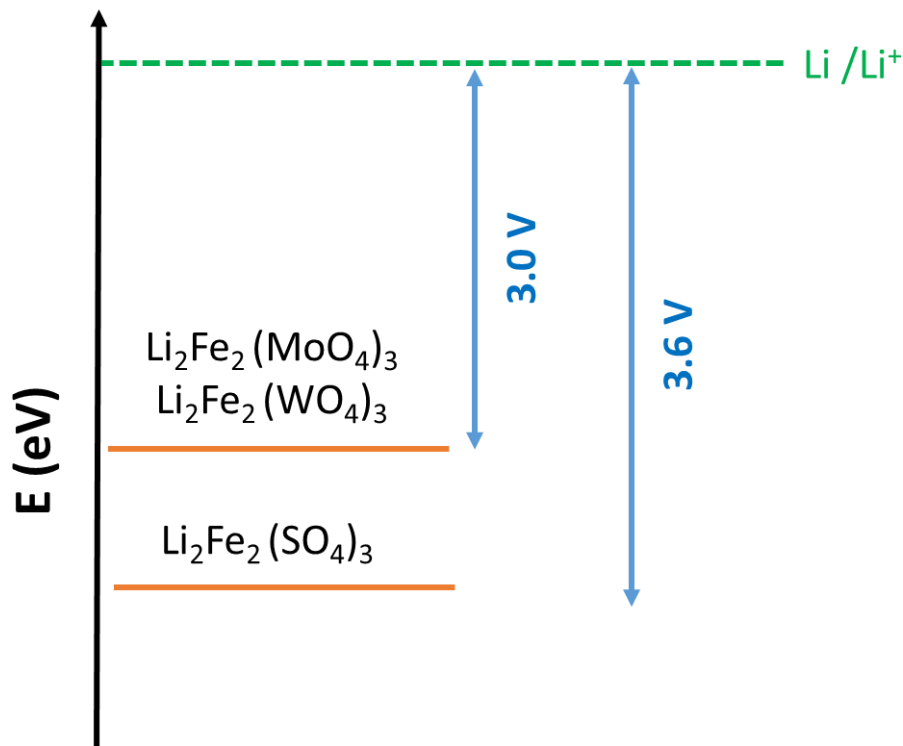


Figure 1.7. Respective positions of the redox couple $\text{Fe}^{2+}/\text{Fe}^{3+}$ vs Li/Li^+ in $\text{Li}_2\text{Fe}_2(\text{XO}_4)_3$ ($X = \text{S}, \text{Mo}, \text{W}$)

The voltage of the cell is also tailored by the electronic structure of transition metal ions as shown in the isostructural LiMnPO_4 (around 4.1 V vs Li/Li^+) and LiFePO_4 (about 3.45 V vs Li/Li^+). According to the electronegativity of iron and manganese, LiFePO_4 should require more energy to remove electrons as iron more strongly attracts electrons. However, the electronic structure of Mn^{2+} ($3d^5$) is $t_{2g}^3 e_g^2$ while that of Fe^{2+} ($3d^6$) is $t_{2g}^4 e_g^2$ in an octahedral coordination considering the crystal field splitting. For Fe^{2+} , the electron involved in the redox couple lies in t_{2g} , which is higher in energy due to a pairing energy cost. In contrast, the fifth electron in Mn^{2+} does not pay the pairing energy, leading to higher working voltage (Fig. 1.8).⁷⁹

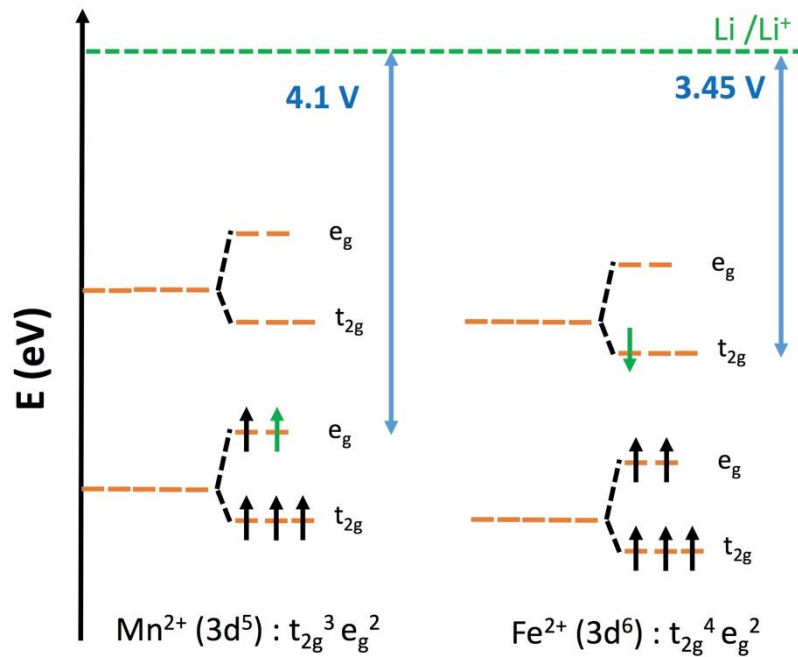


Figure 1.8. Crystal field splitting of Mn^{2+} and Fe^{2+} in the octahedral coordination. The green arrow represents the electron involved in the redox.

- **Anion redox for higher specific capacities**

The conventional way to design positive electrode materials for rechargeable ion batteries considers the compounds in which the amount of ion transport is balanced by the transition metals' redox process to compensate charge in the host crystal. The theoretical gravimetric specific capacity in this system is determined by the number of electrons that the transition metal ions can exchange per unit mass. However, in layered structure lithium-rich oxides the oxidation of oxygen anions is activated at high voltage. The oxygen redox activity strongly depends on the electronic structure of the materials. In the band structure of lithium-rich layered oxides, orbital overlaps between transition metal d orbitals and oxygen $2p$ orbitals result in bonding (M-O) and antibonding (M-O)* bands with oxygen and metal characters, respectively. Considering localised electrons, three different scenarios are recognised based on the bands where the redox process occurs.⁸¹ The conventional cationic redox is shown in Fig. 1.9a where the redox process involves solely the antibonding (M-O)* bands. The second situation represents cumulative cationic and reversible anionic redox (Fig. 1.9b), which arises from the appropriate position of unhybridised oxygen $2p$ bands. The last case is that electrons are removed from the oxygen non-bonding bands, leading to O_2 release (Fig. 1.9c).

The oxygen redox reaction has the potential to achieve high energy density as it delivers additional capacity beyond the theoretical value from the transition metal redox process.

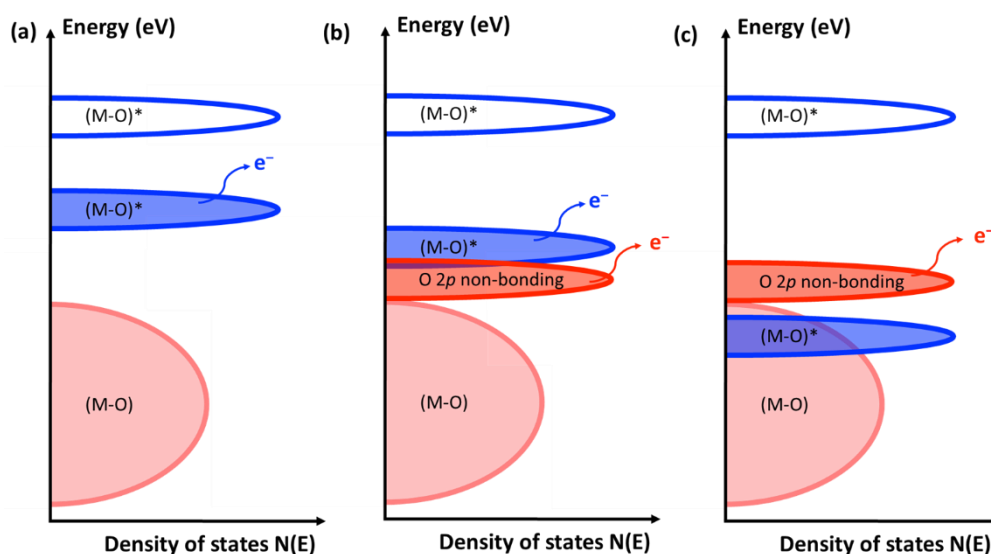


Figure 1.9. Schematic of band structures illustrating (a) classical cation redox, (b) reversible anion redox and (c) irreversible anion redox accompanied with O_2 release in lithium-rich layered oxides.

Among lithium-rich layered oxides, manganese-based lithium-rich oxide, Li_2MnO_3 , is the most studied model material. The formula can be written as $Li[Li_{1/3}Mn_{2/3}]O_2$, representing that lithium is substituted for one-third of the manganese in the transition metal layers with cation ordering. It was generally believed that the quantity of lithium ion removal is limited in $Li[Li_{1/3}Mn_{2/3}]O_2$ as the maximum oxidation state of manganese is tetravalent in an octahedral environment.⁸² However, additional lithium ion extraction can occur beyond the conventional redox process where the oxidation of transition metals is involved.^{83,84} As these oxides show anomalously large capacity, several explanations for this phenomenon have been advanced by different groups. In general, oxygen in the crystal structure is responsible for the extra capacity to balance charge upon lithium ion deintercalation. However, how the oxygen participates in the electrochemical reaction is the subject of intense debate.

For example, simultaneous oxygen loss with lithium ion deintercalation, forming lithium oxide (Li_2O) in nickel-doped $Li[Li_{1/3}Mn_{2/3}]O_2$ was proposed by Lu *et al.*⁸⁵ Later, direct evidence of Li_2O formation on the surface of $Li[Li_{0.2}Ni_{0.2}Mn_{0.6}]O_2$ was reported using *in-situ* surface-enhanced Raman spectroscopy (SERS). The proposed mechanism of the degradation of the material is that the activated oxygen forms Li_2O on the surface, which reacts subsequently

with the electrolyte. Accordingly, the acidity of the electrolyte solution is changed, leading to the production of lithium carbonate (Li_2CO_3) during the discharge process.⁸⁶

In addition, Armstrong *et al.*¹³ suggested that the oxygen removal occurs from the surface of $\text{Li}[\text{Li}_{0.2}\text{Ni}_{0.2}\text{Mn}_{0.6}]\text{O}_2$ in combination with the redistribution of transition metal ions from surface to bulk where lithium vacancies are created by lithium ion removal. In this study, *in-situ* differential electrochemical mass spectrometry (DEMS) was used to demonstrate directly the O_2 evolution during the charge process. Recently, the role of oxygen vacancies on the surface of material was proposed based on combined experimental observations using scanning transmission electron microscopy (STEM) and electron energy loss spectroscopy (EELS) and computational studies.⁸⁷ It was observed that the oxygen vacancies are created near the surface of $\text{Li}[\text{Li}_{1/6}\text{Ni}_{1/6}\text{Co}_{1/6}\text{Mn}_{1/2}]\text{O}_2$ after most transition metals are fully oxidised. The computational calculation for $\text{Li}[\text{Li}_{1/6}\text{Ni}_{1/4}\text{Mn}_{7/12}]\text{O}_2$ as a model compound for $\text{Li}[\text{Li}_{1/6}\text{Ni}_{1/6}\text{Co}_{1/6}\text{Mn}_{1/2}]\text{O}_2$ suggested that the oxygen vacancies are most likely to form when they are coordinated by the lithium layer and the lithium-nickel-manganese combinations in the transition metal layer. The diffusion barriers for nickel or manganese cations in the octahedral sites can be significantly reduced in the presence of oxygen vacancies, leading to the migration of transition metal cations from the surface to the bulk.⁸⁷

Oishi *et al.*⁸⁸ proposed the oxygen redox mechanism for $\text{Li}[\text{Li}_{1/3}\text{Mn}_{2/3}]\text{O}_2$ using O K-edge and Mn L-edge X-ray absorption spectroscopy (XAS) with two different detection modes: a fluorescence yield (FY) and a total electron yield (TEY), which is sensitive to bulk and to the surface of samples, respectively. It is revealed that the oxygen redox is activated on the first charge along with the rearrangement of electrons in the hybridised orbital between Mn 3d and O 2p orbitals, causing the partial reduction of Mn^{4+} to Mn^{3+} in the bulk. On subsequent cycles, the appearance (disappearance) of peroxo-like species is confirmed by both the FY and TEY modes during charging (discharging), supporting the reversible oxygen redox reaction. In contrast, the oxidation of Mn^{2+} to Mn^{4+} is observed on the surface rather than the oxidation of Mn^{2+} to Mn^{3+} in the high voltage region where the oxygen redox is pronounced, which may contribute to additional capacity.

The reduction of the transition metal has been discussed by Tarascon's group in $\text{Li}[\text{Li}_{1/3}\text{Fe}_{1/3}\text{Sb}_{1/3}]\text{O}_2$ ⁸⁹ and $\text{Li}[\text{Li}_{1/3}\text{Ru}_{1/3}\text{Sn}_{1/3}]\text{O}_2$ ⁹⁰ where the reversibility of oxygen oxidation is accompanied by the reduction of the transition metal: Fe^{4+} to Fe^{3+} and Ru^{6+} to Ru^{5+} , respectively. In the latter case, the presence of Sn^{4+} stabilises the peroxo-like species,

preventing O₂ release. Through the survey of various compounds including Li[Li_{1/3}Ru_{1/3}Mn_{1/3}]O₂,⁹¹ Li[Li_{1/3}Ir_{2/3}]O₂,⁹² and those mentioned above, this group reported that the strong hybridisation formed between 4d or 5d transition metals and oxygen is the key to activate reversible oxygen redox.

Bruce and co-workers suggested that in the 3d transition metal compound Li[Li_{0.20}Ni_{0.13}Co_{0.13}Mn_{0.54}]O₂, the formation of localised holes in oxygen orbitals rather than peroxo-like species is the origin of the oxygen redox process.⁹³ In this study, the evolution of CO₂ was detected by *operando* DEMS, which arises from the decomposition of the electrolyte caused by the extracted oxygen from the lattice. However, the oxygen loss accounts for very little charge compensation. The combined spectroscopic techniques O K-edge resonant inelastic X-ray scattering spectroscopy (RIXS), Raman spectroscopy and XAS with different edges including O K-edge, Ni K-edge, Co K-edge and Mn K-edge confirm that the oxygen hole is created at a certain local environment, i.e., coordinated by Mn⁴⁺ and Li⁺, which delivers extra charge capacity.

Computational studies identified specific chemical and structural features to enable electrochemically active oxygen in lithium-rich layered oxides.⁹⁴ In specific Li-O-Li configurations, unhybridised O 2p orbitals are present due to the large energy difference between O 2p and Li 2s orbitals, which are responsible for the oxygen redox activity. When the lithium-rich layered oxides are highly delithiated, labile oxygen originating from these Li-O-Li configurations are oxidised, leading to the creation of holes. Under certain conditions, the formation of peroxo-like species can be more easily facilitated as observed in Li[Li_{1/3}Ru_{1/3}Sn_{1/3}]O₂,⁹⁰ and Li[Li_{1/3}Fe_{1/3}Sb_{1/3}]O₂.⁸⁹ Recently, it was reported that isostructural Li[Li_{0.2}Ni_{0.2}Mn_{0.6}]O₂ and Li[Li_{0.2}Ni_{0.2}Ru_{0.6}]O₂ exhibit different electrochemical behaviour. Both transition metal and oxygen oxidation was observed in Li[Li_{0.2}Ni_{0.2}Mn_{0.6}]O₂ with O₂ evolution, whereas only the oxidation of the transition metal was observed in Li[Li_{0.2}Ni_{0.2}Ru_{0.6}]O₂.⁹⁵ This study implies that the transition metal plays an important role to activate the anion redox despite the presence of suitable Li-O-Li configurations.

Oxygen redox activity has been also reported in Li-rich compounds crystallising in cation disordered rock-salt structure since Ceder's group⁹⁶ reported that excess lithium in cation disordered rock-salt materials can create active Li diffusion channels where lithium ions hop from one octahedral to another octahedral site *via* an intermediate tetrahedral site without sharing any faces with octahedral transition metals. Yabuuchi *et al.*⁹⁷ reported transition

metal dependent reversibility of oxygen redox in $\text{Li}_{1.3}\text{Nb}_{0.3}\text{M}_{0.4}\text{O}_2$ ($M = \text{Fe}, \text{Mn}, \text{V}$). While $\text{Li}_{1.3}\text{Nb}_{0.3}\text{Fe}_{0.4}\text{O}_2$ and $\text{Li}_{1.3}\text{Nb}_{0.3}\text{Mn}_{0.4}\text{O}_2$ exhibit large charge capacity with a well-defined voltage plateau from oxidation of oxygen anions, $\text{Li}_{1.3}\text{Nb}_{0.3}\text{V}_{0.4}\text{O}_2$ delivers limited charge capacity solely from the oxidation of V^{3+} to V^{5+} on the first cycle. The oxygen redox is reversible in $\text{Li}_{1.3}\text{Nb}_{0.3}\text{Mn}_{0.4}\text{O}_2$ without the electron transfer from oxidised oxygen anions to Mn^{4+} whereas the oxidised oxygen anions tend to form superoxide species (O_2^-) which are decomposed during charging, resulting in O_2 evolution in $\text{Li}_{1.3}\text{Nb}_{0.3}\text{Fe}_{0.4}\text{O}_2$. In the study of $\text{Li}_{1.2}\text{Ni}_{1/3}\text{Ti}_{1/3}\text{Mo}_{2/15}\text{O}_2$,⁹⁸ oxygen redox is observed with O_2 release, which is alleviated through surface modification with LiNbO_3 .

1.3. High energy positive electrode materials in LIBs and SIBs

Increasing dependence on rechargeable batteries for energy storage calls for the improvements in energy density of batteries. Towards this goal, the introduction of positive electrode materials with high operating voltage and/or storage capacity is in high demand. In LIBs, lithium cobalt phosphate is an attractive material thanks to its high working voltage (4.8 V vs Li/Li^+), however its unsatisfactory performance impedes its wide application. Solutions to overcome the limits in a sustainable way need to be investigated. In addition, the limited abundance of lithium demands relatively low cost alternatives. SIBs could be an option for large energy storage systems where cost is more important factor. Sodium based manganese based oxides are a key family due to relatively low cost and the environmentally friendly nature of manganese. Their structural similarity to lithium-rich oxides could permit the use of anion redox, enhancing capacity. The following section will review the positive electrode materials relevant to the thesis; lithium cobalt phosphate and manganese based sodium oxides. These materials will be focused on the subsequent chapters.

1.3.1. Lithium cobalt phosphate for LIB

Lithium cobalt phosphate, LiCoPO_4 , has been a strong candidate as a high voltage positive electrode material since first identified by Amine *et al.*, albeit with a limited initial discharge capacity of 70 mAh g^{-1} .⁹⁹ LiCoPO_4 crystallises in an olivine structure where PO_4 tetrahedra and CoO_6 octahedra share corners and lithium ions are on edge-shared octahedral sites, forming lithium ion channels along the b -axis (Fig. 1.10).

The structural evolution of LiCoPO_4 during electrochemical delithiation reveals that this involves two stages as indicated in schemes i and ii, with an intermediate phase of composition $\text{Li}_{2/3}\text{CoPO}_4$.¹⁰⁰⁻¹⁰²



Both processes are reversible upon cycling producing two plateaus in the charge/discharge curves, indicating a two-phase mechanism. Grey's group reported that the $\text{Li}_{2/3}\text{CoPO}_4$ shows an ordering between Co^{2+} and Co^{3+} within a supercell obtained by tripling the unit cell in the b direction, corresponding to $\text{Li}_{2/3}(\text{Co}^{2+})_{2/3}(\text{Co}^{3+})_{1/3}\text{PO}_4$.¹⁰¹

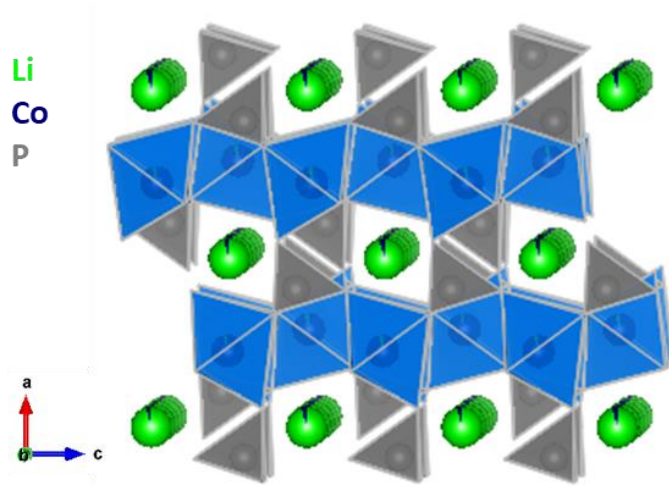


Figure 1.10. Structural representation of LiCoPO_4 .

While the isostructural LiFePO_4 has been used commercially, the unsatisfactory electrochemical performance of LiCoPO_4 associated with low electronic¹⁰³⁻¹⁰⁵ and ionic¹⁰⁶ conductivities as well as poor cycling stability^{107,108} limits its wide application. Extensive studies have been devoted to mitigating these limitations including partial substitution of cobalt with transition¹⁰⁹⁻¹¹⁵ or alkaline-earth metals,¹¹⁶⁻¹¹⁹ surface modification¹²⁰⁻¹²³ and reduction of particle size.¹²⁴⁻¹²⁶ The use of novel separators^{127,128} and functional electrolytes^{48,49,129} has been also reported to improve the electrochemical properties.

In numerous studies, doped LiFePO_4 exhibits improved electrochemical performance although the role of doping either lithium site or iron site is still under debate.¹⁸ In the case of LiCoPO_4 , doping of aliovalent elements such as vanadium (V^{3+}),^{109,130} iron (Fe^{3+}),^{104,110,111} yttrium (Y^{3+}),¹³¹ or chromium (Cr^{3+})¹³² on the cobalt sites has shown enhanced

electrochemical performance. It has been reported that aliovalent doping can create lithium vacancies, increase ionic conductivity with less activation energy and reduce detrimental reactions with the electrolyte. Among isovalent cations, iron (Fe^{2+})^{104,110-115,133,134} substitution for cobalt has been studied most intensively. Kosova *et al.* reported that the characteristic two-phase structural evolution during electrochemical cycling alters to a solid-solution like single-phase mechanism for $\text{LiFe}_{0.5}\text{Co}_{0.5}\text{PO}_4$ with enhanced lithium ion diffusion.¹¹⁴ Subsequently, the delithiation mechanism of a series of iron-doped LiCoPO_4 compositions ($\text{LiFe}_x\text{Co}_{1-x}\text{PO}_4$, where $x = 0, 0.05, 0.125, 0.25, 0.5, 0.75, 0.875, 0.95, 1$) was investigated and revealed that the single-phase mechanism occurs for iron-rich compounds while cobalt-rich materials retain the two-phase mechanism in a particle.¹³⁴ In addition, the suppression of Li/Co anti-site defects due to preferential iron occupation of the 4c sites was proposed to stabilise cycling performance, leading to the enlargement of the lithium ion pathway.¹¹² However, very few studies have been carried out on electrochemically inactive dopants such as magnesium (Mg^{2+}) and calcium (Ca^{2+}), although magnesium doping was found to reduce the lattice mismatch between lithiated and delithiated phases in lithium manganese phosphate, LiMnPO_4 and modify the redox couples for LiFePO_4 and LiMnPO_4 *via* an increase in their working voltage.^{135,136}

Surface modification with carbon or metal oxides has been applied to improve the electrochemical properties of LiCoPO_4 . As carbon coating on the particle surface is an effective way to enhance electronic conductivity of overall electrodes, various carbon sources^{123,137} and coating methods¹³⁸ either *ex-situ*^{122,123,126,139,140} or *in-situ*^{137,139,141} have been reported. The studies have reported that carbon coating not only enhances electronic conductivity but also reduces the particle size. In addition, the successful formation of a thin and homogeneous coating can provide the additional benefit of preventing surface degradation triggered by electrolyte decomposition.¹⁴² Coating with metal oxides such as NiO ¹²⁰ and VO_x ¹²³ was applied to stabilise the interface between the active material and the electrolyte, limiting the detrimental side reactions with the electrolyte. Ornek *et al.*¹²⁰ obtained a nanoscale NiO coating (8-10 nm) on the surface of particles using a specially designed synthetic method, that shows enhancement of cycling performance. In contrast, VO_x coating¹²³ exhibits no improvement as the thick coating significantly increases the resistance of the electrode, limiting initial capacity.

1.3.2. Manganese-based sodium layered oxides for SIB

Manganese-based sodium layered oxides, $\text{Na}_x\text{M}_y\text{Mn}_{1-y}\text{O}_2$ ($0.4 \leq x \leq 1.0$, $0.34 \leq y \leq 0.66$, $M = \text{Li, Mg, Al, Ti, Fe, Co, Ni, Cu, Zn}$ and mixture of elements), are a major family of positive electrode materials for SIBs.⁶² They adopt one of the polymorphs O3, P3 and P2, referred to in section 1.2.1.

Electrochemical behaviour of O'3-type NaMnO_2 (prime indicates a structural distortion to a monoclinic lattice) was first reported by Mendiboure *et al.*¹⁴³ with very limited reversible sodium ion extraction (0.2 per formula unit). Later, this material was revisited and it is found that 0.85 (210 mAh g⁻¹) and 0.80 (197 mAh g⁻¹) sodium ions per formula unit are deintercalated and intercalated, respectively, on the first cycle in the voltage window between 2.0 and 3.8 V vs Na/Na⁺. However, its capacity retention is unsatisfactory, accompanied by pronounced stepwise plateaus in the voltage profile, indicating structural transitions.¹⁴⁴

Since the first electrochemical performance of P2-type $\text{Na}_{0.7}\text{MnO}_2$ was investigated,¹⁴³ considerable research on partial substitution of metals for manganese has been carried out to increase the average working voltage, enhance cyclability and activate oxygen redox. Doping with a small amount of electrochemically inactive elements such as lithium, magnesium and zinc in P2-type Na_xMnO_2 ($0.6 \leq x \leq 0.83$) has been shown to suppress phase transitions and Jahn-Teller distortion during cycling, enhancing cycling performance. For example, $\text{Na}_{5/6}\text{Li}_{1/4}\text{Mn}_{3/4}\text{O}_2$ exhibits smooth charge/discharge curves as well as high capacity (190 mAh g⁻¹ at a rate of 10 mA g⁻¹) and rate capability (150 mAh g⁻¹ at a rate of 236 mA g⁻¹) in the voltage window 1.5-4.5 V vs Na/Na⁺. This compound also shows an oxygen redox process along with the pronounced hysteresis in the voltage profile. The disappearance of cation ordering in the transition metal layers implies that structural rearrangement occurs possibly with oxygen loss from the lattice.¹⁴⁵ Nazar and co-workers¹⁴⁶ observed similar results for $\text{Na}_{0.6}\text{Li}_{0.2}\text{Mn}_{0.8}\text{O}_2$, which delivers stable and high capacity of 190 mAh g⁻¹ over 100 cycles within the voltage window 2.0-4.6 V vs Na/Na⁺. The partial substitution of lithium for manganese suppresses several plateaus observed for P2-type $\text{Na}_{0.6}\text{MnO}_2$. In addition, they suggested that a long plateau at around 4.4 V vs Na/Na⁺ on a few initial cycles can be attributed to oxygen redox with lithium extraction from the transition metal layers.

Doping magnesium as a spectator ion in P2-type manganese-based sodium layered oxides has also demonstrated benefits. The investigation of $\text{Na}_{0.67}\text{Mg}_x\text{Mn}_{1-x}\text{O}_2$ ($0 \leq x \leq 0.2$) showed

that only small content of magnesium (5%) is sufficient to smooth the voltage profile without reducing the capacity. The doping of magnesium (Mg^{2+}) dilutes Jahn-Teller active manganese (Mn^{3+}), leading to the enhancement of cycling stability.¹⁴⁷ Yabuuchi *et al.*¹⁴⁸ studied $\text{Na}_{2/3}\text{Mg}_{0.28}\text{Mn}_{0.72}\text{O}_2$ and suggested the presence of a superlattice due to in-plane ordering between manganese and magnesium. The compound delivers an extremely large capacity of 220 mAh g^{-1} in the voltage range 1.5-4.4 V vs Na/Na^+ . Later, Bruce and co-workers¹⁴⁹ reported that the abnormal capacity is driven by the oxygen redox process without oxygen loss from the lattice. It was observed that P2-type $\text{Na}_{2/3}\text{Mg}_{0.28}\text{Mn}_{0.72}\text{O}_2$ is transformed to an O2 phase, where oxygen is coordinated by one magnesium and two manganese cations and three vacancies created from sodium ion removal, upon charging. In this case, the holes in O 2p orbitals are stable owing to the interaction with at least one cation in the transition metal layers even at the sodium-deficient phase, preventing O_2 release. In contrast, in the lithium-rich layered oxides e.g., $\text{Li}[\text{Li}_{0.20}\text{Ni}_{0.13}\text{Co}_{0.13}\text{Mn}_{0.54}]\text{O}_2$,⁹³ the delithiated phase contains the non-bonding O 2p orbitals without any interaction with adjacent cations which render the O 2p states unstable in the lattice and lead to O_2 evolution.

Tarascon's group¹⁵⁰ carried out research on P2-type $\text{Na}_{2/3}\text{Zn}_{2/9}\text{Mn}_{7/9}\text{O}_2$, where the more electronegative element zinc (Zn^{2+}) replaces magnesium (Mg^{2+}), as a counterpart of P2-type $\text{Na}_{2/3}\text{Mg}_{0.28}\text{Mn}_{0.72}\text{O}_2$. In this study, the oxygen redox process is active without O_2 evolution but structural changes associated with cation migration into the vacant sodium sites result in poor cycling performance. According to computational studies, the interaction between zinc and oxygen (Zn-O) has less ionic character than that of magnesium and oxygen (Mg-O), but the ionic character is strong enough to create non-bonding O 2p orbitals, which permits oxygen redox upon charging.

Among electrochemically active dopants in manganese-based sodium layered oxides, nickel has been extensively investigated as the element can deliver higher capacity thanks to the $\text{Ni}^{2+}/\text{Ni}^{4+}$ redox couple. Structural evolution of P2-type $\text{Na}_{2/3}\text{Ni}_{1/3}\text{Mn}_{2/3}\text{O}_2$ was examined by Dahn's group and demonstrates that fully reversible sodium ion deintercalation/intercalation are possible with multiple phase changes.¹⁵¹ Wang *et al.* studied the electrochemical cycling performance of P2-type $\text{Na}_{2/3}\text{Ni}_{1/3}\text{Mn}_{2/3}\text{O}_2$, varying the cut-off voltages. The results show that the active material maintains the P2 structure when cycled between 2.0 and 4.0 V vs Na/Na^+ , whereas either increasing the upper voltage to 4.5 V vs Na/Na^+ or decreasing lower voltage to 1.6 V vs Na/Na^+ has detrimental effects on its cyclability due to the poorly reversible

structure change to the O2 phase.¹⁵² Analogous results reported that the phase transformation from P2 to O2, occurring above 4.2 V vs Na/Na⁺, significantly affects the cycling stability of P2-type Na_{2/3}Ni_{1/3}Mn_{2/3}O₂.¹⁵³ In order to alleviate this issue, substitution of electrochemically inert elements for nickel has been investigated. For instance, the effect of lithium doping on structural and electrochemical properties of P2-type Na_xNi_yLi_zMn_{1-y-z}O₂ (0 < x, y, z < 1) was studied by Meng and co-workers.¹⁵⁴ P2-type Na_{0.80}Ni_{0.22}Li_{0.12}Mn_{0.66}O₂ exhibits a smooth voltage profile, indicating solid-solution behaviour during the charge/discharge process. The compound shows enhanced capacity retention of 91% over 50 cycles when cycled between 2.0 and 4.4 V vs Na/Na⁺. The structural change to O2 is delayed due to the presence of lithium, allowing the sodium ion to reside in the prismatic sites. Local stacking faults are observed, which induces the lithium migration from the transition metal layers to octahedral or tetrahedral sites in sodium ion layers. However, the migration of lithium is largely reversible, therefore the initial P2 structure is maintained over cycling.

Improved cycling performance through magnesium doping has been reported.¹⁵⁵⁻¹⁵⁸ Research on P2-type Na_{0.67}Ni_{0.33-x}Mg_xMn_{0.67}O₂ (x = 0, 0.02, 0.05, 0.10, 0.15) showed a good cycling performance over 100 cycles for P2-type Na_{0.67}Ni_{0.23}Mg_{0.10}Mn_{0.67}O₂ in the voltage window of 2.0-4.5 V vs Na/Na⁺. The authors claimed that the improvement may be attributed to the enlarged the lattice parameters via magnesium doping.¹⁵⁵ Suppression of the undesired phase transition to O2 via magnesium doping in P2-type Na_{0.67}Ni_{0.33}Mn_{0.67}O₂ was also reported by Wang *et al.*¹⁵⁶ Examination of the electrochemical performance of P2-type Na_{0.67}Ni_{0.33-x}Mg_xMn_{0.67}O₂ (0 ≤ x ≤ 0.33), cycled between 2.5 and 4.35 V vs Na/Na⁺, revealed that the increased magnesium content provides better capacity retention. As magnesium in the transition metal layers enables sodium ions to remain in the prismatic sites, the P2 structure is stabilised. Later, it was reported that P2-type Na_{0.67}Ni_{0.3-x}Mg_xMn_{0.7}O₂ (x = 0.05, 0.10) undergoes a reversible phase transition from P2 to OP4, described as an intergrowth structure between the P2 and O2 structures. This allows the P2-type Na_{0.67}Ni_{0.2}Mg_{0.1}Mn_{0.7}O₂ compound to deliver an excellent capacity retention of 95% over 50 cycles in the voltage range of 2.0-4.5 V vs Na/Na⁺.¹⁵⁷ The formation of OP4 phase in P2-type Na_{0.67}Ni_{0.2}Mg_{0.1}Mn_{0.7}O₂ was further supported by experimental and computational studies conducted by Tapia-Ruiz *et al.*¹⁵⁸ The OP4 phase is thermodynamically stable and is formed because sodium ions stay in the vicinity of magnesium to preserve local charge neutrality at high voltage.

Oxygen redox activity in P2-type $\text{Na}_{0.78}\text{Ni}_{0.23}\text{Mn}_{0.69}\text{O}_2$ was explored by Meng and co-workers.¹⁵⁹ This compound shows an abnormally large charge capacity (180 mAh g^{-1}) on the first cycle and good cycling performance when cycled to 4.5 V vs Na/Na^+ . The latter is accounted for by the suppression of phase change to O2 due to its larger sodium content (0.78 per formula unit) compared to the P2-type $\text{Na}_{2/3}\text{Ni}_{1/3}\text{Mn}_{2/3}\text{O}_2$ reported previously.^{152,153} They proposed that the large charge capacity delivered at the first cycle is a result of the participation of oxygen in the redox processes. The decrease in the oxidation state of transition metals from bulk to surface, observed by EELS and Ni L-edge and O K-edge XAS, supports the participation of lattice oxygen and the changes in the crystal and electronic structures on the surface. The presence of vacancies (7%) in the transition metal layers is considered to be the origin of the creation of unhybridised oxygen $2p$ orbitals.

The critical role of vacancies for the reversible oxygen redox reaction was investigated by Yamada and co-workers.¹⁶⁰ In their research, stable oxygen redox takes place solely when O3-type Na_2RuO_3 exhibits ordering between sodium and ruthenium in the transition metal slabs. In the ordered Na_2RuO_3 , also described as $\text{Na}[\text{Na}_{1/3}\text{Ru}_{2/3}]\text{O}_2$ (square brackets represent transition metal layers), the sodium ion is removed from $[\text{Na}_{1/3}\text{Ru}_{2/3}]$ slabs prior to sodium ion layers. The vacancies created in the transition metal layers upon charging suppress the irreversible structure change to P3, rendering the oxygen-oxygen (O-O) bonds in RuO_6 octahedra shorter and inducing the rearrangement of electronic structure of the system, leading to the oxygen redox chemistry. In addition, O_2 release is limited by the strong interaction between ruthenium $4d$ and oxygen $2p$ orbitals as observed in lithium-rich layered oxides.

The same group demonstrated the reversible oxygen redox for $\text{Na}_{4/7}\square_{1/7}\text{Mn}_{6/7}\text{O}_2$ (empty square represents vacancies in manganese sites), crystallising in the triclinic space group $P\bar{1}$ where the edge-sharing MnO_6 octahedra build up $\square_{1/7}\text{Mn}_{6/7}\text{O}_2$ slabs and sodium ions are located between the slabs. Of note, the vacancies in the transition metal slabs are periodic.¹⁶¹ Similar to ordered O3-type Na_2RuO_3 , the vacancies stabilise the $P\bar{1}$ structure, resulting in good cycle stability in the voltage range 3.0-4.7 V vs Na/Na^+ where only oxygen is involved in the charge compensation. The study carried out by Li *et al.*¹⁶² also showed the reversible oxygen redox for $\text{Na}_{4/7}\text{Mn}_{6/7}\text{O}_2$ with negligible structural changes in the bulk as well as on the surface upon cycling in the voltage window of 1.5-4.4 V vs Na/Na^+ .

The oxygen redox chemistry in P3-type compounds has been less explored compared to P2-type materials. The group of Goodenough reported that P3-type $\text{Na}_{0.6}\text{Li}_{0.2}\text{Mn}_{0.8}\text{O}_2$ shows a plateau at around 4.2 V vs Na/Na⁺ in the voltage profile, attributed to the oxidation of oxygen.¹⁶³ Later, Rong *et al.*¹⁶⁴ proposed that the stable crystal structure and the presence of peroxo-like species of P3-type $\text{Na}_{0.6}\text{Li}_{0.2}\text{Mn}_{0.8}\text{O}_2$, revealed by neutron pair distribution function (PDF) analysis, enable the material to deliver the initial discharge capacity of 80 mAh g⁻¹ solely from the oxygen redox in the voltage window of 3.5-4.5 V vs Na/Na⁺. The oxygen redox chemistry was also investigated in the research on P3-type $\text{Na}_{2/3}\text{Mg}_{1/3}\text{Mn}_{2/3}\text{O}_2$. This material shows a plateau originating from oxygen redox at around 4.2 V vs Na/Na⁺, with the discharge plateau located at 2.7 V vs Na/Na⁺. The large gap is justified by the irreversible structural change to O3 accompanied by the migration of magnesium to the interlayer tetrahedral sites. Although this migration is reversible, possible oxygen loss from the surface may degrade the structure and oxidise the electrolyte, leading to capacity fade.¹⁶⁵

1.4. Aims of project

The thesis aims to investigate promising positive electrode materials, which can deliver high energy density in either LIB or SIB. As larger energy density is achieved by increasing either the working voltage of electrode materials and/or their capacity, two aspects were separately studied in each system.

The selected material for the LIB is LiCoPO_4 as a high voltage electrode material with a working voltage around 4.8 V vs Li/Li⁺, however LiCoPO_4 suffers from unsatisfactory cycling stability mainly caused by the degradation of active material and the increase in anti-site defects. To overcome these issues, most used approaches include surface modification and substitution of electrochemically active dopants for cobalt. In this thesis, two strategies are applied to alleviate the degradation of the active material, initiated by the electrolyte decomposition. Firstly, systematic studies on the electrode formulation using aqueous binders are carried out in Chapter 3 as water-soluble binders have been shown to act not only for binding components of the electrodes but also for providing additional benefits such as mechanical buffer and scavenging HF. Following from the modification of the electrode, doping of the electrochemically inactive dopant, magnesium, is investigated in Chapter 4. The effect of magnesium doping is thoroughly studied in various ways including morphology, surface, electrochemical performance and structural evolution during cycling.

The work then focuses on P3-type manganese based materials for SIB which can deliver high capacity using both cation and anion redox processes. Among polymorphs of sodium manganese based oxides, O3- and P2-type compounds have been extensively studied and some materials exhibit oxygen redox. It is therefore of interest to investigate P3-type compounds to provide fundamental understanding of the oxygen redox chemistry and to propose potential solutions to stabilise the oxygen redox in P3-type materials. Two P3-type sodium manganese oxides: $\text{Na}_{0.67}\text{Mg}_{0.2}\text{Mn}_{0.8}\text{O}_2$ (Chapter 5) and $\text{Na}_{0.67}\text{Ni}_{0.2}\text{Mn}_{0.8}\text{O}_2$ (Chapter 6) are explored to shed light on the critical roles of vacancies and electrochemically active dopants on manganese sites in P3-type materials.

1.5. References

- 1 R. Schmuch, R. Wagner, G. Hörpel, T. Placke and M. Winter, *Nat. Energy*, 2018, **3**, 267–278.
- 2 B. Dunn, H. Kamath and J.-M. Tarascon, *Science*, 2011, **334**, 928–935.
- 3 J. Leadbetter and L. G. Swan, *J. Power Sources*, 2012, **216**, 376–386.
- 4 D. M. Davies, M. G. Verde, O. Mnyshenko, Y. R. Chen, R. Rajeev, Y. S. Meng and G. Elliott, *Nat. Energy*, 2019, **4**, 42–50.
- 5 J. N. Reimers, *J. Electrochem. Soc.*, 1992, **139**, 2091–2097.
- 6 Y. Shao-Horn, S. Levasseur, F. Weill and C. Delmas, *J. Electrochem. Soc.*, 2003, **150**, A366–A373.
- 7 J. R. Dahn, E. W. Fuller, M. Obrovac and U. Von Sacken, *Solid State Ionics*, 1994, **69**, 265–270.
- 8 L. Croguennec and M. R. Palacin, *J. Am. Chem. Soc.*, 2015, **137**, 3140–3156.
- 9 C. Zhao, Q. Wang, Y. Lu, Y.-S. Hu, B. Li and L. Chen, *J. Phys. D: Appl. Phys.*, 2017, **50**, 183001–118324.
- 10 A. Grimaud, W. T. Hong, Y. Shao-Horn and J.-M. Tarascon, *Nat. Mater.*, 2016, **15**, 121–126.
- 11 J.-S. Kim, C. S. Johnson, J. T. Vaughey, M. M. Thackeray, S. A. Hackney, W. Yoon and C. P. Grey, *Chem. Mater.*, 2004, **16**, 1996–2006.
- 12 Z. Lu and J. R. Dahn, *J. Electrochem. Soc.*, 2002, **149**, A815–A822.
- 13 A. R. Armstrong, M. Holzapfel, P. Novák, C. S. Johnson, S.-H. Kang, M. M. Thackeray and P. G. Bruce, *J. Am. Chem. Soc.*, 2006, **128**, 8694–8698.
- 14 H. Koga, L. Croguennec, M. Ménétrier, P. Mannessiez, F. Weill and C. Delmas, *J. Power Sources*, 2013, **236**, 250–258.
- 15 P. Rozier and J.-M. Tarascon, *J. Electrochem. Soc.*, 2015, **162**, A2490–A2499.
- 16 H. Huang, S. C. Yin and L. F. Nazar, *Electrochem. Solid-State Lett.*, 2001, **4**, A170–A172.
- 17 N. Ravet, Y. Chouinard, J. F. Magnan, S. Besner, M. Gauthier and M. Armand, *J. Power Sources*, 2001, **97-98**, 503–507.
- 18 J. Wang and X. Sun, *Energy Environ. Sci.*, 2015, **8**, 1110–1138.
- 19 C. Masquelier and L. Croguennec, *Chem. Rev.*, 2013, **113**, 6552–6591.
- 20 L.-X. Yuan, Z.-H. Wang, W.-X. Zhang, X.-L. Hu, J.-T. Chen, Y.-H. Huang and J. B. Goodenough, *Energy Environ. Sci.*, 2011, **4**, 269–284.
- 21 D. Liu, W. Zhu, J. Trottier, C. Gagnon, F. Barray, A. Guerfi, A. Mauger, H. Groult, C. M.

- Julien, J. B. Goodenough and K. Zaghib, *RSC Adv.*, 2013, **4**, 154–167.
- 22 A. Manthiram, K. Chemelewski and E.-S. Lee, *Energy Environ. Sci.*, 2014, **7**, 1339–1350.
- 23 K. Zhang, X. Han, Z. Hu, X. Zhang, Z. Tao and J. Chen, *Chem. Soc. Rev.*, 2015, **44**, 699–728.
- 24 M. M. Thackeray, W. I. F. David, P. G. Bruce and J. B. Goodenough, *Mater. Res. Bull.*, 1983, **18**, 461–472.
- 25 M. M. Thackeray, *Prog. Solid State Chem.*, 1997, **25**, 1–71.
- 26 M. Kunduraci, J. F. Al-Sharab and G. G. Amatucci, *Chem. Mater.*, 2006, **18**, 3585–3592.
- 27 S. Patoux, L. Daniel, C. Bourbon, H. Lignier, C. Pagano, F. Le Cras, S. Jouanneau and S. Martinet, *J. Power Sources*, 2009, **189**, 344–352.
- 28 S. Choi, J. Yoon, S. Muhammad and W.-S. Yoon, *J. Electrochem. Sci. Technol.*, 2013, **4**, 34–40.
- 29 J. Xiao, X. Chen, P. V. Sushko, M. L. Sushko, L. Kovarik, J. Feng, Z. Deng, J. Zheng, G. L. Graff, Z. Nie, D. Choi, J. Liu, J.-G. Zhang and M. S. Whittingham, *Adv. Mater.*, 2012, **24**, 2109–2116.
- 30 L. Cai, Z. Liu, K. An and C. Liang, *J. Mater. Chem. A*, 2013, **1**, 6908–6914.
- 31 E. Lee and K. A. Persson, *Chem. Mater.*, 2013, **25**, 2885–2889.
- 32 H. Komatsu, H. Arai, Y. Koyama, K. Sato, T. Kato, R. Yoshida, H. Murayama, I. Takahashi, Y. Orikasa, K. Fukuda, T. Hirayama, Y. Ikuhara, Y. Ukyo, Y. Uchimoto and Z. Ogumi, *Adv. Energy Mater.*, 2015, **5**, 1500638–1500645.
- 33 L. Boulet-Roblin, P. Borel, D. Sheptyakov, C. Tessier, P. Novák and C. Villevieille, *J. Phys. Chem. C*, 2016, **120**, 17268–17273.
- 34 R. Fong, U. von Sacken and J. R. Dahn, *J. Electrochem. Soc.*, 1990, **137**, 2009–2013.
- 35 T. Ohzuku, A. Ueda and N. Yamamoto, *J. Electrochem. Soc.*, 1995, **142**, 1431–1435.
- 36 J. S. Bridel, T. Azaïs, M. Morcrette, J.-M. Tarascon and D. Larcher, *Chem. Mater.*, 2010, **22**, 1229–1241.
- 37 I. Kovalenko, B. Zdyrko, A. Magasinski, B. Hertzberg, Z. Milicev, R. Burtovyy, I. Luzinov and G. Yushin, *Science*, 2011, **334**, 75–79.
- 38 S.-L. Chou, Y. Pan, J.-Z. Wang, H.-K. Liu and S.-X. Dou, *Phys. Chem. Chem. Phys.*, 2014, **16**, 20347–20359.
- 39 J. W. Choi and D. Aurbach, *Nat. Rev. Mater.*, 2016, **1**, 16013–16029.
- 40 D. Guyomard and J.-M. Tarascon, *J. Electrochem. Soc.*, 1992, **139**, 937–948.
- 41 V. Etacheri, R. Marom, R. Elazari, G. Salitra and D. Aurbach, *Energy Environ. Sci.*, 2011,

- 4**, 3243–3262.
- 42 E. Markevich, R. Sharabi, H. Gottlieb, V. Borgel, K. Fridman, G. Salitra, D. Aurbach, G. Semrau, M. A. Schmidt, N. Schall and C. Bruenig, *Electrochem. Commun.*, 2012, **15**, 22–25.
- 43 R. Sharabi, E. Markevich, V. Borgel, G. Salitra, G. Gershtinsky, D. Aurbach, G. Semrau, M. A. Schmidt, N. Schall and C. Stinner, *J. Power Sources*, 2012, **203**, 109–114.
- 44 N.-S. Choi, J.-G. Han, S.-Y. Ha, I. Park and C.-K. Back, *RSC Adv.*, 2015, **5**, 2732–2748.
- 45 I. H. Cho, S.-S. Kim, S. C. Shin and N.-S. Choi, *Electrochem. Solid-State Lett.*, 2010, **13**, A168.
- 46 J. Manzi and S. Brutti, *Electrochim. Acta*, 2016, **222**, 1839–1846.
- 47 Y. Wang, H. Ming, J. Qiu, Z. Yu, M. Li, S. Zhang and Y. Yang, *J. Electroanal. Chem.*, 2017, **802**, 8–14.
- 48 T. Fukutsuka, T. Nakagawa, K. Miyazaki and T. Abe, *J. Power Sources*, 2016, **306**, 753–757.
- 49 R. Sharabi, E. Markevich, K. Fridman, G. Gershtinsky, G. Gershtinsky, G. Salitra, G. Semrau, D. Aurbach, N. Schall, M. A. Schmidt and C. Bruenig, *Electrochem. Commun.*, 2013, **28**, 20–23.
- 50 V. Aravindan, Y. L. Cheah, W. C. Ling and S. Madhavi, *J. Electrochem. Soc.*, 2012, **159**, A1435–A1439.
- 51 N. Shao, X.-G. Sun, S. Dai and D.-E. Jiang, *J. Phys. Chem. B*, 2012, **116**, 3235–3238.
- 52 E. Markevich, G. Salitra and D. Aurbach, *ACS Energy Lett.*, 2017, **2**, 1337–1345.
- 53 E. Markevich, G. Salitra, K. Fridman, R. Sharabi, G. Gershtinsky, A. Garsuch, G. Semrau, M. A. Schmidt and D. Aurbach, *Langmuir*, 2014, **30**, 7414–7424.
- 54 M. H. Han, E. Gonzalo, G. Singh and T. Rojo, *Energy Environ. Sci.*, 2015, **8**, 81–102.
- 55 C. Delmas, C. Fouassier and P. Hagenmuller, *Physica B. C*, 1980, **99**, 81–85.
- 56 C. Delmas, J. BRACONNIER, C. Fouassier and P. Hagenmuller, *Solid State Ionics*, 1981, **3-4**, 165–169.
- 57 R. Berthelot, D. Carlier and C. Delmas, *Nat. Mater.*, 2010, **10**, 74–80.
- 58 P. Vassilaras, X. Ma, X. Li and G. Ceder, *J. Electrochem. Soc.*, 2012, **160**, A207–A211.
- 59 N. Yabuuchi, K. Kubota, M. Dahbi and S. Komaba, *Chem. Rev.*, 2014, **114**, 11636–11682.
- 60 N. Yabuuchi, M. Kajiyama, J. Iwatate, H. Nishikawa, S. Hitomi, R. Okuyama, R. Usui, Y. Yamada and S. Komaba, *Nat. Mater.*, 2012, **11**, 512–517.
- 61 D. Kundu, E. Talaie, V. Duffort and L. F. Nazar, *Angew. Chem., Int. Ed.*, 2015, **54**, 3431–

- 3448.
- 62 N. Ortiz-Vitoriano, N. E. Drewett, E. Gonzalo and T. Rojo, *Energy Environ. Sci.*, 2017, **10**, 1051–1074.
- 63 Y. You and A. Manthiram, *Adv. Energy Mater.*, 2018, **8**, 1701785–1701796.
- 64 J. Kim, D.-H. Seo, H. Kim, I. Park, J.-K. Yoo, S.-K. Jung, Y.-U. Park, W. A. Goddard III and K. Kang, *Energy Environ. Sci.*, 2015, **8**, 540–545.
- 65 M. M. Rahman, I. Sultana, S. Mateti, J. Liu, N. Sharma and Y. Chen, *J. Mater. Chem. A*, 2017, **5**, 16616–16621.
- 66 Y. Liu, N. Zhang, F. Wang, X. Liu, L. Jiao and L.-Z. Fan, *Adv. Funct. Mater.*, 2018, **28**, 1801917–1801926.
- 67 K. Zaghib, J. Trottier, P. Hovington, F. Brochu, A. Guerfi, A. Mauger and C. M. Julien, *J. Power Sources*, 2011, **196**, 9612–9617.
- 68 S.-M. Oh, S.-T. Myung, J. Hassoun, B. Scrosati and Y.-K. Sun, *Electrochem. Commun.*, 2012, **22**, 149–152.
- 69 P. Thomas, J. Ghanbaja and D. Billaud, *Electrochim. Acta*, 1999, **45**, 423–430.
- 70 M. M. Doeff, Y. Ma, S. J. Visco and L. C. De Jonghe, *J. Electrochem. Soc.*, 1993, **140**, L169–L170.
- 71 D. A. Stevens and J. R. Dahn, *J. Electrochem. Soc.*, 2000, **147**, 4428–4431.
- 72 D. A. Stevens and J. R. Dahn, *J. Electrochem. Soc.*, 2000, **147**, 1271–1273.
- 73 D. A. Stevens and J. R. Dahn, *J. Electrochem. Soc.*, 2001, **148**, A803–A811.
- 74 C. Liu, C. Liu, Z. G. Neale, G. Cao, Z. G. Neale and G. Cao, *Mater. Today*, 2016, **19**, 109–123.
- 75 J. B. Goodenough and Y. Kim, *Chem. Mater.*, 2010, **22**, 587–603.
- 76 A. Kraytsberg and Y. Ein-Eli, *Adv. Energy Mater.*, 2012, **2**, 922–939.
- 77 P. Peljo and H. H. Girault, *Energy Environ. Sci.*, 2018, **11**, 2306–2309.
- 78 P. G. Bruce, Ed., *Solid state electrochemistry*, Cambridge University Press, Cambridge, 2009.
- 79 A. Gutierrez, N. A. Benedek and A. Manthiram, *Chem. Mater.*, 2013, **25**, 4010–4016.
- 80 A. Manthiram, J. B. G. 1989, *J. Power Sources*, 1989, **26**, 403–408.
- 81 G. Assat and J.-M. Tarascon, *Nat. Energy*, 2018, **3**, 373–386.
- 82 B. Ammundsen and J. Paulsen, *Adv. Mater.*, 2001, **13**, 943–956.
- 83 A. D. Robertson and P. G. Bruce, *Chem. Mater.*, 2003, **15**, 1984–1992.
- 84 A. R. Armstrong and P. G. Bruce, *Electrochem. Solid-State Lett.*, 2004, **7**, A1–A4.

- 85 Z. Lu, D. D. MacNeil and J. R. Dahn, *Electrochem. Solid-State Lett.*, 2001, **4**, A200–A203.
- 86 S. Hy, F. Felix, J. Rick, W.-N. Su and B.-J. Hwang, *J. Am. Chem. Soc.*, 2014, **136**, 999–1007.
- 87 D. Qian, B. Xu, M. Chi and Y. S. Meng, *Phys. Chem. Chem. Phys.*, 2014, **16**, 14665–14668.
- 88 M. Oishi, K. Yamanaka, I. Watanabe, K. Shimoda, T. Matsunaga, H. Arai, Y. Ukyo, Y. Uchimoto, Z. Ogumi and T. Ohta, *J. Mater. Chem. A*, 2016, **4**, 9293–9302.
- 89 E. McCalla, M. T. Sougrati, G. Rousse, E. J. Berg, A. Abakumov, N. Recham, K. Ramesha, M. Sathiya, R. Dominko, G. Van Tendeloo, P. Novák and J.-M. Tarascon, *J. Am. Chem. Soc.*, 2015, **137**, 4804–4814.
- 90 M. Sathiya, G. Rousse, K. Ramesha, C. P. Laisa, H. Vezin, M. T. Sougrati, M.-L. Doublet, D. Foix, D. Gonbeau, W. Walker, A. S. Prakash, M. Ben Hassine, L. Dupont and J.-M. Tarascon, *Nat. Mater.*, 2013, **12**, 827–835.
- 91 M. Sathiya, K. Ramesha, G. Rousse, D. Foix, D. Gonbeau, A. S. Prakash, M.-L. Doublet, K. Hemalatha and J.-M. Tarascon, *Chem. Mater.*, 2013, **25**, 1121–1131.
- 92 E. McCalla, A. M. Abakumov, M. Saubanere, D. Foix, E. J. Berg, G. Rousse, M.-L. Doublet, D. Gonbeau, P. Novák, G. Van Tendeloo, R. Dominko and J.-M. Tarascon, *Science*, 2015, **350**, 1516–1521.
- 93 K. Luo, M. R. Roberts, R. Hao, N. Guerrini, D. M. Pickup, Y.-S. Liu, K. Edström, J. Guo, A. V. Chadwick, L. C. Duda and P. G. Bruce, *Nat. Chem.*, 2016, **8**, 684–691.
- 94 D.-H. Seo, J. Lee, A. Urban, R. Malik, S. Kang and G. Ceder, *Nat. Chem.*, 2016, **8**, 692–697.
- 95 J. Xu, M. Sun, R. Qiao, S. E. Renfrew, L. Ma, T. Wu, S. Hwang, D. Nordlund, D. Su, K. Amine, J. Lu, B. D. McCloskey, W. Yang and W. Tong, *Nat. Commun.*, 2018, **9**, 947–957.
- 96 J. Lee, A. Urban, X. Li, D. Su, G. Hautier and G. Ceder, *Science*, 2014, **343**, 519–522.
- 97 N. Yabuuchi, M. Nakayama, M. Takeuchi, S. Komaba, Y. Hashimoto, T. Mukai, H. Shiiba, K. Sato, Y. Kobayashi, A. Nakao, M. Yonemura, K. Yamanaka, K. Mitsuhashi and T. Ohta, *Nat. Commun.*, 2016, **7**, 13814–10.
- 98 M. A. Cambaz, B. P. Vinayan, H. Geßwein, A. Schiele, A. Sarapulova, T. Diemant, A. Mazilkin, T. Brezesinski, R. J. Behm, H. Ehrenberg and M. Fichtner, *Chem. Mater.*, 2019, **31**, 4330–4340.
- 99 K. Amine, H. Yasuda and M. Yamachi, *Electrochem. Solid-State Lett.*, 2000, **3**, 178–179.
- 100 M. G. Palmer, J. T. Frith, A. L. Hector, A. W. Lodge, J. R. Owen, C. Nicklin and J. Rawle,

- Chem. Commun.*, 2016, **52**, 14169–14172.
- 101 F. C. Strobridge, R. J. Clément, M. Leskes, D. S. Middlemiss, O. J. Borkiewicz, K. M. Wiaderek, K. W. Chapman, P. J. Chupas and C. P. Grey, *Chem. Mater.*, 2014, **26**, 6193–6205.
- 102 M. Kaus, I. Issac, R. Heinzmann, S. Doyle, S. Mangold, H. Hahn, V. S. K. Chakravadhanula, C. Kübel, H. Ehrenberg and S. Indris, *J. Phys. Chem. C*, 2014, **118**, 17279–17290.
- 103 J. Wolfenstine, *J. Power Sources*, 2006, **158**, 1431–1435.
- 104 J. L. Allen, T. Thompson, J. Sakamoto, C. R. Becker, T. R. Jow and J. Wolfenstine, *J. Power Sources*, 2014, **254**, 204–208.
- 105 M. E. Rabanal, M. C. Gutierrez, F. Garcia-Alvarado, E. C. Gonzalo and M. E. Arroyo-de Dompablo, *J. Power Sources*, 2006, **160**, 523–528.
- 106 M. Prabu, S. Selvasekarapandian, A. R. Kulkarni, S. Karthikeyan, G. Hirankumar and C. Sanjeeviraja, *Solid State Sci.*, 2011, **13**, 1714–1718.
- 107 N. N. Bramnik, K. G. Bramnik, T. Buhrmester, C. Baehtz, H. Ehrenberg and H. Fuess, *J. Solid State Electrochem.*, 2004, **8**, 558–564.
- 108 S. Brutti, J. Manzi, A. De Bonis, D. Di Lecce, F. Vitucci, A. Paolone, F. Trequattrini and S. Panero, *Mater. Lett.*, 2015, **145**, 324–327.
- 109 K. J. Kreder, G. Assat and A. Manthiram, *Chem. Mater.*, 2016, **28**, 1847–1853.
- 110 S. Brutti, J. Manzi, D. Meggiolaro, F. M. Vitucci, F. Trequattrini, A. Paolone and O. Palumbo, *J. Mater. Chem. A*, 2017, **5**, 14020–14030.
- 111 J. L. Allen, T. R. Jow and J. Wolfenstine, *J. Power Sources*, 2011, **196**, 8656–8661.
- 112 Y.-M. Kang, Y.-I. Kim, M.-W. Oh, R.-Z. Yin, Y. Lee, D.-W. Han, H.-S. Kwon, J. H. Kim and G. Ramanath, *Energy Environ. Sci.*, 2011, **4**, 4978–4983.
- 113 F. C. Strobridge, D. S. Middlemiss, A. J. Pell, M. Leskes, R. J. Clément, F. Pourpoint, Z. Lu, J. V. Hanna, G. Pintacuda, L. Emsley, A. Samoson and C. P. Grey, *J. Mater. Chem. A*, 2014, **2**, 11948–11957.
- 114 N. V. Kosova, O. A. Podgornova, E. T. Devyatkina, V. R. Podugolnikov and S. A. Petrov, *J. Mater. Chem. A*, 2014, **2**, 20697–20705.
- 115 L. Fang, H. Zhang, Y. Zhang, L. Liu and Y. Wang, *J. Power Sources*, 2016, **312**, 101–108.
- 116 M. V. V. M. S. Kishore and U. V. Varadaraju, *Mater. Res. Bull.*, 2005, **40**, 1705–1712.
- 117 L. Dimesso, C. Spanheimer and W. Jaegermann, *J. Power Sources*, 2013, **243**, 668–675.
- 118 L. Dimesso, D. Becker, C. Spanheimer and W. Jaegermann, *Prog. Solid State Chem.*,

- 2014, **42**, 184–190.
- 119 L. Dimesso, D. Becker, C. Spanheimer and W. Jaegermann, *J Solid State Electrochem.*, 2012, **16**, 3791–3798.
- 120 A. Örnek, *J. Power Sources*, 2017, **356**, 1–11.
- 121 Y. Maeyoshi, S. Miyamoto, Y. Noda, H. Munakata and K. Kanamura, *J. Power Sources*, 2017, **337**, 92–99.
- 122 B. Wu, H. Xu, D. Mu, L. Shi, B. Jiang, L. Gai, L. Wang, Q. Liu, L. Ben and F. Wu, *J. Power Sources*, 2016, **304**, 181–188.
- 123 N. Laszczynski, A. Birrozzi, K. Maranski, M. Copley, M. E. Schuster and S. Passerini, *J. Mater. Chem. A*, 2016, **4**, 17121–17128.
- 124 X. Rui, X. Zhao, Z. Lu, H. Tan, D. Sim, H. H. Hng, R. Yazami, T. M. Lim and Q. Yan, *ACS Nano*, 2013, **7**, 5637–5646.
- 125 M. K. Devaraju, D. Rangappa and I. Honma, *Electrochim. Acta*, 2012, **85**, 548–553.
- 126 J. Liu, T. E. Conry, X. Song, L. Yang, M. M. Doeff and T. J. Richardson, *J. Mater. Chem.*, 2011, **21**, 9984–9987.
- 127 R. Sharabi, E. Markevich, V. Borgel, G. Salitra, D. Aurbach, G. Semrau, M. A. Schmidt, N. Schall and C. Stinner, *Electrochem. Commun.*, 2011, **13**, 800–802.
- 128 Y. Maeyoshi, S. Miyamoto, H. Munakata and K. Kanamura, *J. Power Sources*, 2017, **350**, 103–108.
- 129 L. Y. Xing, M. Hu, Q. Tang, J. P. Wei, X. Qin and Z. Zhou, *Electrochim. Acta*, 2012, **59**, 172–178.
- 130 F. Wang, J. Yang, Y. NuLi and J. Wang, *J. Power Sources*, 2010, **195**, 6884–6887.
- 131 H. Li, Y. Wang, X. Yang, L. Liu, L. Chen and J. Wei, *Solid State Ionics*, 2014, **255**, 84–88.
- 132 J. L. Allen, J. L. Allen, T. Thompson, S. A. Delp, J. Wolfenstine and T. R. Jow, *J. Power Sources*, 2016, **327**, 229–234.
- 133 D. Di Lecce, J. Manzi, F. M. Vitucci, A. De Bonis, S. Panero and S. Brutti, *Electrochim. Acta*, 2015, **185**, 17–27.
- 134 F. C. Strobridge, H. Liu, M. Leskes, O. J. Borkiewicz, K. M. Wiaderek, P. J. Chupas, K. W. Chapman and C. P. Grey, *Chem. Mater.*, 2016, **28**, 3676–3690.
- 135 T. Muraliganth and A. Manthiram, *J. Phys. Chem. C*, 2010, **114**, 15530–15540.
- 136 M. Köntje, M. Memm, P. Axmann and M. Wohlfahrt-Mehrens, *Prog. Solid State Chem.*, 2014, **42**, 106–117.
- 137 Y. Maeyoshi, S. Miyamoto, Y. Noda, H. Munakata and K. Kanamura, *J. Power Sources*,

- 2017, **337**, 92–99.
- 138 J. Ni, L. Gao and L. Lu, *J. Power Sources*, 2013, **221**, 35–41.
- 139 J. Ni, H. Wang, L. Gao and L. Lu, *Electrochim. Acta*, 2012, **70**, 349–354.
- 140 S.-M. Oh, S.-T. Myung and Y.-K. Sun, *J. Mater. Chem.* 2012, **22**, 14932–14937.
- 141 F. Wang, J. Yang, Y. NuLi and J. Wang, *J. Power Sources*, 2011, **196**, 4806–4810.
- 142 M. Zhang, N. Garcia-Araez and A. L. Hector, *J. Mater. Chem. A*, 2018, **6**, 14483–14517.
- 143 A. Mendiboure, C. Delmas and P. Hagenmuller, *J. Solid State Chem.*, 1985, **57**, 323–331.
- 144 X. Ma, H. Chen and G. Ceder, *J. Electrochem. Soc.* 2011, **158**, A1307–A1312.
- 145 N. Yabuuchi, R. Hara, M. Kajiyama, K. Kubota, T. Ishigaki, A. Hoshikawa and S. Komaba, *Adv. Energy Mater.*, 2014, **4**, 1301453–1301476.
- 146 E. de la Llave, E. Talaie, E. Levi, P. K. Nayak, M. Dixit, P. T. Rao, P. Hartmann, F. Chesneau, D. T. Major, M. Greenstein, D. Aurbach and L. F. Nazar, *Chem. Mater.*, 2016, **28**, 9064–9076.
- 147 J. Billaud, G. Singh, A. R. Armstrong, E. Gonzalo, V. Roddatis, M. Armand, T. Rojo and P. G. Bruce, *Energy Environ. Sci.*, 2014, **7**, 1387–1391.
- 148 N. Yabuuchi, R. Hara, K. Kubota, J. Paulsen, S. Kumakura and S. Komaba, *J. Mater. Chem. A*, 2014, **2**, 16851–16855.
- 149 U. Maitra, R. A. House, J. W. Somerville, N. Tapia-Ruiz, J. G. Lozano, N. Guerrini, R. Hao, K. Luo, L. Jin, M. A. Pérez-Osorio, F. Massel, D. M. Pickup, S. Ramos, X. Lu, D. E. McNally, A. V. Chadwick, F. Giustino, T. Schmitt, L. C. Duda, M. R. Roberts and P. G. Bruce, *Nat. Chem.*, 2018, **10**, 288–295.
- 150 X. Bai, M. Sathiya, B. M. Sánchez, A. Iadecola, J. Vergnet, R. Dedryvère, M. Saubanère, A. M. Abakumov, P. Rozier and J.-M. Tarascon, *Adv. Energy Mater.*, 2018, **8**, 1802379–1802391.
- 151 Z. Lu and J. R. Dahn, *J. Electrochem. Soc.*, 2001, **148**, A1225–A1229.
- 152 H. Wang, B. Yang, X.-Z. Liao, J. Xu, D. Yang, Y.-S. He and Z.-F. Ma, *Electrochim. Acta*, 2013, **113**, 200–204.
- 153 D. H. Lee, J. Xu and Y. S. Meng, *Phys. Chem. Chem. Phys.*, 2013, **15**, 3304–3312.
- 154 J. Xu, D. H. Lee, R. J. Clément, X. Yu, M. Leskes, A. J. Pell, G. Pintacuda, X.-Q. Yang, C. P. Grey and Y. S. Meng, *Chem. Mater.*, 2013, **26**, 1260–1269.
- 155 H. Hou, B. Gan, Y. Gong, N. Chen and C. Sun, *Inorg. Chem.*, 2016, **55**, 9033–9037.
- 156 P.-F. Wang, Y. You, Y.-X. Yin, Y.-S. Wang, L.-J. Wan, L. Gu and Y.-G. Guo, *Angew. Chem.*

- Int. Ed*, 2016, **55**, 7445–7449.
- 157 G. Singh, N. Tapia-Ruiz, J. M. Lopez del Amo, U. Maitra, J. W. Somerville, A. R. Armstrong, J. Martinez de Ilarduya, T. Rojo and P. G. Bruce, *Chem. Mater.*, 2016, **28**, 5087–5094.
- 158 N. Tapia-Ruiz, W. M. Dose, N. Sharma, H. Chen, J. Heath, J. W. Somerville, U. Maitra, M. S. Islam and P. G. Bruce, *Energy Environ. Sci.*, 2018, **11**, 1470–1479.
- 159 C. Ma, J. Alvarado, J. Xu, R. J. Clément, M. Kodur, W. Tong, C. P. Grey and Y. S. Meng, *J. Am. Chem. Soc.*, 2017, **139**, 4835–4845.
- 160 B. M. de Boisse, G. Liu, J. Ma, S.-I. Nishimura, S.-C. Chung, H. Kiuchi, Y. Harada, J. Kikkawa, Y. Kobayashi, M. Okubo and A. Yamada, *Nat. Commun.*, 2016, **7**, 11397–113406.
- 161 B. M. de Boisse, S.-I. Nishimura, E. Watanabe, L. Lander, A. Tsuchimoto, J. Kikkawa, E. Kobayashi, D. Asakura, M. Okubo and A. Yamada, *Adv. Energy Mater.*, 2018, **8**, 1800409–1800416.
- 162 Y. Li, X. Wang, Y. Gao, Q. Zhang, G. Tan, Q. Kong, S. Bak, G. Lu, X.-Q. Yang, L. Gu, J. Lu, K. Amine, Z. Wang and L. Chen, *Adv. Energy Mater.*, 2018, **9**, 1803087–1803098.
- 163 K. Du, J. Zhu, G. Hu, H. Gao, Y. Li and J. B. Goodenough, *Energy Environ. Sci.*, 2016, **9**, 2575–2577.
- 164 X. Rong, E. Hu, J. Liu, Y. Liu, Y. Wang, J. Wu, X. Yu, K. Page, Y.-S. Hu, W. Yang, H. Li, X.-Q. Yang, L. Chen and X. Huang, *Joule*, 2018, **2**, 125–140.
- 165 B. Song, E. Hu, J. Liu, Y. Zhang, X.-Q. Yang, J. Nanda, A. Huq and K. Page, *J. Mater. Chem. A*, 2019, **7**, 1491–1498.

2. Experimental

2.1. Synthesis techniques

2.1.1. Solvothermal method

Solvothermal synthesis refers to the synthesis through decomposition and/or chemical reactions between precursors in solvents above the boiling temperature of solvents in a closed reaction vessel. As the electrochemical performance of electrode materials is highly dependent on their particle size and shape, solvothermal synthesis represents a versatile approach to modify size distribution and particle morphology of electrode materials.

The main experimental factors of the solvothermal method can be categorised into two: chemical and thermodynamic. The chemical factors include the nature of precursors, solvents, additives and pH of reaction medium. Different types of precursor and additive have been shown to affect the solubility of reagents and the affinity between anions and cations in the reaction medium, permitting the design of different morphologies of materials.^{1,2} The concentration and nature of the solvent can influence the kinetics of reaction, leading to production not only of various morphologies, but also different crystal structures.³⁻⁵ As the pH of the reagents plays a critical role in facilitating initial nucleation, the optimisation of the ratio between precursors is necessary to obtain a single-phase product.¹ The thermodynamic factors such as reaction temperature, time and pressure can alter the kinetics of chemical reactions, the solubility and stability of precursors and the oxidation state of transition metals.⁶

The solvothermal method was used to synthesise lithium cobalt phosphate (chapter 3) and magnesium doped lithium cobalt phosphate (chapter 4). Detailed synthetic conditions and procedures are described in each chapter.

2.1.2. Co-precipitation method

Co-precipitation synthesis has been applied in the production of electrode materials as this method can overcome the disadvantages of conventional ceramic route e.g., long synthetic protocol involving repeated grinding, high temperature and difficulties in the control of particle size and shape.

The co-precipitation route can be classified into two: hydroxide and carbonate co-precipitation, depending on the nature of mixed metal precipitate. In the synthesis of lithium metal oxides, both methods have been widely applied. Although co-precipitation conditions including pH, stirring rate and the concentration of chelating ligands vary to control particle size and morphology, the principal procedure can be outlined as follows. The stoichiometric amount of metal precursors such as nitrates, sulphates and acetates are dissolved in deionised water. The aqueous solution is added into a lithium hydroxide or sodium carbonate aqueous solution to form mixed metal hydroxide or carbonate, respectively. The resulting precipitate is filtered, washed and dried then mixed with an appropriate amount of lithium source e.g., lithium carbonate. The mixed powder is then heated at the desired temperature for a specified time at a suitable ramping rate to yield lithium metal oxides. It has been shown that the carbonate co-precipitation route favours maintaining the oxidation states of transition metals by chelating carbonate anion groups.⁷⁻⁹ In the preparation of sodium metal oxides, both hydroxide and carbonate co-precipitation methods have been used with sodium carbonate as a sodium source.^{10,11}

The carbonate co-precipitation method was used to prepare P3-type magnesium doped sodium manganese oxide (chapter 5) and P3-type nickel doped sodium manganese oxide (chapter 6). Detailed synthetic conditions and procedures are summarised in each chapter.

2.2. Analysis techniques

2.2.1. Powder X-ray diffraction (PXRD)

PXRD is a powerful tool to understand the crystal structure of polycrystalline materials. Most commonly, the X-rays themselves are generated in laboratory sources by striking a metal target (e.g., a copper or iron target) with electrons. When the electrons have sufficient energy to knock out inner shell electrons, characteristic X-ray wavelengths are produced such as K_{α} and K_{β} (Fig. 2.1). The K_{α} X-ray is emitted when an electron falls from the L shell to the K shell, which consists of two characteristic wavelengths called as $K_{\alpha 1}$ and $K_{\alpha 2}$, corresponding to transitions from $2p_{3/2}$ to $1s$ and from $2p_{1/2}$ to $1s$, respectively. Similarly, when the K shell vacancy is filled with an electron from the M shell, K_{β} radiation is emitted.

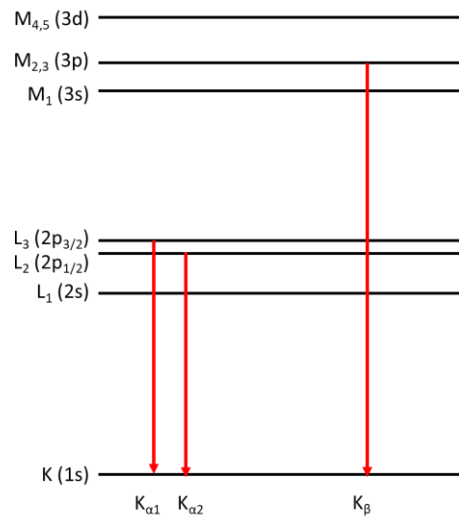


Figure 2.1. Electronic energy levels of a target metal.

Typical wavelengths of commonly used target metals are summarised in Table 2.1. Consideration in selecting radiation is important to acquire satisfactory diffraction patterns. For example, the radiation from copper is absorbed by cobalt containing samples and the copper radiation causes strong X-ray fluorescence background from cobalt. Therefore, the use of iron radiation for cobalt based materials is preferred.

Table 2.1. Characteristic wavelengths of target materials where $\lambda_{K\alpha} = (2\lambda_{K\alpha1} + \lambda_{K\alpha2})/3$.¹²

Target material	Wavelength (Å)			
	K_{α}	$K_{\alpha1}$	$K_{\alpha2}$	K_{β}
Fe	1.93739	1.93608	1.94002	1.75664
Co	1.79030	1.78900	1.79289	1.62082
Cu	1.54187	1.54059	1.54441	1.39225
Mo	0.71075	0.709317	0.71361	0.63230

Bragg's law (Equ.2.1) establishes the relationship between wavelength, diffraction angle and the distance between lattice planes, as shown in the equation below.

$$n\lambda = 2d_{hkl}\sin\theta \quad (\text{Equation 2.1})$$

(n : an integer, λ : wavelength of the radiation, d_{hkl} : distance between lattice planes, θ : angle of incident X-ray)

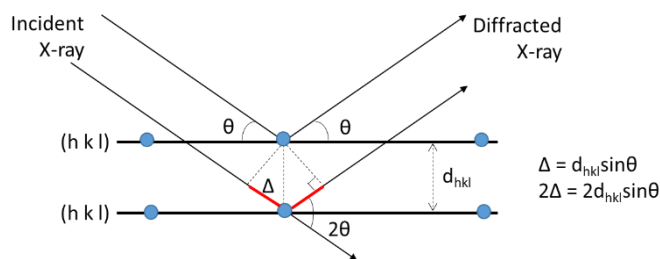


Figure 2.2. Illustration of Bragg's law (d_{hkl} : distance between lattice planes, θ : angle of incident X-ray, Δ in red: half of path difference between two radiations).

In this work, PXRD patterns for lithium cobalt phosphate and magnesium doped lithium cobalt phosphates were collected using a STOE STADI/P diffractometer in transmission mode with Fe $K\alpha_1$ radiation ($\lambda = 1.936 \text{ \AA}$) in the range $20\text{--}80^\circ$ except where indicated. Samples were ground manually then supported between two clear polythene discs, held together by vacuum grease in an Ar-filled glovebox for air-sensitive samples or under ambient atmosphere for other samples. During the measurement, the sample holder was spun to reduce preferred orientation effects.

For the studies on P3-type magnesium doped sodium manganese oxide and P3-type nickel doped sodium manganese oxide, PXRD patterns were recorded on a PANalytical Empyrean diffractometer in Bragg-Brentano geometry with Cu $K\alpha_1$ radiation ($\lambda = 1.5406 \text{ \AA}$) in the range $10\text{--}80^\circ$. In the case of post-cycled samples of P3-type magnesium doped sodium manganese oxide, contained in 0.7 mm glass capillaries and sealed using vacuum grease in an Ar-filled glovebox, were characterised using a STOE STADI/P diffractometer in transmission mode with Fe $K\alpha_1$ radiation ($\lambda = 1.936 \text{ \AA}$) in the range $18\text{--}90^\circ$ or a PANalytical Empyrean diffractometer in transmission mode with Mo $K\alpha$ radiation ($\lambda = 0.7107 \text{ \AA}$) in the range $5\text{--}40^\circ$.

2.2.2. Powder neutron diffraction (PND)

Analogous to X-rays, neutrons interact with crystalline samples, resulting in diffraction patterns, used to elucidate structural information of materials. The main differences compared to PXRD are that neutrons are scattered by the nucleus and scattering length varies independently of rather than proportional to atomic number. These characters provide the high sensitivity to light elements e.g., lithium, and high contrast between neighbouring elements such as manganese and nickel. The scattering length of elements studied in this thesis are summarised in Table. 2.2.

Table 2.2. Coherent scattering length of selected elements.¹³

	Li	O	Na	Mg	P	Mn	Co	Ni
Coherent scattering length (fm)	-1.90	5.803	3.63	2.375	5.13	-3.73	2.49	10.3

Due to the weak interactions of neutrons with the material, large amounts of sample or longer acquisition time are typically needed.

For the purpose of this work, time-of-flight PND data were obtained on the Polaris or GEM diffractometer at ISIS at the Rutherford Appleton Laboratory. The pulsed neutron source at ISIS is generated by a nuclear proton-neutron reaction, known as a spallation source. The produced neutrons initially have very high energy, thus are slowed in moderators, filled with e.g., liquid methane, to the energy needed for neutron diffraction studies. On the diffractometer, several banks of detectors are placed at different scattering angles to cover a wide range of d-spacing and ensure high neutron count rate.

For the PND measurements, magnesium doped lithium cobalt phosphates were loaded in 6 mm cylindrical vanadium cans. Typical collection times for these samples were 1 to 2 hours. In the case of cycled samples for P3-type magnesium doped sodium manganese oxide and P3-type nickel doped sodium manganese oxide, samples were filled in 2 mm quartz capillaries and sealed using vacuum grease in an Ar-filled glovebox then sealed permanently using glue under ambient atmosphere. Collection times were adjusted depending on samples quantities and crystallinities.

2.2.3. Refinement

PXRD and PND patterns provide information about phase composition, lattice parameters and crystal structure of a sample. In order to identify an unknown phase of the sample, recorded diffraction peaks are compared with one or more databases using different search-match algorithms. The Le Bail method can be applied to find suitable parameters as initial approximation prior to Rietveld refinement. The Le Bail method involves the extraction of intensity of individual diffraction peaks and fits the diffraction pattern with predetermined approximate unit cell parameters and space group using a least-squares method. The refinement includes lattice parameters, profile parameters and peak intensities. To further

obtain detailed crystallographic information such as atomic positions, site occupancies and thermal parameters, the Rietveld method is used. The refinement algorithm is basically same as the Le Bail method, the main difference is that the intensities are computed from an assigned crystal structure in the Rietveld technique, which can result in higher weighted-profile R factor (R_{wp}) than that obtained by the Le Bail method. In contrast, the Rietveld method can quantify phase contents in a sample, permitting the investigation of phase transformations during electrochemical cycling.

The quality of refinement results and data are evaluated by the R values such as R_{wp} (Equ.2.2) and R_{exp} (Equ.2.3), respectively.

$$R_{wp} = \{\sum_i w_i [y_i(obs) - y_i(cal)]^2 / \sum_i w_i [y_i(obs)]^2\}^{1/2} \quad (Equation 2.2)$$

($y_i(obs)$): observed intensity at step i, $y_i(cal)$: calculated intensity at step i, w_i : weight)

$$R_{exp} = [(N - P) / \sum_i^N w_i y_i (obs)^2]^{1/2} \quad (Equation 2.3)$$

($y_i(obs)$: observed intensity at step i, w_i : weight, N: number of observations, P : number of parameters)

Ideally, the R_{wp} should approach the R_{exp} and this is often quoted in the literature as the goodness-of-fit: $\chi^2 (R_{wp}/R_{exp})^2$. Along with good R factors, chemically sensible results are critical to assess the refinements.¹⁴

In order to obtain lattice parameters and crystallographic information for the materials studied in this thesis, the Le Bai¹⁵ and the Rietveld refinement, respectively, was carried out using different software: GSAS,¹⁶ the Fullprof suite¹⁷ and TOPAS Academic.¹⁸

2.2.4. Scanning electron microscopy (SEM)

SEM provides microstructural information such as morphology and the particle size of the sample. An electron beam is emitted from a tungsten filament or a field emission gun then accelerated through a potential difference. When the focused electron beam reaches the sample, various signals can be detected including secondary electrons, backscattered electrons and X-rays. The secondary electrons, emitted from a surface, provide topological detail of the sample. The backscattered electrons originate from deeper within the sample and yield compositional information with lower resolution images.¹⁹

For the work in this thesis, as-synthesised samples were examined using a JEOL JSM-6700F and post-cycled electrodes were analysed using a FEI Scios microscope. In order to minimise moisture/air exposure to the air-sensitive electrodes, samples were loaded in a sample holder in an Ar-filled glovebox and quickly transferred to the microscope.

2.2.5. Transmission electron microscopy (TEM)

TEM is an analogous technique to SEM where accelerated electron beams are used to acquire images. The main difference from SEM is that TEM uses transmitted electrons, that interact with a sample, to provide information about morphology and crystal structure. In order to transmit sufficient electrons, preparation of an ultra-thin sample (≤ 500 nm) is important. The contrast in a conventional bright field image originates from compositional density and crystal orientation of the sample. Electron diffraction is also applied to analyse the crystal structure of crystalline materials.

In this thesis, pre- and post-cycled samples were examined using a FEI Titan Themis 200. The post-cycled samples were loaded in a sample holder inside of Ar-filled glovebox and transferred to a FEI Scios microscope for milling the sample, then kept under vacuum until TEM measurements.

2.2.6. Scanning transmission electron microscopy (STEM)

STEM is a combined electron microscopy technique. The difference from TEM is that a focused electron beam is scanned over a sample and scattered electrons are detected in an annular detector. The main advantage of STEM relies on a high angle annular dark field image, which provides an atomic resolution image with the contrast directly related to atomic numbers.²⁰

In the study of magnesium doped lithium cobalt phosphates, STEM images of pre- and post-cycled samples were recorded using a FEI Titan Themis 200. The post-cycled samples were carefully handled as described in section 2.2.5.

2.2.7. Energy dispersive X-ray spectroscopy (EDS)

When an electron beam bombards a sample, X-rays are emitted as a consequence of the interaction between the electron beam and the sample. The characteristic X-ray generated from the sample is detected and converted for an elemental analysis. In order to obtain a reasonable peak to background ratio, the incident beam energy should be at least twice the

critical excitation energy - the minimum energy to create an initial vacancy. There are two methods most widely used: point analysis and elemental mapping, which can provide qualitative and quantitative analysis.

In this thesis, EDS spectra were collected using an FEI Scios microscope coupled with EDAX Octane Plus EDS detector. EDS mapping was carried out using either an FEI Scios microscope coupled with EDAX Octane Plus EDS detector or an FEI Titan Themis 200 equipped with a Super-X high sensitivity windowless EDX detector. For air-sensitive samples, samples were carefully prepared as dedcribed in section 2.2.4 and 2.2.5.

2.2.8. Inductively coupled plasma optical emission spectroscopy (ICP-OES)

ICP-OES is a technique to determine the composition of a sample. Materials in solid form are dissolved in acid; the solution is then introduced into the inductively coupled plasma where elements are excited by plasma energy. When the excited elements return to low energy, radiation at the wavelengths corresponding to the particular elements is released; these are measured with a spectrometer. The intensity of the emissions determines the concentration of the elements.²¹

Prior to the ICP-OES analysis, all samples reported in this thesis were dissolved in an aqua regia. The analysis was performed using a iCAP 6000 series for lithium cobalt phosphate and magnesium doped lithium cobalt phosphates. For P3-type magnesium doped sodium manganese oxide and P3-type nickel doped sodium manganese oxide, all samples were sealed in an Ar-filled glovebox and sent to Yonsei University where the measurements were carried out using a PerkinElmer Optima 8300, except where indicated.

2.2.9. Fourier transform infra-red spectroscopy (FT-IR)

FT-IR is a technique to obtain a vibrational spectrum of a sample by absorbing radiation in the infra-red region. When the sample is exposed to infra-red radiation, some radiation is absorbed at the frequency corresponding to the frequency of vibrations from bonds within the sample. Using a Fourier transform, raw signals are converted into the spectrum with absorbance or transmittance as a function of wavenumber. As the vibrations of molecules are affected by the nature of vibration either stretching or bending, strength of bonds, atomic mass and adjacent groups, FT-IR can identify the chemical structure of the sample.²²

In this thesis, FT-IR experiments were carried out on a Shimadzu IRAffinity-1S spectrometer for samples in powder form. In order to collect FT-IR spectra for pre- and post- cycled electrodes, pellets were prepared by grinding approximately 5 wt % of the material with dried potassium bromide powder then pressed in a 10 mm diameter die. The spectra were recorded using a Nicolet Magna 860 spectrometer.

2.2.10. X-ray photoelectron spectroscopy (XPS)

XPS is a useful technique to study the surface of a sample - in general around 10 nm into the sample. The sample is subjected to X-rays, generally aluminium K_{α} , and the kinetic energy of the ejected electron from the surface under investigation is measured. Using the equation (Equ.2.4.), the binding energy of the electron is determined.²³

$$E_B = E_{\text{photon}} - (E_K + \phi) \quad (\text{Equation 2.4})$$

(E_B : binding energy of electron, E_{photon} : energy of X-ray photon, E_K : kinetic energy of electron measured by the instrument, ϕ : work function)

The binding energy depends on the element and orbital from which the electron is ejected, as well as the chemical environment of the element from where the electron is emitted. A typical XPS spectrum consists of the counts of the ejected electrons (intensities) and a series of peaks, originating from the elements emitting electrons with characteristic energies. In general, a survey spectrum is first measured to examine all elements present on the sample surface and subsequent high-resolution XPS spectra of each element are recorded. The high-resolution spectra permit the analysis of chemical or electronic states of the elements.

For the study on P3-type magnesium doped sodium manganese oxide, XPS analysis was performed at the Ångström laboratory of Uppsala University. The measurements were carried out using a PHI 5500 system with monochromatic aluminium K_{α} X-ray source ($E_{\text{photon}} = 1487$ eV). All samples were sealed in an Ar-filled glovebox and sent to Uppsala University. The samples were opened in an Ar-filled glovebox and cleaned with dimethyl carbonate before transferred to the spectrometer in a transfer chamber to avoid exposure to moisture/air. The obtained data were plotted using the software Igor Pro 6.34A. All peaks were calibrated based on the hydrocarbon species C 1s peak at 285 eV.

2.2.11. X-ray absorption spectroscopy (XAS)

XAS is a technique generally used to investigate oxidation state and local structure of a sample. When the X-ray beam hits the sample, some X-rays are absorbed by the element. This excites an electron of the sample from its core orbital to an unoccupied state. The empty core orbital can be filled by an electron from a higher energy level, accompanied by fluorescence or further emission of an Auger electron. The most common way to deduce the amount of absorption is comparing the transmitted intensity of the X-ray to that of the incident beam. Based on the Beer-Lambert law, the absorption fraction can be described as a function of energy (Equ. 2.5.).

$$I_t = I_0 e^{-\mu(E)x} \rightarrow \ln\left(\frac{I_0}{I_t}\right) = x\mu(E) \quad (\text{Equation 2.5})$$

(I_t : transmitted intensity, I_0 : incident intensity, $\mu(E)$: absorption coefficient, x : thickness of sample)

A typical XAS spectrum consists of the pre-edge, X-ray absorption near edge structure (XANES) and extended X-ray absorption fine structure (EXAFS). An example of the Mn K-edge XAS spectrum of MnO_2 is shown in Fig.2.3. The pre-edge is located just after the energy, E_0 , where an electron can be excited from the Mn 1s orbital. Then a sharp jump with several peaks and small shoulders appear, described as XANES. Conventionally, XANES refers to both pre-edge and XANES within 50 eV of the E_0 . As an element with a higher oxidation state requires more energy to excite its core electron, XANES is sensitive to the oxidation state of the absorbing element. Starting from XANES to 1000 eV above E_0 , there is an oscillatory region called EXAFS. As oscillations depend on the distance between the absorbing element and scattering elements near the absorbing element, EXAFS provides information about local environment of the absorbing element.²⁴

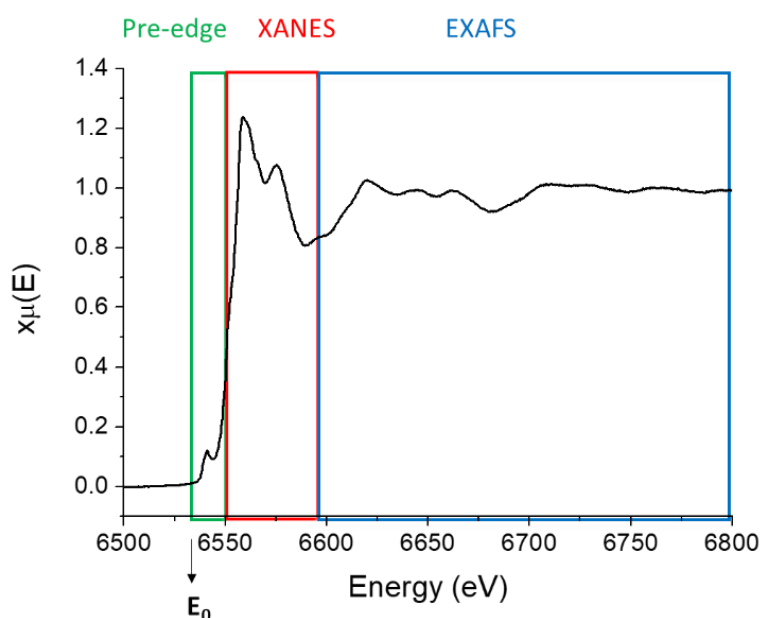


Figure 2.3. Mn K-edge XAS spectrum of MnO_2 .

All XAS spectra for transition metals were collected in transmission mode at beamline B18 at the Diamond Light source. Pellets of 13 mm diameter were prepared by grinding dried cellulose and the active material in a pre-determined mass ratio then pressed at 5 tons for 3 min in an Ar-filled glovebox. Air-sensitive samples were transferred to the specially designed sample holder inside an Ar-filled glovebox and other samples were attached to the general rod using a Kapton tape. The collected spectra were processed using the software Athena. XAS spectra for oxygen were recorded in TFY and TEF modes at the beamline BL27SU at Spring 8 in Japan. All electrodes, cut into stripes (5 mm x 10 mm) and fixed on a copper tape with 3 mm gap between each sample, were sealed in an Ar-filled glovebox and sent to the Spring 8. The samples were opened in an Ar-filled glovebox and transferred to the rod to avoid exposure to moisture/air.

2.2.12. Resonant inelastic X-ray scattering (RIXS)

RIXS is a technique which has been used to probe directly oxygen states in the bulk. When a material absorbs a soft X-ray in the energy range 525-550 eV, a two-step process occurs; O $1s$ core electrons are excited to unoccupied O $2p$ (K-edge) and the $1s$ holes are subsequently filled with electrons relaxed from occupied $2p$ states with resonant inelastic X-ray scattering, where the energy loss from the absorption to emission corresponds to the excitation energy from occupied $2p$ to unoccupied $2p$ states (Fig. 2.4).^{25,26}

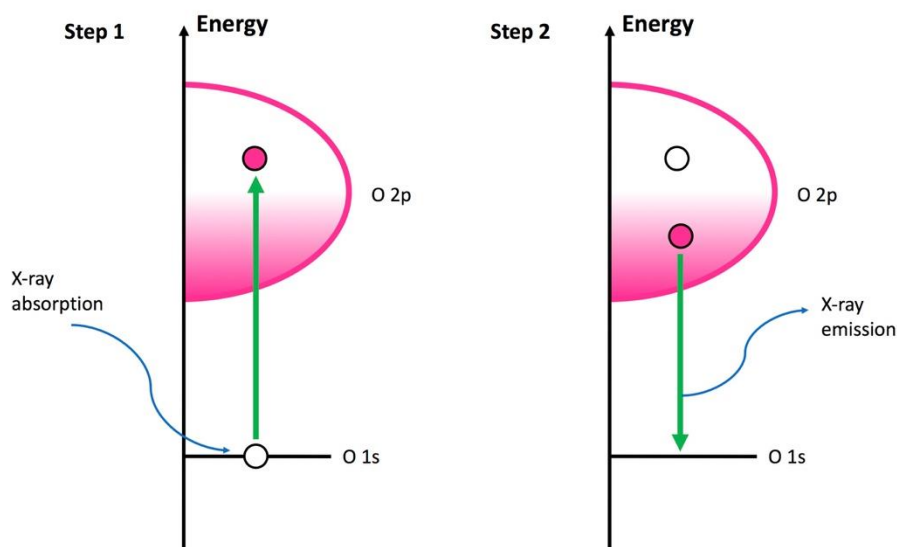


Figure 2.4. Schematic RIXS process for O K-edge.

For the study on P3-type nickel doped sodium manganese oxide, RIXS measurements were carried out at beamline BL27SU at the Spring 8. All samples were carefully handled as described in section 2.2.11.

2.3. Cell assembly

2.3.1. Fabrication of electrodes

- **Cast electrodes**

All coin cells in this work were assembled with cast electrodes made by slurries; they were prepared using the active material, super C65 carbon and binder in the mass ratio 75 : 15 : 10, except where indicated, in a solvent, which was then cast on aluminium foil using a doctor blade. After drying under ambient atmosphere, electrode discs were punched then dried at 80 °C or 130 °C for n-methyl-2-pyrrolidone based slurries or aqueous slurries, respectively, under vacuum for 12 h.

- **Loose powder electrodes**

For Swagelok-type cells and *in-situ* XRD cells, working electrodes were constructed by mixing active material and super C65 carbon in the desired mass ratio without binder. The mixture powder was dried at 110 °C under vacuum for 12 h.

2.3.2. Coin cell and Swagelok-type cell assembly

Coin cells were assembled from CR2325 or LIR2032 coin cell parts with a disc electrode, a separator soaked with a chosen electrolyte and a selected metal as a counter/reference electrode (Fig. 2.5a).

Swagelok-type cells were assembled using a certain amount of loose powder electrode, glass fibre separators soaked with the desired electrolyte and a selected metal as a counter/reference electrode (Fig. 2.5b).

In both cases, cells were assembled in an Ar-filled glovebox.

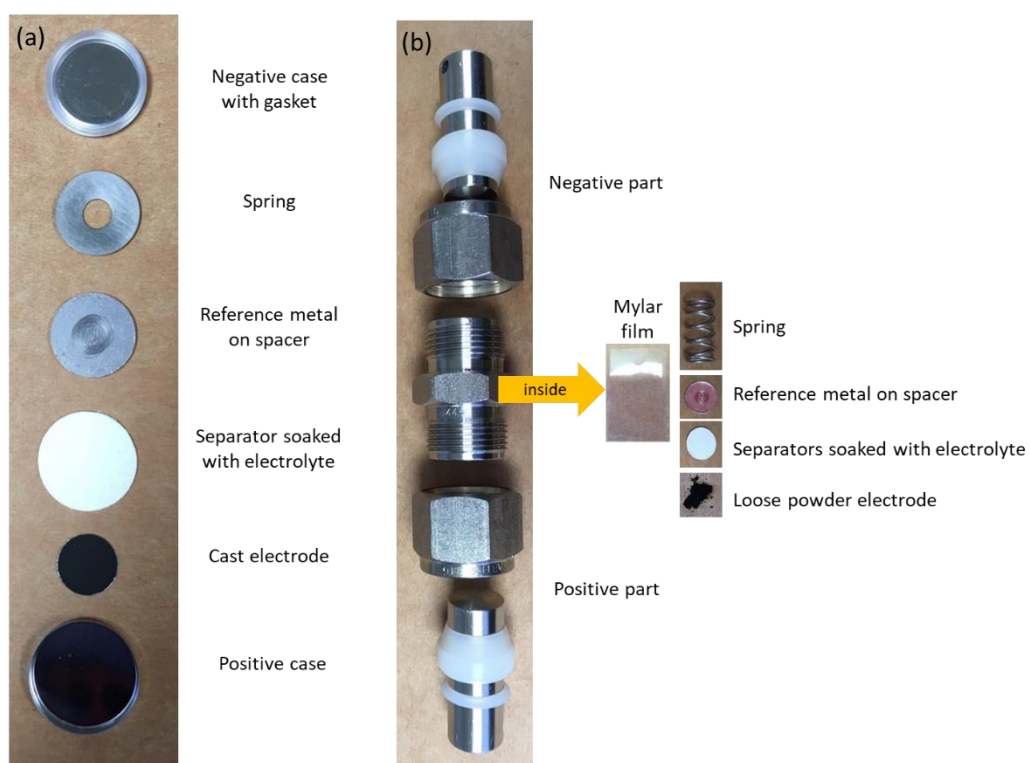


Figure 2.5. Photos of (a) CR2325 coin cell and (b) Swagelok-type cell assembly.

2.4. Electrochemical characterisation

2.4.1. Battery metrics

- **Capacity**

The theoretical capacity of materials represents the quantity of electrons involved in the electrochemical reaction per molar weight of an active material (Equ. 2.6).

$$Q_{th} = \frac{n \times F}{M_w} \quad (\text{Equation 2.6})$$

(Q_{th} : theoretical capacity, n : number of electrons exchanged per formula unit, F : Faraday constant, M_w : molar weight of an active material)

The equation implies that smaller molecular weight and greater number of electrons exchanged per formula unit can deliver higher capacity in theory. The theoretical capacities of the materials studied in this thesis are summarised in Table. 2.3.

Table 3.3. Theoretical capacity based on one electron exchanged per formula unit.

	LiCoPO₄	Na_{0.67}Mg_{0.2}Mn_{0.8}O₂	Na_{0.67}Ni_{0.2}Mn_{0.8}O₂
Q_{th} (mAh g⁻¹)	167	279	260

Specific capacity is an essential value to evaluate the active materials. It is determined by the relation described in Equ. 2.7.

$$Q_{sp} = \frac{I \times t}{M_w} \quad (\text{Equation 2.7})$$

(Q_{sp} : specific capacity, I : current passed , t : charge/discharge time, M_w : molar weight of an active material)

- **Specific energy and power density**

Specific energy density of materials is determined collectively by the specific discharge capacity and the discharge voltage of an active material (Equ. 2.8).

$$E_{sp} = Q_{dis} \times V_{dis} \quad (\text{Equation 2.8})$$

(E_{sp} : specific energy density, Q_{dis} : specific discharge capacity, V_{dis} : discharge voltage)

Specific power density of materials is the product of the electric current passed during discharging and the discharge voltage of an active material (Equ. 2.9).

$$P_{sp} = I_{dis} \times V_{dis} \quad (\text{Equation 2.9})$$

(P_{sp} : specific power density, I_{dis} : current passed during discharge , V_{dis} : discharge voltage)

2.4.2. Galvanostatic cycling

This technique consists of applying a positive or negative constant current, often expressed as a C-rate, and recording the evolution of a cell potential with time (Fig. 2.6). The C-rate is a measure of the rate at which the cell is charged or discharged relative to its theoretical (or practical) capacity. For example, a rate of 1C means that the cell is fully charged and discharged in an hour. During charge a working electrode material is oxidized by the positive current up to a predefined upper voltage limit. During discharge the reverse process happens, i.e., the working electrode is reduced with an applied negative current until a predefined lower voltage limit is reached. In galvanostatic cycling for positive electrode materials, the current is continually reversed in positive and subsequently negative sweeps after each cycle.

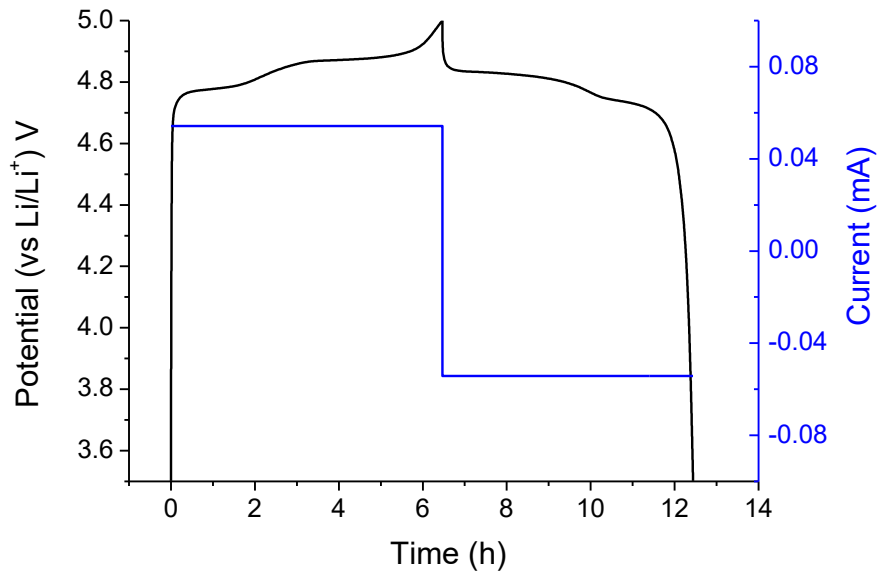


Figure 2.6. Evolution of current and recorded potential as a function of time during discharge and charge of LiCoPO_4 at a rate of $C/10$ ($1C = 167 \text{ mA g}^{-1}$).

2.4.3. Cyclic voltammetry

In this technique, the potential of a working electrode is controlled, measuring current over time at a desired scan rate (Fig. 2.7a). Cyclic voltammetry is a set of linear sweep voltammetry measurements where the potential is swept in positive and negative directions alternately. For example, at the end of the first scan of linear sweep voltammetry with applied positive potential, a negative potential is applied whilst scanning the current. The voltammogram, plotting current versus applied potential, provides information about possible redox processes of the working electrode. Fig. 2.7b exhibits two sets of oxidation and reduction peaks at the voltages where the working electrode material, LiCoPO_4 , is oxidized and reduced, respectively.

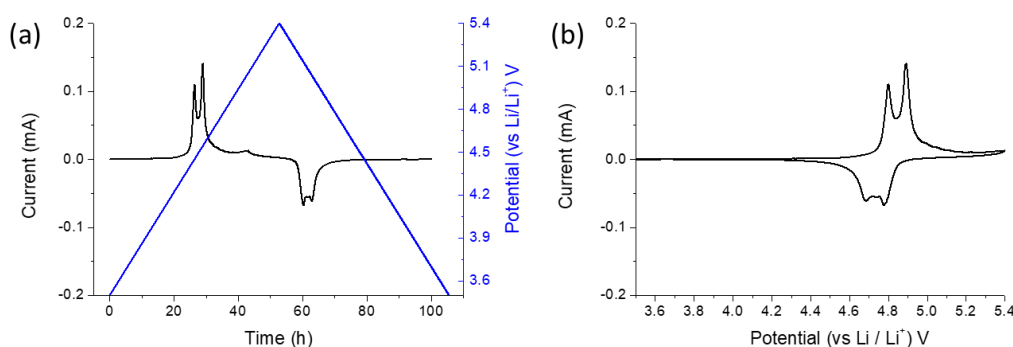


Figure 2.7. (a) Evolution of potential and recorded current as a function of time of LiCoPO_4 , (b) Voltammogram of LiCoPO_4 at a scan rate of $10 \mu\text{V}^{-1}$.

2.4.4. Electrochemical impedance spectroscopy (EIS)

EIS measurements are often used to identify electrochemical processes, separated by their characteristic timescales, that permit both qualitative and quantitative analysis. EIS measures current through a cell by applying an alternating potential, resulting in an impedance (Z) as a function of frequency ($\omega=2\pi f$) in general represented in Nyquist plot as shown in Fig. 2.8. Of note, a small alternating potential (1 to 10 mV) is applied to the cell to ensure the system is pseudo-linear, which simplifies analysis. The Nyquist plot consists of real (Z') and imaginary (Z'') parts with each point corresponding to impedance measured at different frequency. The main drawback of the Nyquist plot is the difficulty to distinguish frequency regions, therefore inserting a few frequencies in the plot is recommended as shown in Fig. 2.8d. Qualitative analysis of EIS involves the assessment of shape and features of the Nyquist plot to determine

different processes. For quantitative analysis, fitting a model using an equivalent circuit is essential to extract values associated with thermodynamic and kinetic parameters.²⁷

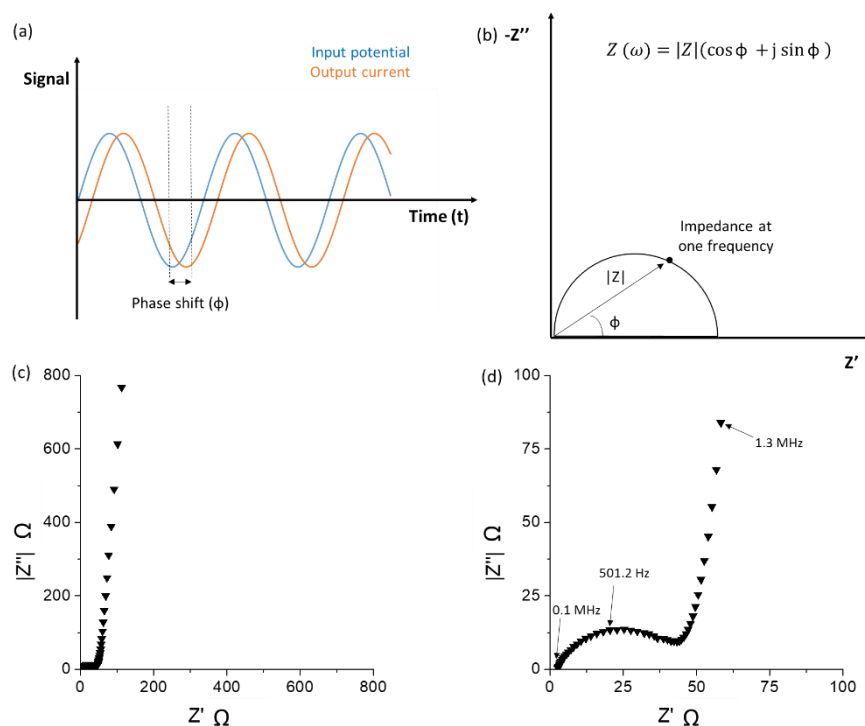


Figure 2.8. (a) Current response to a sinusoidal potential input in pseudo linear system, (b) Impedance as a function of frequency in Nyquist plot, (c) Nyquist plot of as-assembled LiCoPO_4 cell, measured at frequencies from 0.1 Hz to 0.1 MHz with perturbation voltage of 10 mV and (d) zoomed image of (c).

2.5. References

- 1 J. Manzi, M. Curcio and S. Brutti, *Nanomaterials*, 2015, **5**, 2212–2230.
- 2 Z. Lu, H. Chen, R. Robert, B. Y. X. Zhu, J. Deng, L. Wu, C. Y. Chung and C. P. Grey, *Chem. Mater.*, 2011, **23**, 2848–2859.
- 3 J. Ludwig, C. Marino, D. Haering, C. Stinner, H. A. Gasteiger and T. Nilges, *J. Power Sources*, 2017, **342**, 214–223.
- 4 B. Wu, H. Xu, D. Mu, L. Shi, B. Jiang, L. Gai, L. Wang, Q. Liu, L. Ben and F. Wu, *J. Power Sources*, 2016, **304**, 181–188.
- 5 K. J. Kreder, G. Assat and A. Manthiram, *Chem. Mater.*, 2015, **27**, 5543–5549.
- 6 G. Demazeau, *Z. Naturforsch*, 2010, **65b**, 999–1006.
- 7 L. Xu, P. Hou, Y. Zhang, H. Zhang, D. Song, X. Shi, X. Wang and L. Zhang, *J. Mater. Chem. A*, 2015, **3**, 21219–21226.
- 8 D. Wang, I. Belharouak, G. M. Koenig, G. Zhou and K. Amine, *J. Mater. Chem.*, 2011, **21**, 9290–9295.
- 9 S. H. Park, S. H. Kang, I. Belharouak, Y. K. Sun and K. Amine, *J. Power Sources*, 2008, **177**, 177–183.
- 10 C. Ma, J. Alvarado, J. Xu, R. J. Clément, M. Kodur, W. Tong, C. P. Grey and Y. S. Meng, *J. Am. Chem. Soc.*, 2017, **139**, 4835–4845.
- 11 J. Xu, D. H. Lee, R. J. Clément, X. Yu, M. Leskes, A. J. Pell, G. Pintacuda, X.-Q. Yang, C. P. Grey and Y. S. Meng, *Chem. Mater.*, 2013, **26**, 1260–1269.
- 12 V. Pecharsky and P. Zavalij, *Fundamentals of Powder Diffraction and Structural Characterization of Materials, Second Edition*, Springer Science & Business Media, 2008.
- 13 V. F. Sears, *Neutron News*, **3**, 26–37.
- 14 L. B. McCusker, R. B. Von Dreele, D. E. Cox, D. Louer and P. Scardi, *J. Appl. Crystallogr.*, 1999, **32**, 36–50.
- 15 A. Le Bail, *Powder Diffraction*, 2005, **20**, 316–.
- 16 B. H. Toby, *J. Appl. Crystallogr.*, 2001, **34**, 210–213.
- 17 J. Rodríguez-Carvajal, *Phys. B*, 1993, **192**, 55–69.
- 18 A. A. Coelho, *J. Appl. Crystallogr.*, 2000, **33**, 899–908.
- 19 J. I. Goldstein, D. E. Newbury, J. R. Michael, N. W. M. Ritchie, J. H. J. Scott and D. C. Joy, *Scanning Electron Microscopy and X-Ray Microanalysis*, Springer, New York, NY, 2017.
- 20 Y. Harada and Y. Ikuhara, in *Handbook of Advanced Ceramics*, Elsevier, 2013, pp. 3–21.
- 21 R. A. Meyers, *Encyclopedia of Analytical Chemistry*, 2006.

- 22 F. W. Fifield and D. Kealey, *Principles and Practice of Analytical Chemistry, 4th Edition*, CRC Press, 1995.
- 23 D. R. Vij, *Handbook of Applied Solid State Spectroscopy*, Springer Science & Business Media, 2007.
- 24 S. Calvin, *XAFS for Everyone*, CRC Press, 2013.
- 25 M. Okubo and A. Yamada, *ACS Appl. Mater. Interfaces*, 2017, **9**, 36463–36472.
- 26 L. Ament, *Rev. Mod. Phys.*, 2011, **83**, 705–767.
- 27 M. D. Murbach and D. T. Schwartz, *J. Electrochem. Soc.*, 2018, **165**, A297–A304.

3. Lithium cobalt phosphate

This work was published in the Journal of Power Sources in 2018 with the title of “Improved electrochemical performance of LiCoPO_4 using eco-friendly aqueous binders” (doi: 10.1016/j.jpowsour.2018.09.073).

3.1. Introduction

Lithium transition metal phosphates with the olivine structure have attracted considerable attention since the electrochemical activity of lithium iron phosphate (LiFePO_4) was first reported.¹ While LiFePO_4 is already used in commercial lithium-ion batteries, there are growing studies on its counterparts with other transition metals. Among the phospho-olivine family, lithium cobalt phosphate (LiCoPO_4 , LCP) has been an attractive candidate as a high voltage positive electrode material since first identified by Amine *et al.*² However, unsatisfactory electrochemical performance, especially poor cycling stability, has impeded its wide application. There are three main reasons for the poor cyclability : 1) the formation of an unstable SEI layer on the surface of LCP,³⁻⁶ 2) the degradation of LCP by HF present in the electrolyte solution^{7,8} and 3) the increase in the number of anti-site defects.⁹⁻¹¹ Most of the attempts to enhance the cycle stability have included modifying LCP itself via doping¹²⁻¹⁷ or surface modification¹⁸⁻²³ in combination with particle size reduction.^{14,24-26} In addition to these strategies, the use of novel separators^{27,28} and the development of functional electrolytes including additives^{4,5,29} have been applied. In contrast, little attention has been paid to the inactive components such as conductive carbons and binders.

Recently, the crucial role of binders in lithium-ion batteries has been highlighted.³⁰ In particular water-soluble binders have gained attention due to their enhanced interaction with active materials, stronger adhesion and mechanical buffer effect for volume change.³¹ Additionally, careful tailoring of electrode structure could be effective to boost electrochemical performance of active materials due to formation of a good percolating network within the electrodes. Divers parameters have been shown to influence the electrode structure including calendaring pressure applied, composition of composite electrode, nature of carbon additives and particle size of the active material.³² Considering the advantages of water-soluble binders and the importance of homogenous electrode structure, the introduction of aqueous binders into LCP electrodes could be an important step for the development of high voltage positive electrode materials.

Chapter 3. Lithium cobalt phosphate

This chapter will detail the synthesis and characterisation of LCP and preparation of LCP electrodes with aqueous binders. The effects of these binders on electrochemical properties are thoroughly investigated.

3.2. Experimental methods

The particular procedures and conditions relevant to the work presented in this chapter are presented below.

3.2.1. Synthesis of LCP

LCP was synthesised by a solvothermal method previously reported by Brutti and coworkers with slight modification.^{33,34} Two aqueous solutions: solution A with lithium hydroxide monohydrate ($\text{LiOH}\cdot\text{H}_2\text{O}$, Sigma-Aldrich, $\geq 98\%$) and solution B containing lithium dihydrogen phosphate (LiH_2PO_4 , Alfa Aesar, 97%), cobalt sulphate heptahydrate ($\text{CoSO}_4\cdot 7\text{H}_2\text{O}$, Sigma-Aldrich, $\geq 99\%$), and D-(+)-glucose (Sigma-Aldrich) were prepared separately. Solution A was added to ethylene glycol to give solution C. Subsequently, solution B was added dropwise into solution C under stirring. The molar ratio of $\text{LiOH}\cdot\text{H}_2\text{O}$: $\text{CoSO}_4\cdot 7\text{H}_2\text{O}$: LiH_2PO_4 : D-(+)-glucose was 1.75 : 1 : 1 : 0.03. The Co^{2+} concentration in the final ethylene glycol/water solution was 0.1 M. The obtained purple suspension was sealed in a 135 ml Teflon-lined autoclave and heated in an oven at 220 °C for 16 h. The product was filtered, washed with water and ethanol then dried at 80 °C.

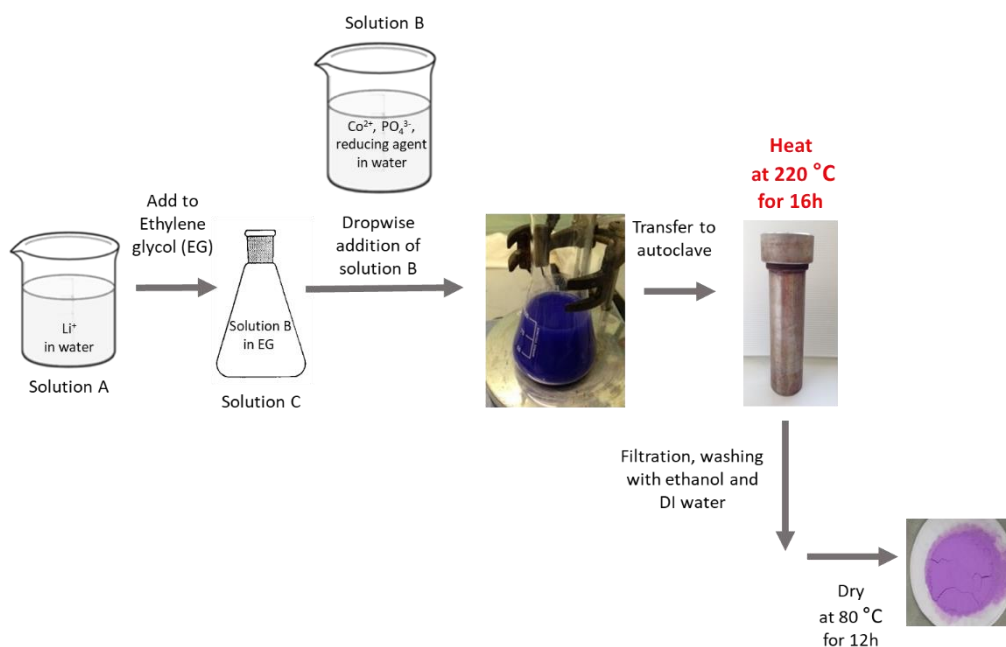


Figure 3.1. Schematic illustration of synthesis procedure.

3.2.2. Analyses and characterisation of as-synthesised LCP

PXRD patterns were collected on a STOE STADI/P diffractometer operating in transmission mode with Fe K α_1 radiation ($\lambda = 1.936 \text{ \AA}$). Crystallographic information was obtained by the Rietveld method using the GSAS package with the EXPGUI interface.³⁵

FT-IR spectra were obtained using a Shimadzu IRAffinity-1S spectrometer at a resolution of 4 cm^{-1} . 40 scans were added together to achieve the desired signal to noise ratio.

SEM images were recorded on a JEOL JSM-6700F.

ICP-OES analysis was performed using a iCAP 6000 Series.

3.2.3. Exposure of LCP to deionised water (DIW)

As-synthesised LCP was dispersed in DIW then stirred for 6 h then filtered and dried under vacuum at 130°C . The dried powder was analysed using PXRD, FT-IR and ICP-OES as described above.

3.2.4. Preparation of electrodes and characterisation of as-prepared electrodes

In order to evaluate the electrochemical performance of electrodes formulated with aqueous binders, slurries were prepared using the active material, super C65 carbon and three different aqueous binders in the mass ratio 75: 15: 10, except where indicated. The aqueous binders used in this study were sodium carboxymethyl cellulose (CMC, Sigma-Aldrich, degree of substitution (D.S.) of 1.2), sodium alginate (ALG, Sigma-Aldrich) and polyacrylic acid sodium salt (PAA, Sigma-Aldrich). The slurry was sonicated for 30 min then cast on aluminium foil using a doctor blade. After drying, 12 mm diameter electrode discs were punched then dried at 130°C under vacuum for 12 h. Additionally, LCP electrodes were prepared with 5wt% and 15wt% CMC. A conventional mixing method, stirring for 4 h, rather than sonication was applied for LCP electrodes with 10wt% CMC in DIW and also for 10wt% Kynar 2801, (a co-polymer based on polyvinylidene fluoride (PVDF)) in n-methyl-2-pyrrolidone. The nomenclature of all electrodes studied in this chapter is summarised in Table 3.1.

Table 3.1. Nomenclature of electrodes

Binders	Ratio (wt%)	Mixing method	Nomenclature
CMC	10	Sonication	LCP-CMC
ALG			LCP-ALG
PAA			LCP-PAA
CMC	5		LCP-CMC-5
CMC	15		LCP-CMC-15
CMC	10	Stirring	LCP-CMC-S
PVDF	10		LCP-PVDF

Morphology, including surface and cross-section of electrodes, and elemental mapping of the electrode surface were obtained using a FEI Scios microscope equipped with EDAX Octane Plus EDS detector.

FT-IR spectra for as-prepared CMC-LCP-15 was prepared by mixing approximately 5wt% of the material in dried potassium bromide powder followed by pressing into a 10 mm diameter pellet were recorded using a Nicolet Magna 860 spectrometer at a resolution of 4 cm⁻¹. 1024 scans were added together to achieve the desired signal to noise ratio.

A PXRD pattern of as-prepared CMC-LCP was collected on a STOE STADI/P diffractometer operating in transmission mode with Fe K α_1 radiation ($\lambda = 1.936 \text{ \AA}$). Crystallographic information was obtained by the Rietveld method using the GSAS package with the EXPGUI interface.³⁵

3.2.5. Preparation of cells and electrochemical tests

CR2325 coin cells were assembled in an Ar-filled glovebox and used for evaluation of electrochemical performance. The cells consisted of a disc electrode, lithium metal as a counter/reference electrode, a glass fibre separator (Whatman, GF/F) and LP30 electrolyte (1M LiPF₆ in ethylene carbonate : dimethyl carbonate = 1:1 w/w).

Galvanostatic charge/discharge cycling was carried out at 30 °C using a Bio-logic Macpile II system. A series of five cycles at progressively increasing C-rates was carried out using a Maccor series 2200 system at 30 °C.

EIS measurements were conducted on coin cells, cycled at 30 °C using a Bio-logic Macpile II

system. Data for the cells after 20 cycles were collected using a Solartron 1255 frequency response analyser coupled with Solartron 1287 electrochemical interface. A perturbation voltage of 10 mV and a frequency range of 0.1 Hz to 0.1 MHz were employed.

3.2.6. *Ex-situ* measurements of cycled electrodes

For all *ex-situ* measurements, cycled cells were transferred to an Ar-filled glovebox before opening and the active material was extracted. The electrodes were rinsed carefully with dry dimethyl carbonate to remove residual electrolyte and then left under vacuum to ensure all solvent had evaporated. Dried *ex-situ* electrodes were analysed using SEM, FT-IR and PXRD to compare with as-prepared electrodes.

3.3. Results and discussion

3.3.1. Characterisation of as-synthesised LCP

A profile fit to the PXRD pattern is shown in Fig. 3.2a. All diffraction peaks can be fully indexed on an orthorhombic olivine structure (space group *Pnma*) with no additional peaks, indicating that single-phase LCP was obtained. The refined cell parameters: $a = 10.2181(10)$ Å, $b = 5.9258(6)$ Å, $c = 4.7065(5)$ Å are in good agreement with previously reported values.^{33,34,36,37} Anti-site defects, involving the partial site exchange of Li and Co between 4a and 4c sites, affect the electrochemical performance by blocking Li ion diffusion via 1D channels parallel to the [010] direction in the olivine structure. Refinement of the disorder revealed the presence of 3.5(1)% anti-site defects. Refinement considering a preferred orientation of the (0 1 0) plane resulted in an improved fit with R_{wp} 5.08%, implying that LCP particles are grown with exposed (010) faces, in keeping with the observed platelet morphology. Additional characterisation was carried out using FT-IR to confirm the successful synthesis of the LCP material. In the FT-IR spectrum (Fig. 3.2b), vibration features are analogous to those in the literature with phosphate stretching modes (1146, 1100, 1036, 977 cm^{-1}) and bending modes (636, 575, 550, 500, 473 cm^{-1}).^{33,38} The low- and high-resolution SEM images of as-synthesized LCP are displayed in Fig. 3.2c-d. The LCP material consists of sub-micron hexagonal platelets, consistent with the reports that the ethylene glycol/water co-solvent system produces hexagonal platelets as well as reducing the particle size.^{37,39,40} In the high-resolution SEM image (Fig. 3.2d), the thickness of the LCP platelet-like particles is shown to be around 100-150 nm.

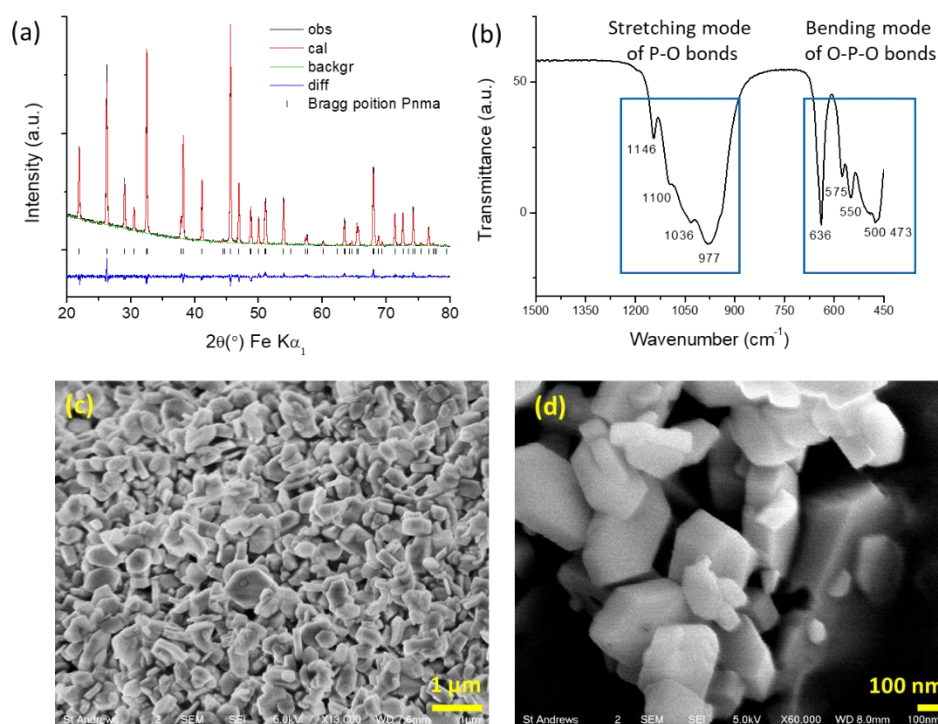


Figure 3.2. Profile fit for the Rietveld refinement of as-synthesised LCP. Observed data points are shown in black, with fitted profile in red and the difference is shown in blue. Tick marks indicate allowed reflections. (b) FT-IR spectrum of as-synthesized LCP. SEM images of as-synthesised LCP at (c) low and (d) high resolution.

3.3.2. Electrode formulation using aqueous binders

In order to check the feasibility of using water-soluble binders with LCP, the active material soaked in DIW for 6 h was examined using PXRD, FT-IR and ICP-OES. As shown in Fig. 3.3 and Table 3.2, no metal leaching or degradation of LCP material was observed, confirming the feasibility of employing aqueous binders to fabricate LCP electrodes.

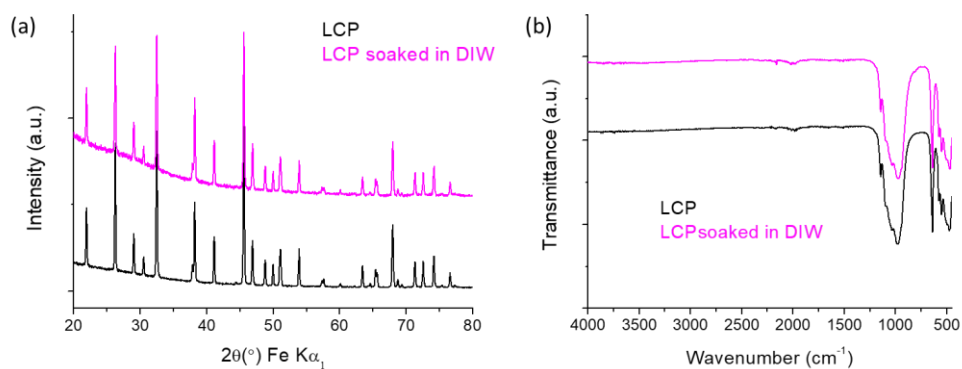


Figure 3.3. (a) PXRD and (b) FT-IR of as-synthesized LCP (black) and DIW-exposed LCP (magenta).

Table 3.2. Stoichiometric ratio derived from ICP-OES. (normalised to Co)

Element	As-synthesised LCP		DIW-exposed LCP	
	Ratio	Relative standard deviation	Ratio	Relative standard deviation
Li	1	± 0.006	1	± 0.006
Co	1	± 0.005	1	± 0.003

3.3.3. Electrochemical properties of LCP electrodes

Electrochemical performance of LCP electrodes formulated with aqueous binders was investigated and compared to that prepared with conventional PVDF-based binder. Major differences in the electrochemical behaviour of all electrodes are evident after 20 cycles at C/10 ($1C = 167 \text{ mA g}^{-1}$) (Fig. 3.4). The remarkable cyclability of LCP-CMC is clearly shown by the highest capacity retention of 94%, followed by 72%, 56% and 38% for LCP-ALG, LCP-PAA and LCP-PVDF, respectively. The initial capacity increase indicates that LCP-CMC requires some conditioning cycles to stabilize capacity.^{41,42}

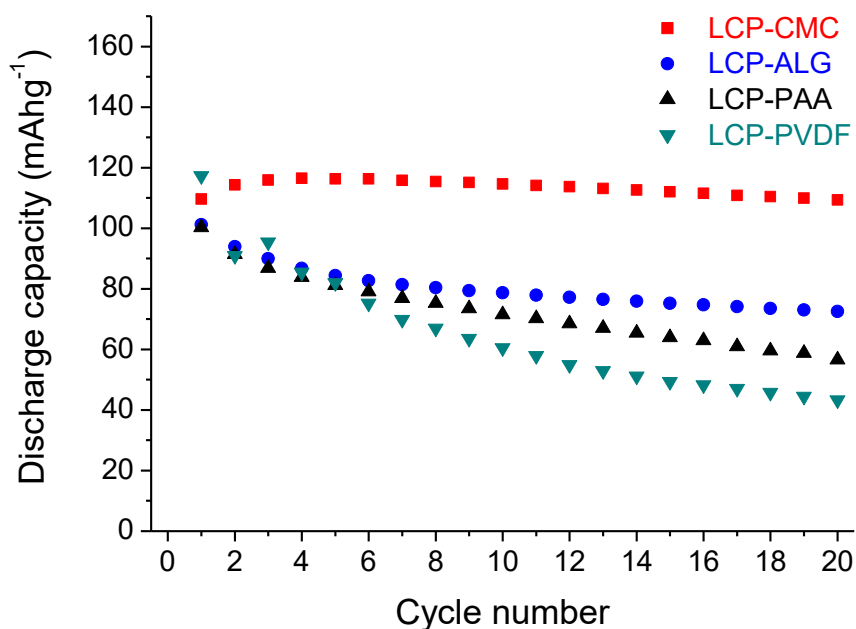


Figure 3.4. Galvanostatic cycling performance of LCP-CMC (red), LCP-ALG (blue), LCP-PAA (black), and LCP-PVDF (dark cyan), cycled at 30 °C between 3.5 and 5.0 V vs Li/Li⁺ at a rate of C/10 ($1C = 167 \text{ mA g}^{-1}$).

Fig. 3.5a-d show the charge/discharge curves of electrodes prepared with different water-soluble binders (CMC, ALG and PAA) and organic-soluble binder (PVDF) at cycle 1, cycle 5 and cycle 20. It is known that the delithiation of LCP occurs in two stages, with an intermediate phase of composition $\text{Li}_{2/3}\text{CoPO}_4$, coexisting with the fully lithiated phase (LiCoPO_4) at higher Li content and with the fully delithiated phase (CoPO_4) at low Li content upon charge.⁴³⁻⁴⁵ For LCP-CMC, both processes are reversible upon cycling at cycle 1, producing two clear plateaus in the voltage profiles (Fig. 3.5a), and two oxidation peaks at around 4.76 and 4.87 V and two reduction peaks at about 4.75 and 4.84 V in differential capacity versus voltage (dQ/dV) curves (Fig. 3.5e). The characteristic charge/discharge curves are maintained at cycle 5 and cycle 20. LCP-ALG (Fig. 3.5b) and LCP-PAA (Fig. 3.5c) exhibit two distinct plateaus at cycle 1 and cycle 5 with slightly larger polarisation than that observed in LCP-CMC. In contrast, two plateaus are only observed during the first charge process in LCP-PVDF (Fig. 3.5d), and only a single reduction peak at cycle 1 (Fig. 3.5e). With large polarisation, no obvious pair of plateaus is present at cycle 5 (Fig. 3.5d). Of note, on the first cycle all electrodes show significant irreversible capacity with Coulombic efficiencies of 31%, 24%, 2 % and 51% for LCP-CMC, LCP-ALG, LCP-PAA and LCP-PVDF, respectively, due to electrolyte decomposition and possible SEI layer formation at high voltage. The Coulombic efficiencies reach 92%, 86%, 85% and 93% after 20 cycles for LCP-CMC, LCP-ALG, LCP-PAA and LCP-PVDF, respectively, implying continuous electrolyte decomposition in this voltage window. The dQ/dV plots at cycle 20 (Fig. 3.5f) reveal the different binder dependent cycling stability. LCP- CMC displays the smallest differences in potential between oxidation (4.77 and 4.88 V) and reduction (4.75 and 4.85 V) peaks for the two processes, suggesting the fastest Li ion insertion/extraction kinetics. In contrast, LCP-ALG exhibits slightly larger gaps with smaller magnitude especially for the first process ($\text{LiCoPO}_4 \rightarrow \text{Li}_{2/3}\text{CoPO}_4 + 1/3 \text{Li}^+ + 1/3 \text{e}^-$) probably due to some degradation of the LCP material. The degradation of LCP is clearly observed in LCP-PAA and LCP-PVDF with the two peaks being barely distinguishable after 20 cycles.

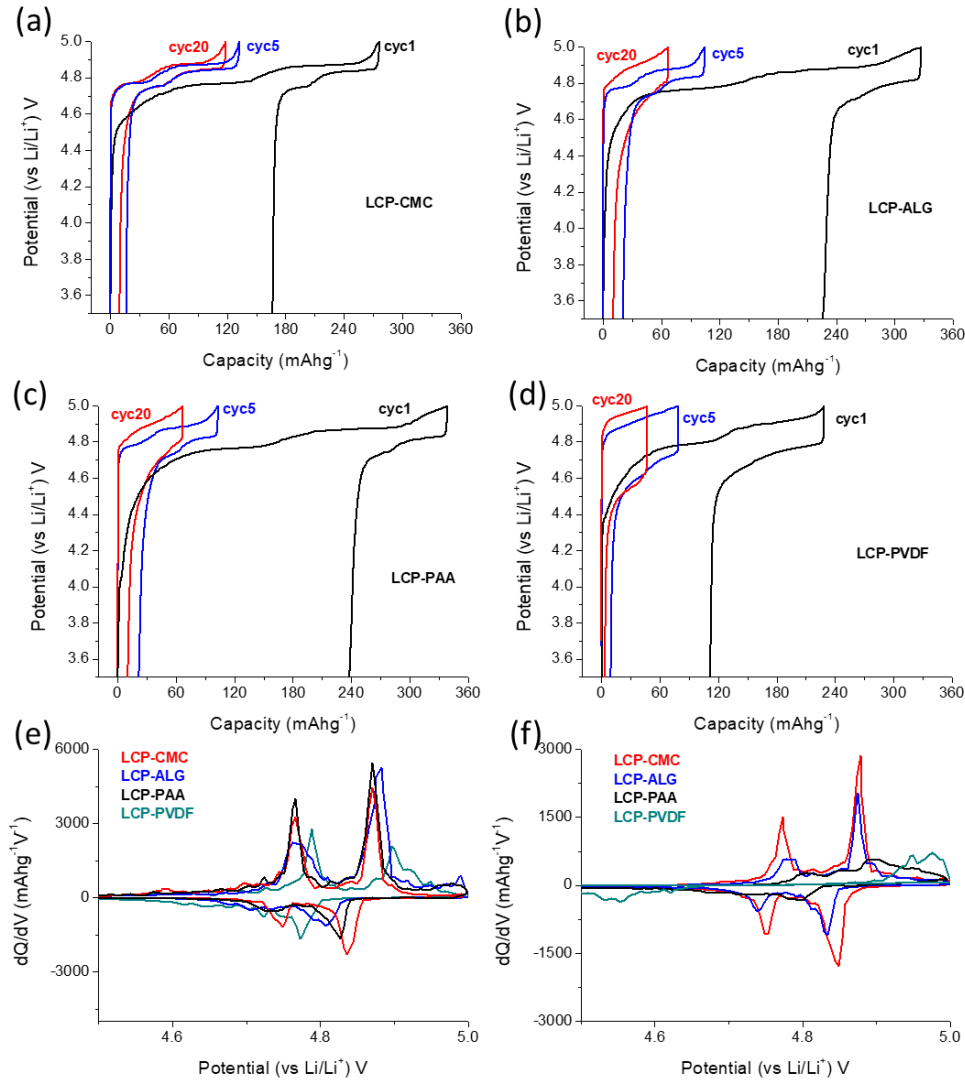


Figure 3.5. Charge/discharge curves at cycle 1 (black), cycle 5 (blue) and cycle 20 (red) for (a) LCP-CMC (b) LCP-ALG (c) LCP-PAA and (d) LCP-PVDF, and dQ/dV curves corresponding to (e) cycle 1 and (f) cycle 20 of LCP-CMC (red), LCP-ALG (blue), LCP-PAA (black) and LCP-PVDF (dark cyan), cycled at 30 °C between 3.5 and 5.0 V vs Li/Li^+ at a rate of $C/10$ ($1C = 167 \text{ mA g}^{-1}$).

The rate capability of electrodes made with different binders was tested by galvanostatic cycling at different C-rates from $C/10$ to $2C$. As shown in Fig. 3.6, LCP-CMC exhibits significantly better rate performance overall, especially at $2C$. LCP-ALG shows a capacity drop at the slowest rate ($C/10$) and stable capacity retention at the remaining C-rates. At the faster regimes, from $C/2$ to $1C$, LCP-ALG delivers moderate capacity, whereas LCP-PAA and LCP-PVDF demonstrate negligible capacity. It is noteworthy that LCP-CMC recovers its capacity at $C/10$, after cycling at higher rates, meaning that LCP materials are preserved without significant degradation.

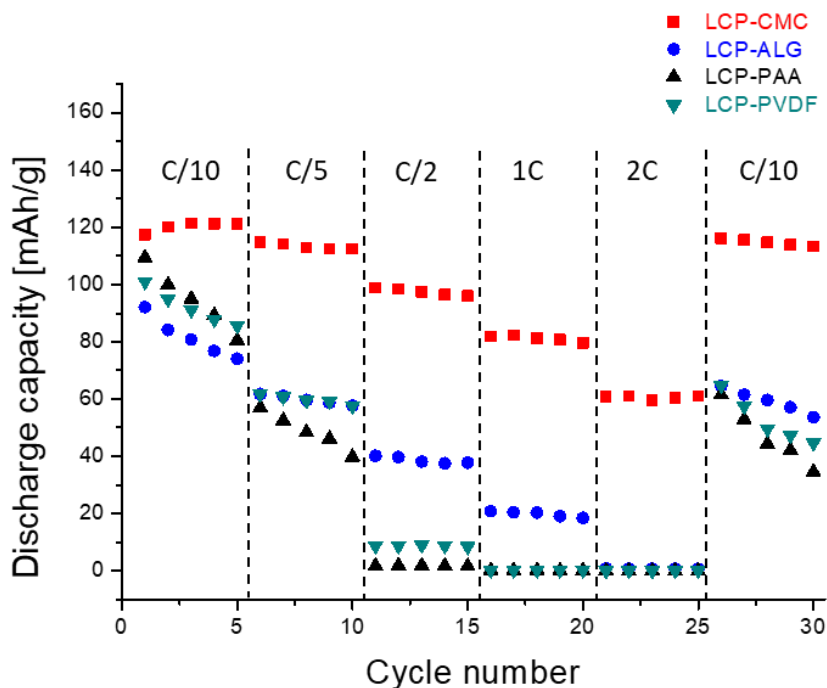


Figure 3.6. Discharge capacity vs C-rate of LCP-CMC (red), LCP-ALG (blue), LCP-PAA (black) and LCP-PVDF (dark cyan), cycled at 30 °C between 3.5 and 5.0 V vs Li/Li⁺.

EIS measurements also confirmed the better performance of LCP-CMC among the electrodes formulated with aqueous binders. Fig. 3.7 shows the Nyquist plots of LCP-CMC, LCP-ALG and LCP-PAA after 20 cycles. LCP-CMC and LCP-ALG display an arc followed by an angled line whereas LCP-PAA exhibits an extra arc. Fitting results using an equivalent circuit (Table 3.3) reveal that analogous processes occur in LCP-CMC, LCP-ALG and LCP-PAA with resistances of 56.4 Ω , 116 Ω and 493 Ω , respectively, due to an electrode process including LCP/electrolyte interface, SEI resistance and charge transfer within the electrodes as well as LCP particles. It is noted that R2 was deleted to fit LCP-CMC and LCP-ALG. Interestingly, the fitting results show the appearance of a new arc for the LCP-PAA which represents a different process from that observed in all other electrodes. Comparing the impedance results of electrodes after 20 cycles confirms that LCP-CMC shows the lowest resistance.

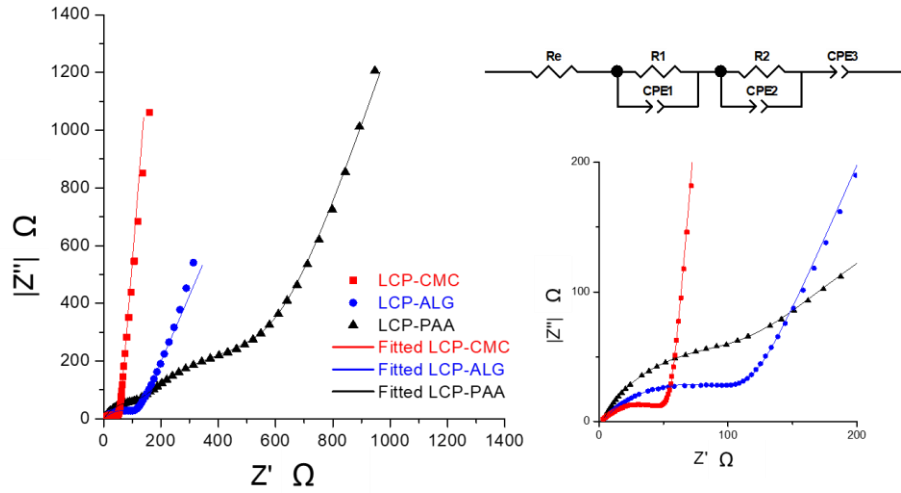


Figure 3.7. Nyquist plots of LCP-CMC (red), LCP-ALG (blue) and LCP-PAA (black) at frequencies from 0.1 Hz to 0.1 MHz, with a zoomed image for high frequency on the bottom right and an equivalent circuit on the top right.

Table 3.3. Results of EIS fitting of LCP-CMC (red), LCP-ALG (blue) and LCP-PAA (black) after 20 cycles using ZView2 applying an equivalent circuit.

	LCP-CMC	LCP-ALG	LCP-PAA
Re (Ω)	1.56 (\pm 0.046)	2.46 (\pm 0.067)	2.65 (\pm 0.023)
R1 (Ω)	56.4 (\pm 0.363)	116 (\pm 0.899)	493 (\pm 13.838)
R2 (Ω)	-	-	107 (\pm 2.507)

The long term cycling performance of LCP-CMC was investigated at a rate of C/10. As shown in Fig. 3.8, LCP-CMC displays good capacity retention of 68% after 100 cycles, which compares favourably with previously reported studies. It is also important to highlight that this LCP was prepared without any special treatments e.g., surface coating or particle size reduction and the electrode was cycled at C/10 where LCP particles were subjected to longer exposure to the electrolyte, whilst other studies reported improved capacity retention of LCP with 62% at C/5²⁷ and 68% at C/2³⁹ through carbon coating or morphology control, respectively.

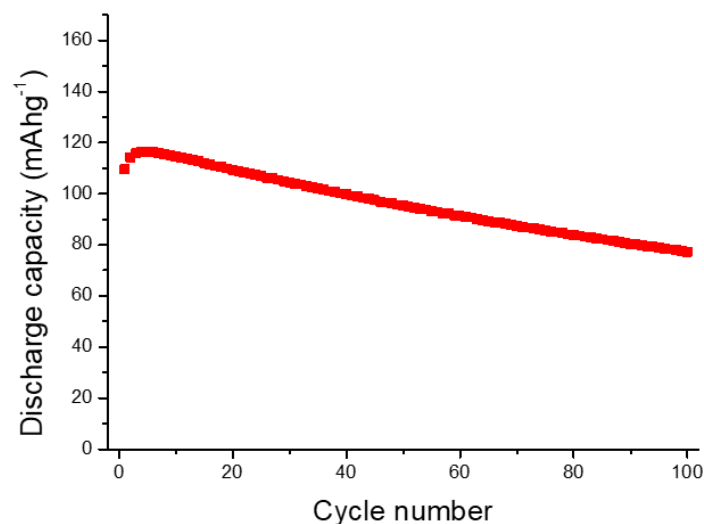


Figure 3.8. Long term cycling performance of LCP-CMC, cycled at 30 °C in between 3.5 and 5.0 V vs Li/Li⁺ at a rate of C/10 (1C = 167 mA g⁻¹).

3.3.4. Role of CMC in enhanced electrochemical performance

Given that LCP-CMC shows improved electrochemical performance compared to LCP-ALG and LCP-PAA, various aspects of the role of CMC were explored.

- **Morphology of electrode surface**

The morphology of as-prepared electrodes was first examined. As shown in Fig. 3.9, the surface of LCP-CMC (Fig. 3.9a-b) shows uniformly dispersed LCP without any cracks, whereas LCP-ALG (Fig. 3.9c-d) and especially LCP-PAA (Fig. 3.9e-f) have cracks on the surface and display aggregated LCP particles. In addition, cross-sectional SEM images also show that LCP-CMC is homogeneous regardless of electrode depth (Fig. 3.9g-h). All electrodes were further characterised by EDS (Fig. 3.10). The integral distribution of Co, P, O, C and Na elements on the LCP-CMC surface is presented in Fig. 3.10b. The Co, representing LCP particles (Fig. 3.10c), and Na, indicating CMC (Fig. 3.10d), are homogeneously distributed within the electrode. In contrast, LCP particles (Co) are aggregated in LCP-ALG (Fig. 3.10e-h) and LCP-PAA surfaces (Fig. 3.10i-l), which also show an inhomogeneous binder distribution. This suggests that the nature of binder influences the morphology of the electrodes, resulting in varying electrochemical performance; i.e., the percolating network between Super C65 carbon and LCP is hindered by the presence of cracks in the electrodes, leading to the increase in polarisation upon cycling.

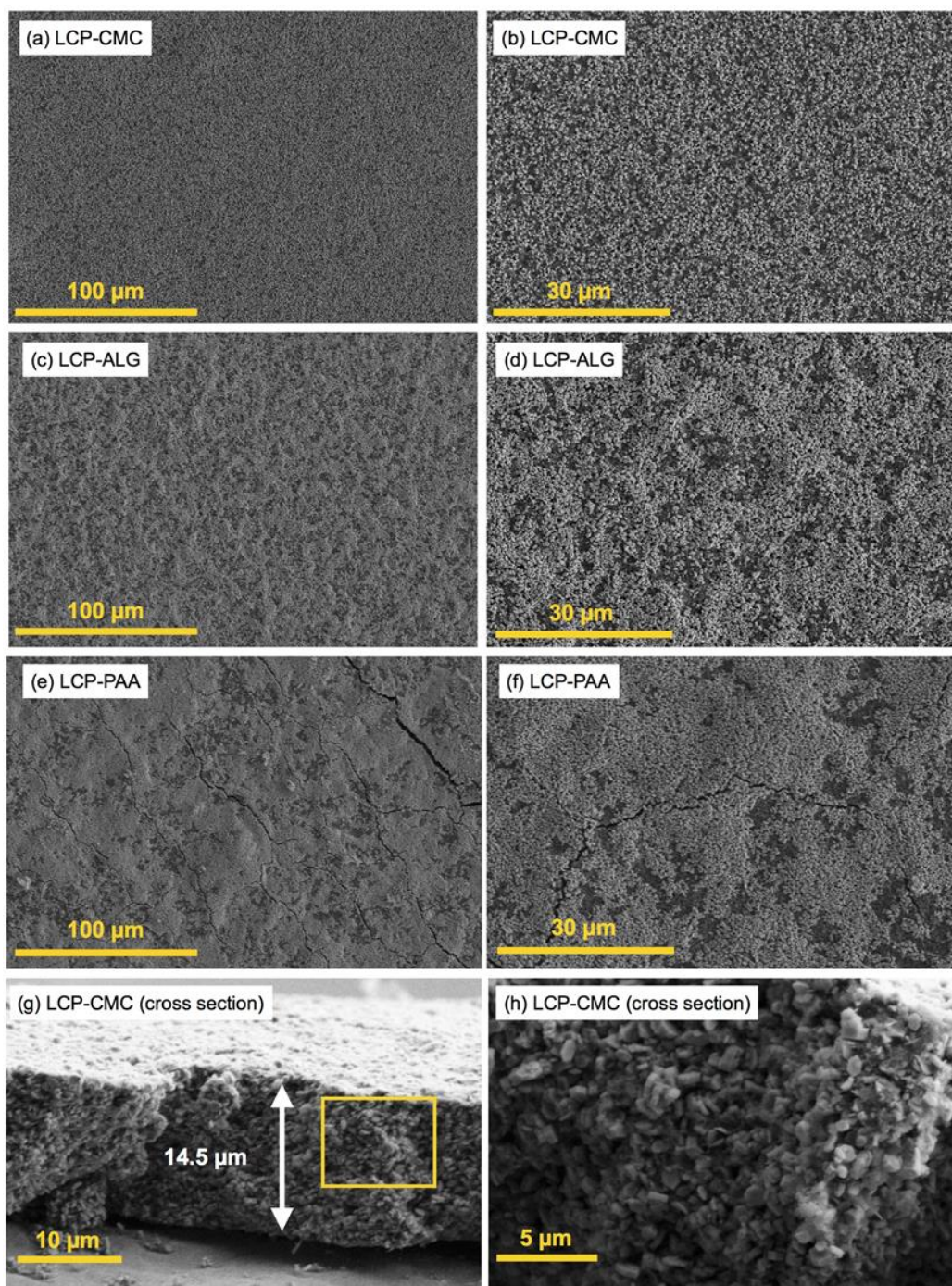


Figure 3.9. SEM images of (a,b) LCP-CMC, (c,d) LCP-ALG, (e,f) LCP-PAA surface, (g,h) cross-sectional SEM images of LCP-CMC. (h) corresponds to the yellow frame of (g). (taken by Dr. Xiangling Yue).

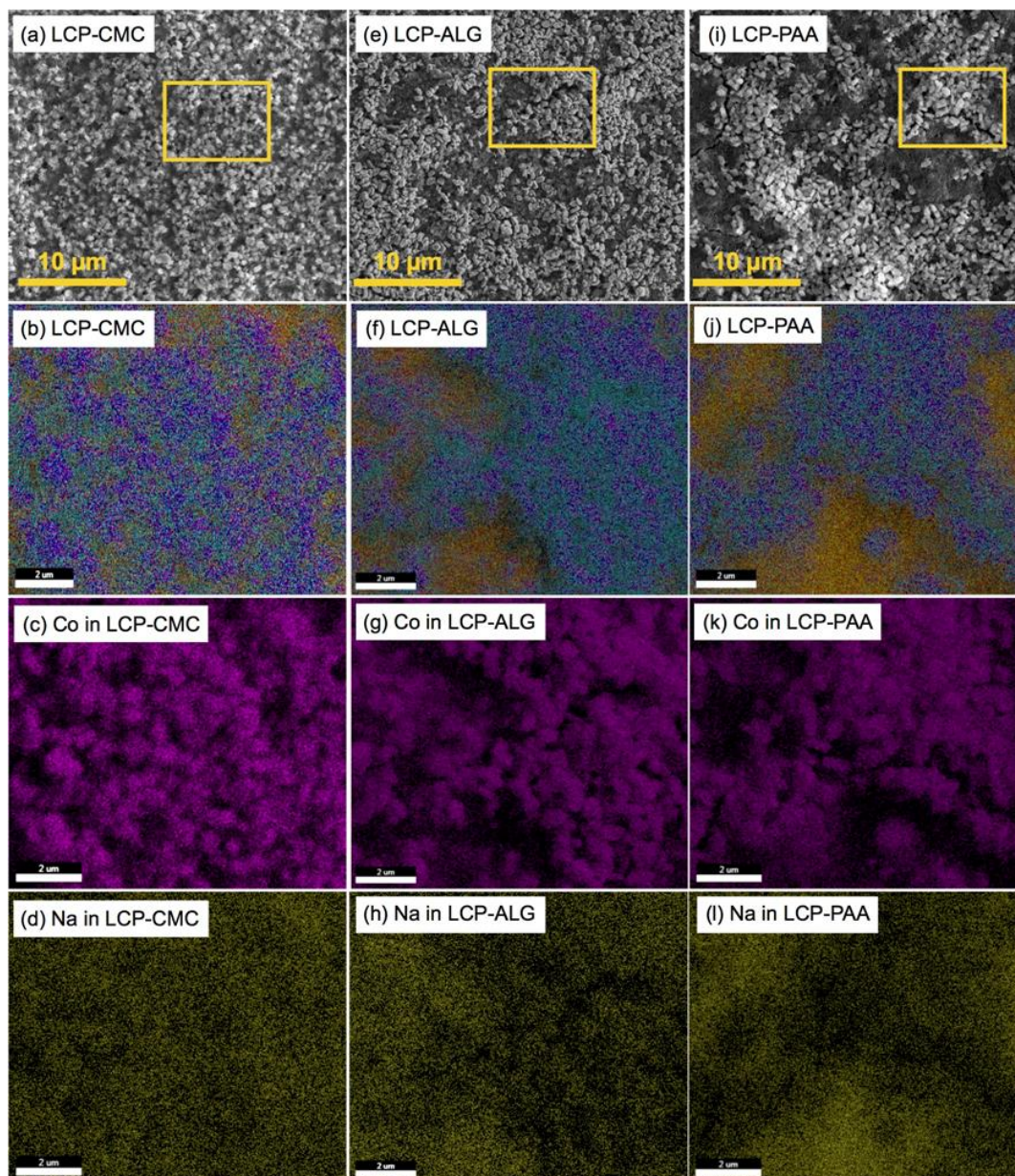


Figure 3.10. SEM image of (a) LCP-CMC, (e) LCP-ALG, (i) LCP-PAA surfaces, EDS mapping (yellow frame) for (b,f,j) the integral distribution of Co (magenta), P (light blue), O (navy), C (orange) and Na (yellow), (c,g,k) Co distribution, (d,h,l) Na distribution in LCP-CMC, LCP-ALG and LCP-PAA surfaces, respectively (taken by Dr. Xiangling Yue).

- **Molecular structure of binders**

The molecular structure of the binders can shed light on the different electrode morphology, especially the origin of cracks. As shown in Fig. 3.11, CMC and ALG demonstrate a typical polysaccharide structure: glucose-like compounds containing 1.2 (CMC) to 1 (ALG) stoichiometric carboxylate groups per constituent unit, whereas PAA is a sodium salt of a homopolymer of acrylic acid with at least three times as many carboxylate groups as CMC or

ALG. Thus, when dissolved in DIW, PAA will have a greater negative charge density on the surface, which could prevent a homogeneous distribution of binder with LCP particles that have a negative charge on the surface due to the PO_4^{3-} in neutral pH.⁴⁶ From a chemical point of view, polysaccharide-type binders such as CMC and ALG are less flexible than acrylic binders (PAA) due to the linear 1,4' β -glycosidic linkages between glucose-like monomers,^{47,48} which enables maintenance of the 3D network of Super C65 and LCP particles upon cycling. In the case of LCP-ALG, the presence of additional non-linear 1,4' α -glycosidic linkages may cause minor cracks in the electrode, resulting in moderate electrochemical performance compared to LCP-CMC.

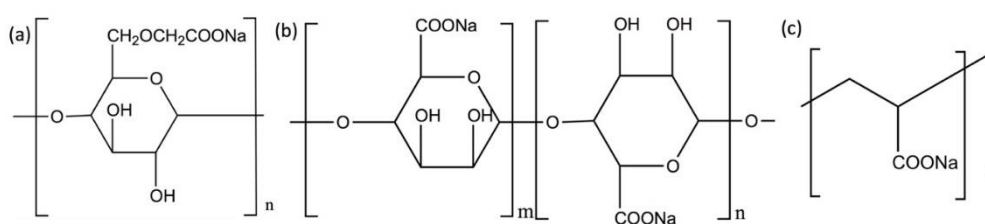


Figure 3.11. Molecular structure of binders (a) CMC, (b) ALG and (c) PAA.

- **Carboxylate groups in binders as a HF scavenger**

The carboxylate groups present in the aqueous binders studied in this work could improve the cycling stability. One of the reasons for the capacity fade of LCP is nucleophilic attack of F^- anions produced in LiPF_6 based electrolyte, resulting in the breakage of P-O bonds of the phosphate anions.^{7,8} Indeed, HF is regenerated catalytically as a side product of the decomposition of LCP, causing a considerable capacity drop in the first few cycles. This detrimental phenomenon has been suppressed by HF scavenging. For example, improved capacity retention of LCP was obtained using quartz separators, as quartz can act as a sacrificial HF scavenger. In a study of $\text{LiNi}_{0.5}\text{Mn}_{1.5}\text{O}_4$, a carboxylate containing binder (PAA-Li) was used not only as the binder but also as a passivating agent to suppress unstable interfaces between the electrode and electrolyte as well as undesirable side reactions by exchanging Li ions in PAA-Li with protons from HF.⁴⁹ Therefore, it is reasonable to assume that the superior performance of the aqueous binder based LCP electrodes over the PVDF-based electrodes could originate from the presence of carboxylate groups that scavenge HF in the electrolyte. As seen in Fig. 3.11, the carboxylate groups in CMC are more accessible compared to those of ALG since CMC has an additional carbon atom between the cyclic backbone and the carboxylate groups. In addition, CMC contains 20% more carboxylate

groups than ALG due to the degree of substitution of 1.2, i.e., 20% more of the hydrogen in the hydroxyl group of a glucose unit is replaced by carboxymethyl. The unique structure of CMC combined with the higher carboxylate content could favour HF-scavenging, resulting in improved performance.

3.3.5. Proof of concept of the role of CMC

Given the beneficial effects of CMC, including good percolating network within electrodes, high mechanical stiffness and HF-scavenging, additional experiments were designed to investigate 1) the effect of the quantity of CMC used and 2) the effect of slurry mixing method on electrochemical performance, considering that uniformly dispersed CMC could effectively cover the LCP by the formation of a protective interface between electrode and electrolyte, thus higher amounts of CMC could display better cycling performance. The cycling performance of LCP electrodes, fabricated with different amounts of CMC and mixed in different ways is shown in Fig. 3.12a. Excellent capacity retention after 20 cycles is delivered by LCP-CMC-15 and LCP-CMC with 93% and 94%, respectively, whereas LCP-CMC-5 exhibits a capacity retention of 85%. LCP-CMC-S shows the lowest capacity retention of 72% without initial capacity gain *via* electrochemical grinding. The charge/discharge curves demonstrate that increased polarisation from cycle 5 to cycle 20 for LCP-CMC-15 (Fig. 3.12b) is less pronounced than LCP-CMC-5 (Fig. 3.12c), suggesting that a higher amount of CMC provides a better protective interface between the LCP particles and the electrolyte. It is worth noting that the initial capacity tends to decrease as the amount of CMC increases, probably due to lower Li ion diffusion. The capacity fade as well as pronounced polarisation at cycle 5 and cycle 20 are observed for LCP-CMC-S (Fig. 3.12d). This could originate from a non-homogenous dispersion of the slurry components due to stirring method. As shown in the cross-sectional SEM images (Fig. 3.13), a homogenous network of active materials and Super C65 is observed for LCP-CMC, whereas LCP-CMC-S has aggregated carbon with isolated LCP particles. These results highlight that homogenous slurry dispersion is a crucial factor to fabricate a uniform electrode, which could also promote better coverage of CMC, permitting enhanced electrochemical performance.

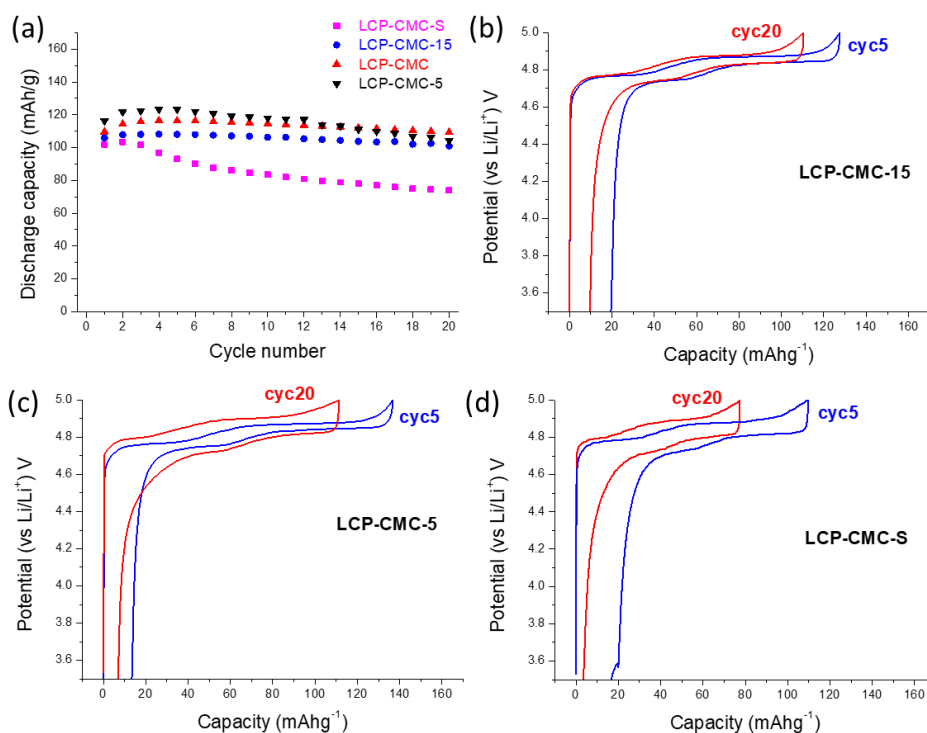


Figure 3.12. (a) Galvanostatic cycling performance of LCP-CMC-S (magenta), LCP-CMC-15 (blue), LCP-CMC (red), and LCP-CMC-5 (black) and charge/discharge curves at cycle 5 (blue) and cycle 20 (red) for (b) LCP-CMC-15 (c) LCP-CMC-5 and (d) LCP-CMC-S, cycled at 30 °C between 3.5 and 5.0 V vs Li/Li⁺ at a rate of C/10 (1C = 167 mA g⁻¹).

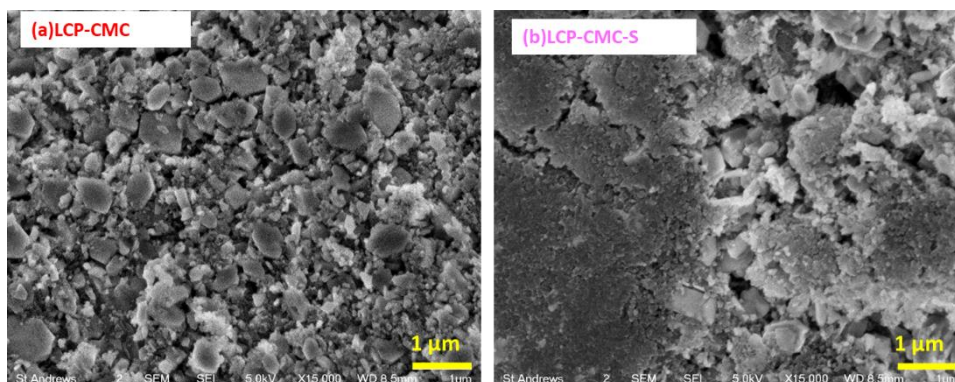


Figure 3.13. Cross-sectional SEM image of (a) LCP-CMC and (b) LCP-CMC-S.

3.3.6. Ex-situ studies of CMC based electrodes

- SEM analysis

The surface morphology of LCP-CMC after 20 cycles was compared to those of LCP-ALG and LCP-PAA. As displayed in Fig. 3.14, there are no obvious cracks for LCP-CMC after 20 cycles, confirming its robustness.

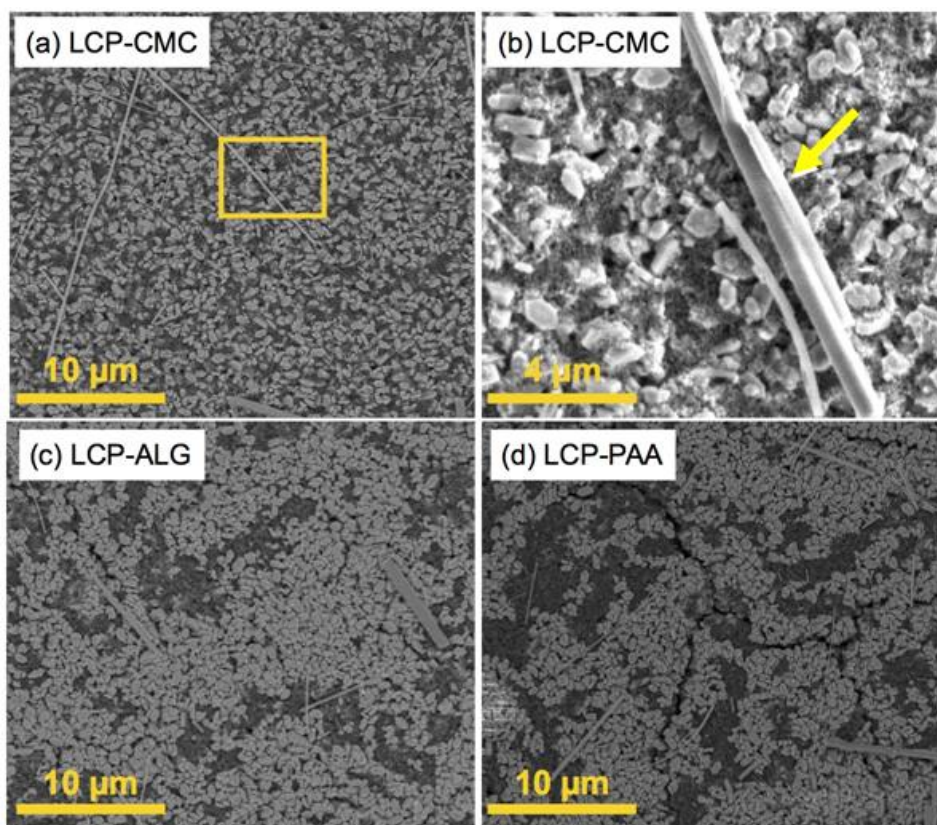
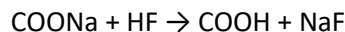


Figure 3.14. SEM images of (a) LCP-CMC (b) yellow frame of LCP-CMC with an arrow indicating a separator fibre confirmed by EDS analysis, (c) LCP-ALG and (d) LCP-PAA surfaces after 20 cycles, respectively (taken by Dr. Xiangling Yue).

- **FT-IR measurements**

In order to prove that CMC can effectively provide HF-scavenging, *ex-situ* FT-IR measurements were carried out for LCP-CMC after 1 and 20 cycles. Fig. 3.15 displays FT-IR spectra for CMC binder, as-prepared LCP-CMC-15 and *ex-situ* LCP-CMC-15 electrodes after 1 and 20 cycles. The FT-IR spectrum of LCP-CMC-15 before cycling (Fig. 3.15b) shows spectral features of CMC and the LCP active material with a strong peak at 1612 cm^{-1} , characteristic of COONa in CMC. After the first cycle (Fig. 3.15c), no significant change was observed except for the appearance of a peak at 807 cm^{-1} , corresponding to P-F stretching, which could be residual LiPF_6 salt or products of electrolyte decomposition.⁵⁰ After 20 cycles (Fig. 3.15d), additional peaks are observed at 1743 cm^{-1} , attributed to the carboxylic acid group (COOH) and at 1803 cm^{-1} , an anhydride -OCOOC-, resulting from the condensation reaction of two carboxylate groups and the loss of H_2O . The appearance of these two peaks supports the scavenging role of CMC through the following reaction:



Moreover, the peak at 1612 cm^{-1} (COONa), which was observed for both the as-prepared electrode and that after the first cycle, shifts to a higher frequency of 1631 cm^{-1} . This peak can be assigned to COOLi^{51} and provides direct evidence of Li ion diffusion by a hopping mechanism via CMC, as previously observed in ALG based Si anodes.⁵²

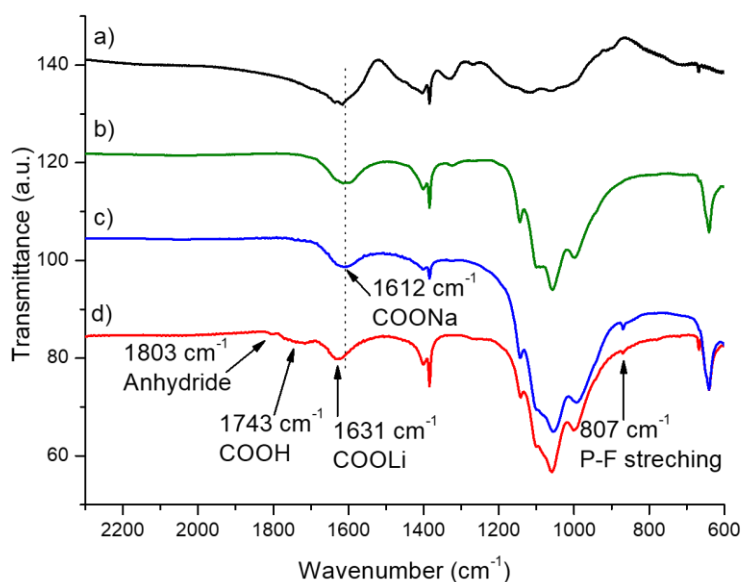


Figure 3.15. FT-IR of (a) CMC binder (black), (b) as-prepared LCP-CMC-15 (green) (c) LCP-CMC-15 after the first cycle (blue) and (d) LCP-CMC-15 after 20 cycles (red) (measured by Dr. Stephen Francis).

• PXRD analysis

As the increase in anti-site defects upon cycling is one of the reasons of significant capacity fade in LCP, an ex-situ PXRD pattern of LCP-CMC after 20 cycles was collected to examine the anti-site defects. The Rietveld refinement results (Fig. 3.16) reveal that there is no significant increase in the anti-site defects after 20 cycles with 3.0(1)% and 3.5(2)% for as-prepared LCP-CMC and that after 20 cycles, respectively (3.5(1)% for as-synthesised LCP powder). It has been reported that the anti-site defects formed during electrochemical cycling are concentrated in the surface region rather than bulk.¹¹ In this work, the use of CMC could minimise harmful reactions at the surface thanks to the HF-scavenging role, impeding the increase of anti-site defects upon cycling.

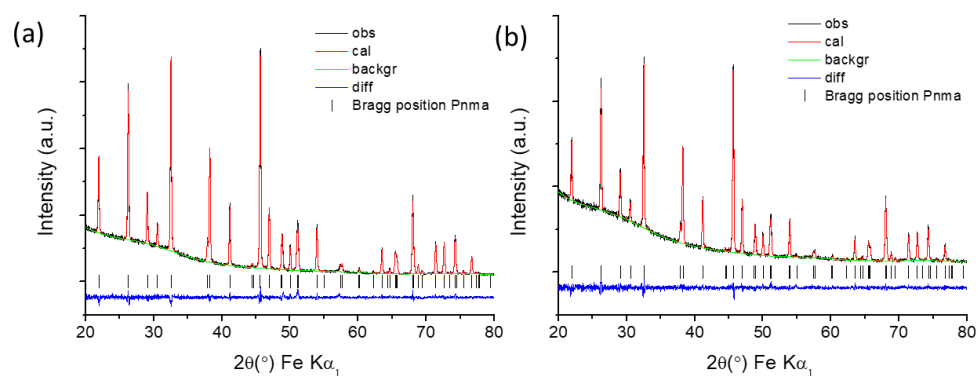


Figure 3.16. Profile fit for the Rietveld refinement of (a) as-prepared LCP-CMC and (b) LCP-CMC after 20 cycles. Observed data points are shown in black, with fitted profile in red and the difference is shown in blue. Tick marks indicate allowed reflections.

3.4. Summary

Aqueous binders were applied to fabricate electrodes with sub-micron sized LCP, synthesised using a solvothermal method. All water-soluble binders used in this study (CMC, ALG, PAA) exhibit improved electrochemical performance compared to the conventional organic-soluble binder (PVDF). In particular, the LCP electrode formulated with CMC (LCP-CMC) demonstrates excellent cycling stability as well as rate capability.

The origin of enhanced electrochemical performance delivered by LCP-CMC was thoroughly investigated e.g., electrode morphology and physico-chemical characteristics based on the molecular structure of CMC. The stiffness and the presence of carboxylate groups of CMC are considered as crucial factors to improve electrochemical properties. The designed experiments, varying CMC amounts and mixing methods in electrode fabrication, and *ex-situ* measurements reveal that CMC can not only provide a uniform electrode surface but also suppress degradation of LCP by scavenging HF in the electrolyte solution.

In conclusion, the carboxylate groups with high accessibility in CMC show excellent ability as both binder and HF scavenger, compared to other binders, leading to enhanced electrochemical performance.

3.5. References

- 1 A. K. Padhi, K. S. Nanjundaswamy and J. B. Goodenough, *J. Electrochem. Soc.*, 1997, **144**, 1188–1194.
- 2 K. Amine, H. Yasuda and M. Yamachi, *Electrochem. Solid-State Lett.*, 2000, **3**, 178–179.
- 3 N. N. Bramnik, K. Nikolowski, C. Baehtz, K. G. Bramnik and H. Ehrenberg, *Chem. Mater.*, 2007, **19**, 908–915.
- 4 R. Sharabi, E. Markevich, K. Fridman, G. Gershinsky, G. Gershinsky, G. Salitra, G. Semrau, D. Aurbach, N. Schall, M. A. Schmidt and C. Bruenig, *Electrochem. Commun.*, 2013, **28**, 20–23.
- 5 L. Y. Xing, M. Hu, Q. Tang, J. P. Wei, X. Qin and Z. Zhou, *Electrochim. Acta*, 2012, **59**, 172–178.
- 6 J. Manzi and S. Brutti, *Electrochim. Acta*, 2016, **222**, 1839–1846.
- 7 R. Sharabi, E. Markevich, V. Borgel, G. Salitra, G. Gershinsky, D. Aurbach, G. Semrau, M. A. Schmidt, N. Schall and C. Stinner, *J. Power Sources*, 2012, **203**, 109–114.
- 8 E. Markevich, R. Sharabi, H. Gottlieb, V. Borgel, K. Fridman, G. Salitra, D. Aurbach, G. Semrau, M. A. Schmidt, N. Schall and C. Bruenig, *Electrochem. Commun.*, 2012, **15**, 22–25.
- 9 Q. D. Truong, M. K. Devaraju, Y. Sasaki, H. Hyodo, T. Tomai and I. Honma, *Chem. Mater.*, 2014, **26**, 2770–2773.
- 10 A. Boulineau and T. Gutel, *Chem. Mater.*, 2015, **27**, 802–807.
- 11 Y. H. Ikuhara, X. Gao, C. A. J. Fisher, A. Kuwabara, H. Moriwake, K. Kohama, H. Iba and Y. Ikuhara, *J. Mater. Chem. A*, 2017, **5**, 9329–9338.
- 12 D. Di Lecce, J. Manzi, F. M. Vitucci, A. De Bonis, S. Panero and S. Brutti, *Electrochim. Acta*, 2015, **185**, 17–27.
- 13 N. V. Kosova, O. A. Podgornova, E. T. Devyatkina, V. R. Podugolnikov and S. A. Petrov, *J. Mater. Chem. A*, 2014, **2**, 20697–20705.
- 14 L. Fang, H. Zhang, Y. Zhang, L. Liu and Y. Wang, *J. Power Sources*, 2016, **312**, 101–108.
- 15 H. Li, Y. Wang, X. Yang, L. Liu, L. Chen and J. Wei, *Solid State Ionics*, 2014, **255**, 84–88.
- 16 J. L. Allen, T. R. Jow and J. Wolfenstine, *J. Power Sources*, 2011, **196**, 8656–8661.
- 17 F. Wang, J. Yang, Y. Nuli and J. Wang, *J. Power Sources*, 2010, **195**, 6884–6887.
- 18 A. Örneke, *J. Power Sources*, 2017, **356**, 1–11.
- 19 Y. Maeyoshi, S. Miyamoto, Y. Noda, H. Munakata and K. Kanamura, *J. Power Sources*, 2017, **337**, 92–99.

- 20 A. Örnek, M. Can and A. Yeşildağ, *Mater. Charact.*, 2016, **116**, 76–83.
- 21 B. Wu, H. Xu, D. Mu, L. Shi, B. Jiang, L. Gai, L. Wang, Q. Liu, L. Ben and F. Wu, *J. Power Sources*, 2016, **304**, 181–188.
- 22 N. Laszczynski, A. Birrozzi, K. Maranski, M. Copley, M. E. Schuster and S. Passerini, *J. Mater. Chem. A*, 2016, **4**, 17121–17128.
- 23 J. Ni, L. Gao and L. Lu, *J. Power Sources*, 2013, **221**, 35–41.
- 24 X. Rui, X. Zhao, Z. Lu, H. Tan, D. Sim, H. H. Hng, R. Yazami, T. M. Lim and Q. Yan, *ACS Nano*, 2013, **7**, 5637–5646.
- 25 M. K. Devaraju, D. Rangappa and I. Honma, *Electrochim. Acta*, 2012, **85**, 548–553.
- 26 J. Liu, T. E. Conry, X. Song, L. Yang, M. M. Doeff and T. J. Richardson, *J. Mater. Chem.*, 2011, **21**, 9984–9987.
- 27 R. Sharabi, E. Markevich, V. Borgel, G. Salitra, D. Aurbach, G. Semrau, M. A. Schmidt, N. Schall and C. Stinner, *Electrochem. Commun.*, 2011, **13**, 800–802.
- 28 Y. Maeyoshi, S. Miyamoto, H. Munakata and K. Kanamura, *J. Power Sources*, 2017, **350**, 103–108.
- 29 T. Fukutsuka, T. Nakagawa, K. Miyazaki and T. Abe, *J. Power Sources*, 2016, **306**, 753–757.
- 30 S.-L. Chou, Y. Pan, J.-Z. Wang, H.-K. Liu and S.-X. Dou, *Phys. Chem. Chem. Phys.*, 2014, **16**, 20347–20359.
- 31 J.-T. Li, Z.-Y. Wu, Y.-Q. Lu, Y. Zhou, Q.-S. Huang, L. Huang and S.-G. Sun, *Adv. Energy Mater.*, 2017, **451**, 1701185–17011215.
- 32 A. Ponrouch and M. R. Palacin, *J. Power Sources*, 2012, **212**, 233–246.
- 33 S. Brutti, J. Manzi, A. De Bonis, D. Di Lecce, F. Vitucci, A. Paolone, F. Trequattrini and S. Panero, *Mater. Lett.*, 2015, **145**, 324–327.
- 34 J. Manzi, M. Curcio and S. Brutti, *Nanomaterials*, 2015, **5**, 2212–2230.
- 35 B. H. Toby, *J. Appl. Crystallogr.*, 2001, **34**, 210–213.
- 36 J. Manzi, F. M. Vitucci, A. Paolone, F. Trequattrini, S. Panero, D. Di Lecce and S. Brutti, *Electrochim. Acta*, 2015, **179**, 604–610.
- 37 J. Ludwig, C. Marino, D. Haering, C. Stinner, H. A. Gasteiger and T. Nilges, *J. Power Sources*, 2017, **342**, 214–223.
- 38 A. A. Salah, P. Jozwiak, K. Zaghib, J. Garbarczyk, F. Gendron, A. Mauger and C. M. Julien, *Spectrochim. Acta, Part A*, 2006, **65**, 1007–1013.
- 39 J. Ludwig, J. Ludwig, C. Marino, C. Marino, D. Haering, C. Stinner, D. Haering, D.

- Nordlund, C. Stinner, D. Nordlund, M. M. Doeff, H. A. Gasteiger, M. M. Doeff, H. A. Gasteiger, T. Nilges and T. Nilges, *RSC Adv.*, 2016, **6**, 82984–82994.
- 40 X. Qin, X. Wang, H. Xiang, J. Xie, J. Li and Y. Zhou, *J. Phys. Chem. C*, 2010, **114**, 16806–16812.
- 41 F. De Giorgio, N. Laszczynski, J. von Zamory, M. Mastragostino, C. Arbizzani and S. Passerini, *ChemSusChem*, 2017, **10**, 379–386.
- 42 W.-Y. Chou, Y.-C. Jin, J.-G. Duh, C.-Z. Lu and S.-C. Liao, *Appl. Surf. Sci.*, 2015, **355**, 1272–1278.
- 43 M. G. Palmer, J. T. Frith, A. L. Hector, A. W. Lodge, J. R. Owen, C. Nicklin and J. Rawle, *Chem. Commun.*, 2016, **52**, 14169–14172.
- 44 F. C. Strobridge, R. J. Clément, M. Leskes, D. S. Middlemiss, O. J. Borkiewicz, K. M. Wiaderek, K. W. Chapman, P. J. Chupas and C. P. Grey, *Chem. Mater.*, 2014, **26**, 6193–6205.
- 45 M. Kaus, I. Issac, R. Heinzmann, S. Doyle, S. Mangold, H. Hahn, V. S. K. Chakravadhanula, C. Kübel, H. Ehrenberg and S. Indris, *J. Phys. Chem. C*, 2014, **118**, 17279–17290.
- 46 J. Li, B. L. Armstrong, J. Kiggans, C. Daniel and D. L. Wood III, *Langmuir*, 2012, **28**, 3783–3790.
- 47 F. Jeschull, F. Lindgren, M. J. Lacey, F. B. refors, K. E. m and D. Brandell, *J. Power Sources*, 2016, **325**, 513–524.
- 48 C. Hwang, S. Joo, N.-R. Kang, U. Lee, T.-H. Kim, Y. Jeon, J. Kim, Y.-J. Kim, J.-Y. Kim, S.-K. Kwak and H.-K. Song, *Sci. Rep.*, 2015, **5**, 14433–14443.
- 49 N. P. W. Pieczonka, V. Borgel, B. Ziv, N. Leifer, V. Dargel, D. Aurbach, J.-H. Kim, Z. Liu, X. Huang, S. A. Krachkovskiy, G. R. Goward, I. Halalay, B. R. Powell and A. Manthiram, *Adv. Energy Mater.*, 2015, **5**, 1501008–1501018.
- 50 C. Schultz, S. Vedder, B. Streipert, M. Winter and S. Nowak, *RSC Adv.*, 2017, **7**, 27853–27862.
- 51 F. M. Courtel, S. Niketic, D. Duguay, Y. Abu-Lebdeh and I. J. Davidson, *J. Power Sources*, 2011, **196**, 2128–2134.
- 52 I. Kovalenko, B. Zdyrko, A. Magasinski, B. Hertzberg, Z. Milicev, R. Burtovyy, I. Luzinov and G. Yushin, *Science*, 2011, **334**, 75–79.

4. Magnesium doped lithium cobalt phosphate

This work was published in the ChemElectroChem in 2019 with the title of “Enhanced cycling performance of magnesium-doped lithium cobalt phosphate” (doi: 10.1002/celc.201901372).

4.1. Introduction

Lithium cobalt phosphate (LiCoPO_4) has been a strong candidate as a high voltage positive electrode material in LIBs since first identified by Amine *et al.*¹ However, unsatisfactory electrochemical performance associated with low electronic²⁻⁴ and ionic⁵ conductivities as well as significant capacity fade^{6,7} have been major obstacles to its wide application. As electrochemical performance of isostructural lithium iron phosphate (LiFePO_4) has been claimed to be improved via aliovalent or isovalent doping of either lithium sites or iron sites albeit the role of dopants has sometimes been controversial.⁸ Partial substitution of transition metals for cobalt has been extensively investigated for dopants such as vanadium, chromium, iron and yttrium.^{3,9-20} However, very few studies have been reported on the electrochemically inactive dopant magnesium²¹⁻²⁴ although its beneficial effects including structural stability during electrochemical cycling and modification of redox processes have been exploited in the phospho-olivine family.²⁵⁻²⁸ For example, magnesium doping was found to reduce the lattice mismatch between lithiated and delithiated phase in lithium manganese phosphate (LiMnPO_4) and to increase working voltage for LiFePO_4 and LiMnPO_4 .

This chapter will present the synthesis and characterisation of magnesium doped lithium cobalt phosphates, $\text{LiMg}_x\text{Co}_{1-x}\text{PO}_4$ ($x = 0, 0.05, 0.10, 0.15$ and 0.20). The effects of magnesium doping on various properties are investigated including morphology, structure, electrochemical properties, surface and phase evolution during electrochemical cycling.

4.2. Experimental methods

The particular procedures and conditions relevant to the work presented in this chapter are presented below.

4.2.1. Synthesis of $\text{LiMg}_x\text{Co}_{1-x}\text{PO}_4$ ($x = 0, 0.05, 0.10, 0.15$ and 0.20)

Samples were synthesised by a solvothermal method previously reported by Brutti and co-workers with slight modification.^{7,29} Two aqueous solutions: solution A with lithium hydroxide monohydrate ($\text{LiOH}\cdot\text{H}_2\text{O}$, Sigma-Aldrich, $\geq 98\%$) and solution B containing lithium dihydrogen phosphate (LiH_2PO_4 , Alfa Aesar, 97%), cobalt sulphate heptahydrate ($\text{CoSO}_4\cdot 7\text{H}_2\text{O}$, Sigma-Aldrich, $\geq 99\%$), and D-(+)-glucose (Sigma-Aldrich) were prepared separately. Solution A was added to ethylene glycol to give solution C. Subsequently solution B was added dropwise into solution C under stirring. The molar ratio of $\text{LiOH}\cdot\text{H}_2\text{O} : \text{CoSO}_4\cdot 7\text{H}_2\text{O} : \text{LiH}_2\text{PO}_4 : \text{D-(+)-glucose}$ was 1.75 : 1 : 1 : 0.03. The Co^{2+} concentration in the final ethylene glycol/water solution was 0.1 M. The obtained purple suspension was sealed in a 45 ml Teflon-lined autoclave and heated in an oven at 220 °C for 16 h. The product was filtered, washed with DIW and ethanol then dried at 80 °C. A series of magnesium substituted LiCoPO_4 , $\text{LiMg}_x\text{Co}_{1-x}\text{PO}_4$ ($x = 0.05, 0.10, 0.15$ and 0.20), was obtained by using an additional reagent magnesium sulphate (MgSO_4 , Sigma-Aldrich, $\geq 99.5\%$) and setting the relative molar ratio of $\text{CoSO}_4\cdot 7\text{H}_2\text{O}$ and MgSO_4 to the desired ratio in solution B.

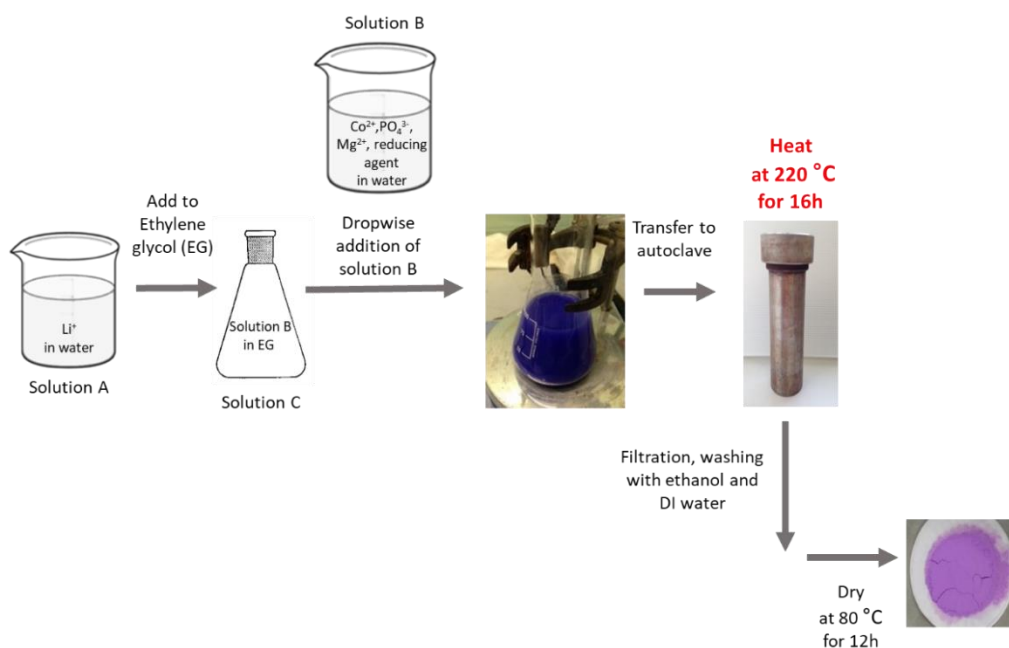


Figure 4.1. Schematic illustration of synthesis procedure.

4.2.2. Analyses and characterisation of as-synthesised samples

PXRD patterns were collected on a STOE STADI/P diffractometer operating in transmission mode with Fe $K\alpha_1$ radiation ($\lambda = 1.936 \text{ \AA}$). Lattice parameters were obtained by the Le Bail method³⁰ using the GSAS package with the EXPGUI interface.³¹ For combined refinements, the pattern for $\text{LiMg}_{0.15}\text{Co}_{0.85}\text{PO}_4$ was collected on a PANalytical Empyrean diffractometer in Bragg-Brentano geometry with Cu $K\alpha_1$ radiation ($\lambda = 1.5406 \text{ \AA}$).

Time-of-flight PND data were obtained on the Polaris diffractometer at ISIS at the Rutherford Appleton Laboratory. Samples were contained in 6 mm vanadium cans. Detailed crystallographic information was obtained from combined refinements using powder neutron and X-ray diffraction data. Rietveld refinements were carried out using the program Topas Academic.³²

ICP-OES analysis was performed using a iCAP 6000 Series.

TEM and STEM images were taken by using a FEI Titan Themis 200 and EDS mapping was collected with a Super-X high sensitivity windowless EDX detector.

EDS spectra were collected at an acceleration voltage of 15 keV using a FEI Scios microscope equipped with EDAX Octane Plus EDS detector.

SEM images were recorded on a JEOL JSM-6700F.

4.2.3. Preparation of electrodes

To evaluate the electrochemical performance of materials, slurries were prepared using the active material, super C65 carbon and Solef 5130 binder (a modified PVDF) in the mass ratio 75: 15: 10 in n-methyl-2-pyrrolidone, which was then cast on aluminium foil using a doctor blade. After drying, electrode sheets were calendered and 13 mm diameter electrode discs were punched then dried at 80 °C under vacuum for 12 h.

For *operando* XRD measurement and ex-situ TEM analysis, working electrodes were constructed by mixing the active material and super C65 carbon in the mass ratio 71: 29. The mixture was dried at 110 °C under vacuum for 12 h.

4.2.4. Preparation of cells and electrochemical tests

LIR2032 coin cells were assembled in an Ar-filled glovebox and used for evaluation of electrochemical performance except EIS measurements where CR2325 coin cells were

assembled. The cells consisted of a disc electrode, lithium metal as a counter/reference electrode, a glass fibre separator (Whatman, GF/B) and LP30 electrolyte (1M LiPF₆ in ethylene carbonate : dimethyl carbonate = 1:1 w/w).

For *ex-situ* TEM measurement, Swagelok-type cells were assembled in an Ar-filled glovebox. The cells consisted of a desired amount of working electrode, consisted of 71wt% active material and 29wt% super C65 with no binder, lithium metal as a counter/reference electrode, glass fibre separators (Whatman, GF/B) and LP30 electrolyte (1M LiPF₆ in ethylene carbonate : dimethyl carbonate = 1:1 w/w).

Galvanostatic charge/discharge cycling and voltage scans (linear sweep voltammetry) were carried out using a Bio-logic VMP 3.

EIS measurements were conducted on CR2325 coin cells, cycled at 30 °C using a Maccor Series 4200 battery cycler. Data for pre- and post- cycled cells were collected using a Solartron 1255 frequency response analyser coupled with Solartron 1287 electrochemical interface. A perturbation voltage of 10 mV and frequency range from 0.1 Hz to 0.1 MHz were employed.

4.2.5. Operando XRD measurements

Operando XRD patterns were recorded on a D8 Advance Bruker diffractometer using Cu K α radiation ($\lambda = 1.5418 \text{ \AA}$) in the 2θ range 10°-44° with a scan step width of 0.0197° and a scan rate of 1.8 s per step, corresponding to an hour of electrochemical reaction per pattern. For the *operando* XRD measurements the in-house *in-situ* cell³³ equipped with a beryllium window was used with a thin aluminum foil (Goodfellow, 99.1%) to prevent the window from possible oxidation at high voltage. Rietveld refinement was carried out using the Fullprof suite.³⁴

4.2.6. Ex-situ TEM measurement

For *ex-situ* TEM measurement, cycled cells were transferred to an Ar-filled glovebox before opening and the active material was extracted. The electrodes were rinsed carefully with dry dimethyl carbonate to remove residual electrolyte and then left under vacuum to ensure all solvent had evaporated. To minimise moisture/air exposure to the sample, the extracted active material was loaded in a sample holder inside the glovebox and quickly transferred to

a FEI Scios microscope for milling the sample, then kept under vacuum until TEM measurement, which was carried out as described for as-synthesised samples.

4.3. Results and discussion

4.3.1. Characterisation of as-synthesised materials

Fig. 4.2 shows the PXRD patterns of $\text{LiMg}_x\text{Co}_{1-x}\text{PO}_4$ ($x = 0, 0.05, 0.10, 0.15$ and 0.20) prepared by solvothermal method. All diffraction peaks can be indexed on the basis of an orthorhombic olivine structure (space group $Pnma$). All samples are single-phase without any additional peaks except $\text{LiMg}_{0.2}\text{Co}_{0.8}\text{PO}_4$, which contains some diffraction peaks from an impurity phase, assigned to Li_3PO_4 (ICSD database no.77095). The refined unit cell parameters using the Le Bail method are shown in Fig. 4.3. The cell parameter a decreases significantly with increased substitution of Mg. This confirms successful substitution of Mg for Co as the radius of Mg^{2+} (0.72 \AA , six-fold coordination) is smaller than that of Co^{2+} (0.745 \AA , six-fold coordination, high spin).

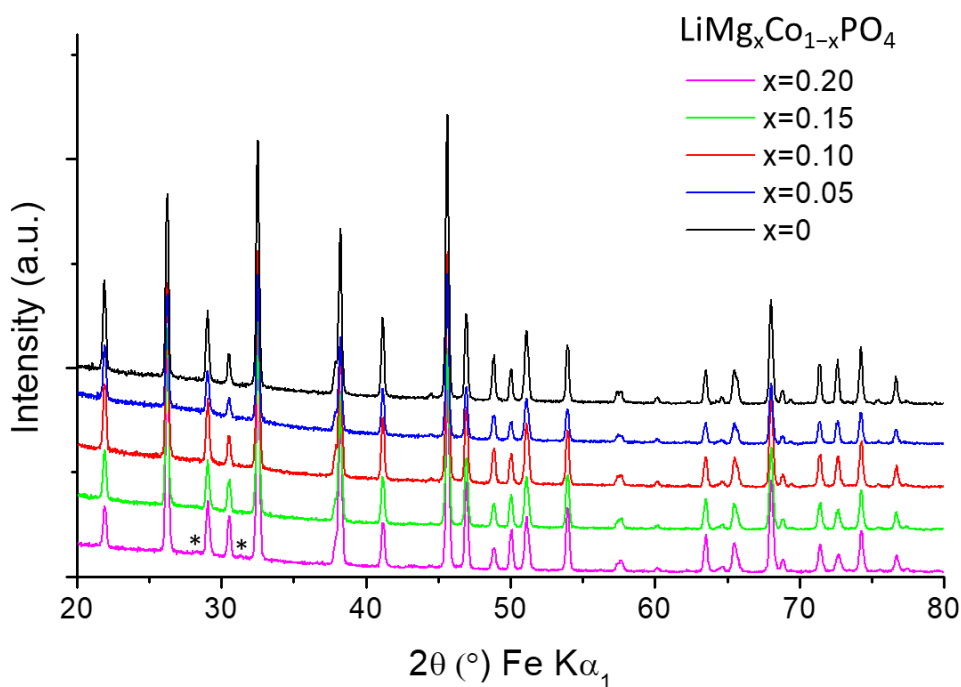


Figure 4.2. XRD patterns of as-synthesised $\text{LiMg}_x\text{Co}_{1-x}\text{PO}_4$, where $x=0$ (black), $x=0.05$ (blue), $x=0.10$ (red), $x=0.15$ (green) and $x=0.20$ (magenta) recorded with $\text{Fe K}\alpha_1$ radiation. * represents impurity peaks from Li_3PO_4 .

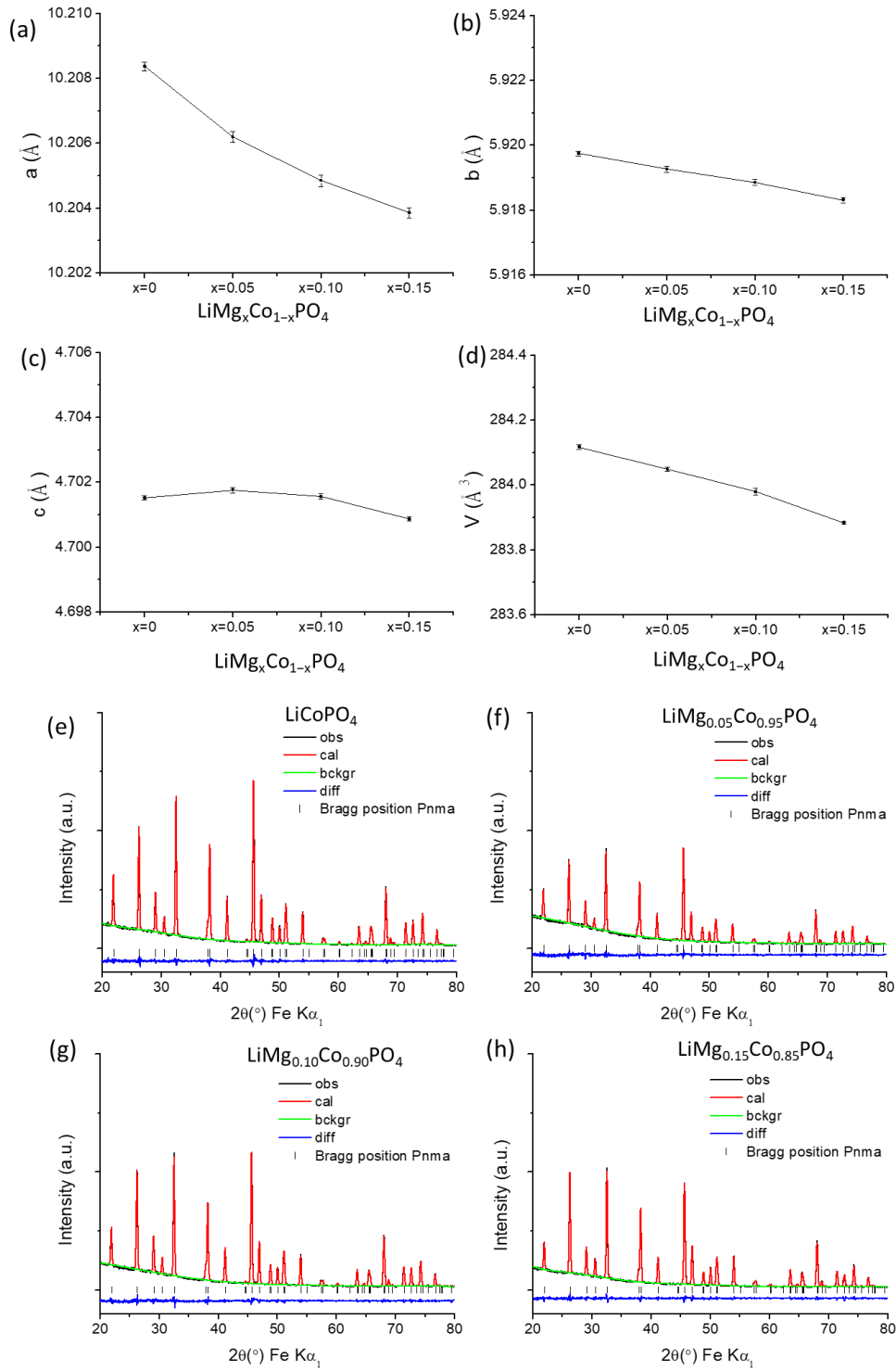


Figure 4.3. Refined results using the Le Bail method (a) unit cell parameter a , (b) unit cell parameter b , (c) unit cell parameter c and (d) unit cell volume. Profile fits for Le Bail refinements of as-synthesised $\text{LiMg}_x\text{Co}_{1-x}\text{PO}_4$, where (e) $x=0$, (f) $x=0.05$, (g) $x=0.10$ and (h) $x=0.15$. Observed data points are shown in black, with fitted profile in red and the difference is shown in blue. Tick marks indicate allowed reflections.

In order to obtain detailed crystallographic information, combined refinements were performed using PXRD and PND data. As aliovalent doping on Li sites is shown to be energetically unfavourable,³⁵ Mg doping on Co sites was solely considered. As shown in Table 4.1, good fits (Appendix I) were obtained with R_{wp} of less than 4%, confirming the model is reliable. The compositions derived from the occupancy of combined refinements are in good agreement with the values deduced by ICP-OES except for $\text{LiMg}_{0.15}\text{Co}_{0.85}\text{PO}_4$ (Table. 4.2). The difference might originate from a Mg-rich phase present around particle edges observed in the STEM image (Fig. 4.4) which is undetectable with diffraction methods. Of note, anti-site defects, involving partial exchange of Li and Co between $4a$ and $4c$ sites, diminish as more Mg is substituted for Co probably due to the preferential Mg occupation of $4c$ sites.

Table 4.1. Combined Rietveld refinement results of as-synthesised $\text{LiMg}_x\text{Co}_{1-x}\text{PO}_4$, where (a) $x=0$, (b) $x=0.05$, (c) $x=0.10$ and (d) $x=0.15$ (refined by Dr. A. Robert Armstrong).

(a) LiCoPO_4						
$R_{\text{exp}} : 2.20\% \ R_{\text{wp}} : 2.17\%$						
Lattice parameters from neutron diffraction $a = 10.20982(10) \text{ \AA}$ $b = 5.92072(6) \text{ \AA}$ $c = 4.70215(4) \text{ \AA}$						
atom	Wyckoff symbol	x/a	y/b	z/c	Occupancy	Biso
Li1/Co1	$4a$	0	0	0	0.978/0.022(1)	1.34(7)
Co2/Li2	$4c$	0.7775(3)	0.25	0.5207(6)	0.978/0.022(1)	0.51(3)
P	$4c$	0.59452(12)	0.25	0.0839(3)	1	0.08(7)
O1	$4c$	0.59855(11)	0.25	0.7612(2)	1	0.58(2)
O2	$4c$	0.95476(10)	0.25	0.2947(3)	1	0.28(10)
O3	$8d$	0.16615(8)	0.04434(11)	0.2816(2)	1	0.03(9)

(b) $\text{LiMg}_{0.05}\text{Co}_{0.95}\text{PO}_4$						
$R_{\text{exp}} : 2.08\% \ R_{\text{wp}} : 2.17\%$						
Lattice parameters from neutron diffraction $a = 10.20833(10) \text{ \AA}$ $b = 5.92035(6) \text{ \AA}$ $c = 4.70253(4) \text{ \AA}$						
atom	Wyckoff symbol	x/a	y/b	z/c	Occupancy	Biso
Li1/Co1	$4a$	0	0	0	0.979/0.021(1)	1.43(6)
Co2/Li2/ Mg1	$4c$	0.7782(2)	0.25	0.5204(5)	0.923/0.021/ 0.056(1)	0.57(3)
P	$4c$	0.59453(10)	0.25	0.0835(2)	1	0.67(12)
O1	$4c$	0.59870(10)	0.25	0.7558(13)	1	0.560(13)
O2	$4c$	0.9482(8)	0.25	0.2983(9)	1	0.595(13)
O3	$8d$	0.1668(5)	0.0379(6)	0.2813(2)	1	0.546(10)

(c) LiMg_{0.10}Co_{0.90}PO₄						
R _{exp} : 2.13% R _{wp} : 2.11%						
Lattice parameters from n neutron diffraction $a = 10.20980(9) \text{ \AA}$ $b = 5.92081(5) \text{ \AA}$ $c = 4.70290(4) \text{ \AA}$						
atom	Wyckoff symbol	x/a	y/b	z/c	Occupancy	Biso
Li1/Co1	4a	0	0	0	0.982/0.018(1)	1.33(6)
Co2/Li2/ Mg1	4c	0.7781(2)	0.25	0.5197(5)	0.899/0.018/ 0.083(6)	0.57(3)
P	4c	0.59483(11)	0.25	0.0831(3)	1	0.36(1)
O1	4c	0.59848(11)	0.25	0.7611(2)	1	0.567(15)
O2	4c	0.95477(10)	0.25	0.2947(3)	1	0.608(15)
O3	8d	0.16629(7)	0.04435(11)	0.2812(2)	1	0.550(11)

(d) LiMg_{0.15}Co_{0.85}PO₄						
R _{exp} : 1.55% R _{wp} : 3.68%						
Lattice parameters from neutron diffraction $a = 10.2050(2) \text{ \AA}$ $b = 5.92066(13) \text{ \AA}$ $c = 4.70081(9) \text{ \AA}$						
atom	Wyckoff symbol	x/a	y/b	z/c	Occupancy	Biso
Li1/Co1	4a	0	0	0	0.988/0.012(2)	1.22(12)
Co2/Li2/ Mg1	4c	0.7777(5)	0.25	0.5194(11)	0.920/0.012/ 0.068(5)	0.66(3)
P	4c	0.5947(2)	0.25	0.0832(5)	1	0.34(3)
O1	4c	0.5985(2)	0.25	0.7603(5)	1	0.55(2)
O2	4c	0.9548(2)	0.25	0.2952(6)	1	0.55(2)
O3	8d	0.1663(2)	0.0443(2)	0.2818(8)	1	0.55(2)

Table 4.2. Stoichiometric ratio derived from combined refinement and ICP-OES, constraining Li/Mg+Co = 1.00 for all samples. The last figure in brackets indicates standard deviation and relative standard deviation for refinement and ICP-OES results, respectively.

Samples	Composition	
	LiMg _x Co _{1-x} PO ₄	ICP-OES
x = 0	Li _{1.000(1)} Co _{1.000(1)} PO ₄	Li _{1.00(7)} Co _{1.00(6)} PO ₄
x = 0.05	Li _{1.000} Mg _{0.056(1)} Co _{0.944(1)} PO ₄	Li _{1.0(5)} Mg _{0.040(1)} Co _{0.96(7)} PO ₄
x = 0.10	Li _{1.000} Mg _{0.083(6)} Co _{0.917(1)} PO ₄	Li _{1.0(2)} Mg _{0.080(6)} Co _{0.92(8)} PO ₄
x = 0.15	Li _{1.000} Mg _{0.068(5)} Co _{0.932(2)} PO ₄	Li _{1.0(6)} Mg _{0.120(7)} Co _{0.88(6)} PO ₄

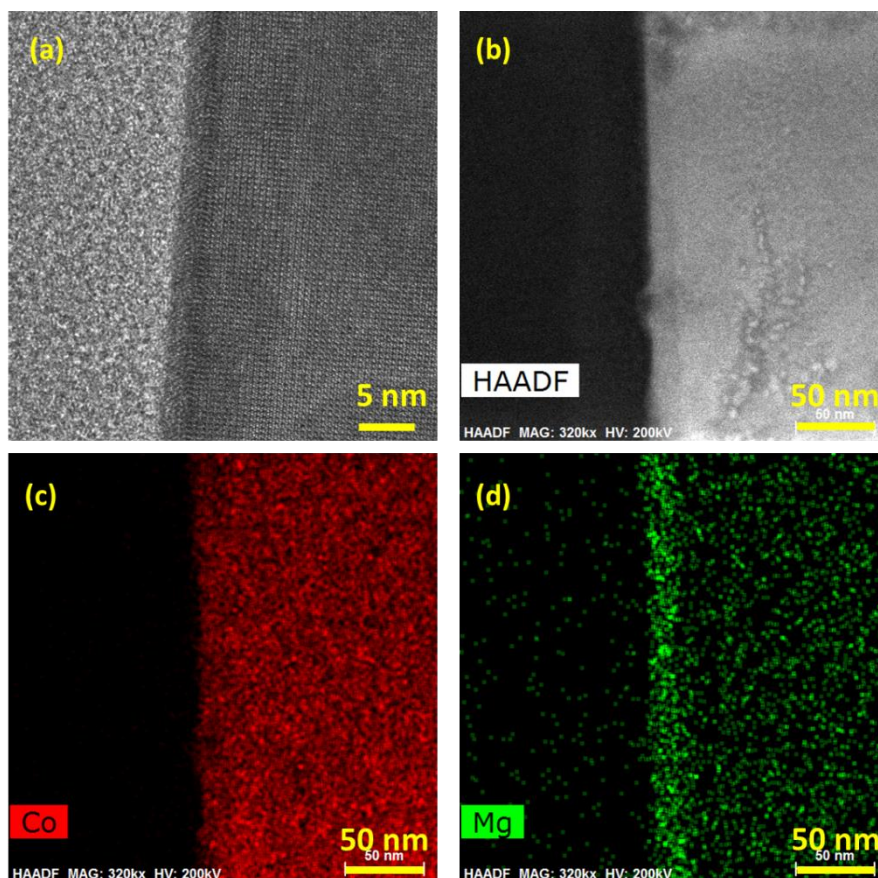


Figure 4.4. (a) Bright-field TEM image, (b) High-angle annular dark-field STEM image and EDS mapping for (c) Co and (d) Mg elements of as-synthesised $\text{LiMg}_{0.15}\text{Co}_{0.85}\text{PO}_4$ (taken by Dr. David Miller).

The EDS spectra of as-synthesised materials collected at 15 keV (Fig. 4.5) demonstrate a continuous increase of the proportion of Mg with decrease in Co content, consistent with the results from ICP-OES. All samples contain traces of sulphur which are probably related to by-products of sulphate anions from the precursors during solvothermal synthesis as previously reported.^{18,36}

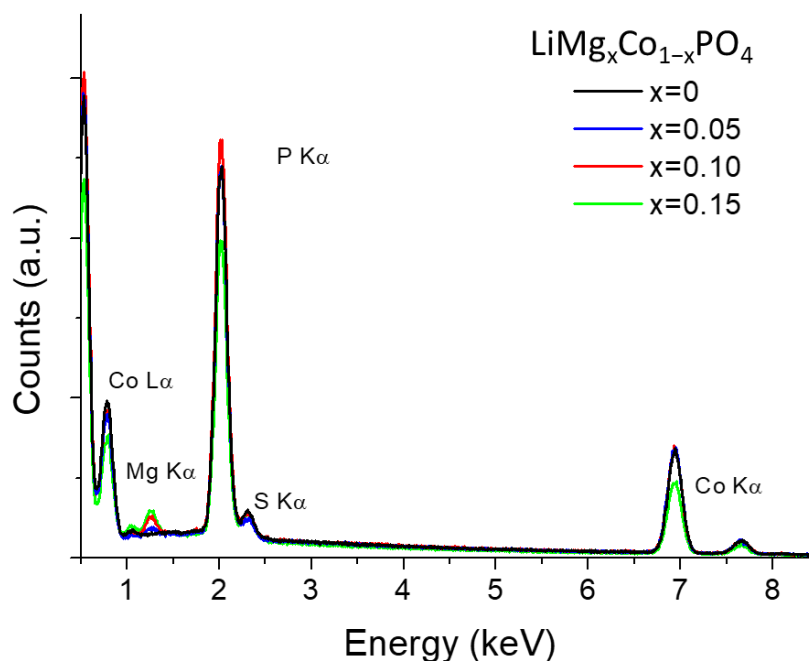


Figure 4.5. EDS spectra of as-synthesised $\text{LiMg}_x\text{Co}_{1-x}\text{PO}_4$, where $x=0$ (black), $x=0.05$ (blue), $x=0.10$ (red) and $x=0.15$ (green) (measured by Dr. David Miller).

The morphology of the as-synthesised samples was investigated using SEM (Fig. 4.6a-d). LiCoPO_4 consists of sub-micron hexagonal platelets with the thickness of 100-150 nm, consistent with the reports that the ethylene glycol/DIW co-solvent system produces hexagonal platelets.^{37,38} The substitution of Mg for Co in LiCoPO_4 tends to enlarge particle size. Large particles emerge from $\text{LiMg}_{0.10}\text{Co}_{0.90}\text{PO}_4$ while $\text{LiMg}_{0.05}\text{Co}_{0.95}\text{PO}_4$ shows little change. A significant particle size difference is observed at $\text{LiMg}_{0.15}\text{Co}_{0.85}\text{PO}_4$ with the particle thickness about 1 μm . An analogous trend was reported in Fe-substituted LiCoPO_4 synthesised by a solvothermal method where a remarkable particle alteration to micrometer particles with a thickness above 500 nm was obtained, which is also observed under different synthesis conditions such as temperature and time.¹⁸ In this study, tentative syntheses reducing solvothermal treatment time from 16 h to 3 h ($\text{LiMg}_{0.15}\text{Co}_{0.85}\text{PO}_4$ - 3h) and temperature from 220 $^\circ\text{C}$ to 180 $^\circ\text{C}$ ($\text{LiMg}_{0.15}\text{Co}_{0.85}\text{PO}_4$ - 180 $^\circ\text{C}$) were carried out. As shown in Fig. 4.6e, shorter reaction time barely affects the morphology. In contrast, lower temperature permits a reduction in the particle size but this leads to inhomogeneous size distribution (Fig. 4.6f) and appearance of impurity phase (Fig. 4.6g).

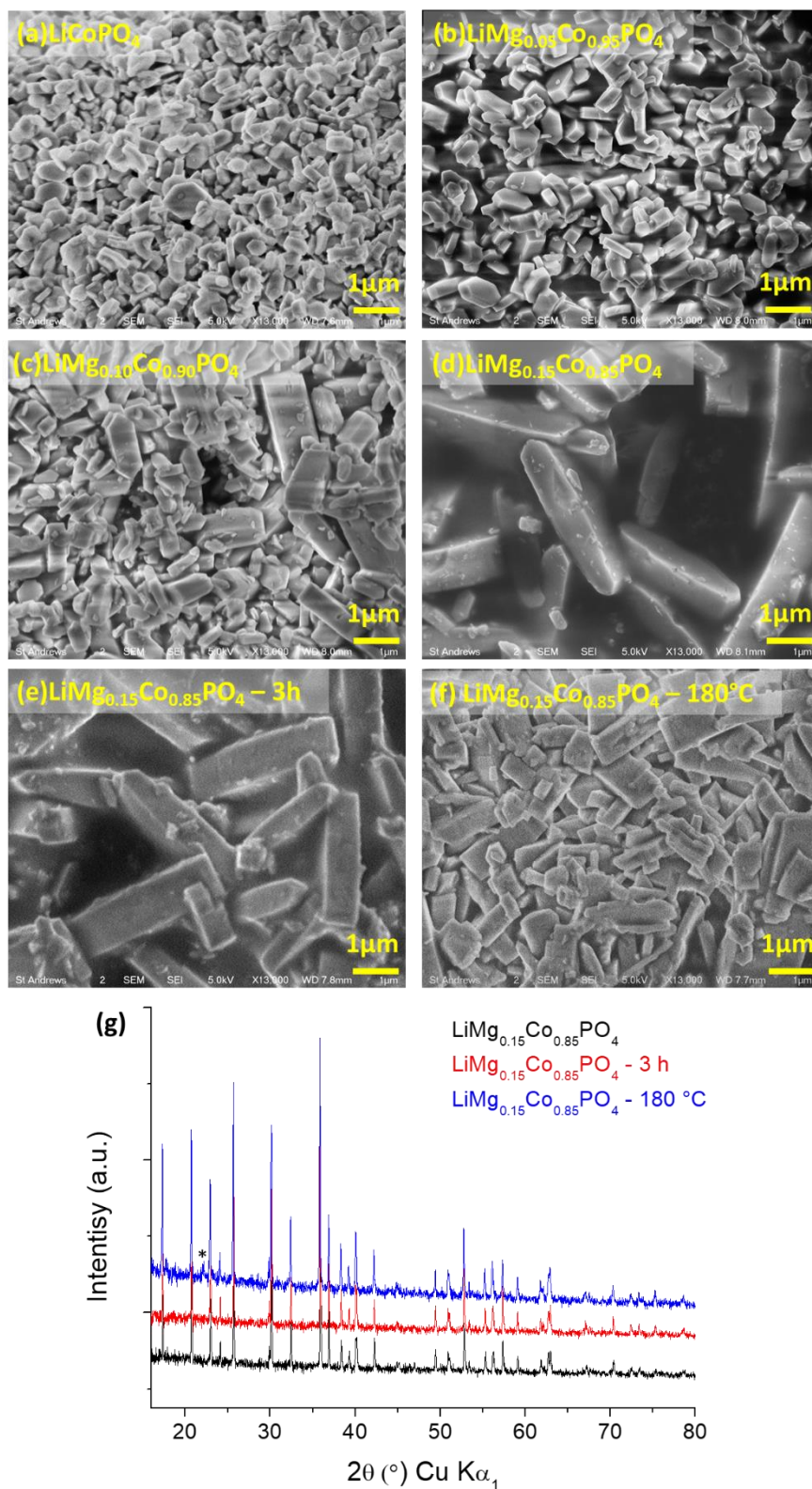


Figure 4.6. SEM images of as-synthesised (a) LiCoPO_4 , (b) $\text{LiMg}_{0.05}\text{Co}_{0.95}\text{PO}_4$, (c) $\text{LiMg}_{0.10}\text{Co}_{0.90}\text{PO}_4$, (d) $\text{LiMg}_{0.15}\text{Co}_{0.85}\text{PO}_4$, (e) $\text{LiMg}_{0.15}\text{Co}_{0.85}\text{PO}_4 - 3\text{h}$ and (f) $\text{LiMg}_{0.15}\text{Co}_{0.85}\text{PO}_4 - 180^\circ\text{C}$. (g) PXRD patterns of $\text{LiMg}_{0.15}\text{Co}_{0.85}\text{PO}_4$ samples synthesised at different synthetic conditions recorded with $\text{Cu K}\alpha_1$ radiation. * represents impurity peaks from Li_3PO_4 .

4.3.2. Electrochemical behaviour of as-synthesised materials

In order to investigate Mg substitution effects on electrochemical performance, electrodes with a series of Mg-doped LiCoPO_4 were prepared and coin cells were tested at a rate of 16.7 mA g^{-1} ($\text{C}/10$ for LiCoPO_4). Fig. 4.7a shows charge/discharge curves of LiCoPO_4 at cycle 1, 5, 10, 20 and 30. Typically two plateaus are present in the voltage profiles at all cycles, indicating two biphasic redox processes. It is known that the redox process of $\text{Co}^{2+}/\text{Co}^{3+}$ in LiCoPO_4 occurs through two schemes, with an intermediate phase of composition $\text{Li}_{2/3}\text{CoPO}_4$, coexisting with the fully lithiated phase (LiCoPO_4) at higher Li content and with the fully delithiated phase (CoPO_4) at lower Li content.³⁹⁻⁴¹ Both reversible processes are maintained for all Mg-substituted samples, producing two plateaus for all cycles (Fig. 4.7b-d). On the first cycle, all samples show significant irreversible capacity with Coulombic efficiencies of 68%, 63%, 64% and 57% for LiCoPO_4 , $\text{LiMg}_{0.05}\text{Co}_{0.95}\text{PO}_4$, $\text{LiMg}_{0.10}\text{Co}_{0.90}\text{PO}_4$ and $\text{LiMg}_{0.15}\text{Co}_{0.85}\text{PO}_4$, respectively, due to electrolyte decomposition and/or possible SEI layer formation at high voltage. The efficiencies however increase, reaching about 92% at the second cycle for all samples and around 98% at cycle 30 (Fig. 4.7e).

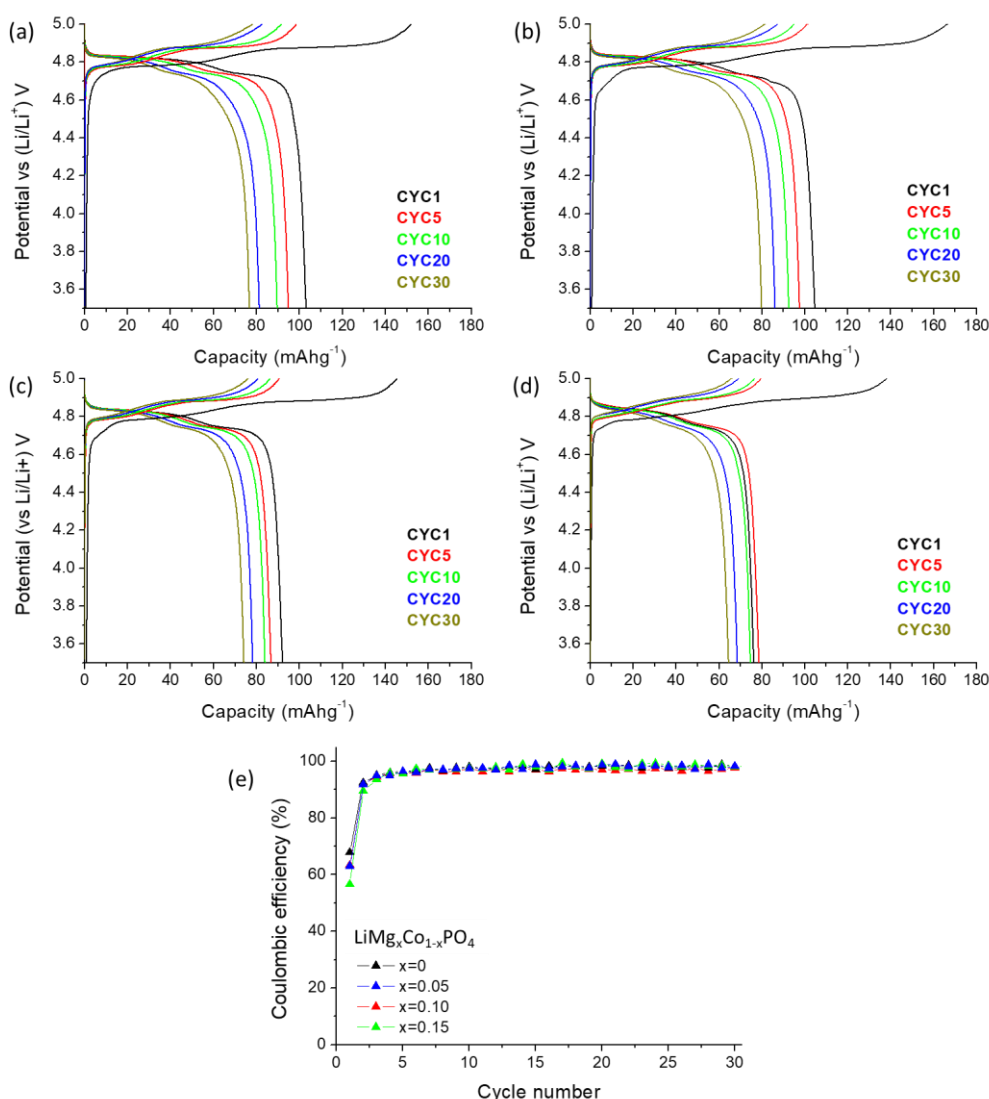


Figure 4.7. Charge/discharge curves at cycle 1 (black), cycle 5 (red), cycle 10 (green), cycle 20 (blue) and cycle 30 (dark yellow) of (a) LiCoPO₄, (b) LiMg_{0.05}Co_{0.95}PO₄, (c) LiMg_{0.10}Co_{0.90}PO₄, (d) LiMg_{0.15}Co_{0.85}PO₄ and (e) Coulombic efficiencies of LiCoPO₄ (black), LiMg_{0.05}Co_{0.95}PO₄ (blue), LiMg_{0.10}Co_{0.90}PO₄ (red) and LiMg_{0.15}Co_{0.85}PO₄ (green), cycled between 3.5 and 5.0 V vs Li/Li⁺ at a rate of 16.7 mA g⁻¹.

Cycling performance of all samples is shown in Fig. 4.8a. It is clearly observed that as more Mg is substituted for Co, a lower initial discharge capacity is delivered. This is attributed to the replacement of the electrochemically active Co²⁺ ions with electrochemically inactive Mg²⁺ ions.⁴² In addition to that, enlargement of the particle size might limit ionic transport, resulting in lower capacity. However, the capacity retention is improved as a function of Mg substitution, as presented in Fig. 4.8b. The normalised capacity retention based on the capacity delivered at the first cycle shows the highest capacity retention of 82% for

$\text{LiMg}_{0.15}\text{Co}_{0.85}\text{PO}_4$, followed by 80%, 76% and 74% for $\text{LiMg}_{0.10}\text{Co}_{0.90}\text{PO}_4$, $\text{LiMg}_{0.05}\text{Co}_{0.95}\text{PO}_4$ and LiCoPO_4 , respectively.

A series of five cycles at progressively increasing current rates from 16.7 mA g^{-1} (C/10 for LiCoPO_4) to 334 mA g^{-1} (2C for LiCoPO_4) was carried out to examine rate capability of Mg-doped samples. As shown in Fig. 4.8.c, at the lowest rate (16.7 mA g^{-1}) no significant effects are observed, whereas $\text{LiMg}_{0.05}\text{Co}_{0.95}\text{PO}_4$ and $\text{LiMg}_{0.10}\text{Co}_{0.90}\text{PO}_4$ demonstrate slightly better capacity compared to LiCoPO_4 at the highest rate (334 mA g^{-1}). This beneficial effect can be accounted for by the reduced anti-site defects as observed in the combined refinement results, which facilitates Li ion migration in the olivine structure. In the case of $\text{LiMg}_{0.15}\text{Co}_{0.85}\text{PO}_4$, the decrease in anti-site defects is probably offset by larger particles. All samples recover their capacity at 16.7 mA g^{-1} after cycling at higher rates, indicating that materials are preserved without significant degradation.

Cyclic voltammograms for all samples were collected by applying an initial positive potential and subsequent negative potential with a scan rate of $10 \mu\text{V s}^{-1}$ within the voltage range of 3.5 - 5.4 V (Fig. 4.8d). Consistent with the charge/discharge curves, two oxidation and reduction peaks exist for all samples. Interestingly, the voltage of the two $\text{Co}^{2+}/\text{Co}^{3+}$ redox couples shift slightly to higher voltage with increasing Mg content from 4.73 and 4.82 V for LiCoPO_4 to 4.77 and 4.87 V for $\text{LiMg}_{0.15}\text{Co}_{0.85}\text{PO}_4$. The shift in redox potential has previously been observed in the phospho-olivine family e.g., $\text{LiMg}_x\text{Fe}_{1-x}\text{PO}_4$, $\text{LiMg}_x\text{Mn}_{1-x}\text{PO}_4$ and $\text{LiMg}_x\text{Co}_{1-x}\text{PO}_4$.^{23,28} As proposed in the other olivine systems, Mg^{2+} may stabilise the redox active $\text{Co}^{2+}/\text{Co}^{3+}$ through the $\text{TM}^{2+}\text{-O-Mg}^{2+}$ interaction.

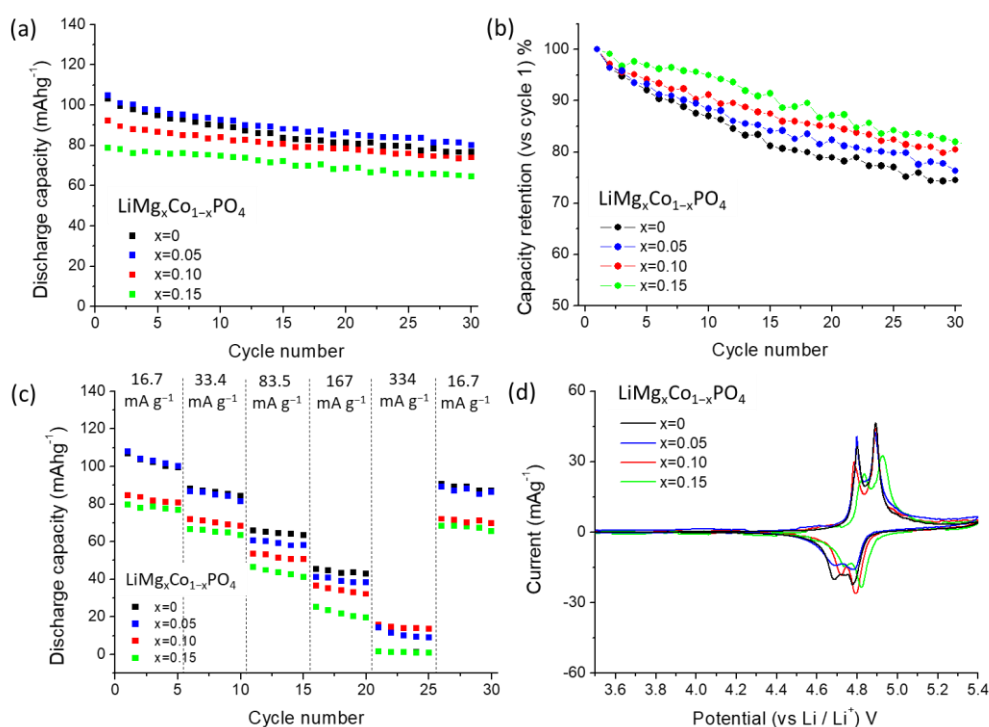


Figure 4.8. (a) Galvanostatic cycling performance at a rate of 16.7 mA g^{-1} cycled between 3.5 and 5.0 V vs Li/Li^+ , (b) Normalised capacity retention based on the first cycle capacity, (c) Discharge capacity vs different current rates cycled between 3.5 and 5.0 V vs Li/Li^+ and (d) Voltammograms collected at a scan rate of $10 \mu\text{V s}^{-1}$ with the voltage window of 3.5 - 5.4 V vs Li/Li^+ of LiCoPO_4 (black), $\text{LiMg}_{0.05}\text{Co}_{0.95}\text{PO}_4$ (blue), $\text{LiMg}_{0.10}\text{Co}_{0.90}\text{PO}_4$ (red) and $\text{LiMg}_{0.15}\text{Co}_{0.85}\text{PO}_4$ (green).

4.3.3. Origin of enhanced cycle stability

In order to gain better understanding of the enhanced cycle stability for Mg-doped LiCoPO_4 , *operando* XRD was carried out. This is a powerful technique to evaluate structural changes during cycling and is essential to investigate the delithiated phase ($\text{Mg}_x\text{Co}_{1-x}\text{PO}_4$) without its amorphisation which has often been observed for *ex-situ* measurements.⁴³ The contour profile maps of the XRD patterns for LiCoPO_4 and $\text{LiMg}_{0.15}\text{Co}_{0.85}\text{PO}_4$ in an *in-situ* cell cycled at a rate of 5.56 mA g^{-1} (C/30 for LiCoPO_4) during the charge process are shown in Fig. 4.9a and in Fig. 4.9b, respectively. The 2θ range 29 to 32° ($\text{Cu K}\alpha$, $\lambda = 1.5418 \text{ \AA}$) shows the (211) and the (020) reflections, which clearly reveals the changes in unit cell parameters upon cycling. For both samples two two-phase reactions, from the lithiated phase ($\text{LiMg}_x\text{Co}_{1-x}\text{PO}_4$, where $x=0$ and $x=0.15$) to the intermediate phase ($\text{Li}_{2/3}\text{Mg}_x\text{Co}_{1-x}\text{PO}_4$, where $x=0$ and $x=0.15$) and from the intermediate phase ($\text{Li}_{2/3}\text{Mg}_x\text{Co}_{1-x}\text{PO}_4$, where $x=0$ and $x=0.15$) to the delithiated phase

($\text{Mg}_x\text{Co}_{1-x}\text{PO}_4$, where $x=0$ and $x=0.15$), are observed through the simultaneous growth of reflections and loss of intensity of a new phase and an original phase, respectively.

Fig. 4.9c shows the XRD patterns of LiCoPO_4 recorded during the first reaction ($\text{LiCoPO}_4 \rightarrow \text{Li}_{2/3}\text{CoPO}_4 + 1/3 \text{Li}^+ + 1/3 \text{e}^-$), there are the concurrent disappearance and appearance of the reflections of starting material and product, respectively, and shifts in the peak positions, implying solid-solution like behaviour as reported in previous studies.^{20,40,41} The peak shifts suggest that small structural changes in a limited range of two main compositions (LiCoPO_4 and $\text{Li}_{2/3}\text{CoPO}_4$) are required to nucleate a minority phase in a particle, reducing the energy between major and minor phases. An analogous phenomenon is observed for $\text{LiMg}_{0.15}\text{Co}_{0.85}\text{PO}_4$ as observed in Fig. 4.9d, suggesting that the introduction of disorder in the olivine structure *via* Mg doping barely affects the appearance of the intermediate phase during the oxidation of Co^{2+} to Co^{3+} and the structural distortion to reduce the interphase energy. The following reaction ($\text{Li}_{2/3}\text{Mg}_x\text{Co}_{1-x}\text{PO}_4 \rightarrow \text{Mg}_x\text{Co}_{1-x}\text{PO}_4 + 2/3 \text{Li}^+ + 2/3 \text{e}^-$, where $x = 0$ and $x = 0.15$) similarly demonstrates two distinct phases with solid-solution like evolution (Fig. 4.9e-f).

Rietveld refinements were carried out using the diffraction patterns acquired during the charge process. Due to the low resolution and different background, each pattern was independently refined. Atomic occupancies were fixed based on the ICP - OES values, whilst lattice parameters were refined to evaluate the unit cell volumes of each phase. Consistent with the shifts in peak positions, the volumes of all phases decrease along with the Li ion removal. Of note, the volume of the intermediate phase for both samples varies noticeably across the region where two phases coexist, implying that the intermediate phase sustains a larger solid solution region compared to the two end members. The intermediate phase is present until the end of charge, most likely due to the slow kinetics. The two major plateaus observed in the galvanostatic charge curve agree with the two-phase reaction regions with a slight lag probably due to the acquisition of each XRD pattern in a non-equilibrium state. It is worth noting that a plateau around 5.0 V in $\text{LiMg}_{0.15}\text{Co}_{0.85}\text{PO}_4$ can be attributed to side reactions whilst no important structural variation is shown (Fig. 4.9f).

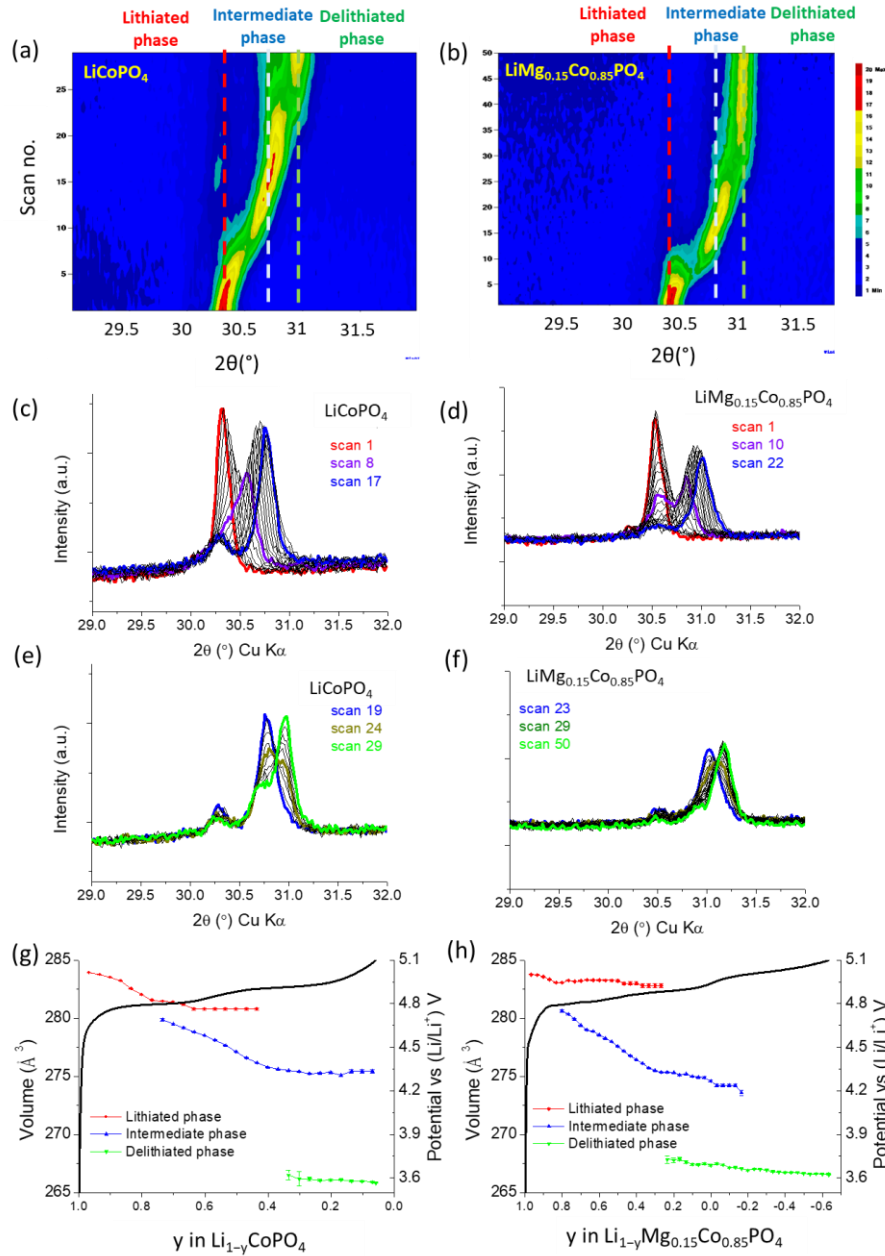


Figure 4.9. The contour profile maps of the XRD patterns for the first charge of (a) LiCoPO_4 and (b) $\text{LiMg}_{0.15}\text{Co}_{0.85}\text{PO}_4$ cycled at a rate of 5.56 mA g^{-1} . The y-axis is scan number and x-axis is 2θ . The region $2\theta = 29$ to 32° shows the (211) and the (020) reflections. The red, light blue and green dotted vertical lines indicate the peak position of lithiated phase, intermediate phase and delithiated phase, respectively. XRD patterns of the phase transition from $\text{LiMg}_x\text{Co}_{1-x}\text{PO}_4$ to $\text{Li}_{2/3}\text{Mg}_x\text{Co}_{1-x}\text{PO}_4$ for (c) $x=0$ (i.e. scan numbers 1-17 with scan 1 in red, scan 8 in violet and scan 17 in blue) and (d) $x=0.15$ (i.e. scan numbers 1-22 with scan 1 in red, scan 10 in violet and scan 22 in blue). XRD patterns of the phase transition from $\text{Li}_{2/3}\text{Mg}_x\text{Co}_{1-x}\text{PO}_4$ to $\text{Mg}_x\text{Co}_{1-x}\text{PO}_4$ for (e) $x=0$ (i.e. scan numbers 19-29 with scan 19 in blue, scan 24 in dark yellow and scan 29 in green) and (f) $x=0.15$ (i.e. scan numbers 23-50 with 23 in blue, scan 29 in dark yellow and scan 50 in green). The Rietveld refinement results showing changes in the unit cell volumes in the three phases ($\text{LiMg}_x\text{Co}_{1-x}\text{PO}_4$ in red $\text{Li}_{2/3}\text{Mg}_x\text{Co}_{1-x}\text{PO}_4$ in blue $\text{Mg}_x\text{Co}_{1-x}\text{PO}_4$ in green) of (g) $x=0$ and (h) $x=0.15$, overlaid onto the galvanostatic charge curve cycled between 3.5 and 5.1 V vs Li/Li^+ at 5.56 mA^{-1} .

The volume change between lithiated and delithiated phase was examined using the Le Bail refinement of the two end XRD patterns acquired from *operando* XRD measurements. The variation of unit cell volume between the pristine and the end of charge phase varies from 6.52% for LiCoPO_4 to 6.15% for $\text{LiMg}_{0.15}\text{Co}_{0.85}\text{PO}_4$. Lower volume variation is found along with the increase in Mg content since electrochemically inactive Mg^{2+} ions reside within the structure during cycling. Reducing the lattice stress caused by the unit cell volume mismatch during electrochemical cycling might be a source of improved cyclability of $\text{LiMg}_{0.15}\text{Co}_{0.85}\text{PO}_4$ at the expense of initial capacity.

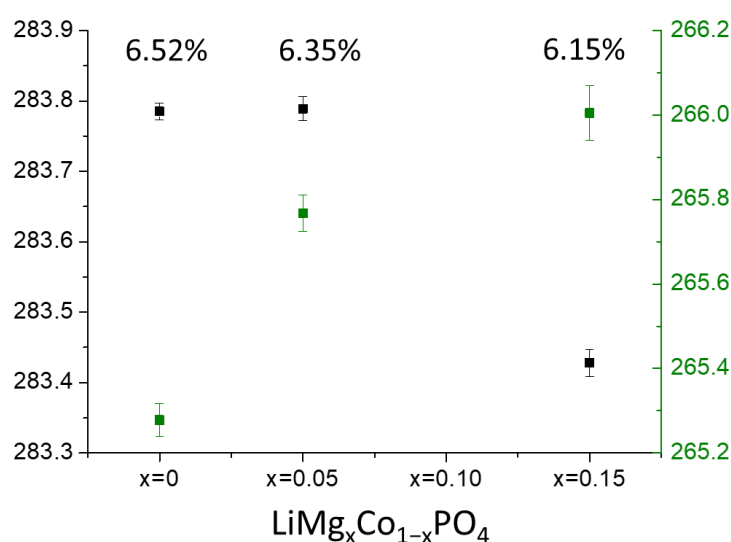


Figure 4.10. Variation of unit cell volume between lithiated and delithiated phase for LiCoPO_4 , $\text{LiMg}_{0.05}\text{Co}_{0.95}\text{PO}_4$ and $\text{LiMg}_{0.15}\text{Co}_{0.85}\text{PO}_4$.

In addition to the structural stabilisation, the Mg-rich layer present in $\text{LiMg}_{0.15}\text{Co}_{0.85}\text{PO}_4$ particles may play a critical role in enhancing cycling stability. One of the reasons for capacity fade of LiCoPO_4 is interfacial reactions between active materials and the electrolyte, i.e., nucleophilic attack of F^- produced in LiPF_6 based electrolyte causes degradation of active materials through the breakage of phosphate groups.^{44,45} One potential method to alleviate the undesired reactions is modifying the surface of the active materials with thin metal oxides such as NiO ,⁴⁶ VO_x ,⁴⁷ or Al_2O_3 .⁴⁸ In various studies of LiCoO_2 , a MgO coating has been revealed as an effective way to improve cycling ability.⁴⁹⁻⁵¹ Assuming that the Mg-rich layer observed on the surface of as-synthesised $\text{LiMg}_{0.15}\text{Co}_{0.85}\text{PO}_4$ can act as a protective layer, inhibiting direct contact between bulk active material and the electrolyte, the surface of $\text{LiMg}_{0.15}\text{Co}_{0.85}\text{PO}_4$ after the first cycle was analysed. As shown in Fig. 4.11, the Mg-rich layer

(about 15 nm) remains after cycling without significant amorphisation of active material, supporting the protective role of Mg-rich layer.

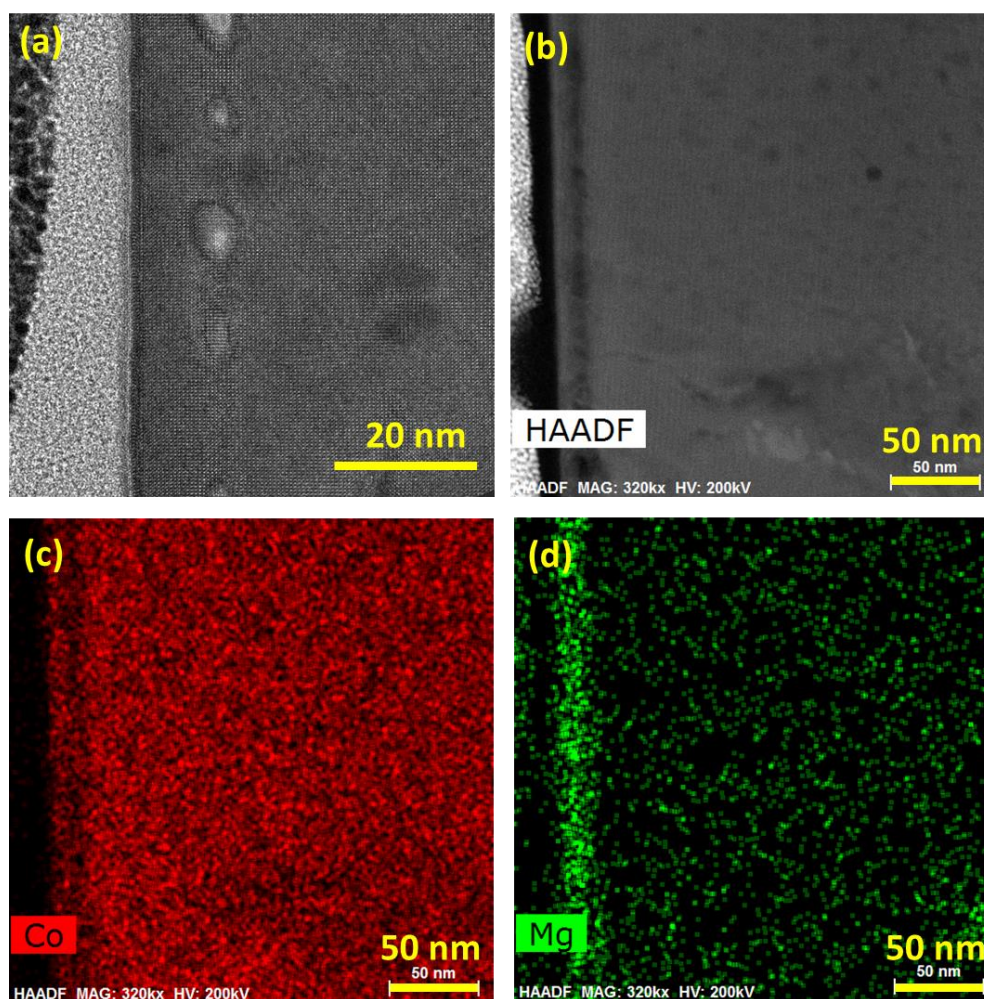


Figure 4.11. (a) Bright-field TEM image, (b) High-angle annular dark-field STEM image and EDS mapping for (c) Co and (d) Mg elements of post-cycled $\text{LiMg}_{0.15}\text{Co}_{0.85}\text{PO}_4$ (taken by Dr. David Miller).

Unlike a carbon coating which provides enhanced overall electronic conductivity of electrodes, metal oxide coating on the surface of active material might impede Li ion diffusion and increase resistance of the electrodes.^{47,49} To evaluate the influence of the Mg-rich layer on the resistance of $\text{LiMg}_{0.15}\text{Co}_{0.85}\text{PO}_4$ electrodes, EIS measurements were carried out. Fig. 4.12 shows the Nyquist plots of LiCoPO_4 and $\text{LiMg}_{0.15}\text{Co}_{0.85}\text{PO}_4$ electrodes before and after cycling. As-assembled LiCoPO_4 and $\text{LiMg}_{0.15}\text{Co}_{0.85}\text{PO}_4$ electrodes display an arc followed by an angled line whereas their post-cycled electrodes exhibit an extra arc before the angled line. The size of the arcs is comparable between LiCoPO_4 and $\text{LiMg}_{0.15}\text{Co}_{0.85}\text{PO}_4$ electrodes in both stages, as-assembled and after cycling, implying that the Mg-rich layer barely affects electrode resistance. Fitting results using an equivalent circuit reveal that similar processes

occur in as-assembled LiCoPO_4 and $\text{LiMg}_{0.15}\text{Co}_{0.85}\text{PO}_4$ electrodes with resistances of 44.3 and 47.5 Ω , respectively, which can be associated with the resistance of the active material/electrolyte interface and charge transfer within the electrodes as well as active material particles. It is noted that R2 was included to fit post-cycled LiCoPO_4 and $\text{LiMg}_{0.15}\text{Co}_{0.85}\text{PO}_4$ electrodes due to the appearance of an additional arc which could represent SEI layer resistance.

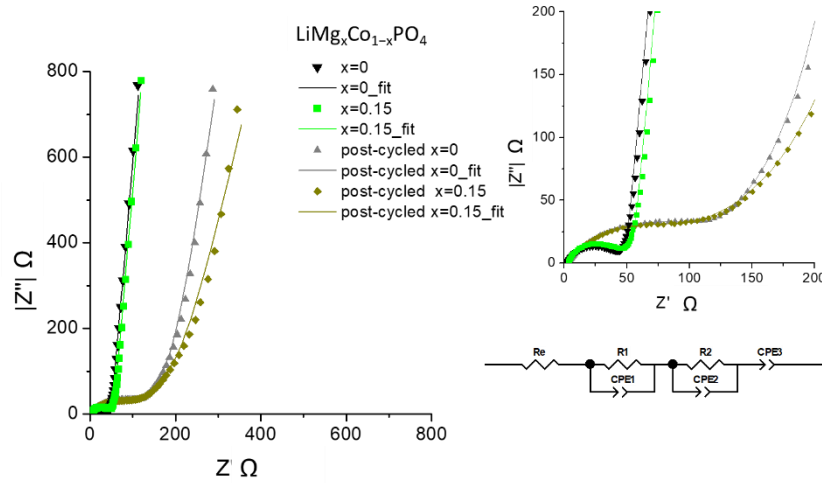


Figure 4.12. Nyquist plots of as-assembled and post-cycled LiCoPO_4 and $\text{LiMg}_{0.15}\text{Co}_{0.85}\text{PO}_4$ electrodes at frequencies from 0.1 Hz to 0.1 MHz, with a zoomed image for high frequency on the top right and an equivalent circuit on the bottom right.

Table 4.3. Results of EIS fitting for as-assembled and post-cycled LiCoPO_4 and $\text{LiMg}_{0.15}\text{Co}_{0.85}\text{PO}_4$ electrodes using ZView2 applying an equivalent circuit.

	LiCoPO_4 as assembled	$\text{LiMg}_{0.15}\text{Co}_{0.85}\text{PO}_4$ as assembled	LiCoPO_4 after cycle 1	$\text{LiMg}_{0.15}\text{Co}_{0.85}\text{PO}_4$ after cycle 1
Re (Ω)	2.37 (± 0.039)	3.33 (± 0.046)	2.69 (± 0.115)	1.83 (± 0.012)
R1 (Ω)	44.34 (± 0.392)	47.5 (± 0.492)	101 (± 12.968)	91.9 (± 13.968)
R2 (Ω)	-	-	125.1 (± 44.72)	138.9 (± 51.041)

4.4. Summary

Magnesium doped lithium cobalt phosphates, $\text{LiMg}_x\text{Co}_{1-x}\text{PO}_4$ ($x = 0, 0.05, 0.10, 0.15$ and 0.20), were synthesised using a solvothermal method. It is shown that 15% substitution of Mg for Co is the limit to obtain a single-phase which crystallises in the olivine structure. Structural investigation using XRD data and elemental analysis using ICP-OES and EDS provide evidence of successful Mg doping in Co sites. Detailed crystallographic information was obtained using combined Rietveld refinement, revealing that preferential occupation of Mg in Co sites reduces anti-site defects. In terms of morphology, the increase in Mg content tends to enlarge particle size, leading to noticeably large particles in $\text{LiMg}_{0.15}\text{Co}_{0.85}\text{PO}_4$.

Given these effects driven by Mg doping, the electrochemical performance of $\text{LiMg}_x\text{Co}_{1-x}\text{PO}_4$ ($x = 0, 0.05, 0.10$ and 0.15) was examined. The two biphasic redox mechanism is maintained for all samples with a slight upward shift in working voltage for $\text{LiMg}_{0.15}\text{Co}_{0.85}\text{PO}_4$. Regarding cycling stability, Mg-doped LiCoPO_4 samples demonstrate better capacity retention. Enhancement in rate capability is observed for $\text{LiMg}_{0.10}\text{Co}_{0.90}\text{PO}_4$ possibly due to reduction of anti-site defects without enlargement of particle size, which favours Li ion migration.

Operando XRD and *ex-situ* TEM measurements shed light on the improved cycling performance of $\text{LiMg}_{0.15}\text{Co}_{0.85}\text{PO}_4$. From a structural point of view, smaller volume changes between lithiated and delithiated phase mitigates lattice stress, leading to the maintenance of the initial capacity upon cycling. A Mg-rich layer present on the surface of particles can act as a protective layer preventing detrimental reactions between the active material and the electrolyte.

In conclusion, Mg substitution for Co in LiCoPO_4 may be one of the strategies to alleviate capacity fade *via* structural stabilisation during cycling and surface protection preventing a direct contact with the electrolyte.

4.5. References

- 1 K. Amine, H. Yasuda and M. Yamachi, *Electrochem. Solid-State Lett.*, 2000, **3**, 178–179.
- 2 J. Wolfenstine, *J. Power Sources*, 2006, **158**, 1431–1435.
- 3 J. L. Allen, T. Thompson, J. Sakamoto, C. R. Becker, T. R. Jow and J. Wolfenstine, *J. Power Sources*, 2014, **254**, 204–208.
- 4 M. E. Rabanal, M. C. Gutierrez, F. Garcia-Alvarado, E. C. Gonzalo and M. E. Arroyo-de Dompablo, *J. Power Sources*, 2006, **160**, 523–528.
- 5 M. Prabu, S. Selvasekarapandian, A. R. Kulkarni, S. Karthikeyan, G. Hirankumar and C. Sanjeeviraja, *Solid State Sci.*, 2011, **13**, 1714–1718.
- 6 N. N. Bramnik, K. G. Bramnik, T. Buhrmester, C. Baehtz, H. Ehrenberg and H. Fuess, *J. Solid State Electrochem.*, 2004, **8**, 558–564.
- 7 S. Brutti, J. Manzi, A. De Bonis, D. Di Lecce, F. Vitucci, A. Paolone, F. Trequattrini and S. Panero, *Mater. Lett.*, 2015, **145**, 324–327.
- 8 J. Wang and X. Sun, *Energy Environ. Sci.*, 2015, **8**, 1110–1138.
- 9 K. J. Kreder, G. Assat and A. Manthiram, *Chem. Mater.*, 2016, **28**, 1847–1853.
- 10 F. Wang, J. Yang, Y. Nuli and J. Wang, *J. Power Sources*, 2010, **195**, 6884–6887.
- 11 S. Brutti, J. Manzi, D. Meggiolaro, F. M. Vitucci, F. Trequattrini, A. Paolone and O. Palumbo, *J. Mater. Chem. A*, 2017, **5**, 14020–14030.
- 12 J. L. Allen, T. R. Jow and J. Wolfenstine, *J. Power Sources*, 2011, **196**, 8656–8661.
- 13 H. Li, Y. Wang, X. Yang, L. Liu, L. Chen and J. Wei, *Solid State Ionics*, 2014, **255**, 84–88.
- 14 J. L. Allen, J. L. Allen, T. Thompson, S. A. Delp, J. Wolfenstine and T. R. Jow, *J. Power Sources*, 2016, **327**, 229–234.
- 15 Y.-M. Kang, Y.-I. Kim, M.-W. Oh, R.-Z. Yin, Y. Lee, D.-W. Han, H.-S. Kwon, J. H. Kim and G. Ramanath, *Energy Environ. Sci.*, 2011, **4**, 4978–4983.
- 16 F. C. Strobridge, D. S. Middlemiss, A. J. Pell, M. Leskes, R. J. Clément, F. Pourpoint, Z. Lu, J. V. Hanna, G. Pintacuda, L. Emsley, A. Samoson and C. P. Grey, *J. Mater. Chem. A*, 2014, **2**, 11948–11957.
- 17 N. V. Kosova, O. A. Podgornova, E. T. Devyatkina, V. R. Podugolnikov and S. A. Petrov, *J. Mater. Chem. A*, 2014, **2**, 20697–20705.
- 18 D. Di Lecce, J. Manzi, F. M. Vitucci, A. De Bonis, S. Panero and S. Brutti, *Electrochim. Acta*, 2015, **185**, 17–27.
- 19 L. Fang, H. Zhang, Y. Zhang, L. Liu and Y. Wang, *J. Power Sources*, 2016, **312**, 101–108.
- 20 F. C. Strobridge, H. Liu, M. Leskes, O. J. Borkiewicz, K. M. Wiaderek, P. J. Chupas, K. W.

- Chapman and C. P. Grey, *Chem. Mater.*, 2016, **28**, 3676–3690.
- 21 M. V. V. M. S. Kishore and U. V. Varadaraju, *Mater. Res. Bull.*, 2005, **40**, 1705–1712.
 - 22 L. Dimesso, C. Spanheimer and W. Jaegermann, *J. Power Sources*, 2013, **243**, 668–675.
 - 23 L. Dimesso, C. Spanheimer and W. Jaegermann, *J. Alloys Compd.*, 2014, **582**, 69–74.
 - 24 L. Dimesso, D. Becker, C. Spanheimer and W. Jaegermann, *Prog. Solid State Chem.*, 2014, **42**, 184–190.
 - 25 V. Ramar and P. Balaya, *Phys. Chem. Chem. Phys.*, 2013, **15**, 17240.
 - 26 M. Memm, M. Koentje, P. Axmann and M. Wohlfahrt-Mehrens, *J. Power Sources*, 2015, **276**, 382–387.
 - 27 M. Köntje, M. Memm, P. Axmann and M. Wohlfahrt-Mehrens, *Prog. Solid State Chem.*, 2014, **42**, 106–117.
 - 28 T. Muraliganth and A. Manthiram, *J. Phys. Chem. C*, 2010, **114**, 15530–15540.
 - 29 J. Manzi, M. Curcio and S. Brutti, *Nanomaterials*, 2015, **5**, 2212–2230.
 - 30 A. Le Bail, *Powder Diffraction*, 2005, **20**, 316–326.
 - 31 B. H. Toby, *J. Appl. Crystallogr.*, 2001, **34**, 210–213.
 - 32 A. A. Coelho, *J. Appl. Crystallogr.*, 2000, **33**, 899–908.
 - 33 M. Morcrette, J. B. Leriche, S. Patoux, C. WURM and C. Masquelier, *Electrochem. Solid-State Lett.*, 2003, **6**, A80–A84.
 - 34 J. Rodríguez-Carvajal, *Physica B*, 1993, **192**, 55–69.
 - 35 C. A. J. Fisher, V. M. H. Prieto and M. S. Islam, *Chem. Mater.*, 2008, **20**, 5907–5915.
 - 36 J. Ludwig, J. Ludwig, C. Marino, C. Marino, D. Haering, C. Stinner, D. Haering, D. Nordlund, C. Stinner, D. Nordlund, M. M. Doeff, H. A. Gasteiger, M. M. Doeff, H. A. Gasteiger, T. Nilges and T. Nilges, *RSC Adv.*, 2016, **6**, 82984–82994.
 - 37 J. Ludwig, C. Marino, D. Haering, C. Stinner, H. A. Gasteiger and T. Nilges, *J. Power Sources*, 2017, **342**, 214–223.
 - 38 X. Qin, X. Wang, H. Xiang, J. Xie, J. Li and Y. Zhou, *J. Phys. Chem. C*, 2010, **114**, 16806–16812.
 - 39 M. G. Palmer, J. T. Frith, A. L. Hector, A. W. Lodge, J. R. Owen, C. Nicklin and J. Rawle, *Chem. Commun.*, 2016, **52**, 14169–14172.
 - 40 F. C. Strobridge, R. J. Clément, M. Leskes, D. S. Middlemiss, O. J. Borkiewicz, K. M. Wiaderek, K. W. Chapman, P. J. Chupas and C. P. Grey, *Chem. Mater.*, 2014, **26**, 6193–6205.
 - 41 M. Kaus, I. Issac, R. Heinzmann, S. Doyle, S. Mangold, H. Hahn, V. S. K. Chakravadhanula,

- C. Kübel, H. Ehrenberg and S. Indris, *J. Phys. Chem. C*, 2014, **118**, 17279–17290.
- 42 J. Billaud, G. Singh, A. R. Armstrong, E. Gonzalo, V. Roddatis, M. Armand, T. Rojo and P. G. Bruce, *Energy Environ. Sci.*, 2014, **7**, 1387–1391.
- 43 N. N. Bramnik, K. G. Bramnik, C. Baehtz and H. Ehrenberg, *J. Power Sources*, 2005, **145**, 74–81.
- 44 R. Sharabi, E. Markevich, V. Borgel, G. Salitra, G. Gershtinsky, D. Aurbach, G. Semrau, M. A. Schmidt, N. Schall and C. Stinner, *J. Power Sources*, 2012, **203**, 109–114.
- 45 E. Markevich, R. Sharabi, H. Gottlieb, V. Borgel, K. Fridman, G. Salitra, D. Aurbach, G. Semrau, M. A. Schmidt, N. Schall and C. Bruening, *Electrochem. Commun.*, 2012, **15**, 22–25.
- 46 A. Örnek, *J. Power Sources*, 2017, **356**, 1–11.
- 47 N. Laszczynski, A. Birrozzi, K. Maranski, M. Copley, M. E. Schuster and S. Passerini, *J. Mater. Chem. A*, 2016, **4**, 17121–17128.
- 48 A. Eftekhari, *J. Electrochem. Soc.*, 2004, **151**, A1456–A1460.
- 49 H. Zhao, L. Gao, W. Qiu and X. Zhang, *J. Power Sources*, 2004, **132**, 195–200.
- 50 Y. Orikasa, D. Takamatsu, K. Yamamoto, Y. Koyama, S. Mori, T. Masese, T. Mori, T. Minato, H. Tanida, T. Uruga, Z. Ogumi and Y. Uchimoto, *Adv. Mater. Interfaces*, 2014, **1**, 1400195–1400202.
- 51 J.-H. Shim, S. Lee and S. S. Park, *Chem. Mater.*, 2014, **26**, 2537–2543.

5. P3-type magnesium doped sodium manganese oxide

5.1. Introduction

Since the redox reaction of oxygen ions was revealed as an alternative approach to increase the capacity of Li-rich layered oxides, extensive studies have been carried out to establish the mechanism of oxygen redox processes in LIBs. The knowledge gained from LIB research has been translated to SIBs. Several studies on P2-type sodium manganese based oxides ($\text{Na}_x\text{M}_y\text{Mn}_{1-y}\text{O}_2$ where $x \approx 0.7$ and $\text{M} = \text{Li, Mg, Fe, Ni, Zn}$ and mixtures of elements) have shown the participation of oxygen ions in the redox processes.¹⁻⁷ Although P3-type sodium manganese oxides are more environmentally friendly due to the lower sintering temperature than P2-type compounds, only very few recent studies on P3-type $\text{Na}_x\text{M}_y\text{Mn}_{1-y}\text{O}_2$ (where $x \approx 0.7$ and $\text{M} = \text{Li, Mg}$) have suggested the contribution of oxygen ions.⁸⁻¹⁰ There are many open questions regarding the fundamental understanding of these P3-type materials including electrochemical performance, structural evolution, surface changes and the charge compensation mechanism.

This chapter will detail the synthesis and characterisation of P3-type $\text{Na}_{0.67}\text{Mg}_{0.2}\text{Mn}_{0.8}\text{O}_2$ annealed under air and oxygen. The abnormally high capacity observed on the first charge is thoroughly investigated using PXRD, XAS and XPS. The participation of oxygen ions in the initial charge compensation mechanism is proposed.

5.2. Experimental method

The particular procedures and conditions relevant to the work presented in this chapter are presented below.

5.2.1. Synthesis of P3-type $\text{Na}_{0.67}\text{Mg}_{0.2}\text{Mn}_{0.8}\text{O}_2$ materials

A stoichiometric amount of sodium carbonate (Na_2CO_3 , Fisher Chemistry, $\geq 99.5\%$) was dissolved in deionised water (solution A). A separate aqueous solution of magnesium acetate tetrahydrate ($\text{Mg}(\text{CH}_3\text{CO}_2)_2 \cdot 4\text{H}_2\text{O}$, Sigma-Aldrich, 99%) and manganese (II) acetate tetrahydrate ($\text{Mn}(\text{CH}_3\text{CO}_2)_2 \cdot 4\text{H}_2\text{O}$, Sigma-Aldrich, $\geq 99\%$) was prepared (solution B). Solution A was added dropwise to solution B under stirring then stirred for 15 min. The water was removed using a rotary evaporator. The resulting solid was heated to $300\text{ }^\circ\text{C}$ for 12 h and cooled to $50\text{ }^\circ\text{C}$. Then, the powder was ground and heated again to $625\text{ }^\circ\text{C}$ for 3 h under air and quenched; the obtained sample is denoted Air- $\text{Na}_{0.67}\text{Mg}_{0.2}\text{Mn}_{0.8}\text{O}_2$. Alternatively, the decomposed powder was ground and heated to $625\text{ }^\circ\text{C}$ for 3 h under oxygen then cooled to $50\text{ }^\circ\text{C}$ to obtain Oxygen- $\text{Na}_{0.67}\text{Mg}_{0.2}\text{Mn}_{0.8}\text{O}_2$.

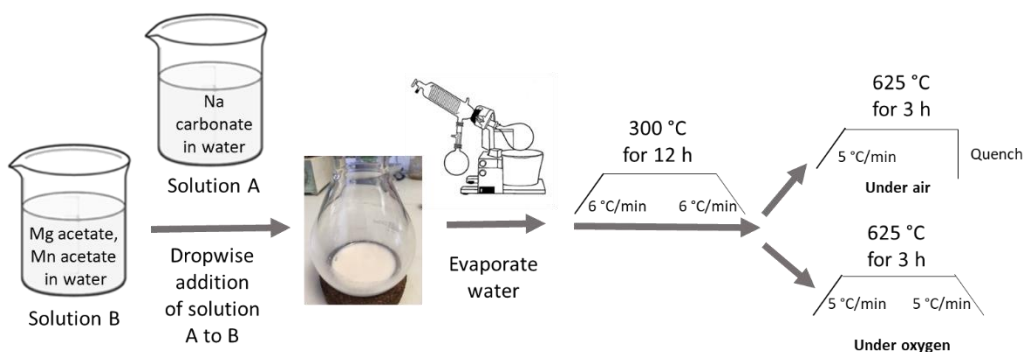


Figure 5.1. Schematic illustration of synthesis procedure.

5.2.2. Analyses and characterisation of as-synthesised materials

PXRD patterns of as-synthesised compounds were recorded on a PANalytical Empyrean diffractometer in Bragg-Brentano geometry with $\text{Cu K}\alpha_1$ radiation ($\lambda = 1.5406\text{ \AA}$). Lattice parameters were obtained by the Le Bail method¹¹ using the GSAS package with the EXPGUI interface.¹²

SEM images of as-synthesised materials were recorded on a JEOL JSM-6700F.

ICP-OES analysis was performed using a PerkinElmer Optima 8300 at Yonsei University and a iCAP 6000 Series for Air- $\text{Na}_{0.67}\text{Mg}_{0.2}\text{Mn}_{0.8}\text{O}_2$ and Oxygen- $\text{Na}_{0.67}\text{Mg}_{0.2}\text{Mn}_{0.8}\text{O}_2$, respectively.

Mn K-edge XAS spectra were collected in transmission mode at the beamline B18 at the Diamond Light source. Reference spectra were collected for each measurement using Mn metal foil. At least three scans were taken for each sample and the data were merged, calibrated, background subtracted and normalised using the program Athena.

XPS analysis for Air- $\text{Na}_{0.67}\text{Mg}_{0.2}\text{Mn}_{0.8}\text{O}_2$ was performed at the Ångström laboratory of Uppsala University. The measurements were carried out using a PHI 5500 system with monochromatic aluminium K_α X-ray source ($E_{\text{photon}} = 1487 \text{ eV}$). The obtained data were plotted using the software Igor Pro 6.34A. All peaks were calibrated based on the hydrocarbon species C 1s peak at 285 eV.

5.2.3. Preparation of electrodes

To evaluate electrochemical performance of the materials, slurries were prepared using the active material (Air- $\text{Na}_{0.67}\text{Mg}_{0.2}\text{Mn}_{0.8}\text{O}_2$ or Oxygen- $\text{Na}_{0.67}\text{Mg}_{0.2}\text{Mn}_{0.8}\text{O}_2$), super C65 carbon and Solef 5130 binder (a modified PVDF) in the mass ratio 75: 15: 10 in *n*-methyl-2-pyrrolidone, which was then cast on aluminium foil using a doctor blade. After drying, 12 mm diameter electrode discs were punched then dried at 80 °C under vacuum for 12 h.

To prepare electrochemically cycled Air- $\text{Na}_{0.67}\text{Mg}_{0.2}\text{Mn}_{0.8}\text{O}_2$ and Oxygen- $\text{Na}_{0.67}\text{Mg}_{0.2}\text{Mn}_{0.8}\text{O}_2$ for *ex-situ* characterisation, working electrodes were constructed by mixing the active material (Air- $\text{Na}_{0.67}\text{Mg}_{0.2}\text{Mn}_{0.8}\text{O}_2$ or Oxygen- $\text{Na}_{0.67}\text{Mg}_{0.2}\text{Mn}_{0.8}\text{O}_2$) and super C65 carbon in the mass ratio 75: 25. The mixture was dried at 110 °C under vacuum for 12 h.

5.2.4. Preparation of cells

CR2325 coin cells were assembled in an Ar-filled glovebox and used for evaluation of electrochemical performance. The cells consisted of a disc electrode, sodium metal as a counter/reference electrode, a glass fibre separator (Whatman, GF/F) and the electrolyte (1M NaClO_4 in propylene carbonate containing 3% fluoroethylene carbonate by weight).

For *ex-situ* XPS for Air- $\text{Na}_{0.67}\text{Mg}_{0.2}\text{Mn}_{0.8}\text{O}_2$, CR2325 coin cells were assembled as described above except that Solupor membranes replaced the glass fibre separator.

For all *ex-situ* measurements except the XPS, Swagelok-type cells were assembled in an Ar-filled glovebox. The cells consisted of a desired amount of working electrode, consisted of 75wt% active material and 25wt% super C65 with no binder, sodium metal as a

counter/reference electrode, glass fibre separators (Whatman, GF/F) and the electrolyte (1M NaClO₄ in propylene carbonate containing 3% fluoroethylene carbonate by weight).

Galvanostatic charge/discharge cycling and voltage scans (linear sweep voltammetry) were carried out at 30 °C using a Maccor Series 4200 battery cycler.

5.2.5. Analyses and characterisation of *ex-situ* samples

For all *ex-situ* measurements, cycled cells were transferred to an Ar-filled glovebox before opening and the active material was extracted. The electrodes were rinsed carefully with dry dimethyl carbonate to remove residual electrolyte and then left under vacuum for 12 h to ensure all solvent had evaporated.

PXRD patterns of pristine and cycled materials were collected on a STOE STADI/P diffractometer operating in transmission mode with Fe K α_1 radiation ($\lambda = 1.936 \text{ \AA}$) or on a PANalytical Empyrean diffractometer operating in transmission mode with Mo K α radiation ($\lambda = 0.7107 \text{ \AA}$). Samples were contained in 0.7 mm glass capillaries. Structures were refined by the Rietveld method using the GSAS package with the EXPGUI interface¹² or Topas Academic.¹³

ICP-OES, XAS and XPS measurements for cycled samples were carried out as described above.

5.3. Results and discussion

5.3.1. Characterisation of as-synthesised compounds

PXRD patterns of as-synthesised Air- $\text{Na}_{0.67}\text{Mg}_{0.2}\text{Mn}_{0.8}\text{O}_2$ and Oxygen- $\text{Na}_{0.67}\text{Mg}_{0.2}\text{Mn}_{0.8}\text{O}_2$ were recorded with Cu $\text{K}\alpha_1$ radiation ($\lambda = 1.5406 \text{ \AA}$). The major Bragg diffraction peaks of the PXRD patterns of both samples can be indexed on the basis of a P3 structural model (space group $R3m$, Fig. 5.2a), where Na ions occupy trigonal prismatic sites while Mg and Mn ions are located in the octahedral sites in ABBCA oxygen stacking. However, the small peaks around $20\text{--}25^\circ$ are unindexed as highlighted by the blue circle in Fig. 5.2c and e for Air- $\text{Na}_{0.67}\text{Mg}_{0.2}\text{Mn}_{0.8}\text{O}_2$ and Oxygen- $\text{Na}_{0.67}\text{Mg}_{0.2}\text{Mn}_{0.8}\text{O}_2$, respectively. Similar characteristic peaks have been reported for P2- and P3-type materials and typically arise from ordering in the transition metal layers. These peaks can be indexed on the basis of a super-lattice model of $\sqrt{3}a_{\text{hex}} \times \sqrt{3}b_{\text{hex}}$ (space group $C2/m$, Fig. 5.2b), in which Mg ions are in the centre of a honeycomb arrangement surrounded by Mn ions (Fig. 5.2d and f). Due to the broad peaks, probably caused by small particle size, refinement was carried out using the Le Bail method and its results are summarised in Table.5.1.

Table 5.1. Le Bail refinement results for as-synthesised Air- $\text{Na}_{0.67}\text{Mg}_{0.2}\text{Mn}_{0.8}\text{O}_2$ and Oxygen- $\text{Na}_{0.67}\text{Mg}_{0.2}\text{Mn}_{0.8}\text{O}_2$ using two different P3-type structure models.

	Space Group	Le Bail refinement results	χ^2	R_{wp}
Air- $\text{Na}_{0.67}\text{Mg}_{0.2}\text{Mn}_{0.8}\text{O}_2$	$R3m$ (Hexagonal setting)	$a=b=2.8817(19) \text{ \AA}$, $c=16.8400(68) \text{ \AA}$	2.07	4.56%
	$C2/m$	$a=4.9923(69) \text{ \AA}$, $b=8.6307(78) \text{ \AA}$, $c=6.5088(69) \text{ \AA}$, $\beta=120.44(8)$	1.33	3.65%
Oxygen- $\text{Na}_{0.67}\text{Mg}_{0.2}\text{Mn}_{0.8}\text{O}_2$	$R3m$ (Hexagonal setting)	$a=b=2.8829(14) \text{ \AA}$, $c=16.8309(47) \text{ \AA}$	1.53	3.24%
	$C2/m$	$a=4.9969(60) \text{ \AA}$, $b=8.6406(65) \text{ \AA}$, $c=6.5147(56) \text{ \AA}$, $\beta=120.50(7)$	1.46	3.16%

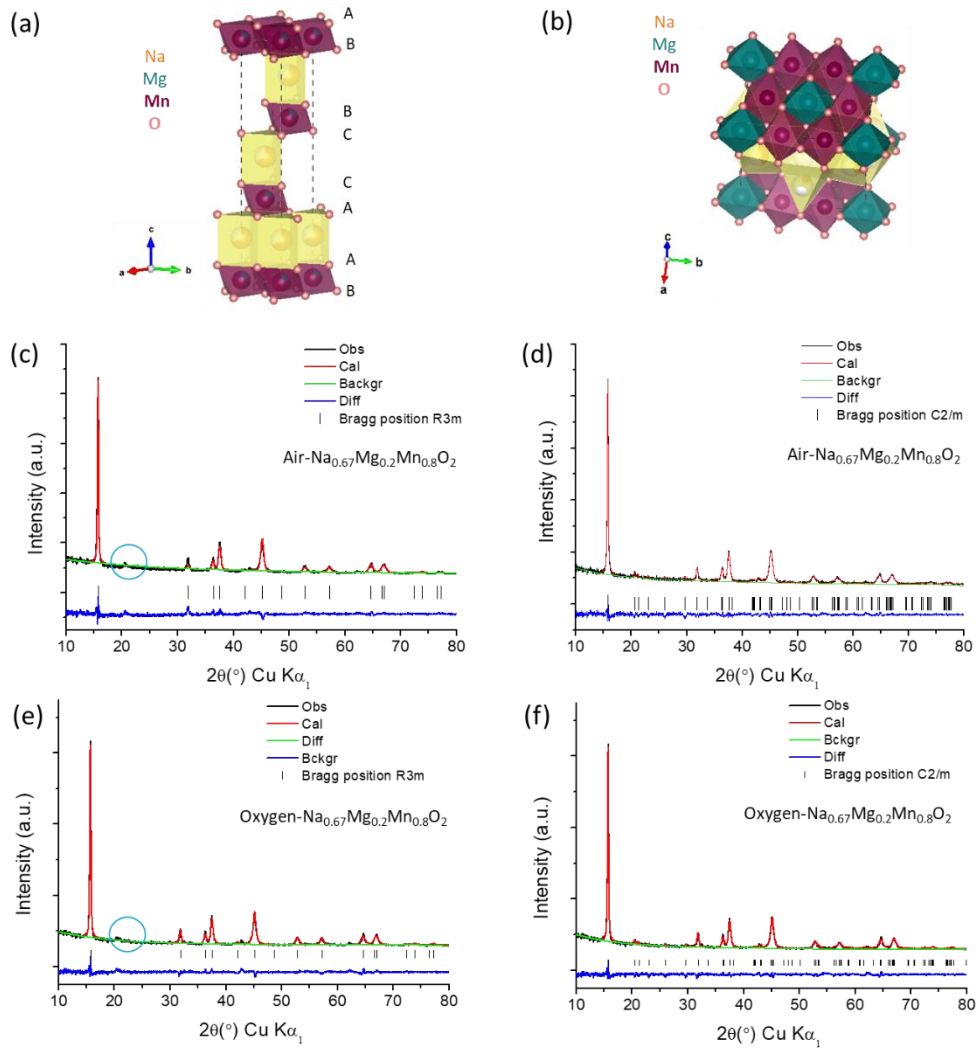


Figure 5.2. Schematic structures of (a) R3m and (b) C2/m. Profile fits for Le Bail refinement of as-synthesised (c) $\text{Air-Na}_{0.67}\text{Mg}_{0.2}\text{Mn}_{0.8}\text{O}_2$, (d) $\text{Air-Na}_{0.67}\text{Mg}_{0.2}\text{Mn}_{0.8}\text{O}_2$ using the space group of R3m and C2/m, respectively and as-synthesised (e) $\text{Oxygen-Na}_{0.67}\text{Mg}_{0.2}\text{Mn}_{0.8}\text{O}_2$, (f) $\text{Oxygen-Na}_{0.67}\text{Mg}_{0.2}\text{Mn}_{0.8}\text{O}_2$ using the space group R3m and C2/m, respectively. Observed data points are shown in black, with fitted profile in red and the difference is shown in blue. Tic marks indicate allowed reflections. Blue circle highlights super-lattice peaks.

Tentative Rietveld refinements were performed based on the space group of R3m whilst fixing Mg occupancy but varying Mn occupancy are presented in Table 5.2 and Fig. 5.3. The refinement results show that lattice parameters are consistent with those obtained from the Le Bail method, as well as hinting at greater presence of vacancies in Mn sites for $\text{Oxygen-Na}_{0.67}\text{Mg}_{0.2}\text{Mn}_{0.8}\text{O}_2$ (9%) rather than $\text{Air-Na}_{0.67}\text{Mg}_{0.2}\text{Mn}_{0.8}\text{O}_2$ (3%).

Table 5.2. Rietveld refinement results of (a) pristine Air- $\text{Na}_{0.67}\text{Mg}_{0.2}\text{Mn}_{0.8}\text{O}_2$, (b) Air- $\text{Na}_{0.67}\text{Mg}_{0.2}\text{Mn}_{0.8}\text{O}_2$ refined by Dr. A. Robert Armstrong.

(a) Air- $\text{Na}_{0.67}\text{Mg}_{0.2}\text{Mn}_{0.8}\text{O}_2$						
$R_{\text{exp}} : 3.14\% R_{\text{wp}} : 3.35\%$						
Lattice parameters P3 Space group $R3m$ $a = b = 2.8817(12) \text{ \AA}$ $c = 16.844(8) \text{ \AA}$						
atom	Wyckoff symbol	x/a	y/b	z/c	Occupancy	Biso
Mn1/Mg1	3a	0	0	0	0.77(4)/0.2	0.35(15)
Na1	3a	0	0	0.1629(9)	0.50(2)	4.1(9)
O1	3a	0	0	0.3788(9)	1	2.5(7)
O2	3a	0	0	0.5963(10)	1	2.5(7)

(b) Oxygen- $\text{Na}_{0.67}\text{Mg}_{0.2}\text{Mn}_{0.8}\text{O}_2$						
$R_{\text{exp}} : 2.61\% R_{\text{wp}} : 3.11\%$						
Lattice parameters P3 Space group $R3m$ $a = b = 2.8819(2) \text{ \AA}$ $c = 16.829(2) \text{ \AA}$						
atom	Wyckoff symbol	x/a	y/b	z/c	Occupancy	Biso
Mn1/Mg1	3a	0	0	0	0.71(4)/0.2	0.20(14)
Na1	3a	0	0	0.1609(8)	0.62(2)	6.3(8)
O1	3a	0	0	0.3942(10)	1	3.1(7)
O2	3a	0	0	0.6152(9)	1	3.1(7)

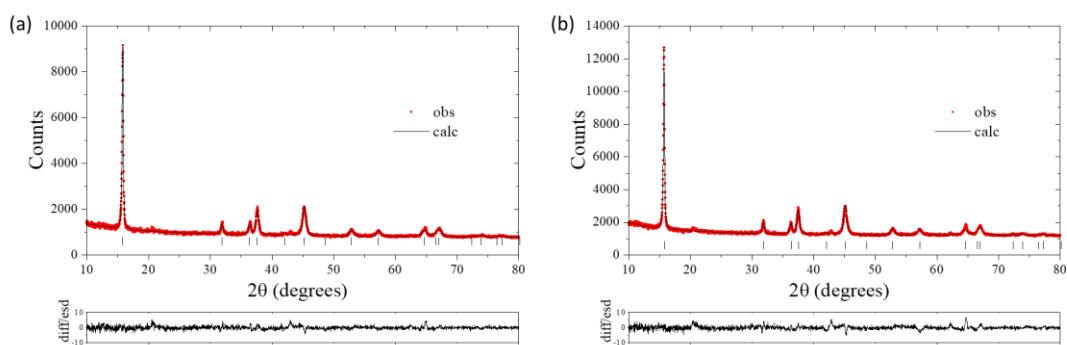


Figure 5.3. Rietveld refined patterns of as-synthesised (a) Air- $\text{Na}_{0.67}\text{Mg}_{0.2}\text{Mn}_{0.8}\text{O}_2$ and (b) Oxygen- $\text{Na}_{0.67}\text{Mg}_{0.2}\text{Mn}_{0.8}\text{O}_2$ (refined by Dr. A. Robert Armstrong). Observed data points are shown in red, with fitted profile in black and the difference is shown in the lower line. Tick marks indicate allowed reflections for the P3 phase.

The morphology of as-synthesised Air- $\text{Na}_{0.67}\text{Mg}_{0.2}\text{Mn}_{0.8}\text{O}_2$ and Oxygen- $\text{Na}_{0.67}\text{Mg}_{0.2}\text{Mn}_{0.8}\text{O}_2$ was characterised by SEM. Both materials consist of primary particles around 100 nm fused together (Fig. 5.4).

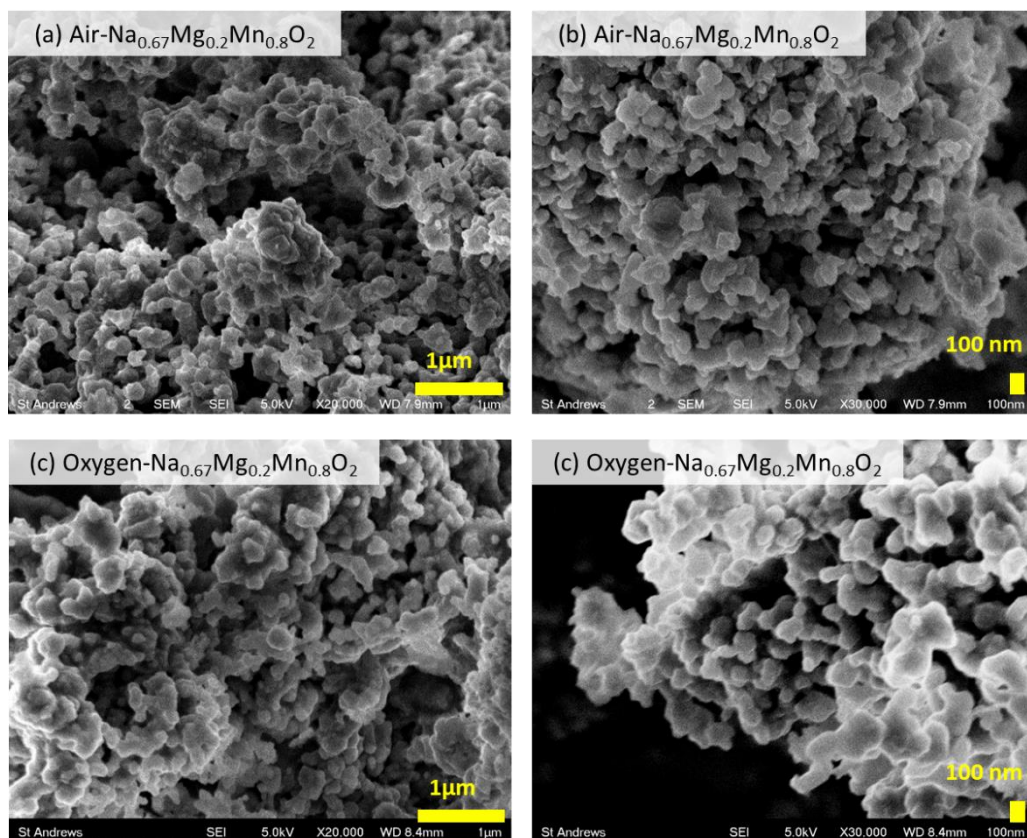


Figure 5. 4. SEM images of as-synthesised (a, b) $\text{Air-Na}_{0.67}\text{Mg}_{0.2}\text{Mn}_{0.8}\text{O}_2$ and (c,d) $\text{Oxygen-Na}_{0.67}\text{Mg}_{0.2}\text{Mn}_{0.8}\text{O}_2$.

The stoichiometry of the as-synthesised compounds was determined by ICP-OES and the formula of $\text{Air-Na}_{0.67}\text{Mg}_{0.19}\text{Mn}_{0.8}\text{O}_2$ (normalised to Mn) and $\text{Oxygen-Na}_{0.62}\text{Mg}_{0.21}\text{Mn}_{0.8}\text{O}_2$ (normalised to Mn) were obtained.

5.3.2. Electrochemical properties

Electrodes with either P3-type $\text{Na}_{0.67}\text{Mg}_{0.2}\text{Mn}_{0.8}\text{O}_2$ synthesised under air or oxygen were prepared and the assembled coin cells were tested. Fig. 5.5a shows the galvanostatic cycling performance of $\text{Air-Na}_{0.67}\text{Mg}_{0.2}\text{Mn}_{0.8}\text{O}_2$ cycled over two different voltage windows. The material cycled between 1.8 and 3.8 V exhibits stable cycling performance, retaining 95% of its initial discharge capacity after 25 cycles. In contrast, the compound cycled between 1.8 and 4.3 V suffers from capacity fade, resulting in the capacity retention of 80% after 25 cycles. It is worth pointing out that the sample charged to 4.3 V delivers a first charge capacity of 124 mAh g^{-1} , which is significantly higher than the theoretical value of 70 mAh g^{-1} , calculated based on the $\text{Mn}^{3+}/\text{Mn}^{4+}$ redox process. Similarly, $\text{Oxygen-Na}_{0.67}\text{Mg}_{0.2}\text{Mn}_{0.8}\text{O}_2$ cycled in the narrower voltage window demonstrates better cyclability, maintaining 96% of its initial discharge capacity whereas the material charged to 4.3 V exhibits capacity retention of 82%

after 25 cycles (Fig. 5.5b). This compound also delivers higher first charge capacity than the value expected solely from the $\text{Mn}^{3+}/\text{Mn}^{4+}$ redox reaction. Note that the first charge capacity for both materials is less than that of the discharge, as is typical for Na deficient oxides. The extraordinary charge capacities on the first cycle will be discussed in section 5.3.7.

Plots of the differential capacity versus voltage collected on cycling both Air- $\text{Na}_{0.67}\text{Mg}_{0.2}\text{Mn}_{0.8}\text{O}_2$ and Oxygen- $\text{Na}_{0.67}\text{Mg}_{0.2}\text{Mn}_{0.8}\text{O}_2$ in the potential range 1.8-3.8 V are shown in Fig. 5.5c and d, respectively. As Mg is substituted for Mn, a number of sharp and low intensity peaks resulting from the Jahn-Teller activity of Mn^{3+} ions disappear for both samples as previously reported for P2 type Mg-doped $\text{Na}_{0.67}\text{Mg}_x\text{Mn}_{1-x}\text{O}_2$ ($0 \leq x \leq 0.2$).^{14,15} In the case of Air- $\text{Na}_{0.67}\text{Mg}_{0.2}\text{Mn}_{0.8}\text{O}_2$, two oxidation peaks at ca. 2.1 and 2.3 V and two reduction peaks at around 1.9 and 2.1 V are present at the second cycle and remain on subsequent cycles (Fig. 5.5c). Interestingly, the sharp peaks in the lowest voltage region considerably diminish for Oxygen- $\text{Na}_{0.67}\text{Mg}_{0.2}\text{Mn}_{0.8}\text{O}_2$ (Fig. 5.5d). It is known that P3-type compounds tend to transform to the O3 structure when the occupancy of Na ions is close to 1,¹⁶ it is therefore reasonable to assume that the intense peaks found in Air- $\text{Na}_{0.67}\text{Mg}_{0.2}\text{Mn}_{0.8}\text{O}_2$ originate from the structural change from P3 to O3. In the case of Oxygen- $\text{Na}_{0.67}\text{Mg}_{0.2}\text{Mn}_{0.8}\text{O}_2$, the presence of vacancies in the transition metal slabs may stabilise the P3 structure during sodiation since vacancies on the transition metal sites are able to carry effective negative charge.¹⁷ Structural analysis confirms that less phase transformation to an O'3 phase (prime indicates a monoclinic distorted phase) is found in Oxygen- $\text{Na}_{0.67}\text{Mg}_{0.2}\text{Mn}_{0.8}\text{O}_2$ (see section 5.3.4).

When the samples were charged to 4.3 V, new oxidation peaks appear at ca. 4.15 and 4.22 V at the first cycle for both compounds. In the plot of Air- $\text{Na}_{0.67}\text{Mg}_{0.2}\text{Mn}_{0.8}\text{O}_2$ (Fig. 5.5e), the two peaks overlap and significantly decrease at the second cycle. As there is no charge compensation by oxidation of Mn^{3+} in this voltage region, shown in Mn K-edge spectra (section 5.3.5), the new peaks may represent oxygen redox along with electrolyte decomposition and/or phase transition. In the case of Oxygen- $\text{Na}_{0.67}\text{Mg}_{0.2}\text{Mn}_{0.8}\text{O}_2$, two different phenomena are distinguishable owing to the clear peak split (Fig. 5.5f). The irreversible oxidation peak at around 4.15 V can be attributed to the electrolyte decomposition and/or phase transition. The oxidation peak at about 4.22 V is reversible with the reduction peak at ca. 4.20 V on subsequent cycles and this redox couple, which is probably associated with the oxygen redox, is preserved until 25 cycles. Another interesting feature found in the samples cycled between 1.8-4.3 V is the disappearance of oxidation and

reduction peaks at 2.1 and 1.9 V, respectively. Since the activation of oxygen redox concurrently induces the rearrangements in both electronic and crystal structures, this observation may be a further indicator of oxygen redox in both materials.

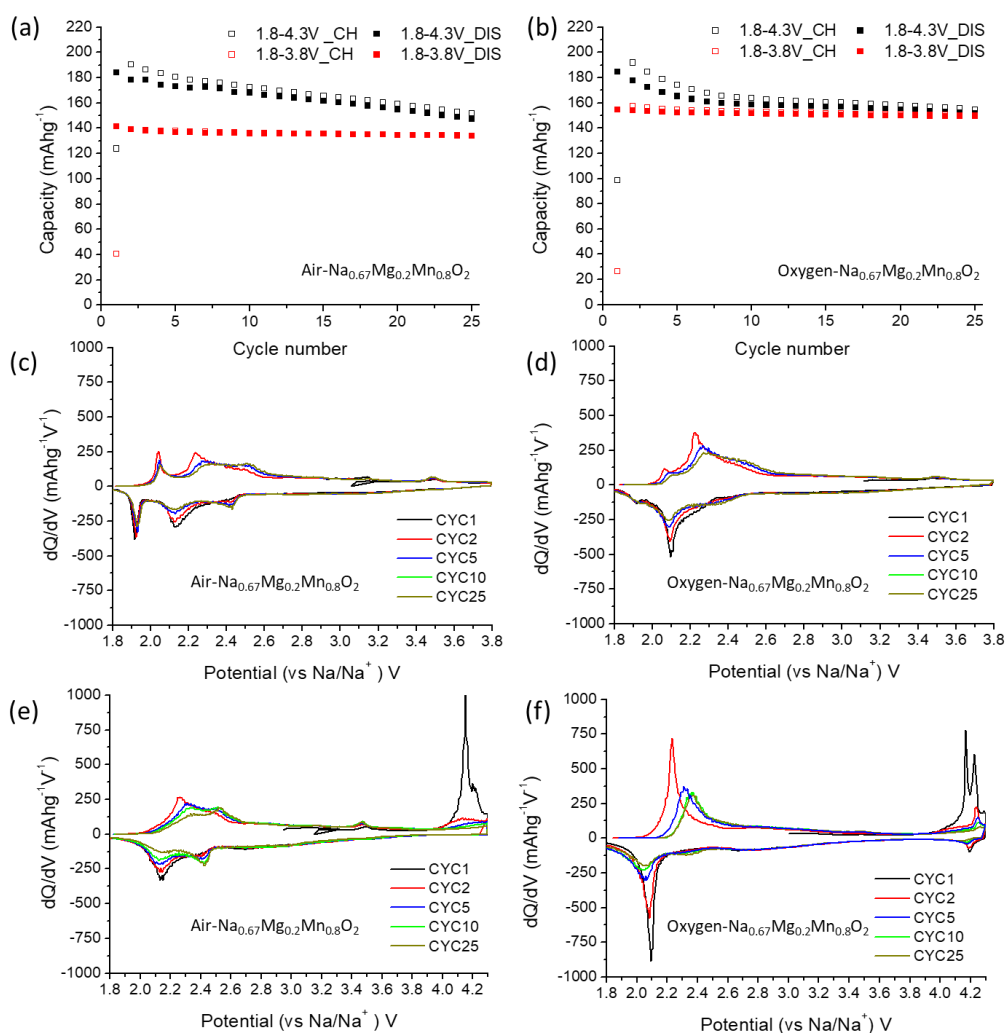


Figure 5.5. Galvanostatic cycling performance of (a) Air-Na_{0.67}Mg_{0.2}Mn_{0.8}O₂ and (b) Oxygen-Na_{0.67}Mg_{0.2}Mn_{0.8}O₂ cycled at 30°C between 1.8 and 3.8 V in red and 1.8 and 4.3 V in black at a rate of 10 mA g⁻¹. Empty and full squares represent charge and discharge capacity, respectively. Differential capacity vs. voltage plots corresponding to cycle 1 (black), cycle 2 (red), cycle 5 (blue), cycle 10 (green) and cycled 25 (dark yellow) for (c) Air-Na_{0.67}Mg_{0.2}Mn_{0.8}O₂, (d) Oxygen-Na_{0.67}Mg_{0.2}Mn_{0.8}O₂ cycled between 1.8 and 3.8 V and for (e) Air-Na_{0.67}Mg_{0.2}Mn_{0.8}O₂, (f) Oxygen-Na_{0.67}Mg_{0.2}Mn_{0.8}O₂ cycled between 1.8 and 4.3 V.

The electrochemical properties of Air-Na_{0.67}Mg_{0.2}Mn_{0.8}O₂ were further investigated, varying current rates and voltage windows. First, rate performance of Air-Na_{0.67}Mg_{0.2}Mn_{0.8}O₂ was evaluated, fixing the voltage window as 1.8-3.8 V. As revealed in Fig. 5.6a, excellent capacity retention is shown at rates of 10, 50 and 200 mA g⁻¹, while the capacity retention after 50

cycles is only 53% at a rate of 500 mA g^{-1} . As the rate increases from the slow regimes (10 and 50 mA g^{-1}) to the faster regimes (200 and 500 mA g^{-1}), the discharge capacity decreases from 141 mAh g^{-1} to 107 mAh g^{-1} . This originates from incomplete sodiation at the first cycle (Fig. 5.6e), leading to the capacity fade at the fastest rate. Fig. 5.6c shows that at rates of 200 and 500 mA g^{-1} , the polarisation in the charge/discharge curves at the second cycle significantly increases in the lower voltage region where the P3-O'3 phase transformation occurs, as confirmed by *ex-situ* PXRD measurements (section 5.3.3). It has been reported that the O2 structure requires larger activation energy for Na ion diffusion compared to the P2 structure since the diffusion path of Na ions is more spacious in the P2 structure.^{3,18} The increased polarisation in Air- $\text{Na}_{0.67}\text{Mg}_{0.2}\text{Mn}_{0.8}\text{O}_2$ at faster rates might arise from the sluggish migration of Na ions in O'3 structure.

In general, phase changes during cycling cause poor cycling stability due to increased lattice stress. However, the phase transformation can yield an extra capacity.¹⁹ To determine the lowest voltage which permits reasonable cyclability and capacity gain, Air- $\text{Na}_{0.67}\text{Mg}_{0.2}\text{Mn}_{0.8}\text{O}_2$ electrodes were cycled over different voltage windows at a rate of 200 mA g^{-1} . As shown in Fig. 5.6b, initial discharge capacity increases when the sample is cycled in a wider voltage window at the expense of cycling stability. Notable capacity drops appear when the material is discharged to 1.6 and 1.5 V , whereas the lower cut-off voltages of 1.8 V and 1.7 V allow the material to maintain its initial discharge capacity with a capacity retention of 92% over 60 cycles. In the Fig. 5.6d, polarisation is pronounced in the lower voltage region most probably due to the sluggish phase transformation. In the differential capacity versus voltage plots of the second cycle (Fig. 5.6f), the oxidation peaks around 2.5 V at the second cycle are slightly more intense when the sample is discharged to 1.6 and 1.5 V , in good agreement with the extended Mn reduction occurring on the previous cycle at wider voltage windows. This could lead to increased phase change to the O'3 structure with the concomitant degradation of the active material, delivering limited capacity after 60 cycles.

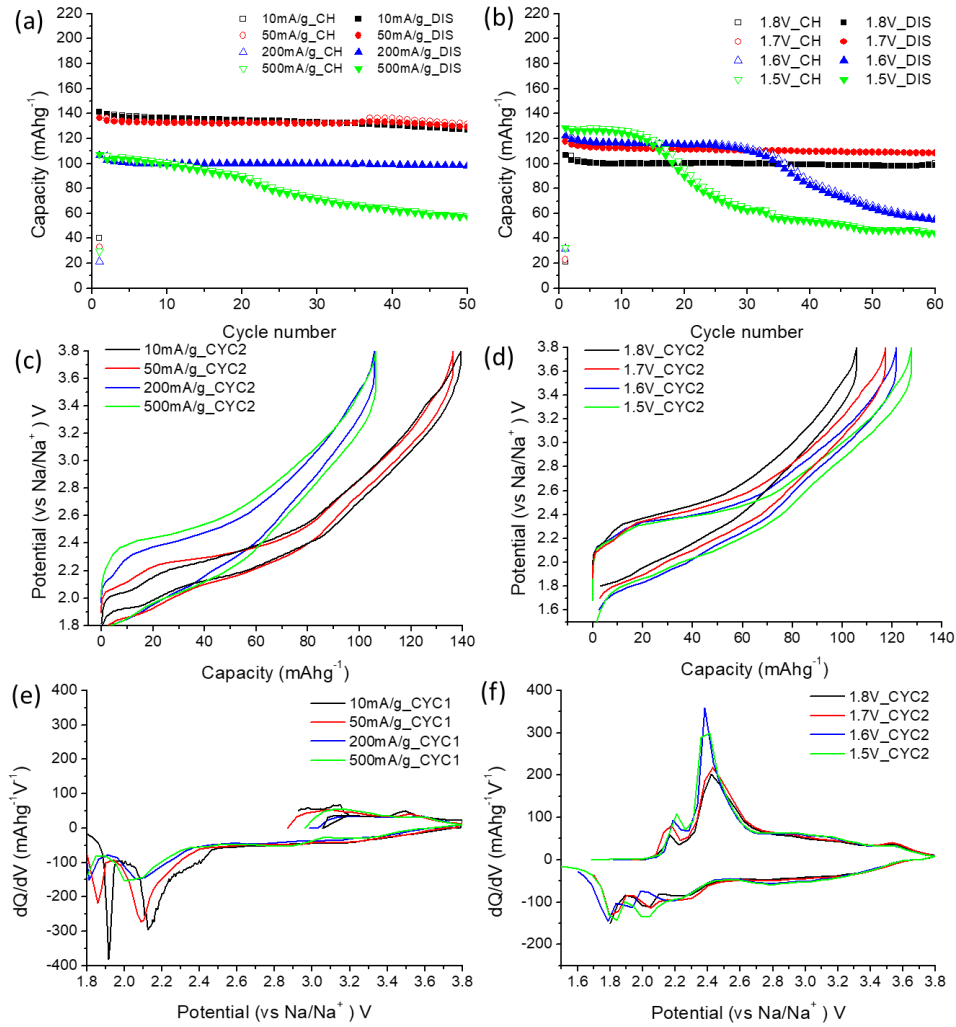


Figure 5.6. (a) Galvanostatic cycling performance of $\text{Air-Na}_{0.67}\text{Mg}_{0.2}\text{Mn}_{0.8}\text{O}_2$ cycled at 30°C between 1.8 and 3.8 V at a rate of 10 mA g^{-1} in black, 50 mA g^{-1} in red, 200 mA g^{-1} in blue and 500 mA g^{-1} in green. Empty and full symbols represent charge and discharge capacity, respectively, (c) Charge/discharge curves for the second cycle from (a), (e) Differential capacity vs. voltage plots for the first cycle from (a). (b) Galvanostatic cycling performance of $\text{Air-Na}_{0.67}\text{Mg}_{0.2}\text{Mn}_{0.8}\text{O}_2$ cycled at 30°C between 1.8 and 3.8 V in black, 1.7 and 3.8 V in red, 1.6 and 3.8 V in blue and 1.5 and 3.8 V in green at a rate of 200 mA g^{-1} . Empty and full symbols represent charge and discharge capacity, respectively, (d) Charge/discharge curves for the second cycle from (b), (f) Differential capacity vs. voltage plots for the second cycle from (b).

5.3.3. Structural evolution upon cycling for $\text{Air-Na}_{0.67}\text{Mg}_{0.2}\text{Mn}_{0.8}\text{O}_2$

To investigate structural changes in $\text{Air-Na}_{0.67}\text{Mg}_{0.2}\text{Mn}_{0.8}\text{O}_2$, *ex-situ* PXRD measurements were carried out for the samples extracted from cells at the end of charge and discharge cycled over two different voltage windows. The refined profile fits and results using Rietveld method are shown in Fig. 5.7 and Table. 5.3.

The PXRD patterns of pristine Air- $\text{Na}_{0.67}\text{Mg}_{0.2}\text{Mn}_{0.8}\text{O}_2$ (Fig. 5.7b) and that charged to 3.8 V (Fig. 5.7c) can be indexed on the P3-type structure with the space group $R3m$. Due to the presence of carbon, the superlattice peaks are barely visible. For the sample charged to 4.3 V, a new peak around 23° appears, which is associated with the O3 phase (Fig. 5.7d). Refined phase fractions of the P3 and O3 phases reveal that about 21% of the P3 phase is converted to the O3 phase. As presented in Table 5.3, during charge, the a lattice parameter, which is dominated by the in-plane metal-metal distances, decreases as expected from the oxidation of Mn^{3+} . On the other hand, the c lattice parameter increases on charging to 3.8 V then decreases on further charging to 4.3 V. The expanded c lattice parameter is caused by the increased electrostatic repulsion between oxygen layers without the screening effect of the Na ions. When further Na ions are removed from the structure, the slabs glide to minimise repulsions, resulting in O3 stacking with a shorter c lattice parameter. Song *et al.* reported that the P3-type $\text{Na}_{2/3}\text{Mg}_{1/3}\text{Mn}_{2/3}\text{O}_2$ is prone to transform to O3 structure upon charge above 4.0 V then the O3 phase remains upon subsequent discharge to 1.6 V rather than the undergoing reversible two-phase reaction from O3 to P3, causing poor electrochemical performance.¹⁰ In the case of Air- $\text{Na}_{0.67}\text{Mg}_{0.2}\text{Mn}_{0.8}\text{O}_2$, discharge to 1.8 V results in a major conversion to an O'3 phase with 12% and 19% of the P3 phase for the sample charged to 3.8 V and 4.3 V, respectively. Both samples show that the ratio between lattice parameters a and b (a/b) in the monoclinic lattice is 1.88, significantly greater than $\sqrt{3}$, indicating Jahn-Teller distortion.²⁰ For the material cycled in the voltage range 1.8-3.8 V, the phase transformation in the lower voltage region (P3 to O'3) is sufficiently reversible to deliver stable cycling performance at rates of 10, 50 and 200 mA g^{-1} .

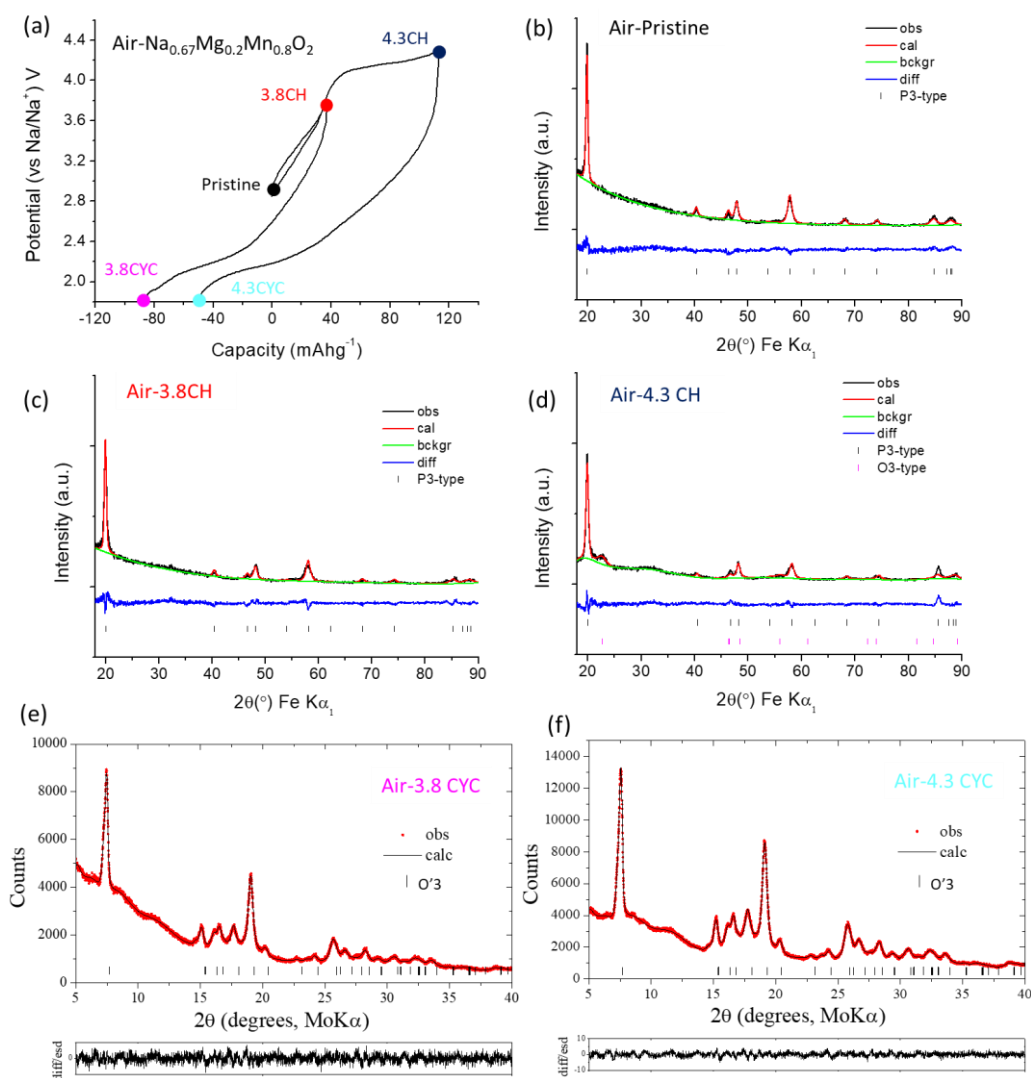


Figure 5.7. (a) Galvanostatic cycling curves recorded at 10 mA g^{-1} for $\text{Air-Na}_{0.67}\text{Mg}_{0.2}\text{Mn}_{0.8}\text{O}_2$ cycled between 1.8-3.8 V and 1.8-4.3 V with the points where PXRD and XAS measurements were conducted. Profile fits for Rietveld refinements of (b) pristine $\text{Air-Na}_{0.67}\text{Mg}_{0.2}\text{Mn}_{0.8}\text{O}_2$, (c) $\text{Air-Na}_{0.67}\text{Mg}_{0.2}\text{Mn}_{0.8}\text{O}_2$ charged to 3.8 V, (d) $\text{Air-Na}_{0.67}\text{Mg}_{0.2}\text{Mn}_{0.8}\text{O}_2$ charged to 4.3 V. Observed data points are shown in black, with fitted profile in red and the difference is shown in blue. Tic marks indicate allowed reflections. Profile fits for Rietveld refinements of (e) $\text{Air-Na}_{0.67}\text{Mg}_{0.2}\text{Mn}_{0.8}\text{O}_2$ cycled between 1.8-3.8 V and (f) $\text{Air-Na}_{0.67}\text{Mg}_{0.2}\text{Mn}_{0.8}\text{O}_2$ cycled between 1.8-4.3 V. Observed data points are shown in red, with fitted profile in black. Tick marks indicate allowed reflections for the O'3 phase. e and f are refined by Dr. A. Robert Armstrong.

Table 5.3. Rietveld refinement results of (a) pristine $\text{Air-Na}_{0.67}\text{Mg}_{0.2}\text{Mn}_{0.8}\text{O}_2$, (b) $\text{Air-Na}_{0.67}\text{Mg}_{0.2}\text{Mn}_{0.8}\text{O}_2$ charged to 3.8 V, (c) $\text{Air-Na}_{0.67}\text{Mg}_{0.2}\text{Mn}_{0.8}\text{O}_2$ charged to 4.3 V, (d) $\text{Air-Na}_{0.67}\text{Mg}_{0.2}\text{Mn}_{0.8}\text{O}_2$ cycled between 1.8-3.8 V and (e) $\text{Air-Na}_{0.67}\text{Mg}_{0.2}\text{Mn}_{0.8}\text{O}_2$ cycled between 1.8-4.3. d and e are refined by Dr. A. Robert Armstrong.

(a) Pristine $\text{Air-Na}_{0.67}\text{Mn}_{0.8}\text{Mg}_{0.2}\text{O}_2$						
χ^2 : 2.16% R_{wp} : 9.68% 100% P3						
Lattice parameters P3 Space group $R3m$ $a = b = 2.874(42)$ Å $c = 16.85(25)$ Å						
atom	Wyckoff symbol	x/a	y/b	z/c	Occupancy	Uiso
Mn1/Mg1	3a	0	0	0	0.8/0.2	0.0063
Na1	3a	0	0	0.167(9)	0.67	0.0152
O1	3a	0	0	0.390(14)	1	0.0076
O2	3a	0	0	0.607(12)	1	0.0076

(b) $\text{Air-Na}_x\text{Mn}_{0.8}\text{Mg}_{0.2}\text{O}_2$ charged to 3.8 V						
χ^2 : 2.18% R_{wp} : 10.92% 100% P3						
Lattice parameters P3 Space group $R3m$ $a = b = 2.863(53)$ Å $c = 16.88(26)$ Å						
atom	Wyckoff symbol	x/a	y/b	z/c	Occupancy	Uiso
Mn1/Mg1	3a	0	0	0	0.8/0.2	0.0063
Na1	3a	0	0	0.167(13)	0.55	0.0152
O1	3a	0	0	0.393(23)	1	0.0076
O2	3a	0	0	0.613(21)	1	0.0076

(c) $\text{Air-Na}_x\text{Mn}_{0.8}\text{Mg}_{0.2}\text{O}_2$ charged to 4.3 V						
χ^2 : 2.18% R_{wp} : 11.66% 79(2)% P3 21% O3						
Lattice parameters P3 Space group $R3m$ $a = b = 2.854(59)$ Å $c = 16.80(30)$ Å						
atom	Wyckoff symbol	x/a	y/b	z/c	Occupancy	Uiso
Mn1/Mg1	3a	0	0	0	0.8/0.2	0.0063
Na1	3a	0	0	0.149(31)	0.26	0.0152
O1	3a	0	0	0.408(14)	1	0.0076
O2	3a	0	0	0.623(13)	1	0.0076
Lattice parameters O3 Space group $R\bar{3}m$ $a = b = 2.832(49)$ Å $c = 14.87(28)$ Å						
Mn1/Mg1	3b	0	0	0	0.8/0.2	0.0063
Na1	3a	0	0	0.5	0.26	0.0152
O1	6c	0	0	0.281(21)	1	0.0076

(d) Air-Na_{0.67}Mg_{0.2}Mn_{0.8}O₂ cycled between 1.8-3.8 V						
R _{exp} : 2.03% R _{wp} : 2.65% 88(3)% O'3 12% P3						
Lattice parameters O'3 Space group <i>C2/m</i> <i>a</i> = 5.472(3) Å <i>b</i> = 2.904(2) Å <i>c</i> = 5.753(3) Å β = 110.10(3)°						
atom	Wyckoff symbol	x/a	y/b	z/c	Occupancy	Biso
Mn1/Mg1	2 <i>a</i>	0	0	0	0.8/0.2	0.5
Na1	2 <i>d</i>	0	0.5	0.5	0.903 (9)	1.2
O1	4 <i>i</i>	0.2694(13)	0	0.7959(12)	1	0.6
Lattice parameters P3 Space group <i>R3m</i> <i>a</i> = <i>b</i> = 2.897(3) Å <i>c</i> = 16.75(15) Å						
Mn1/Mg1	3 <i>a</i>	0	0	0	0.8/0.2	0.5
Na1	3 <i>a</i>	0	0	0.173(2)	0.74(8)	1.2
O1	3 <i>a</i>	0	0	0.381(11)	1	0.6
O2	3 <i>a</i>	0	0	0.613(8)	1	0.6

(e) Air-Na_{0.67}Mg_{0.2}Mn_{0.8}O₂ cycled between 1.8-4.3 V						
R _{exp} : 2.35% R _{wp} : 2.84% 81(2)% O'3 19% P3						
Lattice parameters O'3 Space group <i>C2/m</i> <i>a</i> = 5.446(12) Å <i>b</i> = 2.898(7) Å <i>c</i> = 5.737(9) Å β = 111.04(8)°						
atom	Wyckoff symbol	x/a	y/b	z/c	Occupancy	Biso
Mn1/Mg1	2 <i>a</i>	0	0	0	0.8/0.2	0.5
Na1	2 <i>d</i>	0	0.5	0.5	0.83 (2)	1.2
O1	4 <i>i</i>	0.278(3)	0	0.788(2)	1	0.6
Lattice parameters P3 Space group <i>R3m</i> <i>a</i> = <i>b</i> = 2.906(9) Å <i>c</i> = 16.62(10) Å						
Mn1/Mg1	3 <i>a</i>	0	0	0	0.8/0.2	0.5
Na1	3 <i>a</i>	0	0	0.166(4)	0.64(6)	1.2
O1	3 <i>a</i>	0	0	0.388(9)	1	0.6
O2	3 <i>a</i>	0	0	0.626(11)	1	0.6

5.3.4. Structural evolution upon cycling for Oxygen-Na_{0.67}Mg_{0.2}Mn_{0.8}O₂

Structural changes in Oxygen-Na_{0.67}Mg_{0.2}Mn_{0.8}O₂ were examined using *ex-situ* PXRD for the samples extracted at different states of charge. The profile fits for Rietveld refinements and the obtained crystallographic information are presented in Fig. 5.8 and Table. 5.4.

When the material is cycled between 1.8-3.8 V, major reflections at the end of discharge correspond to the O'3 phase (82%), analogous to Air-Na_{0.67}Mg_{0.2}Mn_{0.8}O₂. It is noteworthy that more P3 phase is preserved in Oxygen-Na_{0.67}Mg_{0.2}Mn_{0.8}O₂ (18%) than Air-Na_{0.67}Mg_{0.2}Mn_{0.8}O₂ (12%) at the end of discharge. The P3 to O'3 phase transformation occurs to minimise the

Coulombic repulsion between sodium and manganese cations.²¹ The presence of vacancies in the transition metal slabs is able to stabilise the trigonal prismatic coordination of NaO_6 via $\square\text{-Na}^+\text{-}\square$ Coulombic attraction. In consequence, Oxygen- $\text{Na}_{0.67}\text{Mg}_{0.2}\text{Mn}_{0.8}\text{O}_2$ with vacancies in the transition metal sites exhibits greater structural reversibility to P3 phase. The beneficial effect is considerable when the material is cycled in the voltage range 1.8-4.3 V. The *ex-situ* PXRD pattern of Oxygen- $\text{Na}_{0.67}\text{Mg}_{0.2}\text{Mn}_{0.8}\text{O}_2$ charged to 4.3 V reveals no phase transformation to the O3 structure. On the following discharge to 1.8 V, a significantly reduced phase transformation to O'3 phase (46%) is found with 54% P3 phase remaining.

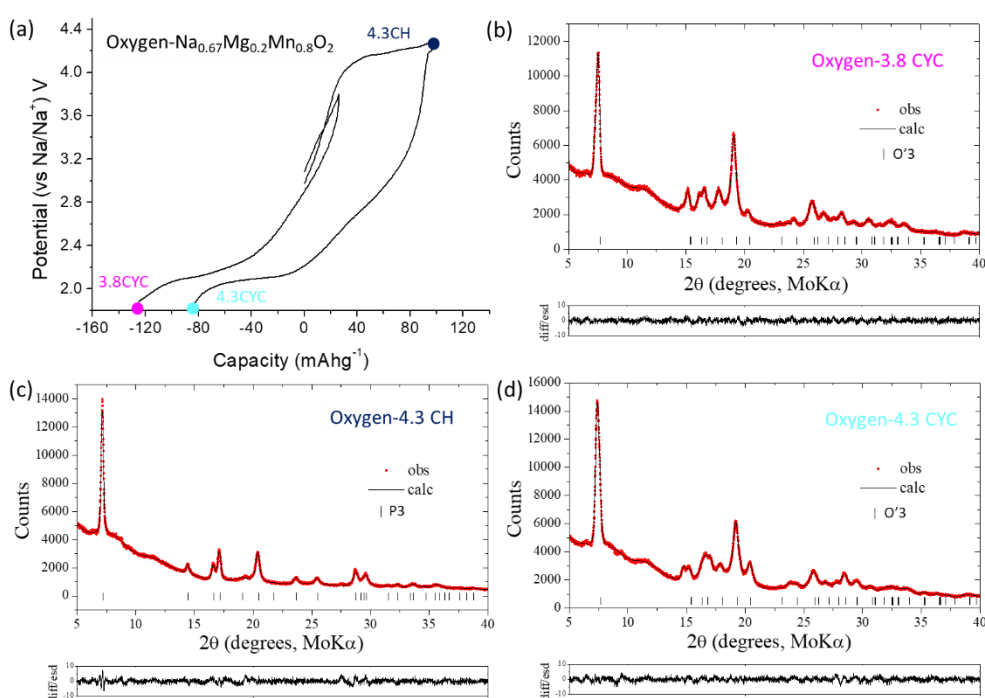


Figure 5.8. (a) Galvanostatic cycling curves recorded at 10 mA g^{-1} for Oxygen- $\text{Na}_{0.67}\text{Mg}_{0.2}\text{Mn}_{0.8}\text{O}_2$ cycled between 1.8-3.8 V and 1.8-4.3 V with the points where PXRD measurements were conducted. Profile fits for Rietveld refinements of (b) Oxygen- $\text{Na}_{0.67}\text{Mg}_{0.2}\text{Mn}_{0.8}\text{O}_2$ cycled between 1.8-3.8 V, (c) Oxygen- $\text{Na}_{0.67}\text{Mg}_{0.2}\text{Mn}_{0.8}\text{O}_2$ charged to 4.3 V and (d) Oxygen- $\text{Na}_{0.67}\text{Mg}_{0.2}\text{Mn}_{0.8}\text{O}_2$ cycled between 1.8-4.3 V. Observed data points are shown in red, with fitted profile in black. Tick marks indicate allowed reflections. (refined by Dr. A. Robert Armstrong.)

Table 4.4. Rietveld refinement results of (a) Oxygen- $\text{Na}_{0.67}\text{Mg}_{0.2}\text{Mn}_{0.8}\text{O}_2$ cycled between 1.8-3.8 V (b) Oxygen- $\text{Na}_{0.67}\text{Mg}_{0.2}\text{Mn}_{0.8}\text{O}_2$ charged to 4.3 V and (c) Oxygen- $\text{Na}_{0.67}\text{Mg}_{0.2}\text{Mn}_{0.8}\text{O}_2$ cycled between 1.8-4.3 V (refined by Dr. A. Robert Armstrong).

(a) Oxygen- $\text{Na}_{0.67}\text{Mg}_{0.2}\text{Mn}_{0.8}\text{O}_2$ cycled between 1.8-3.8 V						
$R_{\text{exp}} : 2.03\%$ $R_{\text{wp}} : 2.44\%$ $82(3)\%$ O'3 18% P3 Lattice parameters O'3 Space group $C2/m$ $a = 5.442(7) \text{ \AA}$ $b = 2.893(2) \text{ \AA}$ $c = 5.752(6) \text{ \AA}$ $\beta = 110.88(5)^\circ$						
atom	Wyckoff symbol	x/a	y/b	z/c	Occupancy	Biso
Mn1/Mg1	2a	0	0	0	0.8/0.2	0.5
Na1	2d	0	0.5	0.5	0.913 (10)	1.2
O1	4i	0.264(2)	0	0.806(2)	1	0.6
Lattice parameters P3 Space group $R3m$ $a = 2.905(4) \text{ \AA}$ $c = 16.63(3) \text{ \AA}$						
Mn1/Mg1	3a	0	0	0	0.8/0.2	0.5
Na1	3a	0	0	0.182(2)	0.74(8)	1.2
O1	3a	0	0	0.389(11)	1	0.6
O2	3a	0	0	0.606(11)	1	0.6

(b) Oxygen- $\text{Na}_x\text{Mn}_{0.8}\text{Mg}_{0.2}\text{O}_2$ charged to 4.3 V						
$R_{\text{exp}} : 2.40\%$ $R_{\text{wp}} : 3.23\%$ 100% P3 Lattice parameters P3 Space group $R3m$ $a = b = 2.8573(8) \text{ \AA}$ $c = 16.890(10) \text{ \AA}$						
atom	Wyckoff symbol	x/a	y/b	z/c	Occupancy	Biso
Mn1/Mg1	3a	0	0	0	0.8/0.2	0.5
Na1	3a	0	0	0.1635(7)	0.499(10)	1.2
O1	3a	0	0	0.3816(14)	1	0.6
O2	3a	0	0	0.6051(12)	1	0.6

(c) Oxygen- $\text{Na}_{0.67}\text{Mg}_{0.2}\text{Mn}_{0.8}\text{O}_2$ cycled between 1.8-4.3 V						
$R_{\text{exp}} : 1.99\%$ $R_{\text{wp}} : 2.6\%$ $46(5)\%$ O'3 54% P3 Lattice parameters O'3 $a = 5.397(11) \text{ \AA}$ $b = 2.894(3) \text{ \AA}$ $c = 5.751(5) \text{ \AA}$ $\beta = 111.44(6)^\circ$						
atom	Wyckoff symbol	x/a	y/b	z/c	Occupancy	Biso
Mn1/Mg1	2a	0	0	0	0.8/0.2	0.5
Na1	2d	0	0.5	0.5	0.845(17)	1.2
O1	4i	0.255(3)	0	0.796(3)	1	0.6
Lattice parameters P3 Space group $R3m$ $a = b = 2.892(2) \text{ \AA}$ $c = 16.65(2) \text{ \AA}$						
Mn1/Mg1	3a	0	0	0	0.8/0.2	0.5
Na1	3a	0	0	0.173(2)	0.62(2)	1.2
O1	3a	0	0	0.377(3)	1	0.6
O2	3a	0	0	0.604(3)	1	0.6

5.3.5. Bulk electronic structure study for Air- $\text{Na}_{0.67}\text{Mg}_{0.2}\text{Mn}_{0.8}\text{O}_2$

XAS measurements were carried out at the Mn K-edge for the samples extracted at the end of charge and discharge cycled over two different voltage windows as shown in Fig. 5.7a. The Mn K-edge XANES spectra are presented in Fig. 5.9a. The Mn valence for each of the samples was calculated from the position of the centroid of the pre-edge (Fig. 5.9b). Comparing the standard references, Mn_2O_3 and MnO_2 to XANES data obtained for the as-synthesised material, the pristine sample contains predominantly Mn^{4+} ions. After charge to 3.8 V, the edge position of the XANES spectrum shifts towards higher energy in agreement with the complete oxidation to Mn^{4+} with a Mn valence of 3.98. The spectrum of the sample further charged to 4.3 V shows no evidence of significant shift, indicating no contribution from the Mn to charge compensation. At the end of discharge, the shape and edge position of the XANES spectra of 3.8 CYC and 4.3 CYC are identical and shift toward lower energy (Fig. 5.9a), representing Mn reduction in good agreement with the Mn oxidation states of 3.21 and 3.17, respectively. Overall, major charge compensation happens *via* Mn before 3.8 V and implies the participation of oxygen beyond 3.8 V.

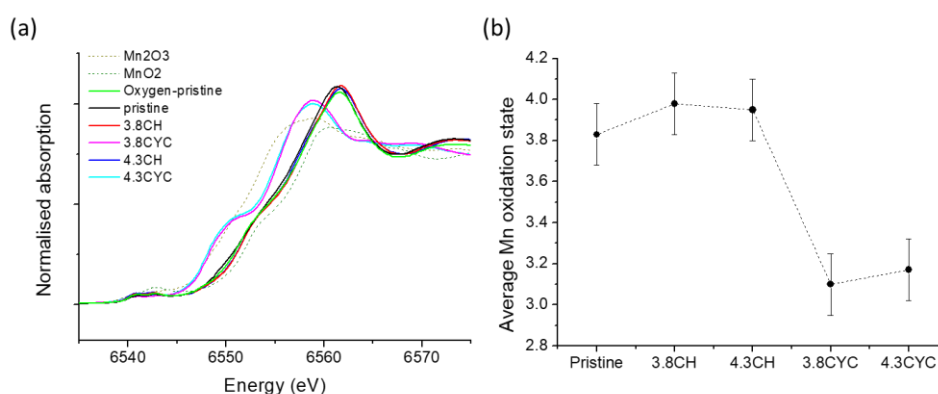


Figure 5.9. (a) Mn K-edge XANES spectra of the ex-situ Air- $\text{Na}_{0.67}\text{Mg}_{0.2}\text{Mn}_{0.8}\text{O}_2$ compared with reference of Mn^{3+} (Mn_2O_3) and Mn^{4+} (MnO_2) and (b) Variation of Mn oxidation state, calculated from the position of the centroid of the pre-edge (analysed by Dr. Dave Pickup at the University of Kent).

5.3.6. Surface study for Air- $\text{Na}_{0.67}\text{Mg}_{0.2}\text{Mn}_{0.8}\text{O}_2$

Changes in the surface of electrochemically cycled electrodes were investigated using XPS. Fig. 5.10 shows the XPS spectra observed for Mn 2p, O 1s and C 1s regions upon cycling in the voltage range 1.8-4.3 V. The points where the spectra were collected are plotted in Fig. 5.10a. The Mn 2p spectra (Fig. 5.10b) demonstrate the existence of Air- $\text{Na}_{0.67}\text{Mg}_{0.2}\text{Mn}_{0.8}\text{O}_2$ materials in the surface of electrodes. Two peaks at 643 and 655 eV can be assigned to

Mn 2p_{3/2} and Mn 2p_{1/2}, respectively.²² There are no significant changes when the material is charged to 3.8 V. In contrast, the intensity of spectra of 4.3 CH and 4.3 CYC is reduced, which might originate from the deposit of electrolyte decomposition products on the active material particle surface. In Fig. 5.10c, the O 1s spectrum of as prepared electrode shows a component at 530 eV, which is characteristic of O²⁻ in the crystal lattice.²³ An additional peak at 532 eV can be attributed to Na₂CO₃, often present in sodium transition metal layered oxides, and/or surface adsorbed species.^{7,24} Two more components at 534 and 535 eV, corresponding to C-O and O=C-O chemical environments are present for all electrodes exposed to the electrolyte. The contribution of these components is substantial especially for the 4.3 CH and 4.3 CYC samples. The release of oxygen from Air-Na_{0.67}Mg_{0.2}Mn_{0.8}O₂ surface may cause chemical oxidation of the electrolyte, which is fundamentally different from the electrolyte decomposition observed for the 3.8 CH where the electrolyte is electrochemically oxidised with the catalytic effect due to the presence of carbon in electrodes.²⁵ In the C 1s spectra (Fig. 5.10d), super C65 mainly contributes to the peak at 285 eV, attributed to C-C and C-H components. The peak at 291 eV can be assigned to C-F in the PVDF backbone and CO₃²⁻ carbon environment. Two additional components at 286.5 and 289 eV, which can be attributed to the C-O and O=C-O components, respectively, are gradually enhanced for the samples charged to 4.3 V. This observation is consistent with that in the O 1s spectra.

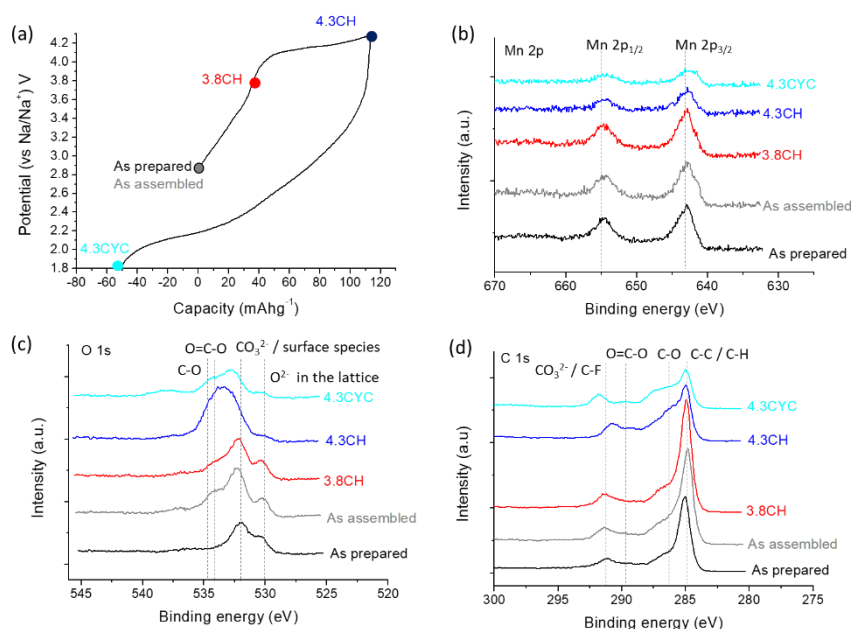


Figure 5.10. (a) Galvanostatic cycling curves recorded at 10 mA g⁻¹ for Air-Na_{0.67}Mg_{0.2}Mn_{0.8}O₂ cycled between 1.8-4.3 V with the points where XPS measurements were conducted. XPS spectra were collected in (b) Mn 2p, (c) O 1s and (d) C 1s regions (measured by Le Anh Ma at Uppsala University).

5.3.7. Exploring abnormal charge capacity on the first cycle

Given that both samples (Air-Na_{0.67}Mg_{0.2}Mn_{0.8}O₂ and Oxygen-Na_{0.67}Mg_{0.2}Mn_{0.8}O₂) charged to 4.3 V deliver abnormal charge capacity on the first cycle beyond their theoretical value and the appearance of plateaus at around 4.2 V is analogous to P3 and P2 type Mg-doped sodium manganese oxides, which exhibit anion redox,^{7,10} the participation of oxygen redox in the initial charge compensation is explored.

Fig. 5.10c shows the charge/discharge curves of Air-Na_{0.67}Mg_{0.2}Mn_{0.8}O₂ cycled between 1.8 and 4.3 V at 10 mA g⁻¹. This sample delivers a first charge capacity of 124 mAh g⁻¹, equivalent to the removal of 0.44 Na ions per formula unit, which is significantly larger than the theoretically expected value (0.25 Na ions). As shown in Fig. 5.10a, the charge compensation of Air-Na_{0.67}Mg_{0.2}Mn_{0.8}O₂ cycled between 1.8 and 3.8 V occurs solely *via* the oxidation of Mn³⁺ with 0.14 Na ions removed. The extra Na ion removal for the sample charged to 4.3 V may take place through the oxygen participation in the charge compensation. To explore this assumption a series of cyclic voltammograms were collected by applying a progressively higher positive potential with a scan rate of 30 μV s⁻¹ from OCV to upper cut-off voltages at 3.3, 3.8 and 4.3 V, fixing the lower cut-off voltage at 1.8 V for each cycle. As shown in Fig. 5.10e, two reduction peaks at around 1.9 and 2.1 V are observed at the first cycle where the

positive potential was applied from OCV to 3.3 V followed by negative potential to 1.8 V. On the subsequent cycle, two oxidation peaks at ca. 2.1 and 2.3 V are observed with the corresponding reduction peaks at around 1.9 and 2.1 V, overlapping with those of the first cycle. This observation indicates that two redox processes related to $\text{Mn}^{3+}/\text{Mn}^{4+}$ occur at about 2.0 and 2.2 V in $\text{Air-Na}_{0.67}\text{Mg}_{0.2}\text{Mn}_{0.8}\text{O}_2$ in a reversible manner. On the following cycle, the oxidation peak at about 4.25 V is coupled to a small reduction peak at about 2.7 V. This large hysteresis is often an electrochemical fingerprint of materials having oxygen redox activity. In addition, the disappearance of the redox process at 1.9 V on the succeeding negative potential sweep implies irreversible changes in the system, perhaps due to a structural transformation with O_2 release.

The stoichiometry of the $\text{Air-Na}_{0.67}\text{Mg}_{0.2}\text{Mn}_{0.8}\text{O}_2$ electrodes extracted at the different states of charge was determined by ICP-OES (normalised to Mn) and the results are presented in Table 5.5. The analysis reveals that the Na content after charging to 3.8 V and 4.3 V is reduced to 0.55 and 0.26, equivalent to the removal of 0.12 and 0.41 Na, respectively. The removed Na amounts agree with those observed from the electrochemical cycling as indicated in Fig. 5.10a and c. The results not only support that the electrochemical reaction until 3.8 V involves a conventional deintercalation mechanism in which Na ions are removed with the simultaneous oxidation of Mn^{3+} to Mn^{4+} but also suggests charge compensation involves oxygen in the high voltage region.

Fig. 5.111b shows the voltage profile of $\text{Oxygen-Na}_{0.67}\text{Mg}_{0.2}\text{Mn}_{0.8}\text{O}_2$ cycled in the range 1.8-3.8 V. The evidence of a lower content of Mn^{3+} in the compound is provided by the smaller charge capacity (26 mAh g^{-1}) compared to that of $\text{Air-Na}_{0.67}\text{Mg}_{0.2}\text{Mn}_{0.8}\text{O}_2$ (40 mAh g^{-1}) at the first cycle. In contrast, slightly higher discharge capacity is delivered from $\text{Oxygen-Na}_{0.67}\text{Mg}_{0.2}\text{Mn}_{0.8}\text{O}_2$. When $\text{Oxygen-Na}_{0.67}\text{Mg}_{0.2}\text{Mn}_{0.8}\text{O}_2$ is charged to 4.3 V, additional Na ions are removed (Fig. 5.111d) analogous to $\text{Air-Na}_{0.67}\text{Mg}_{0.2}\text{Mn}_{0.8}\text{O}_2$ (Fig. 5.111c). The contribution of oxygen redox in this voltage region was examined by collecting a series of cyclic voltammograms following the same protocol as above. As shown in Fig. 5.10f, the oxidation peak at ca. 4.25 V is coupled with a reduction peak at ca. 4.2 V and a broad peak at 2.7 V. Of note, the former reduction peak only emerges in the material prepared under oxygen and the redox pair is reversible on successive cycles as observed in dQ/dV plots (Fig. 5.5f).

Previous work by Meng and co-workers⁵ on P2-type $\text{Na}_{0.78}\text{Ni}_{0.23}\text{Mn}_{0.69}\text{O}_2$ showed that the presence of vacancies in the transition metal slabs can be a source of activation of oxygen

oxidation. Yamada and co-workers²⁶ reported the important role of vacancies in transition metal layers. For example, the extracted Na ions in the transition metal layer of O3-type $\text{Na}[\text{Na}_{1/3}\text{Ru}_{2/3}]\text{O}_2$ (square brackets represent transition metal layers), which exhibits cation ordering in the transition metal slabs, create vacancies as a result of Na ion removal from $[\text{Na}_{1/3}\text{Ru}_{2/3}]$ layers prior to extraction from Na ion layers. The vacancies formed in this way induce oxygen-oxygen bond shortening as well as the rearrangement of electronic structure, in consequence oxygen redox is triggered. The same group demonstrated reversible oxygen redox for $\text{Na}_{4/7}[\square_{1/7}\text{Mn}_{6/7}]\text{O}_2$ (empty square represents vacancies in manganese sites), crystallising in the triclinic space group $P\bar{1}$ where the edge-sharing MnO_6 octahedra build up $\square_{1/7}\text{Mn}_{6/7}\text{O}_2$ slabs with ordering between vacancies and Mn ions and sodium ions located between the slabs.²⁷ In this material, nonbonding oxygen $2p$ orbitals are generated along $\text{Na}^+-\text{O}-\square$ or $\square-\text{O}-\square$ that participate in the reversible oxygen redox. In addition, Coulombic attraction between Na ions and vacancies maintains the transition metal slabs, leading to good cycling stability in the voltage range 3.0-4.7 V where only oxygen is involved in the charge compensation. Li *et al.* also showed reversible oxygen redox for $\text{Na}_{4/7}[\square_{1/7}\text{Mn}_{6/7}]\text{O}_2$ with negligible structural changes in the bulk as well as on the surface upon cycling in the voltage window of 1.5-4.4 V. Experimental and computational studies support that the stable structure originates from the presence of vacancies in transition metal slabs and the absence of Mn cation migration to Na layers.²⁸ Based on the Mn K-edge XANES spectrum (Fig. 5.9a) and the electrochemical behaviour of Oxygen- $\text{Na}_{0.67}\text{Mg}_{0.2}\text{Mn}_{0.8}\text{O}_2$, it is suggested that the presence of vacancies in transition metal slabs in Oxygen- $\text{Na}_{0.67}\text{Mg}_{0.2}\text{Mn}_{0.8}\text{O}_2$ facilitates reversible oxygen redox.

Unlike Oxygen- $\text{Na}_{0.67}\text{Mg}_{0.2}\text{Mn}_{0.8}\text{O}_2$ which exhibits reversible anion redox over several cycles, the oxygen redox in Air- $\text{Na}_{0.67}\text{Mg}_{0.2}\text{Mn}_{0.8}\text{O}_2$ is only dominant at the first cycle and irreversible reactions in the high voltage region limits its cycling performance. In contrast, greater charge capacity gained from wider voltage window can be a benefit in the system. Therefore, cycling in the voltage range 1.8-3.8 V after an initial charging step to 4.3 V was carried out. As shown in Fig. 5.11g, Air- $\text{Na}_{0.67}\text{Mg}_{0.2}\text{Mn}_{0.8}\text{O}_2$ delivers a first charge capacity of 112 mAh g^{-1} and demonstrates stable discharge capacity with capacity retention of 96% over 30 cycles. Plots of the differential capacity versus voltage (Fig. 5.11h) reveal that the anion redox activated on the first charge process results in less phase transformation to O'3 upon discharge to 1.8 V, which is maintained on subsequent cycles in the voltage range 1.8-3.8 V.

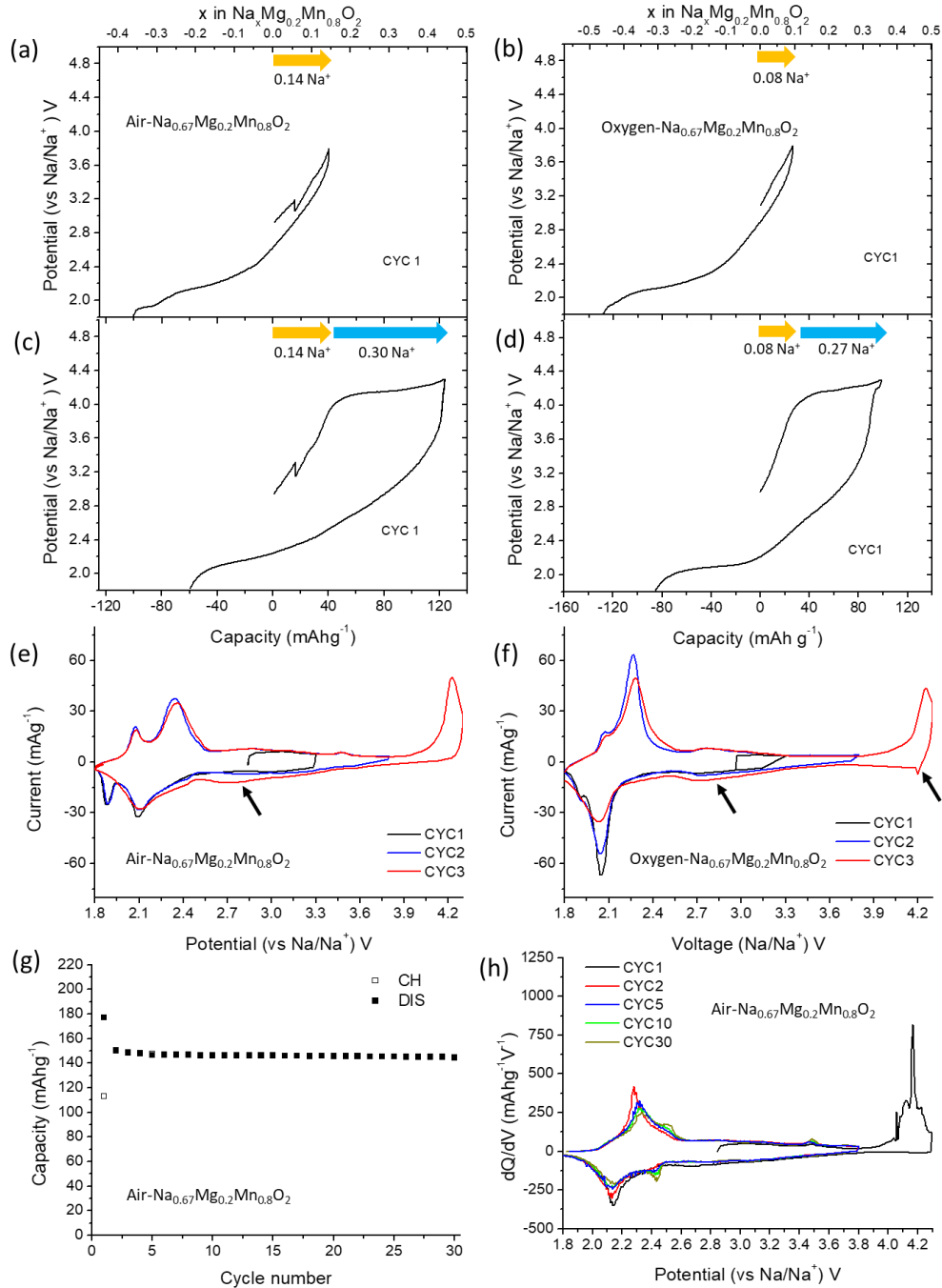


Figure 5.11. Galvanostatic charge/discharge curves of the first cycle recorded at 10 mA g^{-1} for $\text{Air-Na}_{0.67}\text{Mg}_{0.2}\text{Mn}_{0.8}\text{O}_2$ cycled between (a) 1.8–3.8 V, (c) 1.8–4.3 V and for $\text{Oxygen-Na}_{0.67}\text{Mg}_{0.2}\text{Mn}_{0.8}\text{O}_2$ cycled between (b) 1.8–3.8 V, (d) 1.8–4.3 V. Arrows indicate two distinct regions on charging, the yellow corresponds to approximate amount of Na deintercalation in lower voltage region and the blue to additional Na deintercalation in higher voltage region. Voltammetric analysis of (e) $\text{Air-Na}_{0.67}\text{Mg}_{0.2}\text{Mn}_{0.8}\text{O}_2$ and (f) $\text{Oxygen-Na}_{0.67}\text{Mg}_{0.2}\text{Mn}_{0.8}\text{O}_2$ at a scan rate of $30 \mu\text{V s}^{-1}$. Black arrows represent reduction peaks associated with oxygen redox. (g) Galvanostatic cycling performance of $\text{Air-Na}_{0.67}\text{Mg}_{0.2}\text{Mn}_{0.8}\text{O}_2$ cycled at 30°C charged to 4.3 V at the first cycle then cycled between 1.8–3.8 V on following cycles at a rate of 10 mA g^{-1} and (h) Differential capacity vs. voltage plots corresponding to cycle 1 (black), cycle 2 (red), cycle 5 (blue), cycle 10 (green) and cycled 30 (dark yellow) from (g).

Table 5.5. Stoichiometric ratios derived from ICP-OES of $\text{Air-Na}_{0.67}\text{Mg}_{0.2}\text{Mn}_{0.8}\text{O}_2$ extracted at different states of charge (measured at the Yonsei University). The last figure in brackets indicates relative standard deviation.

	Composition from ICP-OES		
	Na	Mg	Mn
Pristine	0.670(6)	0.190(2)	0.800(6)
$\text{Air-Na}_{0.67}\text{Mg}_{0.2}\text{Mn}_{0.8}\text{O}_2$ charged to 3.8 V	0.550(9)	0.200(2)	0.800(7)
$\text{Air-Na}_{0.67}\text{Mg}_{0.2}\text{Mn}_{0.8}\text{O}_2$ charged to 4.3 V	0.260(2)	0.190(1)	0.800(4)

It is known that one of the inherent drawbacks of Li-rich layered oxides is significant voltage decay upon cycling, which limits their commercial use despite their extra capacity delivered by accumulated cation and anion redox processes.²⁹ In contrast, in $\text{Air-Na}_{0.67}\text{Mg}_{0.2}\text{Mn}_{0.8}\text{O}_2$ and $\text{Oxygen-Na}_{0.67}\text{Mg}_{0.2}\text{Mn}_{0.8}\text{O}_2$, the average voltage increases upon cycling over all voltage windows tested as shown in Fig. 5.12a. Comparing the discharge curves at cycle 10 clearly reveals that the materials cycled between 1.8–4.3 V exhibit higher voltage than those cycled over the narrower voltage range (Fig. 5.12b). $\text{Air-Na}_{0.67}\text{Mg}_{0.2}\text{Mn}_{0.8}\text{O}_2$ samples show slightly higher voltage than $\text{Oxygen-Na}_{0.67}\text{Mg}_{0.2}\text{Mn}_{0.8}\text{O}_2$ regardless of voltage cut-off. Interestingly, an initial charge step to 4.3 V increases the voltage of $\text{Air-Na}_{0.67}\text{Mg}_{0.2}\text{Mn}_{0.8}\text{O}_2$ cycled between 1.8–3.8 V on subsequent cycles. The changes in crystal and electronic structures by oxygen redox triggered beyond 3.8 V may be an origin of this phenomenon.

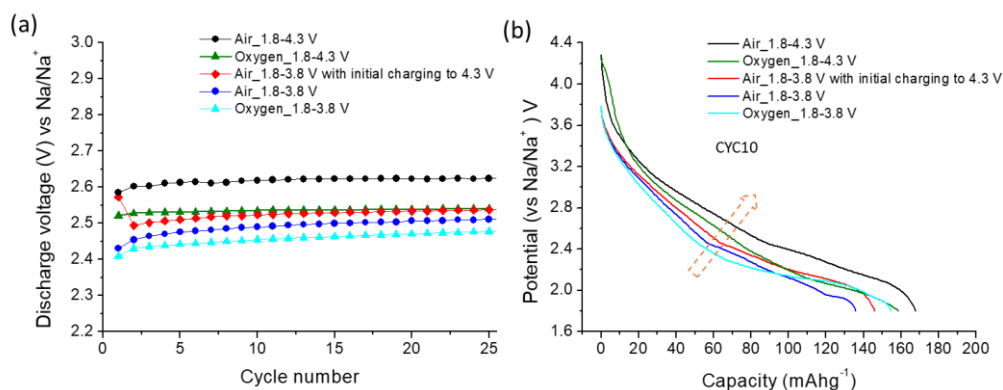


Figure 5.12. (a) Discharge voltage evolution and (b) discharge curves at cycle 10 of $\text{Air-Na}_{0.67}\text{Mg}_{0.2}\text{Mn}_{0.8}\text{O}_2$ cycled between 1.8–4.3 V in black, $\text{Oxygen-Na}_{0.67}\text{Mg}_{0.2}\text{Mn}_{0.8}\text{O}_2$ cycled between 1.8–4.3 V in green, $\text{Air-Na}_{0.67}\text{Mg}_{0.2}\text{Mn}_{0.8}\text{O}_2$ cycled between 1.8–3.8 V with an initial charging step to 4.3 V in red, $\text{Air-Na}_{0.67}\text{Mg}_{0.2}\text{Mn}_{0.8}\text{O}_2$ cycled between 1.8–3.8 V in blue and $\text{Oxygen-Na}_{0.67}\text{Mg}_{0.2}\text{Mn}_{0.8}\text{O}_2$ cycled between 1.8–3.8 V in cyan, cycled at a rate of 10 mA g^{-1} .

5.4. Summary

The P3-type Air- $\text{Na}_{0.67}\text{Mg}_{0.2}\text{Mn}_{0.8}\text{O}_2$ and Oxygen- $\text{Na}_{0.67}\text{Mg}_{0.2}\text{Mn}_{0.8}\text{O}_2$ show stable cycling performance in the voltage range 1.8-3.8 V where the electrochemical reaction is entirely based on the $\text{Mn}^{3+}/\text{Mn}^{4+}$ redox couple. Over the wider voltage window from 1.8 to 4.3 V, the abnormal charge capacity on the initial charge of Air- $\text{Na}_{0.67}\text{Mg}_{0.2}\text{Mn}_{0.8}\text{O}_2$ was carefully examined using *ex-situ* PXRD, XAS, XPS and ICP-OES. It is found that the excess capacity during the first charge mainly originates from the high voltage region and oxygen anions are involved in the charge compensation mechanism accompanied by structural transformation and detrimental reactions on the surface. The limited oxygen-based redox processes at the first cycle for Air- $\text{Na}_{0.67}\text{Mg}_{0.2}\text{Mn}_{0.8}\text{O}_2$ is extended for Oxygen- $\text{Na}_{0.67}\text{Mg}_{0.2}\text{Mn}_{0.8}\text{O}_2$ with a reversible oxygen redox couple observed over 25 cycles. It is believed that the presence of vacancies in the transition metal layers can stabilise labile oxygen. To preserve the P3 structure and promote more vacancies, it would be beneficial to design high Na content and manganese deficient compounds, which are expected to exhibit stable cycling performance as well as reversible oxygen redox.

5.5. References

- 1 N. Yabuuchi, M. Kajiyama, J. Iwatate, H. Nishikawa, S. Hitomi, R. Okuyama, R. Usui, Y. Yamada and S. Komaba, *Nat. Mater.*, 2012, **11**, 512–517.
- 2 N. Yabuuchi, R. Hara, K. Kubota, J. Paulsen, S. Kumakura and S. Komaba, *J. Mater. Chem. A*, 2014, **2**, 16851–16855.
- 3 N. Yabuuchi, R. Hara, M. Kajiyama, K. Kubota, T. Ishigaki, A. Hoshikawa and S. Komaba, *Adv. Energy Mater.*, 2014, **4**, 1301453–1301476.
- 4 E. de la Llave, E. Talaie, E. Levi, P. K. Nayak, M. Dixit, P. T. Rao, P. Hartmann, F. Chesneau, D. T. Major, M. Greenstein, D. Aurbach and L. F. Nazar, *Chem. Mater.*, 2016, **28**, 9064–9076.
- 5 C. Ma, J. Alvarado, J. Xu, R. J. Clément, M. Kodur, W. Tong, C. P. Grey and Y. S. Meng, *J. Am. Chem. Soc.*, 2017, **139**, 4835–4845.
- 6 X. Bai, M. Sathiya, B. M. Sánchez, A. Iadecola, J. Vergnet, R. Dedryvère, M. Saubanère, A. M. Abakumov, P. Rozier and J.-M. Tarascon, *Adv. Energy Mater.*, 2018, **8**, 1802379–1802391.
- 7 U. Maitra, R. A. House, J. W. Somerville, N. Tapia-Ruiz, J. G. Lozano, N. Guerrini, R. Hao, K. Luo, L. Jin, M. A. Pérez-Osorio, F. Massel, D. M. Pickup, S. Ramos, X. Lu, D. E. McNally, A. V. Chadwick, F. Giustino, T. Schmitt, L. C. Duda, M. R. Roberts and P. G. Bruce, *Nat. Chem.*, 2018, **10**, 288–295.
- 8 X. Rong, E. Hu, J. Liu, Y. Liu, Y. Wang, J. Wu, X. Yu, K. Page, Y.-S. Hu, W. Yang, H. Li, X.-Q. Yang, L. Chen and X. Huang, *Joule*, 2018, **2**, 125–140.
- 9 K. Du, J. Zhu, G. Hu, H. Gao, Y. Li and J. B. Goodenough, *Energy Environ. Sci.*, 2016, **9**, 2575–2577.
- 10 B. Song, E. Hu, J. Liu, Y. Zhang, X.-Q. Yang, J. Nanda, A. Huq and K. Page, *J. Mater. Chem. A*, 2019, **7**, 1491–1498.
- 11 A. Le Bail, *Powder Diffraction*, 2005, **20**, 316–326.
- 12 B. H. Toby, *J. Appl. Crystallogr.*, 2001, **34**, 210–213.
- 13 A. A. Coelho, *J. Appl. Crystallogr.*, 2000, **33**, 899–908.
- 14 J. Billaud, G. Singh, A. R. Armstrong, E. Gonzalo, V. Roddatis, M. Armand, T. Rojo and P. G. Bruce, *Energy Environ. Sci.*, 2014, **7**, 1387–1391.
- 15 R. J. Clément, J. Billaud, A. R. Armstrong, G. Singh, T. Rojo, P. G. Bruce and C. P. Grey, *Energy Environ. Sci.*, 2016, **9**, 3240–3251.
- 16 C. Delmas, J. Braconnier, C. Fouassier and P. Hagenmuller, *Solid State Ionics*, 1981, **3-4**,

165–169.

- 17 A. R. Armstrong and P. G. Bruce, *Electrochem. Solid-State Lett.*, 2004, **7**, A1–A4.
- 18 D. H. Lee, J. Xu and Y. S. Meng, *Phys. Chem. Chem. Phys.*, 2013, **15**, 3304–3312.
- 19 H. Wang, B. Yang, X.-Z. Liao, J. Xu, D. Yang, Y.-S. He and Z.-F. Ma, *Electrochim. Acta*, 2013, **113**, 200–204.
- 20 J.-P. Parant, R. Olazcuaga, M. Devalette, C. Fouassier and P. Hagenmuller, *J. Solid State Chem.*, 1971, **3**, 1–11.
- 21 B. M. de Boisse, M. Reynaud, J. Ma, J. Kikkawa, S.-I. Nishimura, M. Casas-Cabanas, C. Delmas, M. Okubo and A. Yamada, *Nat. Commun.*, 2019, **10**, 1–7.
- 22 N. Yabuuchi, K. Yoshii, S.-T. Myung, I. Nakai and S. Komaba, *J. Am. Chem. Soc.*, 2011, **133**, 4404–4419.
- 23 L. Dahéron, R. Dedryvère, H. Martinez, M. Ménétrier, C. Denage, C. Delmas and D. Gonbeau, *Chem. Mater.*, 2008, **20**, 583–590.
- 24 J.-B. Gieu, V. Winkler, C. Courrèges, L. El Ouatani, C. Tessier and H. Martinez, *J. Mater. Chem. A*, 2017, **5**, 15315–15325.
- 25 R. Jung, M. Metzger, F. Maglia, C. Stinner and H. A. Gasteiger, *J. Phys. Chem. Lett.*, 2017, **8**, 4820–4825.
- 26 B. M. de Boisse, G. Liu, J. Ma, S.-I. Nishimura, S.-C. Chung, H. Kiuchi, Y. Harada, J. Kikkawa, Y. Kobayashi, M. Okubo and A. Yamada, *Nat. Commun.*, 2016, **7**, 11397–113406.
- 27 B. M. de Boisse, S.-I. Nishimura, E. Watanabe, L. Lander, A. Tsuchimoto, J. Kikkawa, E. Kobayashi, D. Asakura, M. Okubo and A. Yamada, *Adv. Energy Mater.*, 2018, **8**, 1800409–1800416.
- 28 Y. Li, X. Wang, Y. Gao, Q. Zhang, G. Tan, Q. Kong, S. Bak, G. Lu, X.-Q. Yang, L. Gu, J. Lu, K. Amine, Z. Wang and L. Chen, *Adv. Energy Mater.*, 2018, **9**, 1803087–1803098.
- 29 P. Rozier and J.-M. Tarascon, *J. Electrochem. Soc.*, 2015, **162**, A2490–A2499.

6. P3-type nickel doped sodium manganese oxide

6.1. Introduction

Since the contribution of oxygen anions to the redox processes of P2-type sodium manganese based oxides ($\text{Na}_x\text{M}_y\text{Mn}_{1-y}\text{O}_2$ where $x \approx 0.7$ and $\text{M} = \text{Li}, \text{Mg}, \text{Fe}, \text{Ni}, \text{Zn}$ and mixture of elements) was reported,¹⁻⁷ the use of cumulative cation and anion redox reactions has become a potential strategy to enhance the capacity of positive electrode materials in sodium ion batteries. Oxygen redox has been also revealed in P3-type sodium manganese based oxides which are partially doped with electrochemically inactive elements such as lithium ($\text{Na}_{0.6}\text{Li}_{0.2}\text{Mn}_{0.8}\text{O}_2$)^{8,9} and magnesium ($\text{Na}_{2/3}\text{Mg}_{1/3}\text{Mn}_{2/3}\text{O}_2$).¹⁰

As reported for the P2-type compounds, the substitution of spectator ions for manganese suppresses several structural transitions and Jahn-Teller distortions during cycling, leading to the enhancement of cycling performance.^{3,5,11} The main drawback of electrochemically inert dopants is the decrease in initial capacity, which can be compensated by doping with nickel owing to the $\text{Ni}^{2+}/\text{Ni}^{4+}$ redox couple.¹²⁻¹⁹ There are no studies carried out on P3-type nickel doped sodium manganese oxide, it is therefore of interest to investigate the substitution of nickel for manganese in P3-type sodium manganese oxide to raise its capacity via the $\text{Ni}^{2+}/\text{Ni}^{4+}$ redox couple as well as possible oxygen redox.

This chapter will detail synthesis and characterisation of novel P3-type $\text{Na}_{0.67}\text{Ni}_{0.2}\text{Mn}_{0.8}\text{O}_2$. The participation of oxygen anions in the initial charge compensation mechanism is thoroughly explored using a range of spectroscopic techniques including XANES, Soft XAS (SXAS) and RIXS.

6.2. Experimental methods

This is a summary of the particular procedures and conditions used for this chapter.

- **Synthesis of P3-type $\text{Na}_{0.67}\text{Ni}_{0.2}\text{Mn}_{0.8}\text{O}_2$**

A stoichiometric amount of sodium carbonate (Na_2CO_3 , Fisher Chemistry, $\geq 99.5\%$) was dissolved in DIW (solution A). A separate aqueous solution of nickel (II) acetate tetrahydrate ($\text{Ni}(\text{CH}_3\text{CO}_2)_2 \cdot 4\text{H}_2\text{O}$, Sigma-Aldrich, $\geq 99\%$) and manganese (II) acetate tetrahydrate ($\text{Mn}(\text{CH}_3\text{CO}_2)_2 \cdot 4\text{H}_2\text{O}$, Sigma-Aldrich, $\geq 99\%$) was prepared (solution B). Solution A was added dropwise to solution B under stirring then stirred for 10 min. The water was removed using a rotary evaporator. The resulting solid was heated to 275°C for 12 h and cooled down to 50°C . The powder produced was ground and heated again to 625°C for 3 h then quenched.

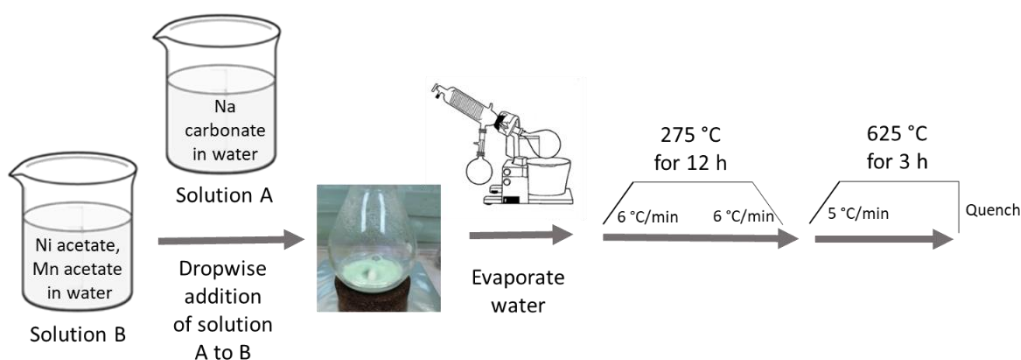


Figure 6.1. Schematic illustration of synthesis procedure.

- **Analyses and characterisation of as-synthesised P3-type $\text{Na}_{0.67}\text{Ni}_{0.2}\text{Mn}_{0.8}\text{O}_2$**

PXRD patterns of as-synthesised P3-type $\text{Na}_{0.67}\text{Ni}_{0.2}\text{Mn}_{0.8}\text{O}_2$ were recorded on a PANalytical Empyrean diffractometer in Bragg-Brentano geometry with $\text{Cu K}\alpha_1$ radiation ($\lambda = 1.5406 \text{ \AA}$). Lattice parameters were obtained by the Le Bail method²⁰ using the GSAS package with the EXPGUI interface.²¹

SEM images of as-synthesised P3-type $\text{Na}_{0.67}\text{Ni}_{0.2}\text{Mn}_{0.8}\text{O}_2$ were recorded on a JEOL JSM-6700F.

ICP-OES analysis was performed using a PerkinElmer Optima 8300 at Yonsei University.

Ni and Mn K-edge XAS spectra were collected in transmission mode at the beamline B18 at the Diamond Light source. Reference spectra were collected for each measurement using Ni and Mn metal foil. At least three scans were taken for each sample and the data were merged, calibrated, background subtracted and normalised using the program Athena.

O K-edge SXAS and RIXS spectra were recorded at the beamline BL27SU at Spring 8 in Japan. The SXAS spectra were normalised following the procedure. i) the signal of sample was divided by the incident intensity. ii) A linear, sloping background is removed by fitting a line to the flat low energy region (520-525 eV) of the SXAS spectrum. iii) The spectrum is normalised by setting the flat low energy region to zero and the post-edge region (560-590 eV) to unity.²²

Time-of-flight PND data were obtained on the GEM diffractometer at ISIS at the Rutherford Appleton Laboratory. Samples were filled in 2 mm quartz capillaries and sealed using vacuum grease in an Ar-filled glovebox then sealed permanently using glue under ambient atmosphere.

- **Preparation of electrodes**

In order to evaluate electrochemical performance of the material, slurries were prepared using the active material (P3-type $\text{Na}_{0.67}\text{Ni}_{0.2}\text{Mn}_{0.8}\text{O}_2$), super C65 carbon and Solef 5130 binder (modified PVDF) in the mass ratio 75: 15: 15 in n-methyl-2-pyrrolidone, which was then cast on aluminium foil using a doctor blade. After drying, 12 mm diameter electrode discs were punched then dried at 80 °C under vacuum for 12 h.

For all *ex-situ* measurements except O K-edge SXAS and RIXS, working electrodes were constructed by mixing the active material (P3-type $\text{Na}_{0.67}\text{Ni}_{0.2}\text{Mn}_{0.8}\text{O}_2$) and super C65 carbon in the mass ratio 75: 25 without binder. The mixture was dried at 110 °C under vacuum for 12 h.

- **Preparation of cells**

CR2325 coin cells were assembled in an Ar-filled glovebox and used for evaluation of electrochemical performance. The cells consisted of a disc electrode, sodium metal as a counter/reference electrode, a glass fibre separator (Whatman, GF/F) and the electrolyte (1M NaClO_4 in propylene carbonate containing 3 % fluoroethylene carbonate by weight).

For *ex-situ* O K-edge SXAS and RIXS measurements, CR2325 coin cells were assembled as described above except that Solupor membranes replaced the glass fibre separator.

For all *ex-situ* measurements except O K-edge SXAS and RIXS, Swagelok-type cells were assembled in an Ar-filled glovebox. The cells consisted of a desired amount of working electrode, sodium metal as a counter/reference electrode, glass fibre separators (Whatman,

GF/F) and the electrolyte (1M NaClO₄ in propylene carbonate containing 3 % fluoroethylene carbonate by weight).

Galvanostatic charge/discharge cycling and voltage scans (linear sweep voltammetry) were carried out at 30 °C using a Maccor Series 4200 battery cycler.

- **Analyses and characterisation of *ex-situ* P3-type Na_{0.67}Ni_{0.2}Mn_{0.8}O₂**

For all *ex-situ* measurements, cycled cells were transferred to an Ar-filled glovebox before opening and the active material was extracted. The electrodes were rinsed carefully with dry dimethyl carbonate to remove residual electrolyte and then left under vacuum for 12 h to ensure all solvent had evaporated.

ICP-OES, XAS, SXAS, RIXS and PND measurements for cycled samples were carried out as described above.

6.3. Results and discussion

6.3.1. Characterisation of as-synthesised P3-type $\text{Na}_{0.67}\text{Ni}_{0.2}\text{Mn}_{0.8}\text{O}_2$

A PXRD pattern of as-synthesised $\text{Na}_{0.67}\text{Ni}_{0.2}\text{Mn}_{0.8}\text{O}_2$ was recorded with Cu $K\alpha_1$ radiation ($\lambda = 1.5406 \text{ \AA}$). As shown in Fig.6.2, all Bragg diffraction peaks of the PXRD pattern can be indexed in the P3 structure model (space group $R3m$), where Na ions occupy trigonal prismatic sites, while Ni and Mn are located in the octahedral sites in a hexagonal unit cell with ABBCCA oxygen stacking. Due to the broad peaks, probably caused by small particle size, refinement was carried out using the Le Bail method and its results are summarised in Table.6.1.

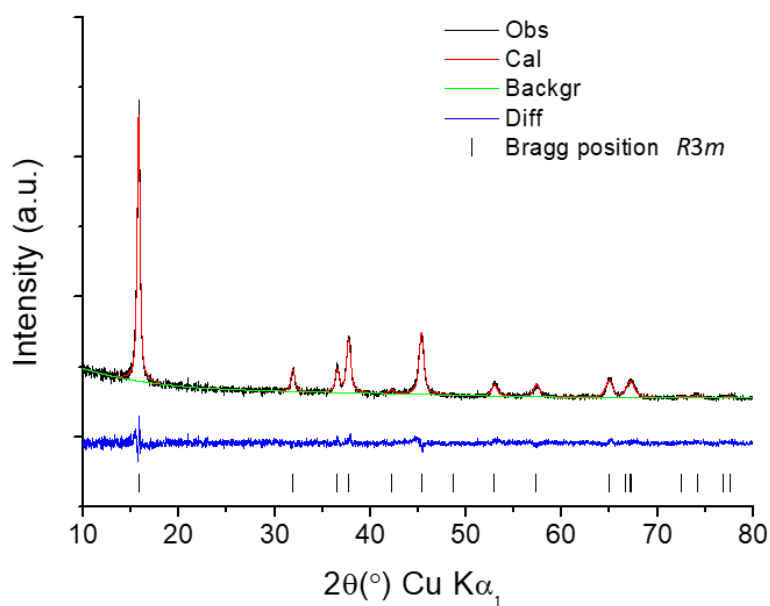


Figure 6.2. Profile fit for Le Bail refinement of as-synthesised $\text{Na}_{0.67}\text{Ni}_{0.2}\text{Mn}_{0.8}\text{O}_2$. Observed data points are shown in black, with fitted profile in red and the difference is shown in blue. Tic marks indicate allowed reflections.

Table 6.5. Le Bail refinement results for as-synthesised $\text{Na}_{0.67}\text{Ni}_{0.2}\text{Mn}_{0.8}\text{O}_2$.

Space Group	Le Bail refinement results	χ^2	R_{wp}
$R3m$ (Hexagonal setting)	$a=b=2.8706(2) \text{ \AA}$, $c=16.8289(8) \text{ \AA}$	0.998	3.77 %

The morphology of as-synthesised $\text{Na}_{0.67}\text{Ni}_{0.2}\text{Mn}_{0.8}\text{O}_2$, characterised by SEM shows primary particles around 100 nm fused together as shown in Fig. 6.3.

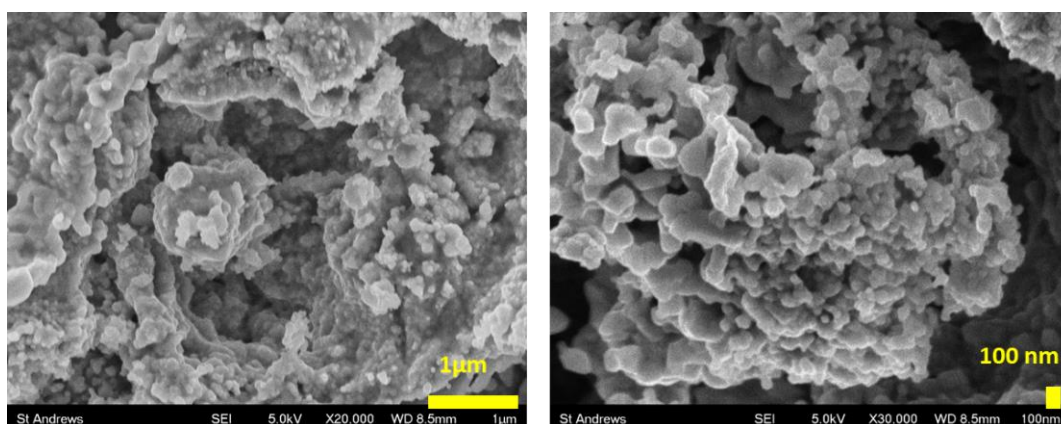


Figure 6.3. SEM images of as-synthesised $\text{Na}_{0.67}\text{Ni}_{0.2}\text{Mn}_{0.8}\text{O}_2$.

The stoichiometry of the as-synthesised compound was determined to be $\text{Na}_{0.600(8)}\text{Ni}_{0.180(2)}\text{Mn}_{0.800}\text{O}_2$ (normalised to Mn) by ICP-OES.

6.3.2. Electrochemical properties

The assembled coin cells with $\text{Na}_{0.67}\text{Ni}_{0.2}\text{Mn}_{0.8}\text{O}_2$ as the active material were galvanostatically cycled over three different voltage windows at a current rate of 10 mA g^{-1} . Based on the composition obtained from ICP-OES, the as-prepared material can theoretically deliver 267 mAh g^{-1} considering one electron transferring. As shown in Fig. 6.4a, the material cycled between 1.8 and 3.8 V delivers a first discharge capacity of 150 mAh g^{-1} and maintains 93% of its initial capacity after 25 cycles. When $\text{Na}_{0.67}\text{Ni}_{0.2}\text{Mn}_{0.8}\text{O}_2$ is charged to 4.1 V, higher initial discharge capacity is delivered (174 mAh g^{-1}) at the expense of cycling stability (capacity retention of 83% over 25 cycles). This trend continues in the widest voltage window (1.8-4.4 V) with an initial discharge capacity of 204 mAh g^{-1} albeit with capacity retention of 49% after 25 cycles. These results are analogous to P2-type $\text{Na}_{2/3}\text{Ni}_{1/3}\text{Mn}_{2/3}\text{O}_2$ whose cycle life is shortened when the material is charged over 4.0 V due to the phase transition to the O2 structure.^{13,14} Over all voltage ranges, the first charge capacity is smaller than that of the discharge as observed in Na deficient oxides. Interestingly, the first charge capacity delivered from the sample charged to either 4.1 or 4.4 V is higher than the value expected solely from the $\text{Ni}^{2+}/\text{Ni}^{4+}$ redox reaction (94 mAh g^{-1}), assuming the Mn remains tetravalent during charging. The excess charge capacity on the first cycle will be further discussed in section 6.3.5.

The differential capacity versus voltage (dQ/dV) plots of $\text{Na}_{0.67}\text{Ni}_{0.2}\text{Mn}_{0.8}\text{O}_2$ cycled in different voltage windows are shown in Fig. 6.4b. The material cycled in the voltage range 1.8-3.8 V

reveals reversible reactions at ca. 1.95, 2.15, 3.27 and 3.57 V. The magnitudes of the latter two redox processes are maintained over 25 cycles whereas those of the former two redox couples continuously diminish along with a shift to higher voltage, leading to an increase in the overall working voltage (Fig. 6.4e). In the dQ/dV plots of the sample cycled between 1.8-4.1 V (Fig. 6.4c), an irreversible oxidation peak at 4.0 V is observed on the first cycle while the four redox couples below 3.8 V are reversible. The irreversible peak can be attributed to a phase change and/or electrolyte decomposition. When the sample is further charged to 4.4 V, new oxidation and reduction peaks appear at ca. 4.2 and 4.1 V, respectively (Fig. 6.4d). The redox process at the highest voltage weakens over cycling accompanied by decreased redox reactions taking place below 3.8 V, resulting in capacity fade.

Cyclic voltammograms were collected by applying a progressively higher positive potential with a scan rate $30 \mu\text{V s}^{-1}$ from OCV to the upper cut-off voltage of 4.4 V with a voltage step 0.2 V, fixing the lower cut-off voltage at 1.8 V. As revealed in Fig. 6.4f, four oxidation peaks are compensated by four reduction peaks in a reversible manner until the upper cut-off voltage reaches 4.0 V. When the positive potential is applied to 4.2 V, a new oxidation peak appears without any corresponding reduction peaks on the following negative potential sweep. On the subsequent cycle, an additional oxidation peak appears at 4.25 V that is coupled to a reduction peak at 4.0 V and a broad peak at 2.7 V. As a large hysteresis is often observed for Li-rich oxides and P3-type $\text{Na}_{2/3}\text{Mg}_{1/3}\text{Mn}_{2/3}\text{O}_2$ ¹⁰ and P2-type $\text{Na}_{2/3}\text{Zn}_{2/9}\text{Mn}_{7/9}\text{O}_2$ ⁷ show a similar feature in their dQ/dV plots, the voltage hysteresis is considered to be an electrochemical fingerprint of oxygen redox active materials. Given that $\text{Na}_{0.67}\text{Ni}_{0.2}\text{Mn}_{0.8}\text{O}_2$ delivers significantly higher first charge capacity than that theoretically expected after charging to 4.4 V and the large hysteresis is found in the sequential voltammograms, it is reasonable to propose the possible participation of oxygen anions in the redox processes of $\text{Na}_{0.67}\text{Ni}_{0.2}\text{Mn}_{0.8}\text{O}_2$.

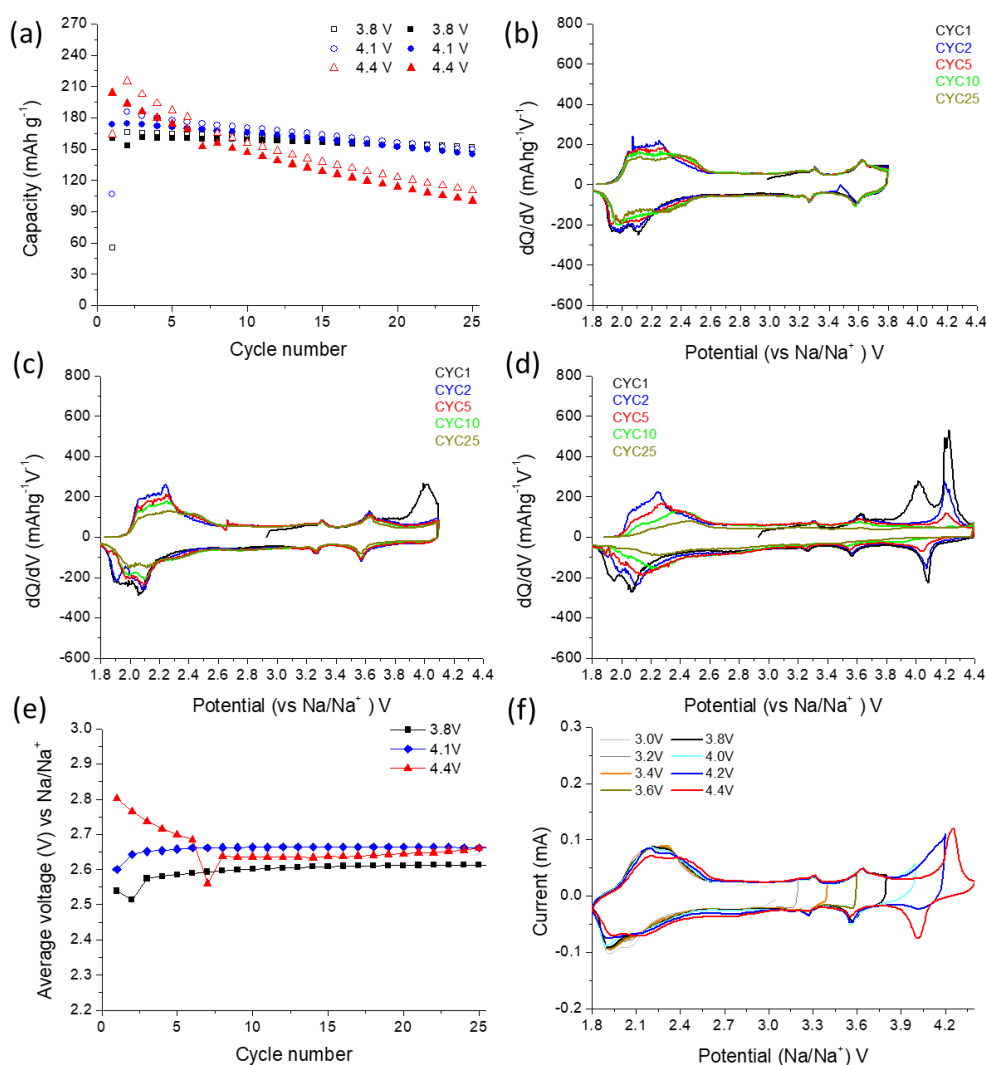


Figure 6.4. (a) Galvanostatic cycling performance of $\text{Na}_{0.67}\text{Ni}_{0.2}\text{Mn}_{0.8}\text{O}_2$ cycled at 30°C in the voltage range 1.8-3.8 V (black), 1.8-4.1 V (blue) and 1.8-4.4 V (red) at a rate of 10 mA g^{-1} . Empty and full symbols represent charge and discharge capacity, respectively. Differential capacity vs. voltage plots corresponding to cycle 1 (black), cycle 2 (blue), cycle 5 (red), cycle 10 (green) and cycled 25 (dark yellow) for $\text{Na}_{0.67}\text{Ni}_{0.2}\text{Mn}_{0.8}\text{O}_2$ cycled at 30°C in the voltage range (b) 1.8-3.8 V, (c) 1.8-4.1 V (d) 1.8-4.4 V at a rate of 10 mA g^{-1} , (e) Discharge voltage evolution of $\text{Na}_{0.67}\text{Ni}_{0.2}\text{Mn}_{0.8}\text{O}_2$ cycled at 30°C in the voltage range of 1.8-3.8 V (black), 1.8-4.1 V (blue) and 1.8-4.4 V (red) at a rate of 10 mA^{-1} , (f) Voltammetric analysis of $\text{Na}_{0.67}\text{Ni}_{0.2}\text{Mn}_{0.8}\text{O}_2$ at a scan rate of $30 \mu\text{V s}^{-1}$.

6.3.3. Bulk electronic structure study for transition metals using XAS

To investigate the changes in oxidation states of Ni and Mn during the first cycle, XAS measurements were conducted at the Ni and Mn K-edges for the samples extracted at different states of charge as presented in Fig. 6.5a. The Ni and Mn K-edge XANES spectra collected during the first cycle are shown in Fig. 6.5b and c, respectively. The Mn valence for

each of the samples was determined from the position of the centroid of the pre-edge (Fig. 6.5d). Due to the lack of references for Ni^{3+} and Ni^{4+} , it was impossible to calculate accurate Ni oxidation states.

Comparing the standard references (NiO , Mn_2O_3 , MnO_2) to data obtained for the as-prepared material, it is evident that the as-synthesised material predominantly consists of Ni^{2+} and Mn^{4+} ions. Mn ions show only a minor participation in the charge compensation and essentially remain tetravalent upon charge and subsequent discharge to 3.8 V. When the sample is further discharged to 1.8 V the edge position of the Mn K-edge spectrum shifts towards lower energy, indicating reduction to Mn^{3+} with a Mn valence of 3.11.

In contrast, Ni ions contribute significantly to the charge compensation mechanism during charging. After charge to 3.8 V, the spectrum of Ni K-edge significantly shifts to higher energy, indicating the oxidation of Ni^{2+} . The spectrum of the sample charged to 4.1 V shows a minor energy shift to higher energy, representing a slight oxidation of Ni ions between 3.8 and 4.1 V. Interestingly, the Ni spectrum shifts towards lower energy when the sample is further charged to 4.4 V, indicating the reduction of Ni ions. The reduction of transition metal cations has been previously reported in $\text{Li}[\text{Li}_{1/3}\text{Fe}_{1/3}\text{Sb}_{1/3}]\text{O}_2$,²³ $\text{Li}[\text{Li}_{1/3}\text{Ru}_{1/3}\text{Sn}_{1/3}]\text{O}_2$ ²⁴ and $\text{Li}[\text{Li}_{1/3}\text{Mn}_{2/3}]\text{O}_2$ ²⁵ (square brackets represent transition metal layers) that accompanies the oxidation of neighbouring oxygen anions, described as the reductive coupling mechanism. Therefore, the reduction of Ni observed after charging to 4.4 V may be an indicator of oxygen redox. Upon successive discharge to 3.8 V, the Ni spectrum shifts back to higher energy, overlapping with that of the sample charged to 3.8 V, implying reversibility of oxygen redox in agreement with the presence of oxidation and reduction peaks at ca. 4.2 and 4.1 V, respectively, in dQ/dV plots over several cycles (Fig. 6.4d). At the end of discharge, Ni ions are reduced with the shifted Ni K-edge spectrum moving to lower energy. These results indicate that, to a large extent, the Ni ions as well as oxygen anions contribute to charge compensation in the voltage range 3.8-4.4 V.

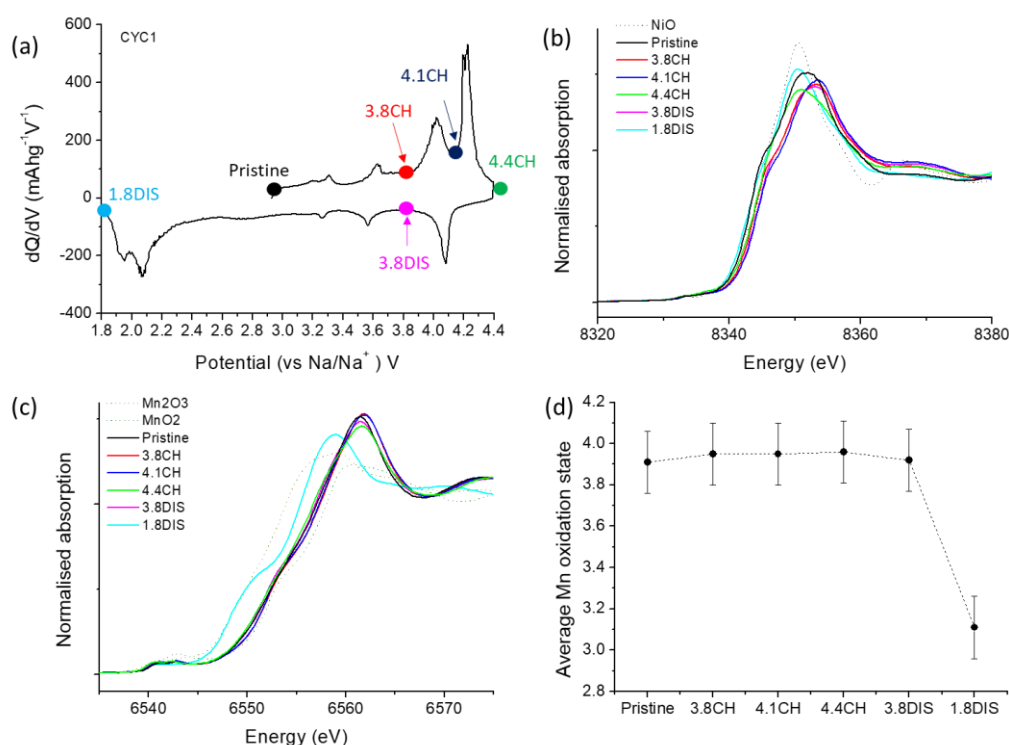


Figure 6.5. (a) Galvanostatic cycling curves recorded at 10 mA g⁻¹ for Na_{0.67}Ni_{0.2}Mn_{0.8}O₂ cycled between 1.8-4.4 V with the points where XAS, SXAS, RIXS and PND measurements were conducted, (b) Ni K-edge XANES spectra of the ex-situ Na_{0.67}Ni_{0.2}Mn_{0.8}O₂ compared with reference of Ni²⁺ (NiO), (c) Mn K-edge XANES spectra of the ex-situ Na_{0.67}Ni_{0.2}Mn_{0.8}O₂ compared with reference of Mn³⁺ (Mn₂O₃) and Mn⁴⁺ (MnO₂) and (d) Variation of Mn oxidation state, calculated from the position of the centroid of the pre-edge (analysed by Dr. Dave Pickup at the University of Kent).

6.3.4. Electronic structure study for oxygen using SXAS and RIXS

To examine the contribution of oxygen to the redox mechanism of Na_{0.67}Ni_{0.2}Mn_{0.8}O₂, SXAS spectra for the O K-edge were collected as a function of the state of charge as shown in Fig. 6.5a. The SXAS was measured using two different detection modes: TFY and TEY mode, which are sensitive to bulk (50 nm) and to surface (2 nm), respectively.

Fig. 6.6a shows the O K-edge SXAS spectra obtained in the TFY mode during the cycle. Each spectrum can be divided into two regions. Pre-edge peaks below 535 eV correspond to the electronic transitions from O 1s states to the unoccupied O 2p hybridised with transition metal 3d orbitals (TM_{3d}-O_{2p}), whereas the broad peaks above 535 eV are attributed to the transitions to the O 2p mixed with transition metal 4s and 4p orbitals (TM_{4sp}-O_{2p}).²⁶ The pre-edge features can be further distinguished by two peaks around 530 eV and 532 eV, corresponding to the characteristic transition to the O 2p orbitals hybridised with transition

metal t_{2g} and e_g states, respectively.^{4,27} Integrated pre-edge peak intensity between 525 and 533 eV can provide information about the distribution of average hole states and the effective charge on the oxygen atoms.^{6,22,25,28} The integrated intensity relative to that of the pristine sample is shown in Fig. 6.6c and is normally a measure of the increased density of hole states upon cycling. When charging $\text{Na}_{0.67}\text{Ni}_{0.2}\text{Mn}_{0.8}\text{O}_2$ to 3.8 V, a decrease in density of hole states is observed, inconsistent with the Ni K-edge XANES results, i.e. the oxidation of Ni is anticipated to create more holes in the $\text{TM}_{3d}\text{-O}_{2p}$ hybrid orbitals. Considering the content of Mn per formula unit and possible O K-edge SXAS transitions, hybridisation with Mn ($\text{Mn}_{3d}\text{-O}_{2p}$) would dominate the O K-edge SXAS spectra.²² In addition, a peak around 534 eV found in the TFY mode may be associated with some components existing on the surface probably caused by electrolyte decomposition as the peak at 534 eV is significantly intense in the TEY mode (Fig. 6.6b). Electrolyte decomposition may induce the reduction of Mn on the surface, leading to the slight decrease in average hole states in $\text{Mn}_{3d}\text{-O}_{2p}$ as reported in Li-rich oxides.²⁹ Further charging to 4.1 V reveals slightly increased hole states but still lower than that of the pristine material. As the spectrum in the TEY mode is analogous to the sample charged to 3.8 V with the presence of a peak at 534 eV, there may be reduction of Mn on the surface. The slight increase might be attributed to oxygen loss from the lattice, affecting the effective charge of oxygen since considerable loss of crystallinity is observed in *ex-situ* PND patterns (Fig. 6.6d). The integrated intensity in the pre-edge region clearly increases at the end of charge to 4.4 V whilst the Mn remains tetravalent and the reduction of Ni is found in the Mn and Ni K-edge XANES spectra. This might be an indicator of the presence of localised holes in O 2p orbitals, which are hardly detectable in the O K-edge SXAS spectra where the $\text{TM}_{3d}\text{-O}_{2p}$ hybridised orbitals dominate spectral features.³⁰ In the case of the sample discharged to 3.8 V, the integrated intensity is reduced possibly as a result of the reduction of oxygen.

In order to reveal more information about the nature of oxygen band states during cycling, RIXS spectra were collected at different excitation energy. The O K-edge RIXS signal arises from the emission from the fully or partially occupied O 2p to the O 1s states, that can provide high sensitivity to define electron and chemical states of oxygen involved in the low energy excitation (525-535 eV). Fig. 6.6e shows the O K-edge RIXS spectra around the 525 eV emission energy for an excitation energy of 530 eV. The intensities are normalised according to the normalised TFY intensities at an incident energy of 530 eV. An interesting feature is a

peak shift from 525.5 eV for the charged sample at 3.8 V to higher energy at 526 eV for the charged sample at 4.4 V. This peak is obviously sensitive to the states of charge during the cycling and can be attributed to hybridised Ni $3d$ -O $2p$ states. This is plausible candidate since partially filled O $2p$ can readily hybridised with Ni $3d$ states. In the previous studies on Li-rich oxides, the appearance and disappearance of a peak at around 524 eV emission energy with excitation energy about 531 eV upon cycling is regarded as a fingerprint of the O $2p$ state changes.^{6,31-33} Clearly, the results of the present study show that a different route for oxygen redox processes is taken. The changes in Ni $3d$ -O $2p$ hybridisation states seem to play an important role. Based on the O K-edge SXAS and RIXS results in combination with Ni and Mn K-edge XANES data, it is reasonable to suggest that oxygen is involved in charge compensation beyond 4.1 V with concomitant changes in both crystal and electronic structures which is often observed in Li-rich oxides having oxygen redox activity.^{22,30,31,34}

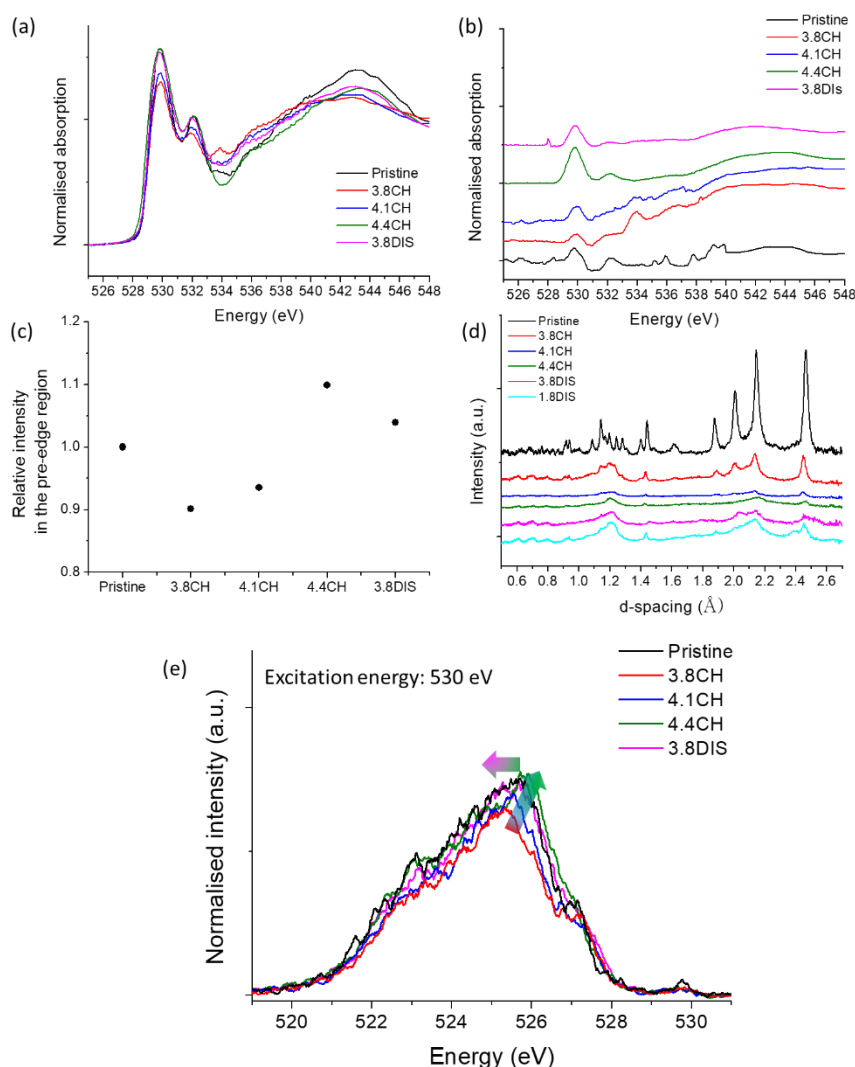


Figure 6.6. O K-edge SXAS spectra recorded in (a) TFY mode (b) TEY mode (measured by Le Anh Ma at the Uppsala University), (c) variation of the relative integrated intensity in the pre-edge region (525–533 eV) for the O K-edge SXAS, (d) PND patterns for $\text{Na}_{0.67}\text{Ni}_{0.2}\text{Mn}_{0.8}\text{O}_2$ extracted at different states of charge and (e) RIXS spectra on the O K-edge with an excitation energy of 530 eV (measured by Le Anh Ma at the Uppsala University).

6.3.5. Oxygen redox activity in $\text{Na}_{0.67}\text{Ni}_{0.2}\text{Mn}_{0.8}\text{O}_2$

From the electrochemical tests and the electronic structure studies using different spectroscopic techniques, it is obvious that oxygen participates in the charge compensation mechanism when $\text{Na}_{0.67}\text{Ni}_{0.2}\text{Mn}_{0.8}\text{O}_2$ is charged to 4.4 V. As shown in Fig. 6.7, the first charge is divided into three regions. In region I (charged to 3.8 V), 0.21 Na ions per formula unit are removed, indicating that the initial charge is entirely compensated by the oxidation of Ni^{2+} , consistent with the composition of the material determined by ICP-OES (Table. 6.2). Subsequent charging to 4.1 V (region II) removes an additional 0.2 Na ions, slightly higher

than that deduced by ICP-OES probably due to the irreversible reactions reflected in the charge capacity value. The removal of 0.32 Na in ICP-OES analysis in general agrees with the completed oxidation to Ni^{4+} (removal of 0.36 Na ions) shown in Ni K-edge spectra. At the end of charging to 4.4 V, the content of Na is reduced to 0.14, equivalent to the removal of 0.46 Na, in a good agreement with the electrochemically removed Na ions in a reversible manner, 0.21 and 0.22 in the region I and III, respectively. These results suggest that the dominant element involved in the charge compensation in the high voltage (region III) is oxygen where the reductive coupling mechanism suppresses further oxygen loss from the lattice.

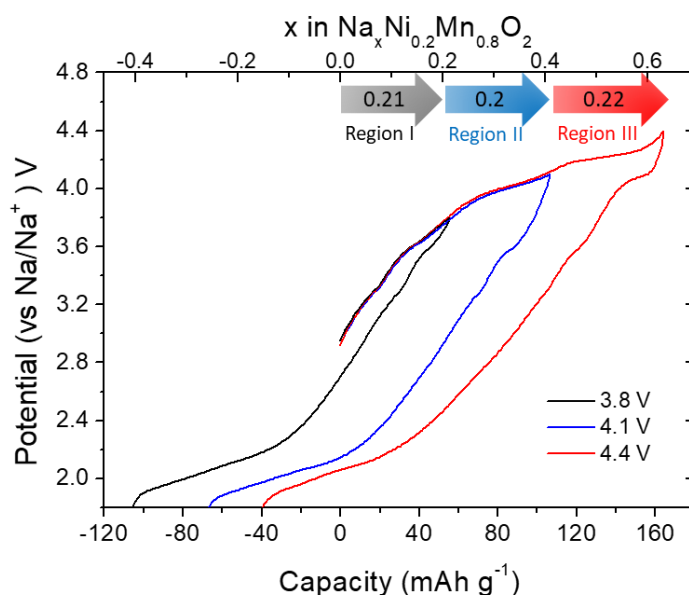


Figure 6.7. Galvanostatic charge/discharge curves of the first cycle recorded at 10 mA g^{-1} for $\text{Na}_{0.67}\text{Ni}_{0.2}\text{Mn}_{0.8}\text{O}_2$ cycled between 1.8–3.8 V (black), 1.8–4.1 V (blue) and 1.8–4.4 V (red). Arrows indicate approximate amount of Na deintercalation in the region I (black), II (blue) and III (red).

Table 6.2. Stoichiometric ratios derived from ICP-OES of $\text{Na}_{0.67}\text{Ni}_{0.2}\text{Mn}_{0.8}\text{O}_2$ extracted at different states of charge (measured at the Yonsei University). The last figure in brackets indicates relative standard deviation.

	Composition from ICP-OES		
	Na	Mg	Mn
Pristine	0.600(8)	0.180(2)	0.800(3)
$\text{Na}_{0.67}\text{Ni}_{0.2}\text{Mn}_{0.8}\text{O}_2$ charged to 3.8 V	0.400(3)	0.170(2)	0.800(6)
$\text{Na}_{0.67}\text{Ni}_{0.2}\text{Mn}_{0.8}\text{O}_2$ charged to 4.1 V	0.280(4)	0.170(2)	0.800(10)
$\text{Na}_{0.67}\text{Ni}_{0.2}\text{Mn}_{0.8}\text{O}_2$ charged to 4.4 V	0.140(1)	0.170(2)	0.800(1)

6.4. Summary

The novel P3-type $\text{Na}_{0.67}\text{Ni}_{0.2}\text{Mn}_{0.8}\text{O}_2$ shows a good cyclability in the voltage range 1.8-3.8 V where the electrochemical reaction is predominantly based on the transition metals. Enlargement of upper cut-off voltage to 4.1 V causes irreversible reactions, leading to the considerable loss of crystallinity. Widening the voltage range to 4.4 V triggers oxygen redox activity stabilised by reduction of Ni. Further work is required to identify the irreversible reactions occurring between 3.8-4.1 V, which is expected to provide strategies to improve cycling performance.

6.5. References

- 1 N. Yabuuchi, M. Kajiyama, J. Iwatate, H. Nishikawa, S. Hitomi, R. Okuyama, R. Usui, Y. Yamada and S. Komaba, *Nat. Mater.*, 2012, **11**, 512–517.
- 2 N. Yabuuchi, R. Hara, K. Kubota, J. Paulsen, S. Kumakura and S. Komaba, *J. Mater. Chem. A*, 2014, **2**, 16851–16855.
- 3 N. Yabuuchi, R. Hara, M. Kajiyama, K. Kubota, T. Ishigaki, A. Hoshikawa and S. Komaba, *Adv. Energy Mater.*, 2014, **4**, 1301453–1301476.
- 4 C. Ma, J. Alvarado, J. Xu, R. J. Clément, M. Kodur, W. Tong, C. P. Grey and Y. S. Meng, *J. Am. Chem. Soc.*, 2017, **139**, 4835–4845.
- 5 E. de la Llave, E. Talaie, E. Levi, P. K. Nayak, M. Dixit, P. T. Rao, P. Hartmann, F. Chesneau, D. T. Major, M. Greenstein, D. Aurbach and L. F. Nazar, *Chem. Mater.*, 2016, **28**, 9064–9076.
- 6 U. Maitra, R. A. House, J. W. Somerville, N. Tapia-Ruiz, J. G. Lozano, N. Guerrini, R. Hao, K. Luo, L. Jin, M. A. Pérez-Osorio, F. Massel, D. M. Pickup, S. Ramos, X. Lu, D. E. McNally, A. V. Chadwick, F. Giustino, T. Schmitt, L. C. Duda, M. R. Roberts and P. G. Bruce, *Nat. Chem.*, 2018, **10**, 288–295.
- 7 X. Bai, M. Sathiya, B. M. Sánchez, A. Iadecola, J. Vergnet, R. Dedryvère, M. Saubanère, A. M. Abakumov, P. Rozier and J.-M. Tarascon, *Adv. Energy Mater.*, 2018, **8**, 1802379–1802391.
- 8 K. Du, J. Zhu, G. Hu, H. Gao, Y. Li and J. B. Goodenough, *Energy Environ. Sci.*, 2016, **9**, 2575–2577.
- 9 X. Rong, E. Hu, J. Liu, Y. Liu, Y. Wang, J. Wu, X. Yu, K. Page, Y.-S. Hu, W. Yang, H. Li, X.-Q. Yang, L. Chen and X. Huang, *Joule*, 2018, **2**, 125–140.
- 10 B. Song, E. Hu, J. Liu, Y. Zhang, X.-Q. Yang, J. Nanda, A. Huq and K. Page, *J. Mater. Chem. A*, 2019, **7**, 1491–1498.
- 11 J. Billaud, G. Singh, A. R. Armstrong, E. Gonzalo, V. Roddatis, M. Armand, T. Rojo and P. G. Bruce, *Energy Environ. Sci.*, 2014, **7**, 1387–1391.
- 12 Z. Lu and J. R. Dahn, *J. Electrochem. Soc.* 2001, **148**, A1225–A1229.
- 13 H. Wang, B. Yang, X.-Z. Liao, J. Xu, D. Yang, Y.-S. He and Z.-F. Ma, *Electrochim. Acta*, 2013, **113**, 200–204.
- 14 D. H. Lee, J. Xu and Y. S. Meng, *Phys. Chem. Chem. Phys.*, 2013, **15**, 3304–3312.
- 15 J. Xu, D. H. Lee, R. J. Clément, X. Yu, M. Leskes, A. J. Pell, G. Pintacuda, X.-Q. Yang, C. P.

- Grey and Y. S. Meng, *Chem. Mater.*, 2013, **26**, 1260–1269.
- 16 H. Hou, B. Gan, Y. Gong, N. Chen and C. Sun, *Inorg. Chem.*, 2016, **55**, 9033–9037.
- 17 P.-F. Wang, Y. You, Y.-X. Yin, Y.-S. Wang, L.-J. Wan, L. Gu and Y.-G. Guo, *Angew. Chem. Int. Ed*, 2016, **55**, 7445–7449.
- 18 G. Singh, N. Tapia-Ruiz, J. M. Lopez del Amo, U. Maitra, J. W. Somerville, A. R. Armstrong, J. Martinez de Ilarduya, T. Rojo and P. G. Bruce, *Chem. Mater.*, 2016, **28**, 5087–5094.
- 19 N. Tapia-Ruiz, W. M. Dose, N. Sharma, H. Chen, J. Heath, J. W. Somerville, U. Maitra, M. S. Islam and P. G. Bruce, *Energy Environ. Sci.*, 2018, **11**, 1470–1479.
- 20 A. Le Bail, *Powder Diffraction*, 2005, **20**, 316–326.
- 21 B. H. Toby, *J. Appl. Crystallogr.*, 2001, **34**, 210–213.
- 22 K. Luo, M. R. Roberts, R. Hao, N. Guerrini, D. M. Pickup, Y.-S. Liu, K. Edström, J. Guo, A. V. Chadwick, L. C. Duda and P. G. Bruce, *Nat. Chem.*, 2016, **8**, 684–691.
- 23 E. McCalla, M. T. Sougrati, G. Rousse, E. J. Berg, A. Abakumov, N. Recham, K. Ramesha, M. Sathiya, R. Dominko, G. Van Tendeloo, P. Novák and J.-M. Tarascon, *J. Am. Chem. Soc.*, 2015, **137**, 4804–4814.
- 24 M. Sathiya, G. Rousse, K. Ramesha, C. P. Laisa, H. Vezin, M. T. Sougrati, M.-L. Doublet, D. Foix, D. Gonbeau, W. Walker, A. S. Prakash, M. Ben Hassine, L. Dupont and J.-M. Tarascon, *Nat. Mater.*, 2013, **12**, 827–835.
- 25 M. Oishi, K. Yamanaka, I. Watanabe, K. Shimoda, T. Matsunaga, H. Arai, Y. Ukyo, Y. Uchimoto, Z. Ogumi and T. Ohta, *J. Mater. Chem. A*, 2016, **4**, 9293–9302.
- 26 F. M. F. de Groot, M. Grioni, J. C. Fuggle, J. Ghijsen, G. A. Sawatzky and H. Petersen, *Phys. Rev. B*, 1989, **40**, 5715–5723.
- 27 S. Hy, J.-H. Cheng, J.-Y. Liu, C.-J. Pan, J. Rick, J.-F. Lee, J.-M. Chen and B.-J. Hwang, *Chem. Mater.*, 2014, **26**, 6919–6927.
- 28 W.-S. Yoon, M. Balasubramanian, K. Y. Chung, X.-Q. Yang, J. McBreen, C. P. Grey and D. A. Fischer, *J. Am. Chem. Soc.*, 2005, **127**, 17479–17487.
- 29 N. Yabuuchi, K. Yoshii, S.-T. Myung, I. Nakai and S. Komaba, *J. Am. Chem. Soc.*, 2011, **133**, 4404–4419.
- 30 J. Wu, Q. Li, S. Sallis, Z. Zhuo, W. E. Gent, W. C. Chueh, S. Yan, Y.-D. Chuang and W. Yang, *Condens. Matter*, 2019, **4**, 1–12.
- 31 J. Xu, M. Sun, R. Qiao, S. E. Renfrew, L. Ma, T. Wu, S. Hwang, D. Nordlund, D. Su, K. Amine, J. Lu, B. D. McCloskey, W. Yang and W. Tong, *Nat. Commun.*, 2018, **9**, 947–957.
- 32 W. E. Gent, K. Lim, Y. Liang, Q. Li, T. Barnes, S.-J. Ahn, K. H. Stone, M. McIntire, J. Hong,

- J. H. Song, Y. Li, A. Mehta, S. Ermon, T. Tyliczszak, D. Kilcoyne, D. Vine, J.-H. Park, S.-K. Doo, M. F. Toney, W. Yang, D. Prendergast and W. C. Chueh, *Nat. Commun.*, 2017, **8**, 1–12.
- 33 M. Okubo and A. Yamada, *ACS Appl. Mater. Interfaces*, 2017, **9**, 36463–36472.
- 34 K. Luo, M. R. Roberts, N. Guerrini, N. Tapia-Ruiz, R. Hao, F. Massel, D. M. Pickup, S. Ramos, Y.-S. Liu, J. Guo, A. V. Chadwick, L. C. Duda and P. G. Bruce, *J. Am. Chem. Soc.*, 2016, **138**, 11211–11218.

7. General conclusion

The work presented in this thesis focuses on high energy positive electrode materials in rechargeable batteries. LiCoPO_4 is explored as a high voltage positive electrode material for LIBs whilst P3-type $\text{Na}_{0.67}\text{Mg}_{0.2}\text{Mn}_{0.8}\text{O}_2$ and $\text{Na}_{0.67}\text{Ni}_{0.2}\text{Mn}_{0.8}\text{O}_2$ are studied as candidates for high capacity positive electrode materials in SIBs.

The first two results chapters propose two strategies to improve electrochemical performance of LiCoPO_4 : using aqueous binders in the electrode system (chapter 3) and substitution of magnesium for cobalt in the active material (chapter 4).

In chapter 3, three different aqueous binders, CMC, ALG, and PAA, were used to fabricate electrodes with LiCoPO_4 synthesised by a solvothermal method. The water-soluble binders show enhanced electrochemical performance compared to the conventional organic-soluble binder (PVDF). In particular, CMC exhibits the best performance in terms of cyclability and rate capability. The origin of the improvements was thoroughly investigated for pre- and post-cycled electrodes using different techniques e.g. SEM, EDS, FT-IR and PXRD. It is revealed that the binder stiffness and the presence of carboxylate groups with high accessibility in CMC are crucial factors to enhance electrochemical properties by providing a uniform electrode surface as well as by suppressing degradation of the active material through scavenging HF in the electrolyte solution.

In chapter 4, magnesium doped lithium cobalt phosphates, $\text{LiMg}_x\text{Co}_{1-x}\text{PO}_4$ ($x = 0, 0.05, 0.10$ and 0.15) were synthesised using a solvothermal method and successful doping was confirmed by PXRD, PND, ICP-OES and EDS. The effects of Mg doping on various properties were investigated including morphology, structure, electrochemical properties, surface and phase evolution during electrochemical cycling. The increased Mg content in the material tends to enlarge particle sizes and reduce anti-site defects. These morphological and structural changes influence electrochemical properties, leading to better capacity retention and rate capability. *Ex-situ* TEM and *operando* PXRD measurements for 15% Mg doped LiCoPO_4 ($\text{LiMg}_{0.15}\text{Co}_{0.85}\text{PO}_4$) reveal the presence of a Mg-rich layer on the surface of the particles and smaller volume changes between lithiated and delithiated phases. Given these results, Mg substitution for Co in LiCoPO_4 may be one of the solutions to mitigate capacity fade owing to the diminished lattice stress during charge and the protective surface layer from detrimental reactions with the electrolyte. To overcome the reduced initial capacity due

to the electrochemical inactivity of Mg and the enlarged particles, it would be beneficial to synthesise Mg doped LiCoPO_4 with smaller particle size.

Combining these two strategies would be interesting to enhance benefits originating from the use of CMC and doping Mg on Co sites. In this way, the degradation of active material due to the detrimental reactions initiated from the electrolyte decomposition at high voltage can be alleviated thanks to the Mg-rich protective layer as well as the HF scavenging role of CMC. Additionally, CMC binder and Mg doping would permit retention of particles and electrode structure upon electrochemical cycling, leading to stable long term cycling performance.

The last two chapters are dedicated to understanding the participation of oxygen in the charge compensation mechanism for P3-type $\text{Na}_{0.67}\text{Mg}_{0.2}\text{Mn}_{0.8}\text{O}_2$ (chapter 5) and $\text{Na}_{0.67}\text{Ni}_{0.2}\text{Mn}_{0.8}\text{O}_2$ (chapter 6) in SIBs as oxygen redox represents an effective way to enhance capacity of electrode materials.

In chapter 5, P3-type $\text{Na}_{0.67}\text{Mg}_{0.2}\text{Mn}_{0.8}\text{O}_2$ was synthesised by a co-precipitation method followed by annealing under air and oxygen to obtain Air- $\text{Na}_{0.67}\text{Mg}_{0.2}\text{Mn}_{0.8}\text{O}_2$ and Oxygen- $\text{Na}_{0.67}\text{Mg}_{0.2}\text{Mn}_{0.8}\text{O}_2$ samples, respectively. Both materials exhibit stable cycling performance in the voltage window 1.8-3.8 V where the electrochemical reaction is entirely based on the $\text{Mn}^{3+}/\text{Mn}^{4+}$ redox couple. The participation of oxygen anions in the charge compensation mechanism is found in the higher voltage region (3.8-4.3 V) through extensive studies of Air- $\text{Na}_{0.67}\text{Mg}_{0.2}\text{Mn}_{0.8}\text{O}_2$ using *ex-situ* PXRD, Mn K-edge XAS, XPS and ICP-OES. Oxygen- $\text{Na}_{0.67}\text{Mg}_{0.2}\text{Mn}_{0.8}\text{O}_2$ shows extended anion redox processes where it is believed that the presence of vacancies in the transition metal layers can stabilise labile oxygen. The oxygen-based redox processes on the first cycle take place with concomitant structural transformation and detrimental reactions on the surface, resulting in capacity fade. The design of high Na content and manganese deficient compounds would be desirable to preserve the P3 structure and promote more vacancies which might permit stable cyclability and reversible anion redox in the wide voltage window (1.8-4.3 V).

In chapter 6, P3-type $\text{Na}_{0.67}\text{Ni}_{0.2}\text{Mn}_{0.8}\text{O}_2$ was synthesised by a co-precipitation method. The material shows stable cycling performance in the voltage range 1.8-3.8 V where the electrochemical reaction is dominated by the transition metals. An irreversible reaction takes place when the material is charged to 4.1 V, causing significant loss of crystallinity. *Ex-situ* measurements using Mn and Ni K-edge XANES, O K-edge SXAS and RIXS reveal that further

charging to 4.4 V activates the oxygen redox, stabilised by Ni reduction. It would be beneficial to identify the irreversible reactions, which could provide hints on enhancement of cycling performance.

In these two P3-type Mg-doped or Ni-doped sodium manganese oxides, irreversible reactions most likely initiated by decomposition of the electrolyte cause capacity fade. However, these studies suggested that the critical role of vacancies and electrochemically active dopant in Mn sites to trigger oxygen redox. It is therefore of interest to substitute other elements such as Li, Ti, Co and mixtures of these elements for Mn to understand the effects of dopants on electrochemical performance. Concomitantly, novel approaches to introduce more vacancies in the transition metal layers need to be considered.

Overall, introduction of aqueous binders and Mg doping in LiCoPO_4 are both promising strategies to enhance electrochemical performance of high voltage LiCoPO_4 for LIBs. Exploring oxygen redox activity in P3-type $\text{Na}_{0.67}\text{Mg}_{0.2}\text{Mn}_{0.8}\text{O}_2$ and $\text{Na}_{0.67}\text{Ni}_{0.2}\text{Mn}_{0.8}\text{O}_2$ provides a possible way to enhance capacity of positive electrode materials for SIBs. To realise high energy LIBs and SIBs whilst exploiting strategies proposed by this thesis study, careful selection of electrolyte and negative electrode material is highly necessary.

Appendix I

Data relating to Chapter 4. Magnesium doped lithium cobalt phosphate.

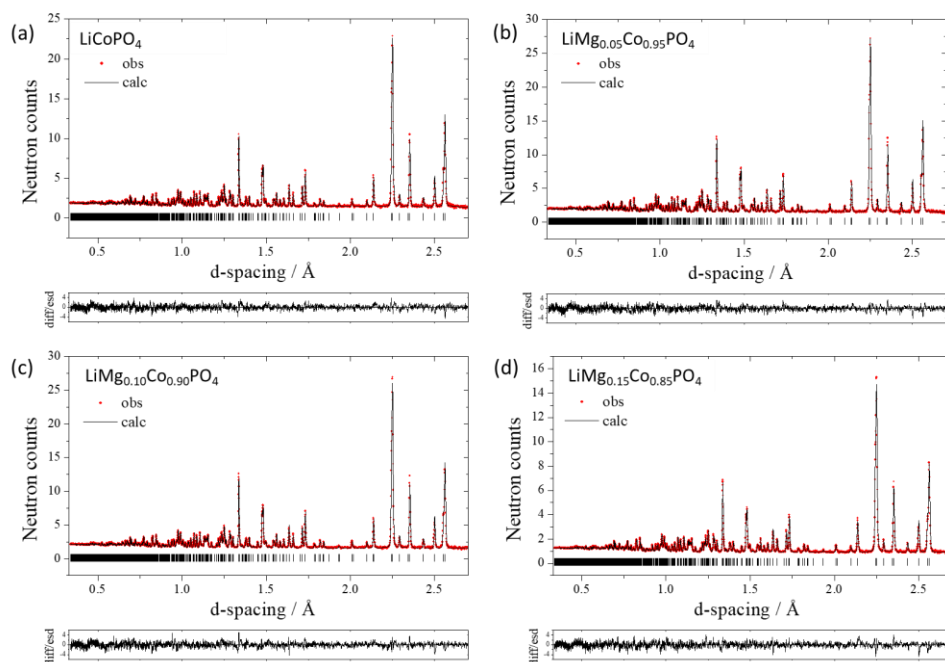


Figure A.I.2. Rietveld refined ND patterns of as-synthesised $\text{LiMg}_x\text{Co}_{1-x}\text{PO}_4$, where (a) $x=0$, (b) $x=0.05$, (c) $x=0.10$ and (d) $x=0.15$ (refined by Dr. A. Robert Armstrong). Observed data points are shown in red, with fitted profile in black and the difference is shown in the lower line.

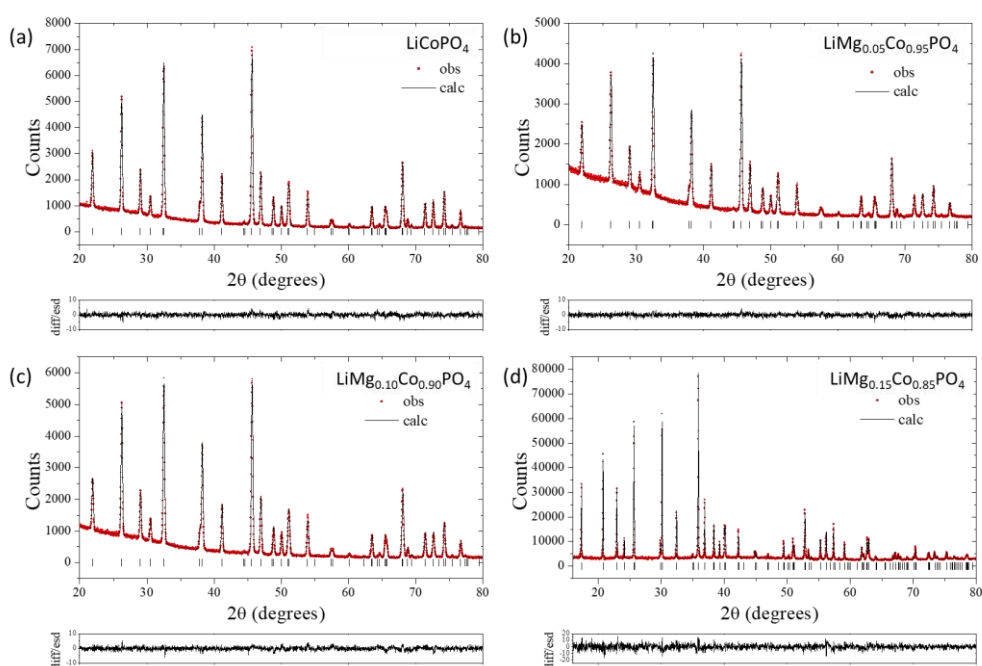


Figure A.I.3. Rietveld refined XRD patterns of as-synthesised $\text{LiMg}_x\text{Co}_{1-x}\text{PO}_4$, where (a) $x=0$, (b) $x=0.05$, (c) $x=0.10$ and (d) $x=0.15$ (refined by Dr. A. Robert Armstrong). Observed data points are shown in red, with fitted profile in black and the difference is shown in the lower line. Tic marks indicate allowed reflections.